

①
Bulletin 48
(Part 4 of 4 Parts)

THE SHOCK AND VIBRATION BULLETIN

Part 4
Vibration Testing, Instrumentation, Loads
and Environments, Tracked Vehicles

SEPTEMBER 1978

A Publication of
THE SHOCK AND VIBRATION
INFORMATION CENTER
Naval Research Laboratory, Washington, D.C.



Office of
The Director of Defense
Research and Engineering

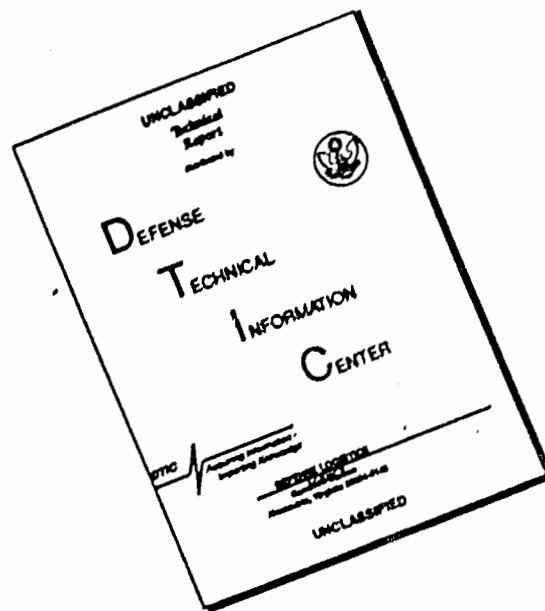
Approved for public release; distribution unlimited.

84 11 20 1978

AD-A148 085

DTIC FILE COPY

DISCLAIMER NOTICE



THIS DOCUMENT IS BEST QUALITY AVAILABLE. THE COPY FURNISHED TO DTIC CONTAINED A SIGNIFICANT NUMBER OF PAGES WHICH DO NOT REPRODUCE LEGIBLY.

SYMPOSIUM MANAGEMENT

THE SHOCK AND VIBRATION INFORMATION CENTER

Henry C. Pusey, Director
Rudolph H. Volin
J. Gordan Showalter
Barbara Szymanski
Carol Healey

Bulletin Production

Graphic Arts Branch, Technical Information Division,
Naval Research Laboratory

Bulletin 48
(Part 4 of 4 Parts)

THE SHOCK AND VIBRATION BULLETIN

September 1978

**A Publication of
THE SHOCK AND VIBRATION
INFORMATION CENTER
Naval Research Laboratory, Washington, D.C.**

The 48th Symposium on Shock and Vibration was held at the Von Braun Civic Center, Huntsville, Alabama on October 18-20, 1977. The U.S. Army Missile Research and Development Command, Redstone Arsenal, Huntsville, Alabama was the host.

**Office of
The Director of Defense
Research and Engineering**

A-1

CONTENTS

PAPERS APPEARING IN PART 4

Vibration Testing

A MATHEMATICAL METHOD FOR DETERMINING A LABORATORY SIMULATION OF THE CAPTIVE-FLIGHT VIBRATIONAL ENVIRONMENT	1
S. Ogden, Pacific Missile Test Center, Point Mugu, CA	
ACOUSTICS OR SHAKERS FOR SIMULATION OF CAPTIVE FLIGHT VIBRATION	5
A.M. Spandrio and M.E. Burke, Pacific Missile Test Center, Point Mugu, CA	
AUTOMATIC ENVIRONMENTAL CONTROL SYSTEM FOR MISSION PROFILE TESTING	15
R. Schilken, Pacific Missile Test Center, Point Mugu, CA	
BROAD-BAND MECHANICAL VIBRATION AMPLIFIER	25
R.T. Fandrich, Harris Corporation, Melbourne, FL	
STABILITY AND FREQUENCY RESPONSE OF HYDRO-MECHANICAL SHAKERS IN VIBRATION RIGS	33
S. Sankar, Concordia University, Montreal, Canada	
MIL-STD-781C RANDOM RELIABILITY TESTING PERFORMED BY USING ACOUSTIC COUPLING	49
S.M. Landre, Harris Corporation, Melbourne, FL	
CONSERVATISM IN RANDOM VIBRATION ANALYSIS AND TESTING	57
T.L. Paez, Sandia Laboratories, Albuquerque, NM	
INCANDESCENT LAMP LIFE UNDER RANDOM VIBRATION	71
C.J. Beck, Jr., Boeing Aerospace Company, Seattle, WA	

Instrumentation

ANGULAR VIBRATION MEASUREMENT TECHNIQUES	83
P.W. Whaley and M.W. Obal, Air Force Flight Dynamics Laboratory, Wright-Patterson AFB, OH	
HIGH FREQUENCY GROUND VIBRATION MEASUREMENT	95
H. Nolle, Monash University, Clayton, Victoria, Australia	

THE RECIPROCITY CALIBRATION OF VIBRATION STANDARDS OVER AN EXTENDED FREQUENCY RANGE	105
R.R. Bouche, Bouche Laboratories, Sun Valley, CA	
A NON-CONTACTING BETA BACKSCATTER GAGE FOR EXPLOSIVE QUANTITY MEASUREMENT	113
P.B. Higgins, F.H. Mathews and R.A. Benham, Sandia Laboratories, Albuquerque, NM	
DATA ACQUISITION SYSTEMS FOR THE IMMEDIATE FUTURE	127
J.F. Schneider, Air Force Weapons Laboratory, Kirtland AFB, NM	

Loads and Environments

THE VIBRATION RESPONSE OF THE PHOENIX MISSILE IN THE F-14 AIRCRAFT CAPTIVE-FLIGHT ENVIRONMENT	139
M.E. Burke, Pacific Missile Test Center, Point Mugu, CA	
SOME DYNAMIC RESPONSE ENVIRONMENTAL MEASUREMENTS OF VARIOUS TACTICAL WEAPONS	151
W.W. Parmenter, Naval Weapons Center, China Lake, CA	
TURBULENT-BOUNDARY-LAYER EXCITATION AND RESPONSE THERETO FOR A HIGH-PERFORMANCE CONICAL VEHICLE	159
C.M. Ailman, McDonnell-Douglas Astro. Corp. Employee for this work. Currently an independent researcher in Los Angeles, CA	
CALCULATION OF ATTACH POINT LOADS DUE TO POSSIBLE COMBUSTION INSTABILITY IN THE SPACE SHUTTLE SOLID ROCKET BOOSTERS	171
F.R. Jensen and D.T. Wang, Hercules Inc., Magna, UT	

Tracked Vehicles

HULL VIBRATORY POWER FLOW AND RESULTING INTERIOR NOISE ON THE M113A ARMORED PERSONNEL CARRIER	181
P.E. Rentz, Bolt Beranek and Newman, Canoga Park, CA	
REDUCING TRACKED VEHICLE VIBRATION AND NOISE HARDWARE CONSIDERATIONS	191
R.B. Hare and T.R. Norris, FMC Corporation, San Jose, CA	
THE USE OF AN EARTH BERM TO REDUCE THE ENVIRONMENTAL NOISE IMPACT OF THE TEST TRACK AT DETROIT ARSENAL	195
N.D. Lewis, U.S. Army Environmental Hygiene Agency, Aberdeen Proving Ground, MD	

PAPERS APPEARING IN PART 1

Keynote Address

KEYNOTE ADDRESS

Dr. John L. McDaniel, Deputy/Technical Director, U.S. Army Missile
Research and Development Command, Redstone Arsenal, AL

Invited Papers

SHOCK RESPONSE RESEARCH AT THE WATERWAYS EXPERIMENT STATION

Colonel John L. Cannon, U.S. Army Engineer Waterways
Experiment Station, Vicksburg, MS

TECHNICAL INFORMATION RESOURCES FOR THE SHOCK AND VIBRATION COMMUNITY

E.J. Kolb, U.S. Army Material Development and Readiness Command
Alexandria, VA

EARTHQUAKES: THEIR CAUSES AND EFFECTS

R.M. Hamilton, U.S. Geological Survey, Reston, VA

Panel Sessions

SOFTWARE EVALUATION

DATA MANAGEMENT

Modal Test and Analysis

FORCE APPORTIONING FOR MODAL VIBRATION TESTING USING INCOMPLETE EXCITATION

G. Morosow, Martin Marietta Corporation, Denver, CO
R.S. Ayre, University of Colorado, Boulder, CO

ON THE DISTRIBUTION OF SHAKER FORCES IN MULTIPLE-SHAKER MODAL TESTING

W.L. Hallauer, Jr. and J.F. Stafford, Virginia Polytechnic Institute
and State University, Blacksburg, VA

MODAL CONFIDENCE FACTOR IN VIBRATION TESTING

S.R. Ibrahim, Old Dominion University, Norfolk, VA

A BUILDING BLOCK APPROACH TO THE DYNAMIC BEHAVIOR OF COMPLEX STRUCTURES USING EXPERIMENTAL AND ANALYTICAL MODAL MODELING TECHNIQUES

J.C. Cromer and M. Lalanne, Institut National des Sciences Appliquées,
Villeurbanne, France
D. Bonnetcase and L. Gaudriot, Metravib, Ecully, France

TRANSFER FUNCTION APPLICATIONS TO SPACECRAFT

STRUCTURAL DYNAMICS

J.R. Fowler, Hughes Aircraft Co., El Segundo, CA

E. Dancy, Hewlett-Packard Co., Los Angeles, CA

LOAD TRANSFORMATION DEVELOPMENT CONSISTENT WITH MODAL SYNTHESIS TECHNIQUES

R.F. Hruda and P.J. Jones, Martin Marietta Corporation, Denver, CO

REDUCED SYSTEM MODELS USING MODAL OSCILLATORS FOR SUBSYSTEMS (RATIONALLY NORMALIZED MODES)

F.H. Wolff and A.J. Molnar, Westinghouse R&D Center, Pittsburgh, PA

CHARACTERIZATION OF TORPEDO STRUCTURAL MODES AND RESONANT FREQUENCIES

C.M. Curtis, R.H. Messier, and B.E. Sandman, Naval Underwater Systems
Center, Newport, R.I. and

R. Brown, Bolt, Beranek and Newman, Cambridge, MA

LAGUERRE FUNCTION REPRESENTATION OF TRANSIENTS

G.R. Spalding, Wright State University, Dayton, OH

PAPERS APPEARING IN PART 2

Isolation and Damping

SPECIFICATION OF DAMPING MATERIAL PERFORMANCE

D.I.G. Jones and J.P. Henderson, Air Force Materials Laboratory,
Wright-Patterson AFB, OH

A REDUCED-TEMPERATURE NOMOGRAM FOR CHARACTERIZATION OF DAMPING MATERIAL BEHAVIOR

D.I.G. Jones, Air Force Materials Laboratory, Wright-Patterson AFB, OH

COMPUTERIZED PROCESSING AND EMPIRICAL REPRESENTATION OF VISCOELASTIC MATERIAL PROPERTY DATA AND PRELIMINARY CONSTRAINED LAYER DAMPING TREATMENT DESIGN

L. Rogers and A. Nashif, Air Force Flight Dynamics Laboratory,
Wright-Patterson AFB, OH

NEW STRUCTURAL DAMPING TECHNIQUE FOR VIBRATION CONTROL

B.M. Patel and G.E. Warnaka, Lord Kinematics, Erie, PA

D.J. Mead, The University Southampton, United Kingdom

VIBRATIONS OF A COMPRESSOR BLADE WITH SLIP AT THE ROOT

D.I. G. Jones, Air Force Materials Laboratory, Wright-Patterson AFB, OH

A. Muszyńska, Institute of Fundamental Technological Research,
Polish Academy of Sciences, Warsaw, Poland

**RESPONSE OF A HELICAL SPRING CONSIDERING HYSTERETIC AND
VISCOUS DAMPING**

P.F. Mlakar and R.E. Walker, U.S. Army Engineer Waterways Experiment
Station, Vicksburg, MS

DAMPING OF AN ENGINE EXHAUST STACK

J.J. DeFelice, Sikorsky Aircraft, Stratford, CT
A.D. Nashif, Anatrol Corporation, Cincinnati, OH

**MULTI-VARIABLE OPTIMIZATION FOR VIBRATION ISOLATION OF
ROAD VEHICLES**

E. Esmailzadeh, Arya Mehr University of Technology, Tehran, Iran

ISOLATION MOUNTS FOR THE HEAO-B X-RAY TELESCOPE

H.L. Hain, Lord Kinematics, Erie, PA
R. Miller, American Science and Engineering, Inc. Cambridge, MA

Impact

BIRD IMPACT LOADING

J.S. Wilbeck, Air Force Materials Laboratory, Wright-Patterson AFB, OH

**FREQUENCY RESPONSE AND DIFFERENTIATION REQUIREMENTS
FOR IMPACT MEASUREMENTS**

A.S. Hu and H.T. Chen, New Mexico State University, Las Cruces, NM

**STRUCTURAL RESPONSE OF EARTH PENETRATORS IN
ANGLE-OF-ATTACK IMPACTS**

J.D. Colton, SRI International, Menlo Park, CA

**SCALING AND PREDICTION OF IMPACT PUNCTURE OF SHIPPING
CASKS FOR RADIOACTIVE MATERIALS**

W.E. Baker, Southwest Research Institute, San Antonio, TX

**FINITE ELEMENT ANALYSIS OF MULTICOMPONENT STRUCTURES
IN RIGID BARRIER IMPACTS**

J.K. Gran, L.E. Schwer, J.D. Colton and H.E. Lindberg,
SRI International, Menlo Park, CA

Blast

**TESTING PIPING CONSTRAINT ENERGY ABSORBERS FOR REACTOR
CONTAINMENT APPLICATIONS**

R.C. Yaeger and R.C. Chou, Franklin Institute Research Laboratories,
Philadelphia, PA

PREDICTION OF CONSTRAINED SECONDARY FRAGMENT VELOCITIES

P.S. Westine, Southwest Research Institute, San Antonio, TX
J.H. Kineke, Jr., Ballistic Research Laboratories, Aberdeen, MD

**IMPEDANCE TECHNIQUES FOR SCALING AND FOR PREDICTING
STRUCTURE RESPONSE TO AIR BLAST**

F.B. Safford, Agbabian Associates, El Segundo, CA

R.E. Walker, U.S. Army Waterways Experiment Station, Vicksburg, MS

T.E. Kennedy, Defense Nuclear Agency, Washington, DC

PROBABILISTIC FAILURE ANALYSIS OF LINED TUNNELS IN ROCK

D.A. Evensen and J.D. Collins, J.H. Wiggins Company, Redondo Beach, CA

PAPERS APPEARING IN PART 3

Structural Analysis

A SOURCE OF LARGE ERRORS IN CALCULATING SYSTEM FREQUENCIES

R.M. Mains, Washington University, St. Louis, MO

**RESEARCH METHOD OF THE EIGENMODES AND GENERALIZED
ELEMENTS OF A LINEAR MECHANICAL STRUCTURE**

R. Fillod and J. Piranda, Laboratoire de Mécanique Appliquée,
Besancon, France

**CALCULATION OF NATURAL FREQUENCIES AND MODE SHAPES OF
MASS LOADED AIRCRAFT STRUCTURES**

P.W. Whaley, Air Force Flight Dynamics Laboratory,
Wright-Patterson AFB, OH

ROCKET MOTOR RESPONSE TO TRANSVERSE BLAST LOADING

N.J. Huffington, Jr. and H.L. Wisniewski, U.S. Army Ballistic Research
Laboratory, Aberdeen Proving Ground, MD

**EXPERIMENTAL AND THEORETICAL DYNAMIC ANALYSIS OF
CARBON-GRAPHITE COMPOSITE SHELLS**

A. Harari and B.E. Sandman, Naval Underwater Systems Center, Newport, RI

**USE OF SHOCK SPECTRA TO EVALUATE JITTER OF A
FLEXIBLE MANEUVERING SPACECRAFT**

W.J. Kacena, Martin Marietta Corporation, Denver, CO

**BUCKLING OF EULER'S ROD IN THE PRESENCE OF
ERGODIC RANDOM DAMPING**

H.H.E. Leipholz, University of Waterloo, Waterloo, Ontario, Canada

**WAVE PROPAGATION IN A CYLINDRICAL SHELL WITH
JOINT DISCONTINUITY**

A. Harari, Naval Underwater Systems Center, Newport, RI

RESPONSE TO MOVING LOADS OVER A CRYSTALLINE HALF-SPACE

S. De, Old Engineering Office, West Bengal, India

**ADJUSTMENT OF A CONSERVATIVE NON GYROSCOPIC MATHEMATICAL
MODEL FROM MEASUREMENT**

L. Bugeat, R. Fillod, G. Lallement, and J. Piranda, Laboratoire de
Mecanique Appliquee, Besancon, France

**FIRST-PASSAGE FAILURE PROBABILITY IN RANDOM VIBRATION
OF STRUCTURES WITH RANDOM PROPERTIES**

N. Nakagawa, and R. Kawai, Kobe University, Kobe, Japan
K. Funahashi, Kawasaki Heavy Industries, Ltd. Kobe, Japan

Fatigue

**FRACTURE MECHANICS APPLIES TO STEP-STRESS FATIGUE UNDER
SINE/RANDOM VIBRATION**

R.G. Lambert, General Electric Company, Utica, NY

RANDOM FATIGUE DAMAGE APPROACH TO MACHINERY MAINTENANCE

T.S. Sankar and G.D. Xistris, Concordia University, Montreal, Quebec, Canada
G.L. Ostiguy, Ecole Polytechnique, Montreal, Quebec, Canada

PAPERS APPEARING IN THE SUPPLEMENT

**ANALYSIS OF ACOUSTIC COATINGS BY THE FINITE
ELEMENT METHOD**

Anthony J. Kalinowski, Naval Underwater Systemc Center,
New London, CT

**DEVELOPMENT AND VALIDATION OF PRELAUNCH SHOCK CAPABILITY
FOR THE NAVY TOMAHAWK CRUISE MISSILE**

W.M. Dreyer, R.E. Martin, R.G. Huntington, General Dynamics
Convair Division, San Diego, CA

VIBRATION TESTING

A MATHEMATICAL METHOD FOR DETERMINING A LABORATORY SIMULATION OF THE CAPTIVE-FLIGHT VIBRATIONAL ENVIRONMENT

SHARON OGDEN
Pacific Missile Test Center
Point Mugu, California

The captive-flight vibrational environment of a missile can be simulated by laboratory induced vibration. The captive-flight vibration levels can be shown to be directly proportional to the dynamic pressure (q) levels. Typically, the captive-flight conditions, combinations of mach number and altitude, can be summarized as a discrete function of time over the entire range of q levels. This paper describes a method for selecting a small number of discrete q levels and associated test time at each level which represents the given captive-flight conditions.

One measurement of how accurately the laboratory test simulates the environment during captive flight is to measure how closely missile failure rate induced by captive flight compares with failure rate induced by the simulation. Ideally the failure rates will be equal. In this method they are made mathematically equivalent with missile failure rate being expressed as a power function of vibration level, and therefore of q level. The exponent of this power function is an unknown but can be approximated by considering a range of numbers of which it is included.

The final solution, a small number of q levels and associated test times, is obtained through iterative calculations. A set of q levels for the laboratory vibration is selected which covers the scope of q levels during captive flight. The time at the selected q levels which yields the same failure rate induced by captive flight over the whole range of levels is calculated for each exponent. The selection of q levels which has the least dependency on the exponent of the failure rate function is the final solution.

This method produces a vibration simulation in terms of a small number of q levels which is based on the whole range of q levels of captive flight. It does not require that the failure rate of a missile nor the exact representation of the failure rate function be known. In fact, the final solution is relatively independent of the failure rate.

INTRODUCTION

The captive-flight vibrational environment of a missile can be simulated by laboratory induced vibration. There are several methods which can be implemented to simulate this environment; many have been developed as a result of mechanical or contractual constraints. The validity of any method depends on the validity of the assumptions, and on the accuracy with which the captive flight vibrational environment can be simulated in the laboratory. This method is primarily a resultant of a contractual restraint placed on the PHOENIX Government Lot Acceptance Test (GLAT) program which is currently simulating the Fleet captive-carry environment with a combined temperature/altitude-vibration test.

The PHOENIX missile in the all-up-round configuration, figure 1, is vibrated with the use of dual shakers during the flight test simulation, (reference 1). The shakers produce vibration levels equivalent to vibration induced by a dynamic pressure (q) of 300 pounds per square foot (psf) and 1,500 psf during captive flight. The percentages of test times at these two q levels are 99.3 and 0.7, respectively. In terms of a typical 72-hour missile test for GLAT the percentages are equivalent to 71.5 hours at 300 psf and 0.5 hours at 1,500 psf. An up-date of these q levels and times was requested for PHOENIX GLAT. The purpose of the following method is to develop a realistic simulation of the captive-flight vibrational environment with the contractual restriction which allows only a small number of q levels for the representation.



Fig. 1 - The AIM-54A PHOENIX Missile

METHOD

Data Base

The captive-flight conditions, combinations of mach number and altitude, of a PHOENIX missile on an F-14A aircraft, can be represented by a function of time over the entire range of q levels. This relation is represented by the bar graph in figure 2, reference (2). A function which relates fraction of captive-flight time to a finite and discrete number of q levels is approximated from figure 2 by reducing the number of q levels to the midpoints of the bar graph; this is shown in table 1. Table 1 will represent the data base information for captive-flight conditions of the PHOENIX missile.

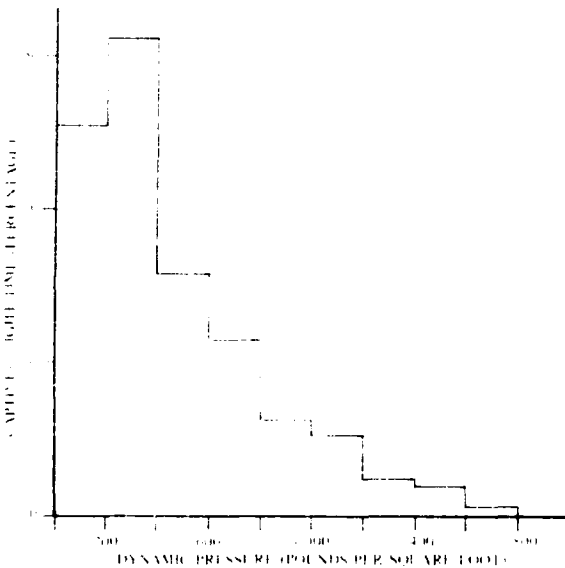


Fig. 2 - PHOENIX Captive-Flight Time Versus Dynamic Pressure

Derivation

Captive-flight vibration and the simulation of captive-flight vibration each induce a certain failure rate in PHOENIX missiles. To measure how accurately the laboratory test simulates the captive-flight environment the failure rates induced by both the simulation and the captive flight are compared. The condition for equality of the failure rates is derived below, in equations (1), (2), and (3), under the assumption of missile failure rate being related to vibration level x . Failure rate may also be related to time, however this relation is not considered.

TABLE 1
Function of q Versus Fraction of
Captive-Flight Time

Value of i	q	$F(q)$
1	100	2.54×10^{-1}
2	300	3.12×10^{-1}
3	500	1.57×10^{-1}
4	700	1.15×10^{-1}
5	900	6.40×10^{-2}
6	1,100	5.20×10^{-2}
7	1,300	2.40×10^{-2}
8	1,500	1.90×10^{-2}
9	1,700	3.00×10^{-3}

The vibration level is directly proportional to the dynamic pressure except through transonic flight, reference (3). The effect of transonic q conditions have been accounted for in the dynamic pressure distribution of table 1.

$$G = cq \quad (1)$$

where

G = Vibration level

c = A constant, dependent on store position and weapon mix

q = Dynamic pressure (psf)

Missile failure rate is a power function of vibration level with an exponent in the range 1 to 5, reference (4).

$$\lambda(G) = G^x/b \quad (2)$$

where

$\lambda(G)$ = Failure rate as a function of vibration level

x = An exponent in the range 1 through 5

b = A constant

therefore,

$$\lambda(q) = k q^x \quad (3)$$

where

$\lambda(q)$ = Failure rate as a function of q

k = A constant, c^x/b

The failure rate induced by captive flight is a summation of the failure rates induced at each of the q levels in the captive-flight envelope multiplied by the fraction of time at those q levels, equation (4).

$$\lambda_{flight} = \int \lambda(q) f(q) dq \quad (4)$$

where

λ_{flight} = Captive-flight failure rate

$f(q)$ = Probability density of q

With the use of table 1 equation (4) is approximated by equation (5):

$$\lambda_{\text{flight}} = \sum_{i=1}^n \lambda(q_i) F(q_i) \quad (5)$$

where

$i = 1$ to n , where n is the number of discrete q levels

$\lambda(q_i)$ = Failure rate as a function of a specific q_i , defined by table 1

$F(q_i)$ = A discrete function that relates fraction of time to q_i , defined by table 1

When equation (3) is substituted into equation (5), equation (6) results.

$$\lambda_{\text{flight}} = k \sum_{i=1}^n q_i^x F(q_i) \quad (6)$$

The failure rate induced by a simulation test is equal to the summation of the fraction of time at each vibration level multiplied by the failure rate caused by those levels of vibration. Each vibration level represents the vibration produced by a different q . The failure rate is expressed by equations (7) and (8):

$$\lambda_{\text{test}} = \sum_{j=1}^m \lambda(G_j) a(q_j) \quad (7)$$

where

$$\sum_{j=1}^m a(q_j) = 1 \quad (8)$$

with

$j = 1$ to m , where m is the number of test levels

λ_{test} = Captive-flight simulation failure rate

$\lambda(G_j)$ = Failure rate as a function of the vibration simulation level G_j used in the simulation

$a(q_j)$ = Fraction of test time spent at the vibration simulation levels representing a specific q_j

Equation (3) is substituted into equation (7) resulting in equation (9).

$$\lambda_{\text{test}} = k \sum_{j=1}^m q_j^x a(q_j) \quad (9)$$

Equations (6) and (9) are equated and simplified to satisfy the mathematical relation which requires that the failure rate of the simulation test be the same as the failure rate of captive-flight vibration stress, yielding equation (10).

$$\sum_{i=1}^n q_i^x F(q_i) = \sum_{j=1}^m q_j^x a(q_j) \quad (10)$$

This is to be interpreted as a condition on the $a(q_i)$ which is to be satisfied (at least approximately) for a certain $F(q_i)$ and x .

Example

To evaluate equation (10) a selection of q levels from the range of captive-flight levels is made; in this example the q levels from the present laboratory test are chosen: 300 psf and 1,500 psf ($m = 2$). Their corresponding times are $a(300)$ and $a(1,500)$. The q levels and associated times for captive flight are taken directly from table 1 ($n = 9$); hence from equation (10) it follows

$$\sum_{i=1}^9 q_i^x F(q_i) = 300^x a(300) + 1,500^x a(1,500)$$

where

$$a(300) + a(1,500) = 1$$

therefore,

$$\sum_{i=1}^9 q_i^x F(q_i) = 300^x a(300) + 1,500^x (1 - a(300))$$

hence

$$a(300) = \left(\sum_{i=1}^9 q_i^x F(q_i) - 1,500^x \right) / (300^x - 1,500^x)$$

The test time is calculated and shown below as a percentage with the value of exponent x ranging from 1 to 5.

Exponent x	$\sum_{i=1}^9 q_i^x F(q_i)$	Percentage of test time	
		$a(300)$	$a(1,500)$
1.0	4.57×10^0	86.9	13.1
2.0	3.32×10^3	88.8	11.2
2.5	9.97×10^4	90.2	9.8
3.0	3.14×10^6	91.4	8.6
3.5	1.03×10^8	92.5	7.5
4.0	3.36×10^9	93.0	7.0
5.0	4.20×10^{12}	94.5	5.5

Selection Criteria

In designing a captive-flight simulation test, the percentage of time, $a(q_j)$, spent at selected vibration levels which represent a specific q , can be calculated using equation (10); however, the value of the exponent x in equation (10) is only known to be within a range of numbers (1 through 5). Since x varies over this range, the ideal percentage of test time to be spent at selected q levels will vary by some Δa . The Δa is the variation in the calculated percentage of test times when a range of values for the parameter x is as shown in equation (10). Table 2 displays the variation in the percentage of test time with the parameter x when selected test levels representing 400 psf and 1,200 psf captive flights are used to simulate Fleet vibration stress. The variation in the test times for this example

is 9.5 percent. If the midpoints were chosen as the test times for simulation, as follows: 88.15 percent at 400 psf and 11.85 percent at 1,200 psf, then Δa would be ± 4.75 percent. To prevent over- or undertesting, it is desirable for this test time to be independent of the value of x , that is Δa equal to zero.

TABLE 2
Variation in Calculated Test Time

Exponent x	Percentage of Test Time at	
	400 psf	1,200 psf
1.0	92.9	7.1
2.0	86.6	13.4
3.0	85.0	15.0
4.0	84.8	15.2
5.0	83.4	16.6

Trial and error is the process used for selecting the q test levels such that the test times are very nearly independent of the exponent x while keeping the number of selected q levels small. Table 3 summarizes the change in Δa in relation to the selection of q levels. Trials one through five use equations (8) and (10) to calculate the time at the two selected levels. Trials six through fourteen also include a judicious selection (based on the data points in table 1) for the time at one of the three selected levels. In the example (table 3) the selected time was chosen for the high q in increments of a half hour of a 72-hour test (0.69 percent is equivalent to 0.5 hours of a 72-hour test). The two q levels of trial three (300 psf and 1,500 psf) are chosen to be a basis for the three level selections for three reasons: (1) these q levels are presently used in PHOENIX GLAT (a contractual reason), (2) they result in a small Δa and (3) they represent a large percentage of the total captive-flight time. The Δa was reduced significantly from the trial three (smallest Δa of two q selections) to trial eleven (smallest Δa of three q selections). However, increasing the number of q levels by adding a fourth q is not beneficial since the Δa would not be reduced a significant amount due to its already small size in trial eleven. Hence, from the viewpoint of contractual and mathematical constraints the three q level selection is necessary and sufficient.

TABLE 3
Variation of Δa With the Selection of q Levels

Trial	Selected q Levels		Δa	Given Percentage of Time at High q^*	
1	200	1,500	7.15		
2	200	1,600	7.2		
3	300	1,500	3.8		
4	300	1,600	4.05		
5	400	1,200	4.75		
6	300	800	1,500	41.27	0.69
7	300	1,000	1,500	7.68	0.69
8	300	1,000	1,500	5.63	1.39
9	300	1,100	1,500	2.06	0.69
10	300	1,100	1,500	0.94	1.39
11	300	1,100	1,500	0.82	2.03
12	300	1,100	1,500	1.69	2.78
13	300	1,200	1,500	0.92	0.69
14	300	1,200	1,500	1.52	1.39

*For three level calculations only.

CONCLUSIONS

A method has been developed which reproduces the vibrational stress of the captive-flight experience of a missile. This method is preferred over current methods for the following reasons:

- (1) It allows for the missile failure rate function to be known only within a set of bounds on parameters;
- (2) It provides for the vibration test to be conducted at a small number of levels;
- (3) It begins with only the range of q levels and associated times at these q levels experienced by a missile.

This method provides a representation of the full range of q levels during captive flight which is independent of the missile failure rate function.

REFERENCES

1. Ryden, C. V. "Dual Shaker Vibration Facility." The Shock and Vibration Bulletin, Bulletin 46, Part 3, pp. 27-53, August 1976.
2. Burke, M. E., S. A. Ogden. "Flight Test Simulation Method for PHOENIX AIM-54A Missile." TP-77-13, Pacific Missile Test Center, Point Mugu, California, publication in process.
3. Piersol, A. G. "Vibration and Acoustic Test Criteria for Captive Flight Externally Carried Aircraft Stores." Digitek Corporation, AFFDL-TR-71-158, December 1971, pp. 21.
4. Elliott, T. W. "Vibro-Acoustic Testing of Air-Launched Guided Missiles at the Pacific Missile Test Center." TP-76-16, Pacific Missile Test Center, Point Mugu, California, 11 August 1976.

ACOUSTICS OR SHAKERS FOR SIMULATION OF CAPTIVE FLIGHT VIBRATION

A. M. Spandrio and M. E. Burke
Pacific Missile Test Center
Point Mugu, California

Laboratory simulation of the failure producing vibration loads to which air-launched missiles are exposed in the captive flight environment has become an important cost effective test method. For the test to be valid, simulation of the failure rate and types of failures produced must be the same as those produced in captive flight. This paper compares two methods that are currently being used to simulate the captive flight vibration loads the PHOENIX missile experiences on the F-14 aircraft. A dual shaker vibration facility was developed for captive flight simulation as part of the PHOENIX GLAT program. Captive flight simulation using acoustical excitation will be used as part of the PHOENIX Logistics Engineering Improvement Program (LEIP). PHOENIX captive flight vibration response will be discussed in terms of direction, spatial and spectral distribution, and then compared to the missile vibration response achieved in the laboratory by the two aforementioned methods. Missile captive flight data was obtained from the PHOENIX T-1/F-14A Flight Test Program and the PHOENIX/F-14 Captive Flight Vibration Measurement Program. In these programs the PHOENIX T-201 Environmental Measurements Missile was used. This same missile was subjected to captive flight simulation using the dual shaker vibration and acoustical vibration. PHOENIX T-201 was assembled in the same instrumentation configuration during both simulations as it was in the captive flight programs. Internal accelerometers were used at 36.8, 57.0, 129.1 and 146.9 inches (0.93, 1.45, 3.28, and 3.73 meters) along the missile length. They were mounted in the lateral, vertical, and horizontal directions. The excitation of the missile by acoustics more nearly resembled that seen in captive flight than the excitation provided by the dual shakers. Since the acoustic excitation allows the missile to vibrate in three axes simultaneously, the simulation technique becomes far superior when the single axis constraint of shakers is considered. In addition, several test specimens may be placed in the acoustic chamber simultaneously (PHOENIX LEIP will have four). As a result, the use of acoustics for simulation of captive flight vibration has demonstrated itself to be an accurate and cost effective test method.

INTRODUCTION

A test method has been developed at the Pacific Missile Test Center (PMTTC), Point Mugu, California whereby the captive flight reliability of an air-launched missile is evaluated under laboratory conditions. The key to this captive flight simulation is the accurate reproduction in the laboratory of the environments seen by the missile under actual captive flight conditions.

One environment deemed significant is that of vibration. Two methods of inducing vibration in the PHOENIX missile are being employed at this time. One method is excitation of the missile by acoustic

noise. This method will be used as part of the PHOENIX Logistics Engineering Improvement Program (LEIP).

The second method of inducing vibration in the PHOENIX missile is accomplished with electrodynamic shakers attached to the missile. This method is used as part of the PHOENIX Government Lot Acceptance Test (GLAT) Program that was established several years ago and is contractually binding for performance of GLAT.

This report will present a comparison of the vibration response of the PHOENIX missile when

excited by shakers. Both responses will be compared to actual captive flight data obtained from two extensive captive flight vibration measurement programs. It will be shown that acoustics provide the superior stimulation of the missile vibration when resemblance to captive flight vibration is used as the scoring criteria. Further, some distinct advantages in using the acoustic test will also be presented.

Test Specimen

The test specimen used to acquire the data illustrated in this report was the Environmental Measurements Missile PHOENIX T-201. Hughes Aircraft Company configured the instrumentation in the missile and took responsibility for its maintenance and calibration.

The missile was configured with internal accelerometers on major structural assemblies at positions located 36.8, 57.0, 129.1, and 146.9 inches (0.93, 1.45, 3.28, and 3.73 meters) from the nose along the length of the missile. These positions were identified as 1, 2, 3, and 4 respectively when referenced to vibration data. Axis orientation is illustrated in figure 1 where the longitudinal is identified as the x direction, lateral is y, and vertical is z. Thus, the response of an accelerometer at a position 57.0 inches (1.45 meters) from the nose of the missile in the lateral direction would be identified as 2y.

All necessary accelerometer signal conditioners and tape recorder were mounted in the missile. Data collection, reduction and plotting were carried out with the same equipment for flight and laboratory simulations to minimize inconsistency of data due to equipment variations.

Captive Flight Vibration

In order to accurately reproduce the vibration conditions encountered by the PHOENIX missile, two programs to gather captive flight vibration data were conducted. Missile captive flight data was obtained from the PHOENIX T-1/F-14A Flight Test Program and the PHOENIX/F-14 Captive Flight Vibration Measurement Program. In these programs, the PHOENIX T-201 Environmental Measurements Missile was used.

Over 720 flight data samples were available for each accelerometer over a wide range of flight speeds and altitudes. Data was selected and plotted in the form of Power Spectral Density (g^2/Hertz) versus Frequency (Hertz). Steady state captive flight conditions varied from Mach numbers of 0.68 to 1.60 and altitudes from 2,000 to 35,000 feet (609.6 to 10,668 meters) for this analysis. Then, using the relationship that overall "g" level for each plot is proportional to flight dynamic pressure, q , in pounds per square foot (psf), the plots were normalized to a q of

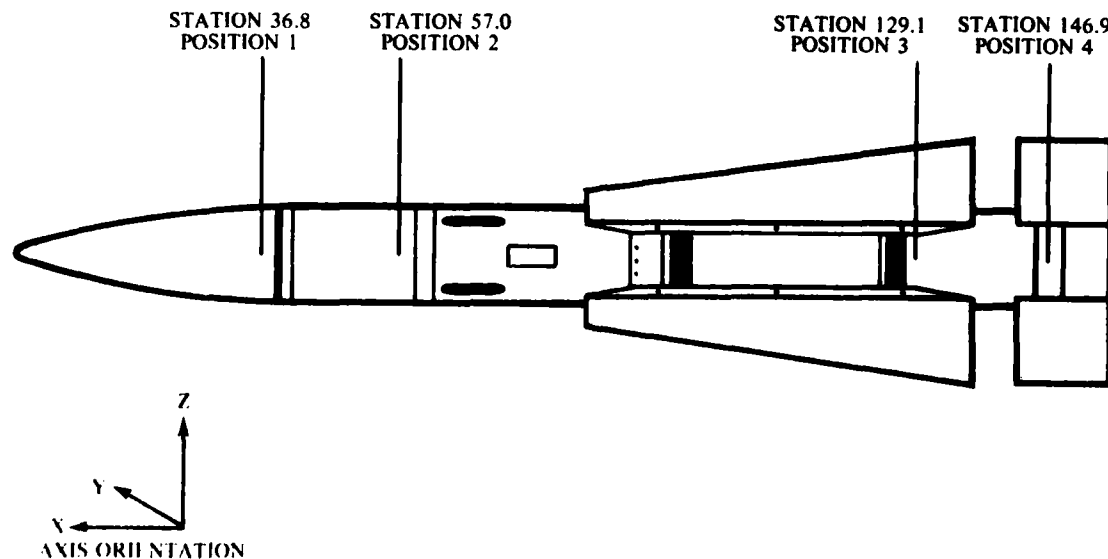


Figure 1. PHOENIX T-201 Environmental Measurements Missile.

980 psf 4.69×10^{-5} dynes per square centimeter, and combined as a composite. An envelope resulted from which an average plot was drawn. This plot is the one presented. Captive flight vibration plots are illustrated in figures at the end of this report.

Reverberant Acoustic Flight Test Simulation

Facility

The simulation of the captive flight vibration of the PHOENIX missile for LEIP will be conducted in a reverberant acoustic chamber. The acoustic chamber is a rectangular room with 8 inch (20.32 centimeters) thick reinforced concrete walls, ceiling and floor. The room dimensions are 16 feet by 13 feet by 10 feet (3.96 by 3.05 meters). The air modulator, supplying the acoustic energy, is a LingModel EPT 1094 rated at 10,000 acoustic watts (10,000 joules per second). The unit operates on compressed air supplied by a large reciprocating compressor. The modulator is coupled to the chamber by a steel and fiberglass exponential horn with a computed low frequency cut-off of 100 Hertz and a one square meter mouth. The electrical control signal to the modulator was shaped from a wide band random noise source to obtain the optimum response from the missile as seen by the response of the individual accelerometers.

Procedure

Since the flight test simulation will be a portion of the PHOENIX LEIP program, it was necessary to conduct a series of tests in the acoustic chamber with the instrumented PHOENIX missile T-201. This series of tests was to develop a chamber/missile configuration that would produce vibration responses in the missile resembling as closely as possible those responses seen in captive flight.

For all tests, a large rectangular box was placed over the nose of the missile to simulate an anechoic chamber. In the LEIP FTS, the anechoic chamber will have a RF radiating source to check the missile's tracking ability. In addition, an acoustically transparent shroud was placed around the missile to simulate the shroud used to channel temperature conditioned air over the outside of the missile.

Results

It was found that a very good resemblance of the captive flight vibration response of the PHOENIX missile could be obtained in the acoustic chamber. An overall sound pressure level of 153 dB (re: 2×10^{-5} newtons/m²) was generated in the chamber. The average response from three microphones placed in the chamber is shown in figure 2.

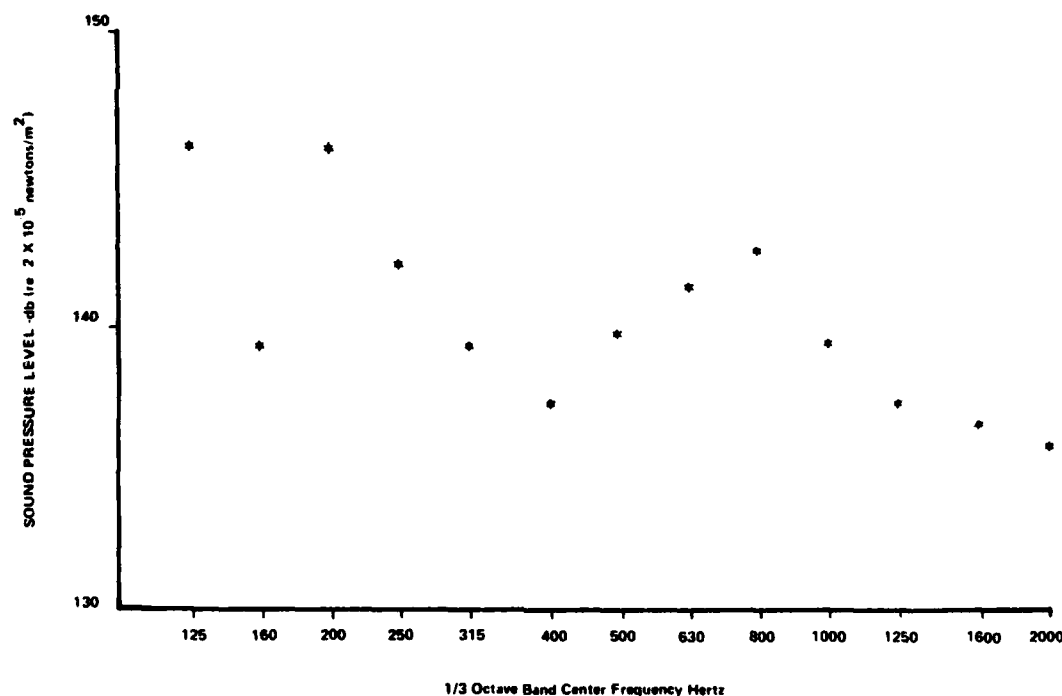


Figure 2. The Average of Sound Pressure Level from Three Microphones in the Reverberant Acoustic Flight Test Simulation Facility.

It was also necessary to acoustically shroud the front half of the missile to reduce the acoustic energy to that area. Captive flight information showed a reduction of vibration levels in these areas of over 2 to 1 when compared to the rear half. It was also determined that suspending the missile in a rigid fashion was as satisfactory as the classical "soft" suspension as reflected in missile response for the frequencies of interest.

Vibration responses of the missile are illustrated at the end of this report.

Dual Shaker Flight Test Simulation

Facility

The PHOENIX GLAT Flight Test Simulation is currently conducted using two electrodynamic shakers

vibrating the missile. One shaker is attached by a collar fixture at station 2 on the missile and the other is attached at station 3. Figure 3 illustrates the installation.

The shakers are Ling Model 310s rated at 10,000 pounds of force (4.45×10^9 dynes). They are controlled via power amplifiers by independent random noise controllers. As with the acoustic test, the input to the shakers was shaped to obtain the optimum response from the missile as seen in the response of the individual accelerometers.

Procedure

Tests were conducted with this installation and missile T-201. The test requires that the missile be

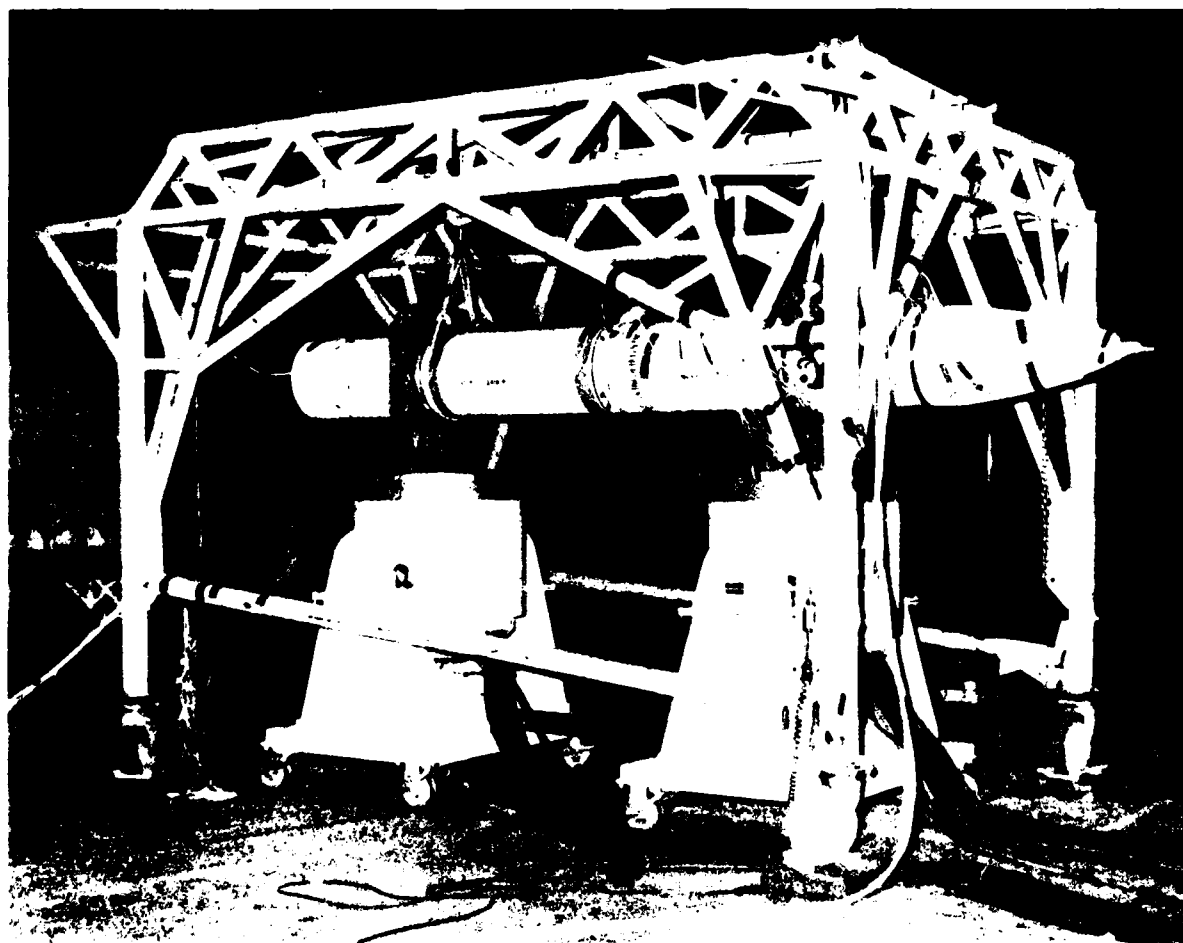


Figure 3 Dual Shaker Flight Test Simulation Installation

vibrated in both the y and z axes and since the shakers tend to constrain the vibration to a single axis, two series of tests had to be run, one in each axis. For each case, however, plots were made of the responses in both directions. For instance, two plots will be shown for 2y, one with excitation in the y direction and one with excitation in the z direction.

Results

An important point was discovered during attempts to obtain optimum missile response by this method.

Vibration input to the missile can be controlled at only two points in one direction at a time. It was soon discovered that obtaining optimum response at the input point, may drive other locations, say one or four, above or below what is optimum for those points. In order to correct for the over test occurring at these points, the input had to be reduced at those critical frequencies. Obviously, the attenuation would detract from the optimization of the vibration response originally obtained at the input point. Figures 4 through 11 represent the best response possible with dual shakers under the constraints imposed.

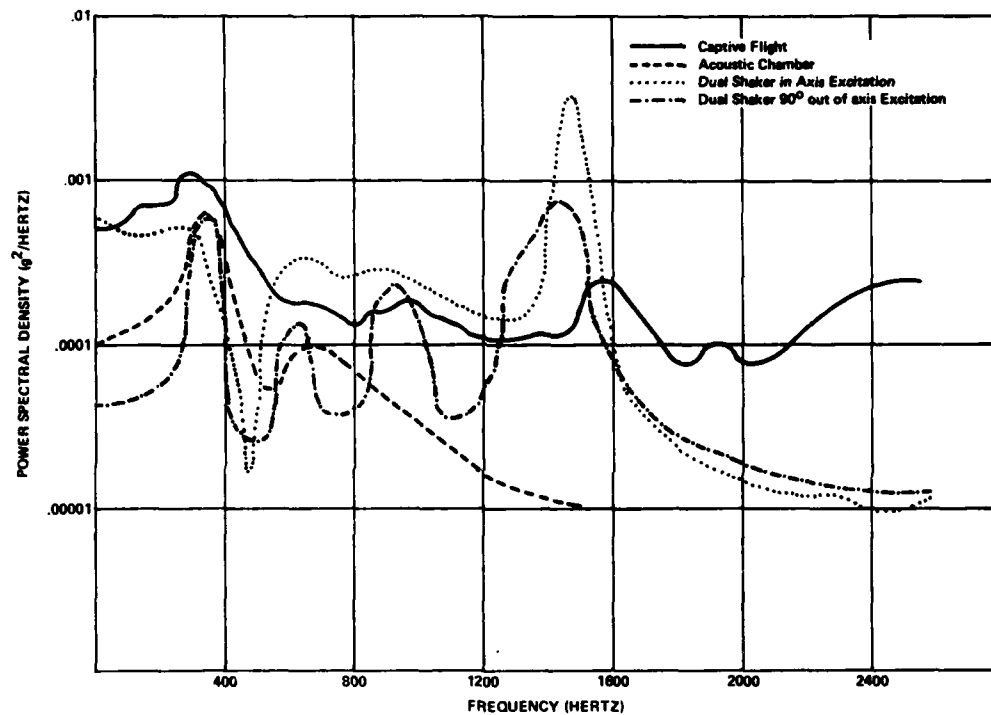


Figure 4. PHOENIX T-201 Missile Vibration Response at Position 1Y.

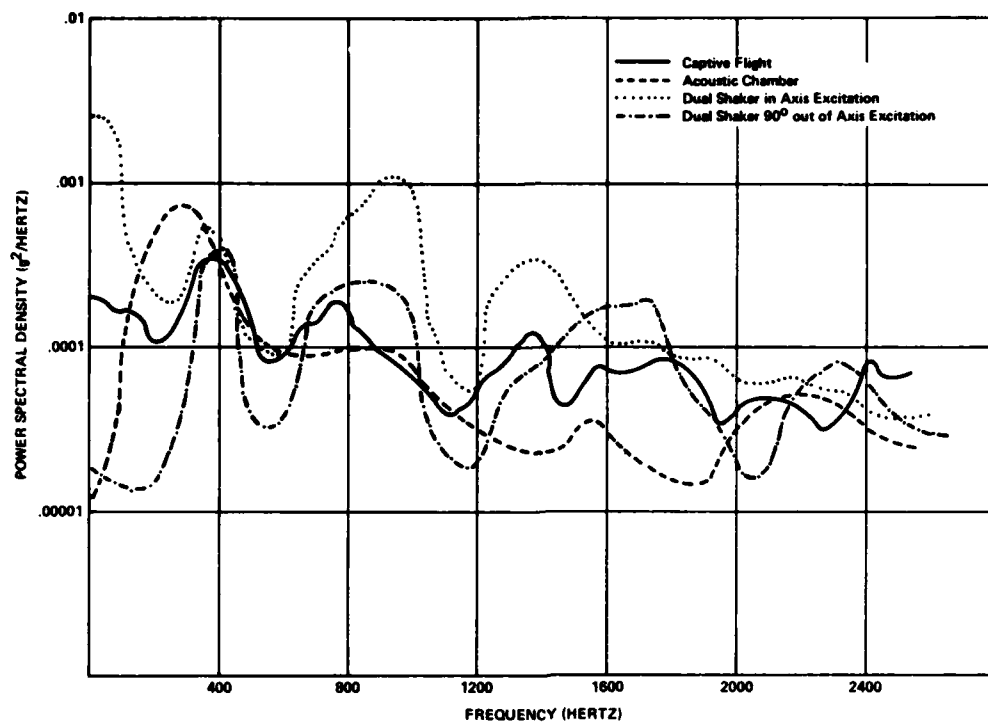


Figure 5. PHOENIX T-201 Missile Vibration Response at Position 1Z.

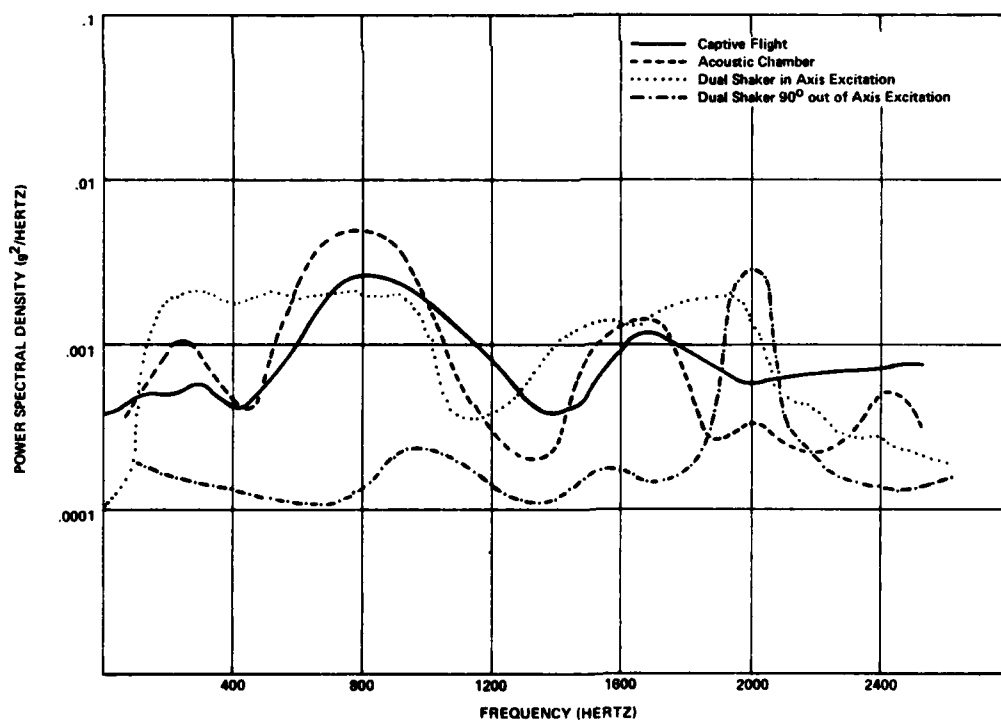


Figure 6. PHOENIX T-201 Missile Vibration Response at Position 2Y.

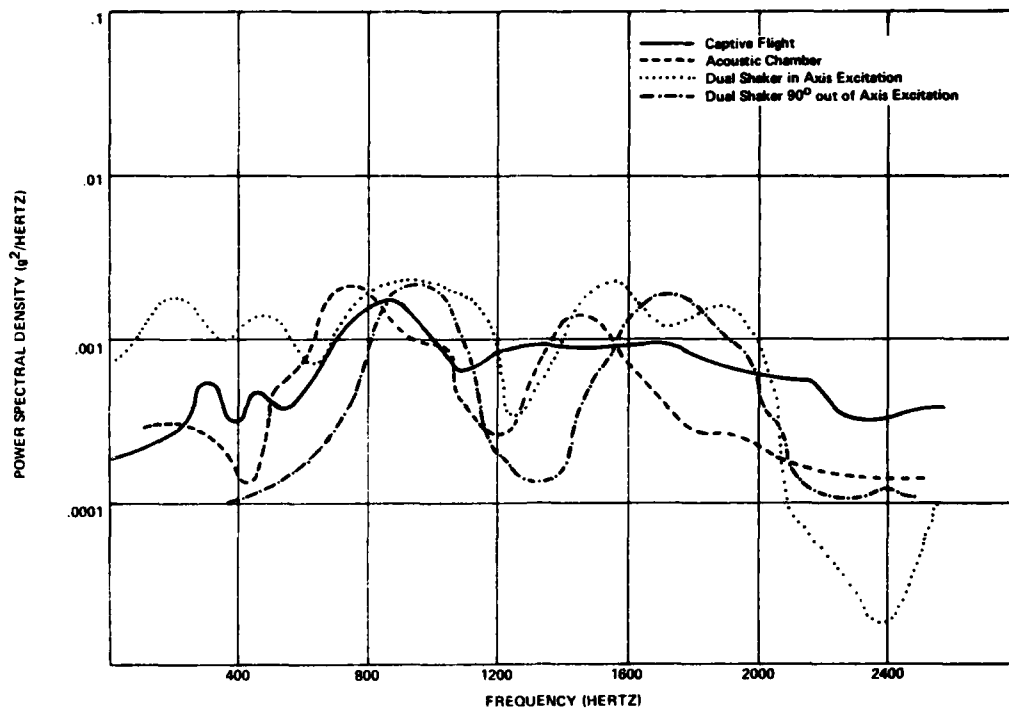


Figure 7. PHOENIX T-201 Missile Vibration Response at Position 2Z.

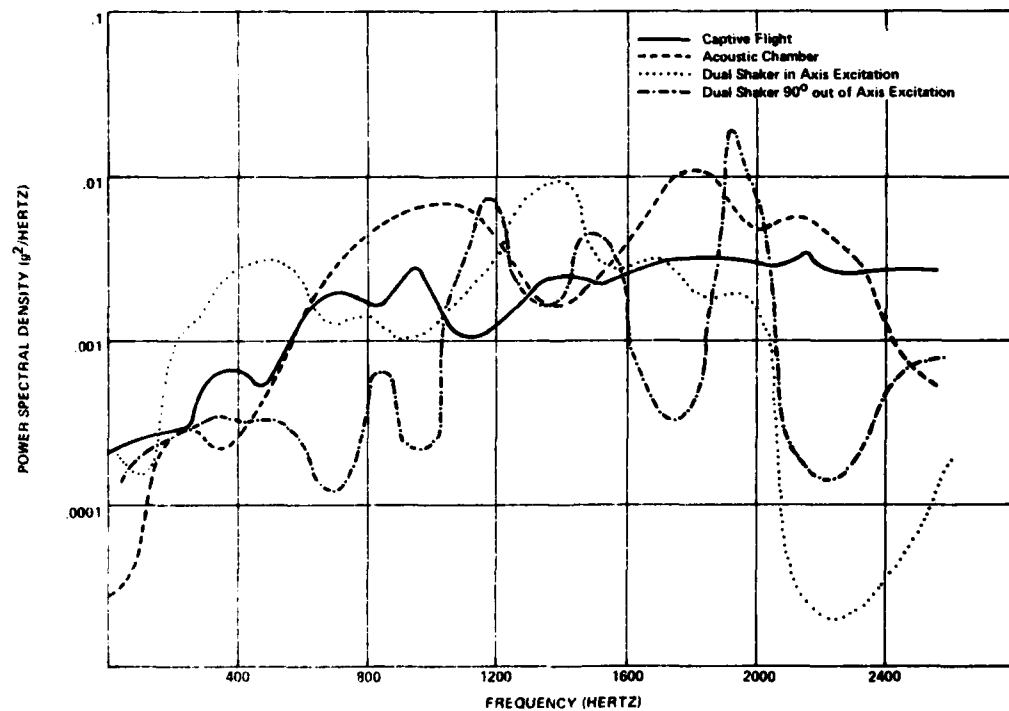


Figure 8. PHOENIX T-201 Missile Vibration Response at Position 3Y.

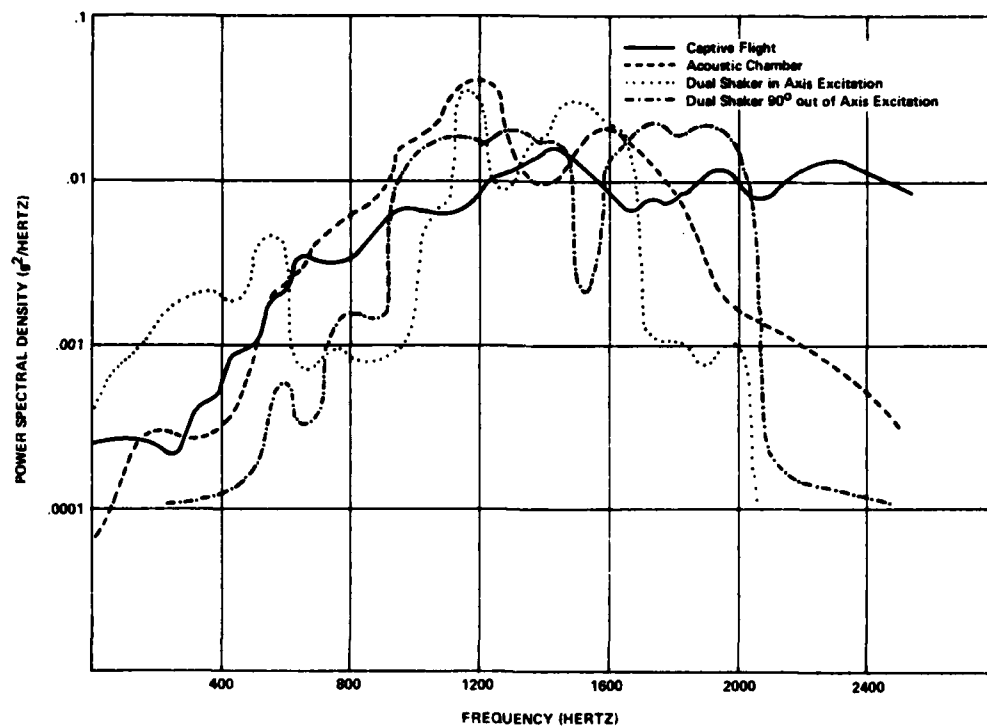


Figure 9. PHOENIX T-201 Missile Vibration Response at Position 3Z.

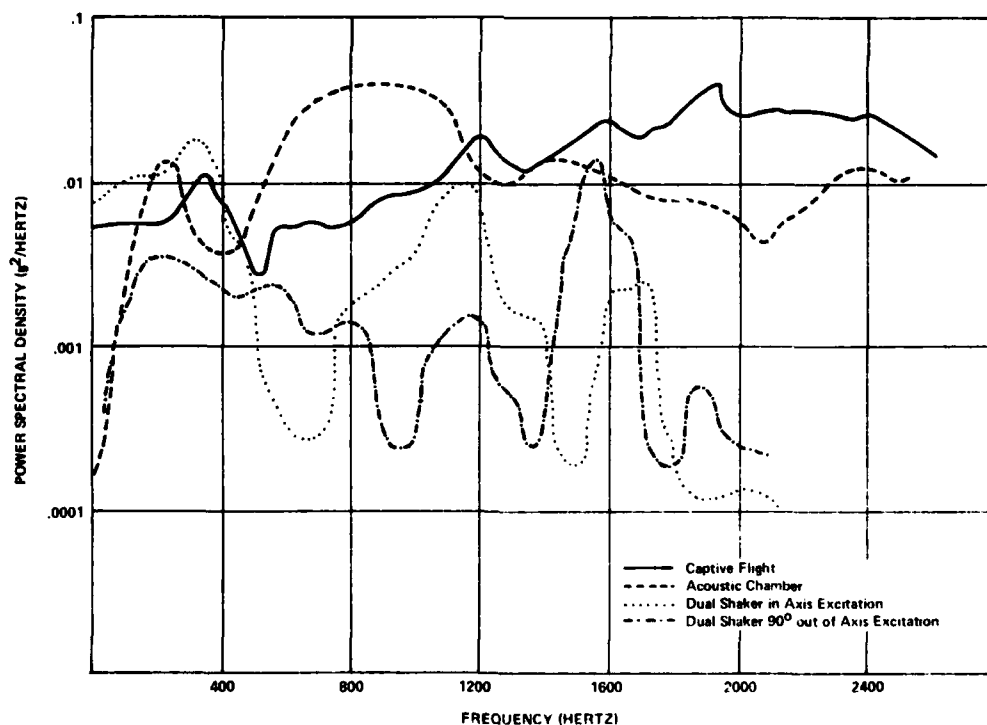


Figure 10. PHOENIX T-201 Missile Vibration Response at Position 4Y

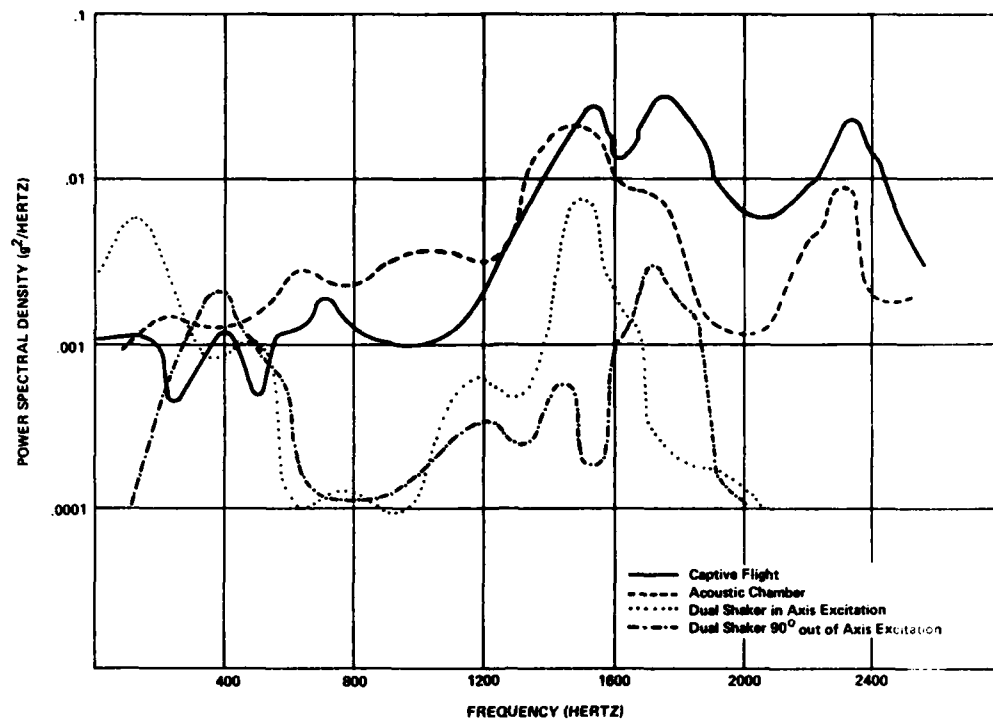


Figure 11. PHOENIX T-201 Missile Vibration Response at Position 4Z.

CONCLUSIONS

After examination of figures 4 through 11, it is concluded that the vibration response of the PHOENIX missile when excited by acoustic energy more nearly resembles that seen in captive flight than the response occurring when the missile is excited by electrodynamic shakers.

Further, the acoustic facilities have illustrated excellent reliability, allow for simple fixturing and handling, have the capacity for more than one test specimen (PHOENIX LEIP will test four missiles simultaneously), and provide multi-axis excitation. As a result, the use of acoustics for simulation of captive flight vibration has demonstrated itself to be an accurate and cost effective test method.

DISCUSSION

Mr. Malmgren (Jet Propulsion Laboratory): You acceptance test or make a reliability test as you call it of all the missiles that are in a production lot?

Mr. Spandrio: No, we sample them.

Mr. Malmgren: Do you power the electronics in some way when you are conducting these tests?

Mr. Spandrio: Yes, hopefully it is a total simulation. We are duplicating the environment we expect it to see and also stimulate the missile with the electronic functions that will occur in flight, hopefully in synchronization with one another.

Mr. Malmgren: Do you have any significant thermal environment associated with the captive flight?

Mr. Spandrio: Yes we do. In the acoustic chamber we have acoustically transparent shroud that goes over each missile. Hot and cold air is conducted across the missile creating the skin temperatures in synchronization with the missile electronics check out and the missile vibration environment.

Mr. Malmgren: You are basically running what might be called a minimal margin sample reliability acceptance program. Is that correct?

Mr. Spandrio: I don't fully understand the terminology.

Mr. Malmgren: Lot acceptance.

Mr. Spandrio: Yes.

Mr. Cristo (Naval Underwater Systems Center): I was wondering could this acoustic testing technique be done in a tank of water if we wanted to vibrate some shells or something?

Mr. Spandrio: I imagine the medium would be a problem. In one case we are using air in your case it would be water transmitting the energy. I don't know.

Mr. Cristo: You don't know if anyone has tested in these areas?

Mr. Spandrio: I don't know.

Voice: What is the approximate cost of the facility of that size?

Mr. Spandrio: The chamber itself costs about \$30,000 to construct, each exponential horn I believe is around \$2,000 now. The modulators required are about \$4,000 to \$6,000 a piece, and of course each modulator requires about 450 cubic feet/min (CFM) of low pressure air so you have to size your compressor to those environments. I would imagine for under \$100,000 that you could create quite a vibration facility.

AUTOMATIC ENVIRONMENTAL CONTROL SYSTEM
FOR
MISSION PROFILE TESTING

ROBERT SCHILKEN
Pacific Missile Test Center
Point Mugu, California

A simple and inexpensive Automatic Environmental Control System was developed for controlling realistic mission profile environmental tests. Hardwired logic and reprogrammable electronic storage were used in the general purpose control system. Coding techniques and a random number generator for simulating temperature day variations in the mission are presented. The entire thermoacoustic environmental generation facility used for missile captive flight simulation is described including a newly developed high efficiency noise modulator driver.

INTRODUCTION

With the advent of a captive-flight mission profile simulation in laboratory environmental testing, the controls for automatically generating the sequence of environmental conditions have increased in complexity by an order of magnitude. Such complexity may cause hesitation to exist in the industry in implementing mission profile tests due to the lack of elaborate automatic systems. This paper describes a simple Automatic Environmental Control System (AECS) developed at the Pacific Missile Test Center (PMTC) Point Mugu, California for totally controlling such mission profile tests.

A brief description is first given of the "thermoacoustic" captive-flight laboratory simulation used in mission profile testing, and the environmental controls loops associated with this method. Development of the AECS from the above requirements is then presented. Next the incorporation of a Random Temperature Offset Generator (RTOG) in the AECS is described which improves the realism of the simulation by randomly generating the spread of temperatures that would naturally occur from mission to mission. Finally a description is given of a specially designed noise modulator drive used in the noise control loop that produces a more efficient noise generation system.

AECS DEVELOPMENT

Real-time laboratory reliability testing at PMTC has been developed around the thermoacoustic testing method which simulates the temperature and vibration stresses of captive flight, the two most degrading stresses to modern missile circuitry. Captive-flight vibration is simulated by

generating high-level random acoustic noise in a reverberant chamber. This noise energy is absorbed by the missile skin as vibration, in a manner similar to that which occurs with aerodynamic turbulence in captive flight. Temperature changes of the missile skin are produced by flowing hot or cold air by the missile. The volume of thermal conditioning air is kept small, to effect rapid temperature changes, by using an acoustically transparent thin fabric shroud around the section of the missile being tested.

Environmental Control Loops

The control loop for the noise generation is shown in figure 1. The amplitude of the noise signal source, derived from an automatic reversing cassette tape player, is varied by a Programmable Gain Amplifier in the AECS, and is fed to a Modulator Driver. The Modulator Driver directly drives the voice coil of the modulator. Both the Modulator and Driver are described in detail at the end of the report. A pressure switch senses when there is less than 5 psi air pressure supplying the modulator and shorts the driver to keep from overheating the voice coil which is normally cooled by the modulated air flow. The modulated air flow is regulated from 9 to 45 psi depending on the noise amplitude required. The pressure is regulated by a pressure balanced diaphragm driven regulating valve whose input is a 9 to 45 psi control pressure. The controlling input is derived from a multiplied 3 to 15 psi Current-to-Pressure transducer which is driven by the AECS current output.

Three microphones (B&K model 4136), a multiplexer (B&K model 266), and a sound level meter (B&K 2606) are used to monitor the chamber noise level. The DC voltage output of the meter is low pass filtered at 0.1 Hz and recorded as Sound Pressure Level (SPL) on a 24-channel print recorder (Esterline Angus L1124).

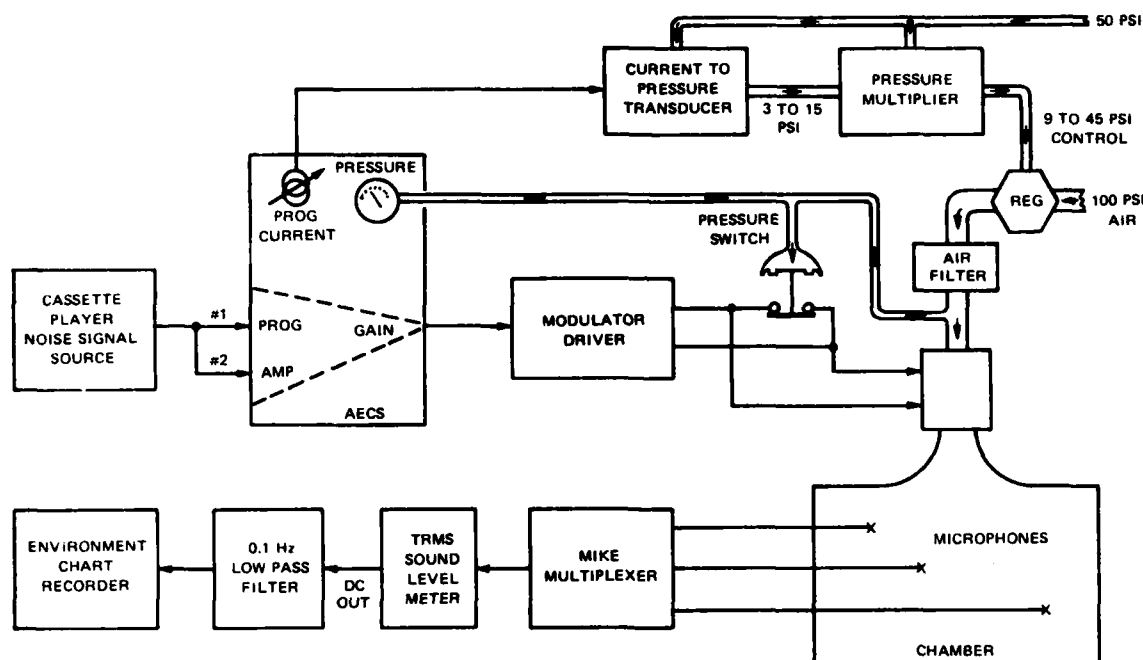


Figure 1. Thermoacoustic Noise Control Loop

The control loop for the temperature conditioning is shown in figure 2. A programmable temperature controller (Love model 49) in the AECS senses the temperature of the missiles with the controlling thermocouple and commands the Thermal Conditioning Unit (TCU) to apply heat or cold to the air which is constantly circulating by the missiles. The TCU contains high and low temperature limit controllers (Love Model 68) which sense with thermocouples the return air temperature after passing by the missiles. Over or under temperatures shut down the TCU.

The temperature of all four missiles under test is sensed with four thermocouples and recorded on the 24-channel printing recorder used for noise SPL recording. The TCU adds heat to the air with either 10 or 20 kW electric heaters and cools the air by flowing liquid nitrogen at two different rates through a heat exchanger. The two heating and cooling rates are controlled by the AECS program (slow command) to present different thermal shocks to the missiles.

Programing

It was decided that a minimum of 50 different programmable stages of environmental control would be necessary to adequately describe the mission profiles that a missile would experience during its life. This made available five to fifteen stages to describe each mission, assuming up to six different missions would be simulated.

An Intel 1702A erasable Programmable Read Only Memory (PROM) was selected for the program storage. The PROM was housed in a rugged 44 pin metal cased plug which screws into the back of the AECS. This physically protected the PROM and allowed for quick program changes, to accommodate different missiles sharing the same testing facilities.

The format of the binary address used to store control data used four 8-bit addresses for defining each stage as follows:

PROM ADDRESS	INFORMATION STORED
Stage #	
XXXXXX 00	Time Interval Code of Stage
XXXXXX 01	Temperature Code and Slow Command
XXXXXX 10	Noise Controlling Code
XXXXXX 11	Special Functions Code

The 6-bit stage number defined stages 0 to 63. The 0th stage instead of containing environmental control data was programed with an identification number. Each time the program is reset (started), or recycles from stage 63 to stage 1, the identification number is read, stored and displayed. This identification is a luxury that was not necessary, but was included in the prototype

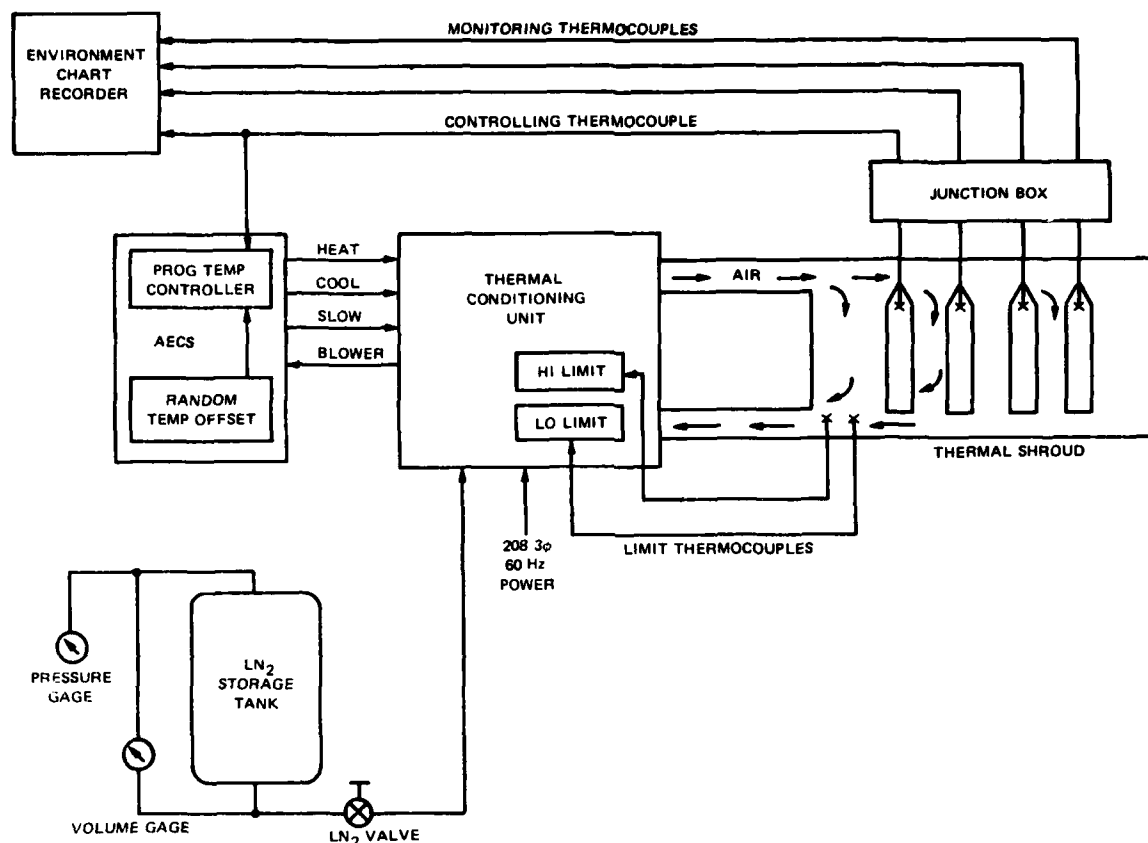


Figure 2. Thermoacoustic Temperature Control Loop

because several different programs were to use the same facilities for testing different missiles.

The codes of the data stored were dictated by the hardwired logic design and the attempt to make the logic simple. The resulting data codes are as follows with binary format and most significant bit first:

Minutes
Time Code -- M M M M M M S S -- in 15 sec intervals
Seconds

Temperature
Temperature Code --- T T T T T T S
Slow heat exchange command

The 7-bit "temperature" word is actually a code itself with a nonlinear (thermocouple) function, the limits being:

Code	Temperature
00000000	-100°F (-73°C)
11111111	+282°F (+139°C)

Driving Signal Gain Code
Noise Code ---- GGG PPPPP
Air Pressure Code

where:

Gain = 0.2 (GGG)
Pressure = 9 psi + (PPPPP) psi

Special Functions Code

BIT	COMMAND
X ₁	Missile Power ON
X ₂	Functional test alarm (set on transition)
X ₃	Noise input #1 OFF
X ₄	Noise input #2 ON
X ₅	Enables Temperature Controller to command heat
X ₆	Enables Temperature Controller to command cool

X₇ Special Function #2
X₈ Special Function #1

Two selectable noise inputs were included for the programmable gain amplifier, to allow simulating the difference spectrally shaped vibration conditions that may exist at different store locations on the aircraft, or with different aircraft. The programming code was arranged to have noise input #1 normally selected with logical zero's programmed in X₃ and X₄. The functional test alarm bit latches an electrical bell (alarm) and a flashing orange light to indicate to the test operator that it is time to perform a functional test of the missile. The alarm is manually reset by a front panel button.

Any stage that has zero minutes programmed is automatically skipped, and at the conclusion of stage #63, the AECS will sequence to stage #1. Because the PROM contains logical zeros in any location not programmed, at the conclusion of the last programmed stage, the AECS will automatically sequence to stage #1 and repeat the program.

The PROM is electrically programmed outside of the AECS using any acceptable programmer such as a PROLOG M-900. A software routine on TYMSHARE

was written to assist the test engineer in converting the environmental requirements into a program code.

Hardware Design

The hardwired design used standard TTL logic and a minimum number of different components. The simplicity of the circuit is made possible by using a presettable counter (74177) as a counter and/or storage register and by selecting 2² addresses for the total storage of information in each stage. The operation of the logic can be seen from the partial block diagram of figure 3. The process for loading the program information (stage #1 to #63) into the temporary storage registers is initiated by setting the Load flip-flop. This enables a 2-kHz logic control clock to increment four counts in the 8-bit address counter. At each of the four counts the programmed data (eight bits) from the PROM is loaded into the proper register by gates G1 through G4. These gates decode the two least significant bits of the address and pass a 10-μsecond loading pulse that is generated by a one-shot from the logic clock. On the fourth count G4 resets the load flip-flop to halt the loading.

Note that all bits of the time code data are inverted before being loaded into the Time register. A

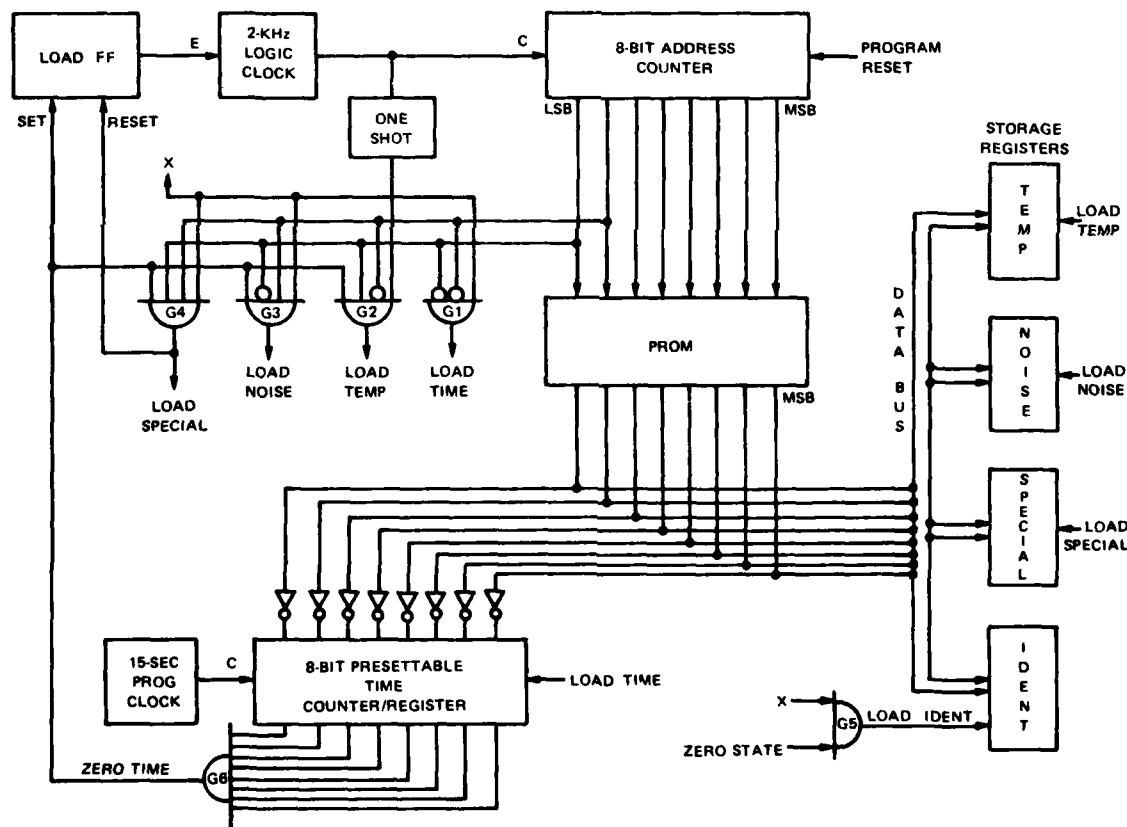


Figure 3. Partial Block Diagram of AECS Logic

program clock increments up the Time counter once every 15 seconds to produce all logical ones when the time interval is completed. An example of the process is as follows:

Desired time of stage: 1 minute, 15 seconds
 Minutes
 Time code programed: 000001 01
 Seconds

Time	Register data
0 sec	11111010 Loaded in register
15 sec	11111011
30 sec	11111100
45 sec	11111101
1 min	11111110
1 min 15 sec	11111111 All ones → Load next stage data

When all time bits are logical ones G6 starts the process for loading the next stage data. If the time of any stage loaded is zero, G6 disables G2 through G4 from loading their respective registers.

The stage zero address is decoded with a gate (not shown) to enable G5 to load the identification code. Also

not shown is the manual advance which sets the load flip flop, the manual stage set which presets the six most significant bits of the address register, and the address and time remaining displays which decode their respective binary data into BCD seven segment format.

The temperature and pressure code data are converted to analog signals to drive their respective controller circuits. The remaining data bits are buffered to drive FET switches, latches, and solid state relays, to effect the desired environmental control.

Physical Design

The AECS was housed in a 19- by 13- by 15-inch (48.2- by 33- by 38-centimeter) rack-mounted box. The front panel as shown in figure 4 included the following displays:

1. Program Identification Number
2. Stage Number
3. Time remaining in Stage (Minutes only)
4. Functional Test Alarm Light
5. Power Interrupt Alarm Light (Power Interrupt Alarm latches whenever the 5-volt logic supply dips below 4.5 volts. Because low power may cause loss of stored data, all of the environmental controls are disabled until the alarm is manually reset.)
6. Command Temperature (Set Point)
7. Controlling Temperature (of Missile)
8. Air Modulator Pressure

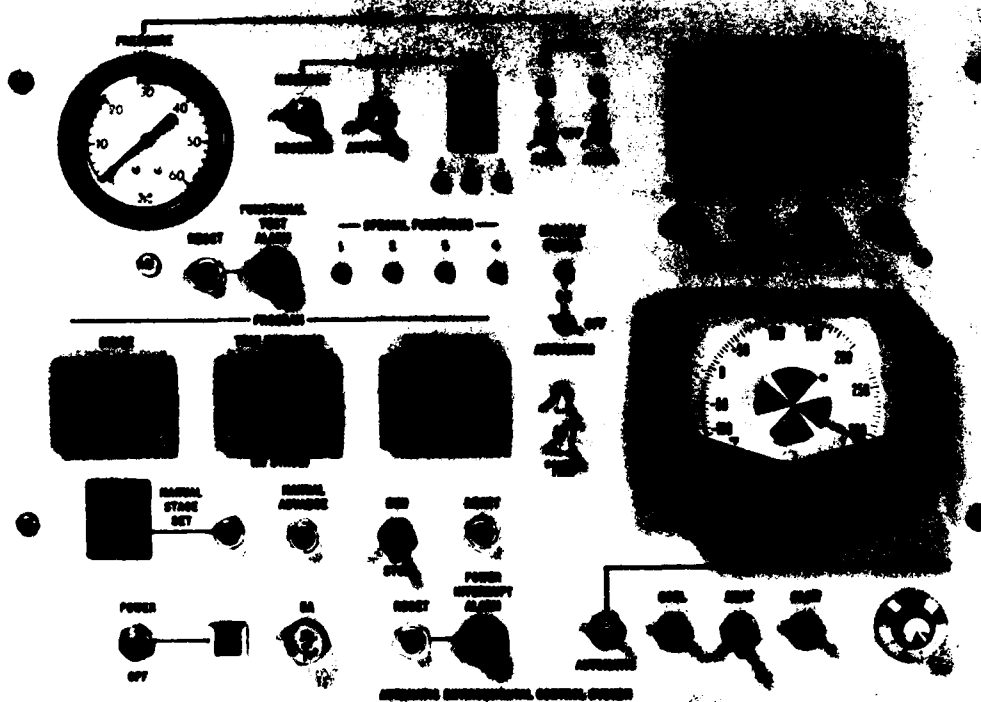


Figure 4. Front Panel of AECS

In addition, LED and neon lights indicate the status of the TCU (heating, cooling, and slow rate), the programed noise gain bits, the noise #1 and #2 inputs, missile power, and special functions #1 and #2.

The front panel controls included the following:

1. Program reset – to read the identification code and start stage #1.
2. Manual Program Advance – to advance to the next stage independent of time.
3. Manual Stage Select – thumbwheel switch and pushbutton to force the program to the selected stage.
4. Functional Test Alarm Reset
5. Power Interrupt Alarm reset.

Toggle switches select Manual or Automatic modes for all of the environmental controls including: heat, cool, slow, pressure increase, pressure decrease, noise input #1, noise input #2, and missile power. A thumbwheel selects the manual noise gain, and a 10 turn pot sets the manual control temperature.

The hardware consisting of approximately 50 integrated circuits was contained on one wire wrapped logic board and one printed circuit analog board. Extreme care was taken to design high noise immunity into the logic. Clock speeds were kept very low, extensive buffering and shielding were used, and capacitive filters were added to slow down critical timing lines. The care in design has paid off in demonstrated system reliability. To date with more than 500 operational hours, no controlling errors have occurred.

It is important to note that none of the displays or controls, except Reset, are necessary for the operation of the control system. The large number of displays and controls of the system described were included in this prototype for ease of program interrogation when errors occurred, and for ease of establishing the mission profile program. To date no such errors have occurred and establishment of the program has proved to be easier than expected. Therefore, subsequent models of the AECS, being built for other missile programs, do not include Identification or Commanded Temperature displays, or the Manual Stage Select.

For a minimum cost and complexity system, it is suggested that the basic system of figure 3 be used with the inclusion of a Program Reset (reset address counter), a Manual Stage Advance (set Load FF), and a stage number display consisting of six Light Emitting Diodes driven by 7404 buffers from the six most significant address lines. Such a system using 555 integrated circuit timers for the Logic Clock, One Shot, and Program Clock could be implemented with the following major components:

Quantity	Item
10	74177 Counter
5	7404 Hex Inverter
3	7430 Dual 4 input Nand
3	555 Timer
1	1702 PROM & Socket

6	LED's Indicators
2	NO Pushbutton switches
1	Dual power supply (+5V, -9V)
1	Board, enclosure, and miscellaneous

With three multiplying Digital to Analog Converters and a Quad Op-Amp for the programmable gain amplifier, temperature controlling voltage, and the modulator pressure control current, the cost for all basic materials is less than \$150.00.

Random Temperature Offset Generator (RTOG)

When the AECS was originally designed, it was intended that the variation in mission profile temperature from a mean standard day temperature would be accounted for by programming several of the same mission, each with a different temperature offset for all stages of that mission. After the AECS was operational, and while one of these lengthy programs was being written the idea occurred to let some kind of intelligent hardware do the temperature offsetting of the missions rather than programing each mission over and over with different offsets. This would save programing time, and would free the available programing space for other missions. This would also produce a more realistic temperature history if the offset were random with a known distribution.

This idea was implemented using an 8-bit psuedo-random number generator and summing weighted values of the 8-bits to give a psuedo-random analog signal. The analog signal (in this case a current) was then summed with the output current of the Digital to Analog Converter (DAC) which drives the temperature controller.

The psuedo-random number generator consisted of an 8-bit parallel out static shift register with bit #1 and #7 exclusive ORed and fed back to the serial input. This configuration, shown in figure 5, resulted in a sequence of words which repeated itself every 128 shifts.

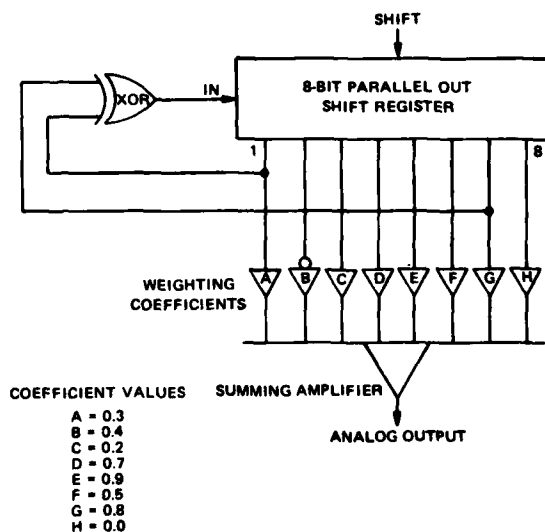


Figure 5. Pseudo-Random Level Generator

A computer program was used to plot the analog output of the summed bits giving the eight weighting coefficients. More than 50 different sets of weighting coefficients were plotted giving outputs that ranged from smooth, slowly changing signals to erratic rapidly changing waveforms.

The weighting selected produced an output as shown in figure 6 that was a compromise between the extremes. This weighting produced an average output, from any 20 consecutive shifts and was approximately equal to the mean of the distribution over its 128 shift periodicity. The weighting coefficients and distribution of this signal are also plotted, and as expected the distribution is gaussian in shape. The 2nd bit only (B-coefficient) is inverted before being weighted and summed.

The final circuit design is as shown in figure 7 where the summing amplifier is configured to produce a current output. When the AECS power is off, the shift register, which is a very low power CMOS device, is powered by a 3-volt mercury battery to retain its information state. This insures that the pseudo-random generator will consistently step through its sequence and will not skip to a new part of the sequence every time the AECS is powered on.

The generator is advanced to a new temperature offsetting output at the first stage of each mission by receiving a negative going (0 volts) signal from the special function #2 program bit of the AECS. The generator circuit board (approximately 4 by 4 inches) (10 by 10 centimeters) was mounted in the AECS and is controlled by two small toggle switches on the front panel. One switch halts or enables the RTOG from being advanced to a new offset, and the other switch connects (ON) or disconnects (OFF) the offsetting current to the temperature controller input.

The mean and spread of the output distribution are adjustable on the circuit board with trimpots. In a recent Navy air-to-air missile program the mean offset was set to $+3^{\circ}\text{F}$ ($\pm 1.7^{\circ}\text{C}$) and the spread to $\pm 35^{\circ}\text{F}$ ($\pm 19.4^{\circ}\text{C}$) or

approximately $\pm 15^{\circ}\text{F}$ ($\pm 8.3^{\circ}\text{C}$) standard deviation. This temperature range was determined using several sources of data predicting the likelihood of service over certain land masses or oceans, and their atmospheric temperature distribution. The temperature distribution for testing other products will vary with the intended use.

ACOUSTIC NOISE MODULATOR DRIVER

Laboratory simulated reliability tests of modern missiles are often quite lengthy (1,000 chamber hours or more). The amount of power consumed in generating the environmental stimulation is becoming significant and with the ensuing world wide energy shortage, more efficient methods of environmental generation are receiving attention. In 1976 PMTC initiated a low profile program to develop a safer, more foolproof acoustic noise driver than was presently being used. The result of this development was not only a safer driver but also a more efficient noise generating system, and is presented here as part of the environmental controls system.

The majority of acoustic air noise modulators are basically voice coil driven linear slide valves that are normally biased with the valve in a half open position. As low air pressure is flowed by this variable restriction, the valve linearly modulates this flow of air producing variations in pressure which are coupled into the chamber as acoustic pressure variations. The slots in the slide valve are designed to provide 100 percent modulation at a specific voice coil excursion. Over excursion causes the modulation to "double back" as shown in figure 8, resulting in actually a reduction of energy produced at the driving frequency. Over excursion also over stresses the flexible electrical voice coil connection contributing to early fatigue and failure.

The response of the modulator to an electrical drive signal (sinusoidal) indicates an inductive property which requires increasingly higher voltages to drive a particular displacement at higher frequencies. The common method of driving the voice coil with a peak-limited voltage

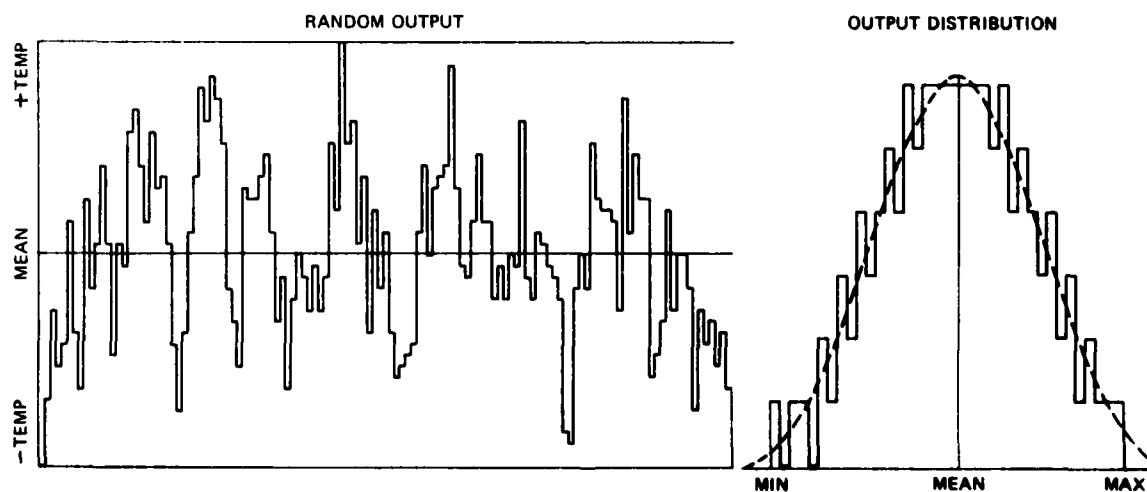


Figure 6. Random Offset Temperature Generator Output

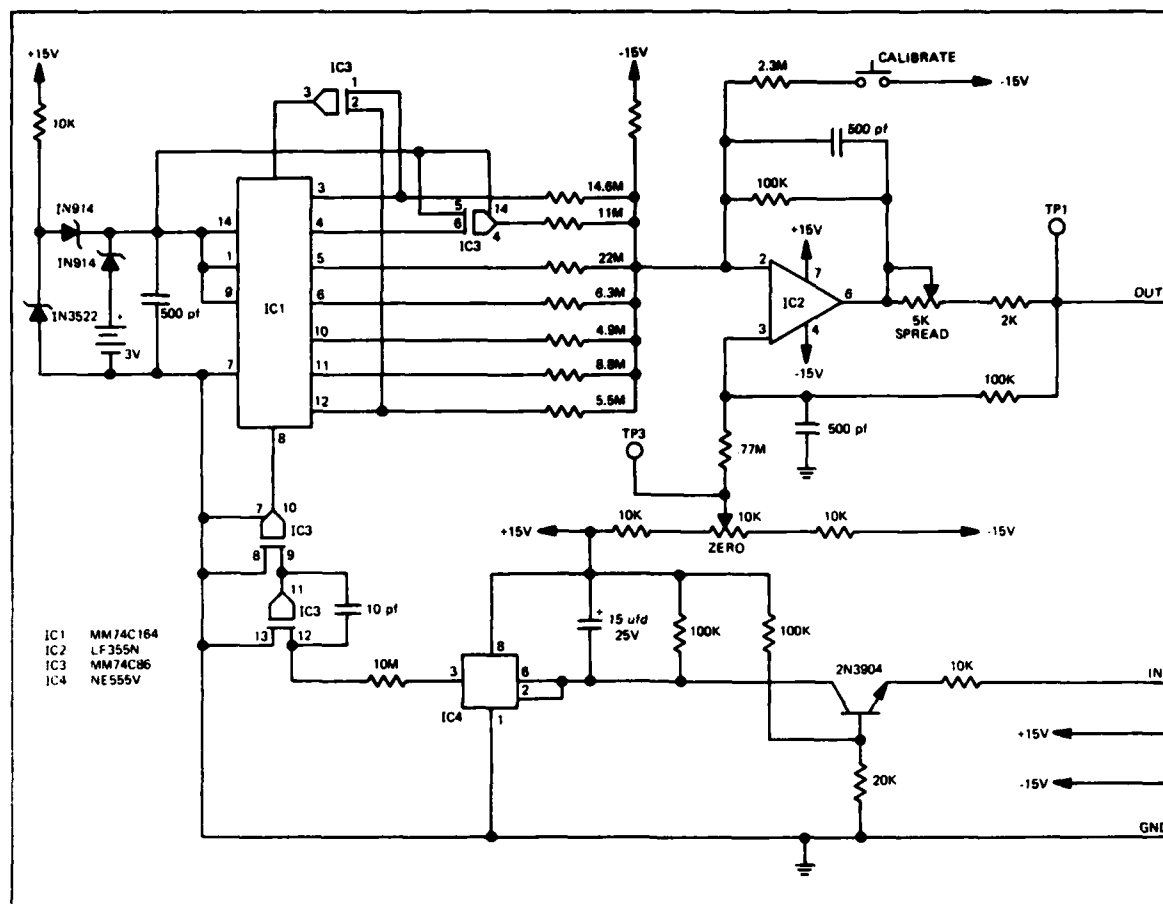


Figure 7. Random Offset Temperature Generator Schematic

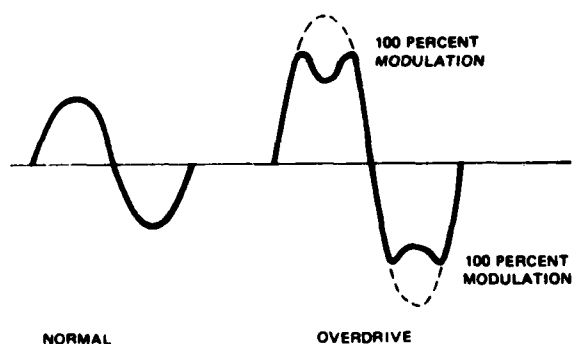


Figure 8. Modulator Valve Overdrive

amplifier, produces peak excursions at one particular frequency. However, it allows over excursion at frequencies below this optimum frequency, and results in under excursion at higher frequencies.

The situation is resolved by observing that over its usable frequency range (50 to 600 Hz), the modulator produces the same excursion when driven by a fixed RMS current sinewave. For the Ling Model 1094 the optimum current for 100 percent modulation is 7 amps RMS, or 10 amps peak. Therefore a simple voltage clipper followed by a voltage controlled current driver was prototyped as a modulator driver in the Environmental Laboratory at PMTC. An additional circuit was added to the prototype to limit the RMS value of the driving current to 7 amps. This absolute maximum value was clearly specified in the modulator literature and was confirmed by the manufacturer as being a voice coil heating limitation. Because of skepticism concerning the area of voice coil stresses as well as driving techniques, PMTC contacted the manufacture and established the maximum acceptable voice coil temperature. A test was then conducted to measure

the resistivity temperature of the copper voice coil immediately following a sustained drive. From this test it was determined that the voice coil could easily withstand the peak current continuously. Therefore, the RMS limiting circuitry was removed from the prototype driver.

Equally important in the design considerations was to make the driver stable. The voltage amplifiers normally used for driving modulators were wide frequency, high fidelity type with large amounts of feedback, and inherent instability. Because of this instability, elaborate protection circuits were included to shut down the amplifier upon sensing over voltage, over current, or over temperature. If the sensing limits were set too narrow the amplifier would periodically shut down causing a disruption in the testing. If the limits were set too wide, modulator destruction could and did occasionally result.

In designing the modulator driver it was determined that a fair amount of distortion in the driving current could be tolerated. This is due to the fact that the signal being driven is random shaped noise. Harmonic and intermodulation distortion in the driver will only tend to reshape the spectrum slightly which will automatically be compensated for in shaping the signal source. All that is required is that the distortion be repeatable. The current output drive was therefore designed using no feedback. This resulted in a drive which is stable with any kind of a load from a shorted to open circuit, and capacitive to inductive impedance. Because the frequency response of the driver need only extend to 1-KHz, low frequency high second-breakdown power transistors were used in a parallel configuration to produce a more transient forgiving reliable driver. The final design shown in figure 9 is a

simple, stable, and reliable configuration using commonly available inexpensive parts. The major portion of the circuitry is contained on one printed circuit board for easy assembly.

As expected, the driver, with its precise modulation limiting, produces 0.5 dB more noise at 7 amps RMS than a voltage amplifier driven at the 7 amps RMS maximum rating of the modulator with a random-noise signal shaped flat from 150 to 600 Hz and with a low pressure air supply of 40 psi. Driving with the same source signal at 9.5 amps RMS which is totally safe with the driver results in a 1.0 dB SPL gain over the 7 amp RMS voltage driver configuration. Total distortion was less than 5 percent. Two drivers have been in use at the Environmental Laboratory since July 1976 and have accumulated over 2,000 operating hours with no driver failure or driver induced modulator failures.

CONCLUSION

The total environmental control system as described has proved to be a functional, economical, and reliable system for thermoacoustic simulation. Although the PROM programed hardwired system is by no means the only approach to automatic control, it has been presented as a simple and inexpensive tool for developing the concept of mission profile testing. As consciousness of the concept grows, it is expected that the control systems will likewise grow into elaborate microprocessor and computer controlled systems. However, at the present time the AECS approach will provide total automatic control with more than enough flexibility to generate the realism desired.

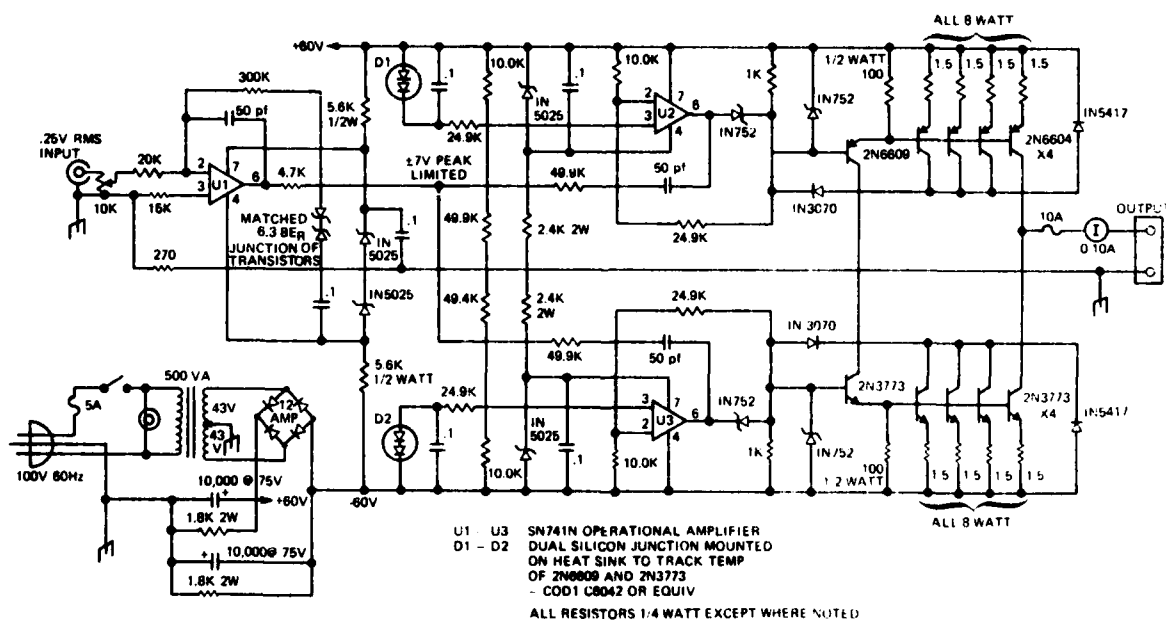


Figure 9. Acoustic Noise Modulator Driver Schematic

BROAD-BAND MECHANICAL VIBRATION AMPLIFIER

R.T. Fandrich
Harris Corporation, Electronic Systems Division
Melbourne, Florida

A test requirement to expose miniature electronic components to high vibration levels encouraged this investigation of a mechanical vibration amplifier. Various testing requirements are imposed on components and many of these requirements are too high to be met using standard laboratory vibration shakers. The solution described in this paper utilizes a mechanical vibration amplifier which increases the available shaker output at all frequencies, simultaneously.

INTRODUCTION

The mechanical system described in this paper amplifies vibration inputs at frequencies above the system isolation frequency (80 Hertz). It utilizes an imbalanced seesaw having a heavy mass on one side and relatively light test item on the other. The pivot point is vibrated vertically and (in the frequency range where the heavy mass is in isolation) the input to the test item is amplified, due simply to the mechanical advantage of the seesaw mechanism. Since this range includes frequencies between 80 and 2000 Hertz, the mechanism is truly a broad band amplifier capable of amplifying either sinusoidal or broad band random inputs.

This paper describes the laboratory experiments which demonstrated the feasibility of this method. The method effectively amplified input vibration levels by a factor of 3 g's/g over an input frequency range of 100 to 2000 Hz, allowing testing at 150 g's while driving the shaker at only 60 g's, thereby saving energy and high level wear-and-tear on the shaker system and extending the upper limit of feasible test levels.

REQUIREMENTS

Various vibration testing requirements, both sinusoidal and random, and ranging up to several hundred g's in the frequency range of 20 to 2000 Hertz

are imposed on miniature electronic components. Many of these requirements cannot be met using standard laboratory vibration shakers designed for 100 g vibration levels. Figure 1 shows a 150 g requirement superimposed over a typical shaker output rating. The requirement is a modification of MIL-STD-883 and consists of a constant displacement of 1.5mm (0.06 in. double amplitude) between 20 and 220 Hertz. The shaker is rated at 2.54cm (double amplitude) or 254cm/second or 100 g's, whichever is smallest. The figure indicates the shaker is incapable of producing the desired level from 180 to 2000 Hertz.

Often the component requires random testing. The required level is typically established by multiplying a system level vibration specification by a transfer function which represents the system dynamic amplification at the component mounting point. When system specifications are conservatively high and components are mounted on low damped printed circuit boards, very high component specifications result. It is usually advisable to test the components in the system and eliminate the need for high shaker levels. However, system fragility and availability usually preclude this solution.

It therefore becomes necessary to generate both sine and random vibration

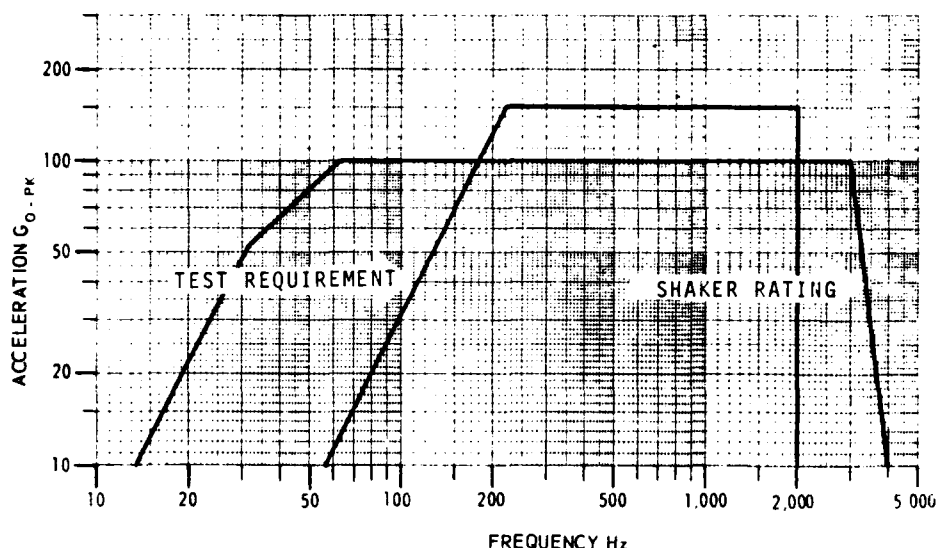


FIGURE I

VIBRATION REQUIREMENT VERSUS SHAKER CAPABILITY

levels of very high amplitudes to fulfill these requirements.

INCREASED GAIN

If these high level requirements are to be met using this type shaker, it is clear that a means of increasing the available vibration output is required. A classical approach to this problem results in the obvious solution of adding a power amplifier having 20 to 2000 Hz band width and a gain of two or three.

Figure II shows the required gain as a function of frequency based on the test requirement in Figure I. Enveloping this requirement is a typical power amplifier gain curve representing a possible solution to the requirement. If this power amplifier was used to increase shaker output, the increase would make it necessary to redesign the shaker to accept the increased electrical power and to withstand the increased mechanical load. This solution is costly and difficult. If the amplifier could be added further down the line, that is, after the shaker and before the test item, then the shaker design would be adequate. The shaker would act as a preamplifier for the new amplifier.

Figure III shows the control loop schematics of these two solutions and demonstrates the advantage of adding the required gain as close to the test item as possible. Solution (a) in the figure uses an electrical power amplifier to increase the gain and therefore, requires a larger shaker. Solution (b) depicts an increase in gain between the shaker and the test item. This is the optimum location for the required gain since no modifications are required by the existing components of the control loop.

MECHANICAL AMPLIFIERS

Many designs of resonant fixtures have been used in the past, but they can acquire very high levels over only a narrow frequency range. High level vibration requirements have encouraged a study of methods for mechanically amplifying vibration levels over a broader frequency range. One of the methods developed during this study simultaneously amplifies input vibration over the entire frequency band, just as an electrical power amplifier does. In fact, this mechanical amplifier has a band width, a gain and a phase shift similar to its electrical counterpart.

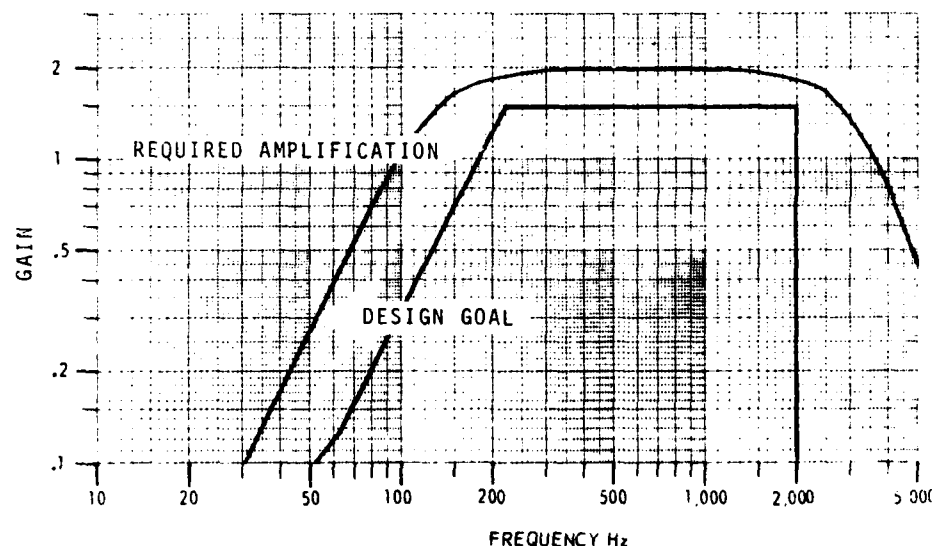
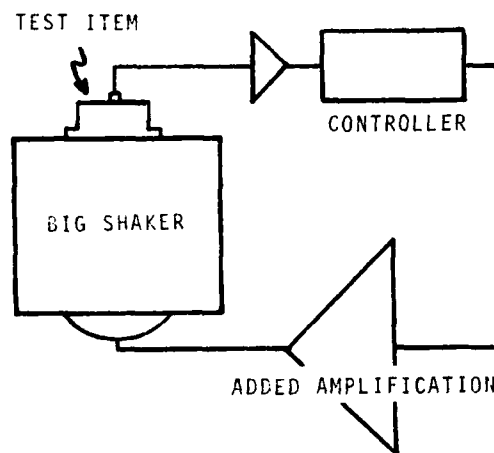


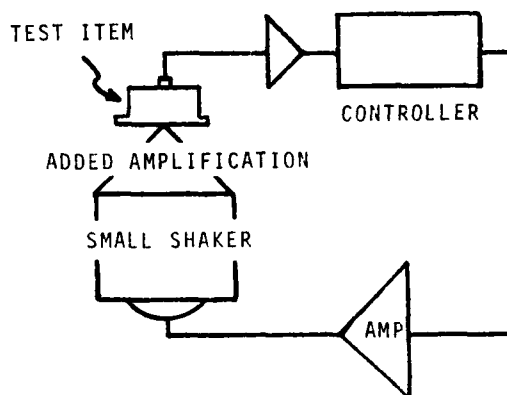
FIGURE II
REQUIRED GAIN
AND
DESIGN GOAL

The basic mechanical amplifier is the lever. Although levers are usually considered force amplifiers, we shall use a lever to amplify displacement, velocity and acceleration. To do this, we must exert a force on the short arm of the lever over a small displacement. The resulting motion on the long arm is a large displacement. The available

force available from the long arm is, of course, less than that applied. Figure IV (a) shows the lever arrangement used. There are two major design problems with this lever. The first problem is that the hinge on the right end of the lever must be attached to a fixed base and must not rattle, even while being cycle-loaded at 2000 cycles

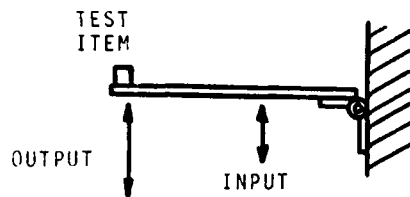


(a) ELECTRICAL GAIN

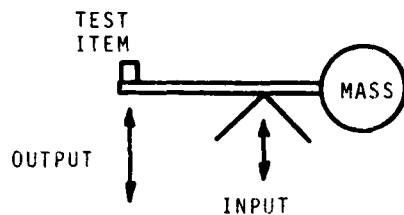


(b) MECHANICAL GAIN

FIGURE III
OPTIMIZATION OF GAIN
IN CONTROL LOOP



(a) MECHANICAL HINGE



(b) INERTIAL HINGE

FIGURE IV

THE BASIC LEVER

per second. The second problem is that the input force must be applied in an arc around the hinge to eliminate stretching the lever and must be applied through a hinge with the same characteristics as the first hinge.

To solve these design problems, we transcend normal design techniques and utilize the principle of inertia to establish a center of rotation or, in other words, a hinge, and find this hinge to be a very cooperative one.

Figure IV (b) shows how a center of rotation is established using a relatively large mass on the right end of the lever. Not only does this mass act as an inertial hinge, it also will move in a horizontal line to eliminate the induced lever arm stretch discussed above. The only problem this inertial hinge does not solve is rotation at the driving member. The angle of rotation of the lever is twice the arc-tangent of the maximum single amplitude vibration required, divided by the long lever arm.

$$\begin{aligned} \text{Angle} &= 2 \arctan \frac{\text{Double Amplitude}/2}{\text{Long Lever Arm}} \\ &= 2 \arctan \frac{.762 \text{ mm}}{130 \text{ mm}} \\ &= .006 \text{ Radians} \end{aligned}$$

Using the requirement described in Figure I and assuming a long lever arm of 130 mm results in a lever angle of .006 radian. Since translation presents no problem to the inertial hinge, and the rotation required is small, a reed hinge can be used to drive the lever. The tangent of the lever angle represents an induced vibration cross talk resulting from this design. Cross talk of up to 50% typically results from other sources so an induced cross talk of 0.6% deserves little concern. The system described works as a lever when the center of gravity is not moving, that is, when it is in vibrational isolation. At very low frequencies, the system is not in isolation and so it will not work as an amplifier. The system was designed to isolate at 50 to 90 Hertz and amplify vibration above its isolation frequency.

It has been mentioned that a greater force is required to drive the amplifier, than is effective at the test item. However, it is important to understand that the available vibration is greater than without the amplifier. The vibration acceleration level available from a shaker is the shaker force rating divided by the moving weight.

Vibration Level Available =

$$\frac{\text{Shaker Force Rating}}{\text{Moving Weight}}$$

$$\frac{\text{Shaker Force Rating}}{\text{Armature Weight (A)} + \text{Fixture Weight (F)} + \text{Test Item Weight (TI)}}$$

Since dead weight is used to shift the center of gravity, the mechanical amplifier will weigh approximately ten times as much as a conventional fixture designed for the same application. At frequencies below amplifier resonance, the available output of the amplifier system is lower than the conventional system because of its greater mass. For this frequency range:

Available Level (Conventional) =

$$\frac{FR}{A+F+TI}$$

Available Level (Amplifier) =

$$\frac{FR}{A+10F+TI}$$

Above amplifier resonance, the vibration level is amplified by the factor of amplification (X) and since the dead weight is in isolation (and therefore

not part of the moving weight) only a fraction of the amplifier weight need be considered. If we assume this fraction is 1/5 or twice the conventional fixture weight, the available output is:

Amplified Output

$$= \frac{(\text{Force Rating}) (X)}{A+2F+TI}$$

Assuming $X = 2$ Yields

$$\text{Amplified Output} = \frac{\text{Force Rating}}{\frac{A}{2} + F + \frac{TI}{2}}$$

This equation shows the amplifier effectively reduces the armature and test item weight by 50%. The assumptions of weights and amplification are easily obtainable through intelligent design of the amplifier, so an effective reduction of 50% of the armature weight is a reasonable goal.

AMPLIFIER DESIGN

A mechanical amplifier was proportioned to produce a 2:1 gain in vibration amplitude. (If displacement is amplified by 2, velocity and acceleration will also be amplified by 2 at all frequencies and assuming sinusoidal vibration.) Instead of the spherical mass depicted in Figure IV, a 7.6 cm square bar 35 cm long was used to produce the required inertia and was located 5.5 cm off the pivot. The lever is aluminum and measures 5 cm thick and extends 12 cm beyond the pivot. It has been lightened with several 4 cm diameter holes. The system is

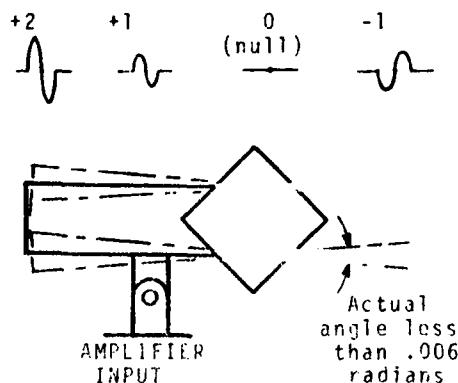


FIGURE V
MECHANICAL CONCEPT
OF
VIBRATION AMPLIFIER

expected to rotate about its center of gravity (approximate). The test item is attached to the lever along its edge.

Figure V shows this mechanical amplifier and the vibration profile along its length. The reed driver is depicted as a hinge. Due to the rotational moment of inertia, the actual center of rotation of the plate is shifted to the right of the center of gravity. This is a direct result of coupling of the linear and rotational modes of the plate. For this reason, the center of gravity was not assumed as the center of rotation for the fixture, but rather a point to the right of the center of gravity was used. The plate was attached to a shaker through a reed hinge and stabilized by a soft rubber snubber. Figure VI is a photo-



FIGURE VI
MECHANICAL AMPLIFIER

graph of this amplifier. The reed driver is to the left of the mass and a rubber snubber restricts the maximum deflection possible to eliminate a loss of control at the plate's rotational resonant frequency. The test item is mounted on the left edge of the plate.

AMPLIFIER PERFORMANCE

The mechanical amplifier described was evaluated to establish its performance characteristics. If we consider the amplifier as an unknown and evaluate its transfer function, we obtain Figure VII. The desired gain from Figure II is included on this figure to provide a comparison of desired versus actual gain. The notch and peak at 80

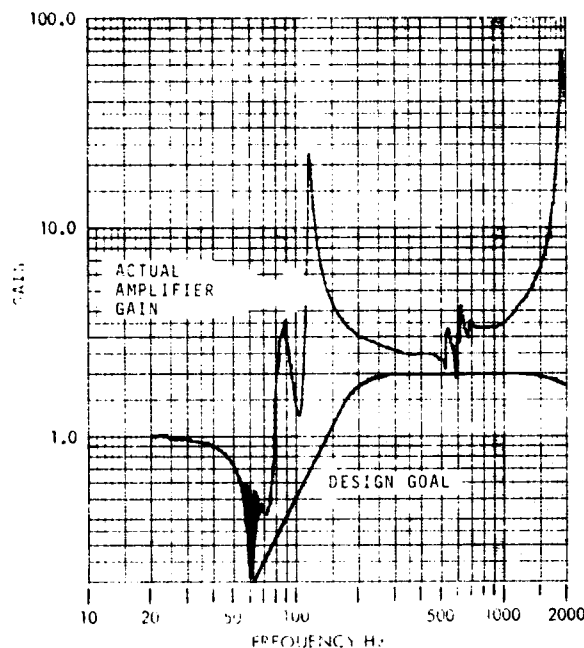


FIGURE VII
AMPLIFIER PERFORMANCE
VERSUS
DESIGN GOAL

Hertz is due to the rotational resonance of the plate on its mounting. Below 20 Hertz the plate and shaker move together, thus, the 1:1 transfer.

Figure VIII represents the 1.5 mm double amplitude/150 g requirement shaker motion. The shaker input remains below 100 g's over the entire frequency range. The amplifier requires a greater input than output at 70 Hertz. However, since most test requirements are low at this frequency, no gain is required.

Figure IX shows a 47 g (RMS) random vibration spectrum (straight lines) which resulted from a 15 g (RMS) input. During random testing, the full bandwidth is required simultaneously, precluding the use of a tunable resonance or narrow band amplifier.

CONCLUSIONS

The concept of a broad band mechanical amplifier was verified with a physical model which performed as predicted with no exceptions. Both sinusoidal and random vibrations can be amplified, facilitating tests at levels heretofore unobtainable.

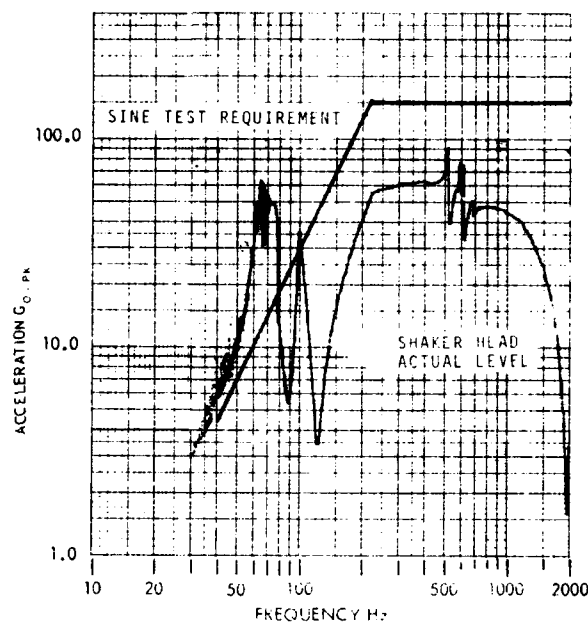


FIGURE VIII
SINE TESTING
INPUT VERSUS OUTPUT

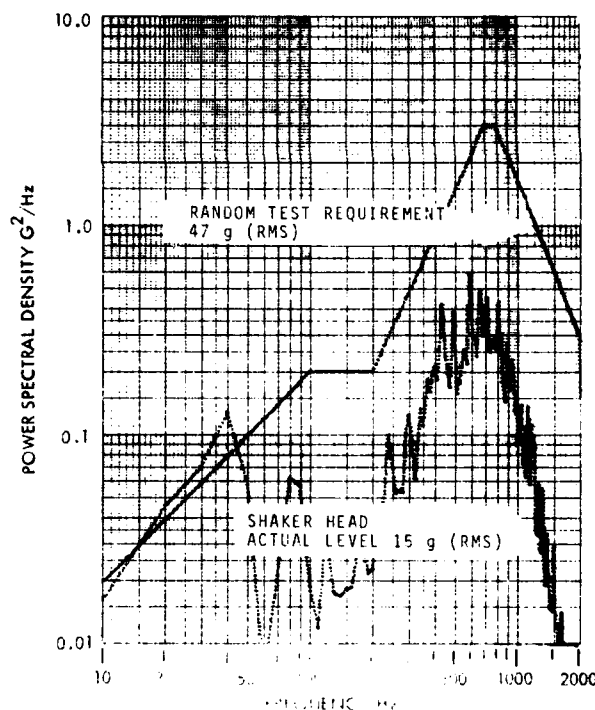


FIGURE IX
RANDOM TESTING
INPUT VERSUS OUTPUT

BIBLIOGRAPHY

- (1) D. Cerasuolo, J. Chin, "Description of a Shock and Vibration Displacement Amplifier" Shock and Vibration Bulletin 42, 1970.
- (2) R.T. Fandrich, "Self-Tuning Resonant Fixtures", 47th Shock and Vibration Symposium, October 1976.
- (3) Francis S. TSE, Ivan E. Morse, Rollant T. Hinkle, "Mechanical Vibrations", Silly and Bacon Inc., 1963.

STABILITY AND FREQUENCY RESPONSE OF HYDRO-MECHANICAL SHAKERS IN VIBRATION RIGS

Seshadri Sankar
Department of Mechanical Engineering
Concordia University, Montreal, Canada

A hydro-mechanical shaker is an effective alternate to an electro-hydraulic shaker for providing low frequency, large displacement and force. This paper presents an analytical study on the stability and frequency response of hydro-mechanical shakers used for generating vibrational signals to drive a vibration rig. The analytical expression for stability are derived based on linearized flow characteristic equations and taking into account the effect of fluid inertance and resistance in the connecting pipes. The results indicate that the size of the connecting pipes and their elasticity influence the stability of the shaker. Simple expressions are derived for the amplitude ratio and phase angle against frequency for both open and closed loop frequency response of the hydro-mechanical shaker based on Buffing's linearization scheme. The analytical expressions derived for stability and frequency response can be directly used for selecting and/or specifying the hydro-mechanical shaker which best meets a given set of requirements.

INTRODUCTION

Electro-hydraulic shaker systems permit vibration testing at force levels, displacements and frequencies outside the capabilities of electro-dynamic shaker systems. As a result, electro-hydraulic shakers are rapidly becoming accepted as effective complement to electro-dynamic exciters in a wide variety of applications such as in testing very large payloads of missiles, transport machineries, shipboard engines and instruments, and other products which are subject to vibration environments.

Table 1 shows the comparison of the capacity of electro-hydraulic and electro-dynamic mechanisms used as a drive for vibration rigs. The comparison outlined in Table 1 reflects that for the size and flexibility (force and displacement ratings), the cost of an electro-hydraulic shaker system is considerably lesser than for the electro-dynamic shaker. However, for industrial applications that require relatively low cost shaker systems, a hydro-mechanical shaker is an effective alternate to an electro-hydraulic shaker. The hydro-mechanical shaker can provide all significant features of an electro-hydraulic

shaker, like low frequency and high displacement and force capabilities. This paper is concerned in the systematic study of stability and frequency response of hydro-mechanical shakers in vibration rigs.

Figure 1 shows a typical hydro-mechanical shaker system used for generating vibratory angular motion. When designing a hydro-mechanical shaker for vibration testing, the size of hydraulic cylinder, valve, connecting pipes between valve and cylinder, and the dynamic behaviour of the mechanism must be known. In addition, the frequency response characteristics of the mechanism is also needed to determine its speed of response and natural frequency. Another important factor that should be known in the design of hydro-mechanical shakers is its stability characteristics. Instability is an inherent problem faced by designers of hydro-mechanical systems [2,3,4]. It is known that alterations in the design stage or selection of completely new parameters based on experience, often lead to dynamic instability in hydro-mechanical systems [5]. This paper presents the results of an analytical study on the stability and frequency response of hydro-mechanical

shakers used for generating vibrational signals to drive a vibration rig.

MATHEMATICAL MODELLING OF THE HYDRO-MECHANICAL SHAKER SYSTEM

The mechanism shown in Figure 1 consists of a platform which supports the test unit to be tested for vibratory input. The platform is supported by a stand and hinged at centre so that it can oscillate about a vertical axis from the force generated by the hydro-mechanical shaker. Any vibrational input signal given to the lever moves the spool valve, which allows hydraulic fluid to flow into the cylinder through the valve ports and thus actuate the piston according to the command signal. A displacement feedback is provided in the mechanism by rigidly connecting the valve body to the platform.

The system of equations that characterize the behaviour of the mechanism should take into account the following features:

- oil flow characteristics in the cylinder, connecting pipes and across the valve orifices;
- dynamic behaviour of the control valve and the action of the flow forces; and
- dynamic behaviour of the platform.

Considering a four-edge controlled, critical centered spool valve for controlling the flow into the hydraulic cylinder, the flow characteristic equations can be written as

$$Q_1 = C_d W e \left[\frac{2}{\pi} |P_s - P_1| \right]^{\frac{1}{2}} \text{sgn}(P_s - P_1) \quad (1)$$

for $e > 0$

$$Q_2 = C_d W e \left[\frac{2}{\pi} |P_2 - P_e| \right]^{\frac{1}{2}} \text{sgn}(P_2 - P_e) \quad (2)$$

and

$$Q_1 = C_d W e \left[\frac{2}{\pi} |P_1 - P_e| \right]^{\frac{1}{2}} \text{sgn}(P_1 - P_e) \quad (3)$$

for $e < 0$

$$Q_2 = C_d W e \left[\frac{2}{\pi} |P_s - P_2| \right]^{\frac{1}{2}} \text{sgn}(P_s - P_2) \quad (4)$$

where Q_1 and Q_2 are the flow rates as shown in Figure 1, and

$$e = x_1 - x_2 \quad (5)$$

Normally, in a hydro-mechanical shaker system the control valve is situated at a distance from the cylinder. This results in longer connecting pipes between the valve and cylinder. Such long pipes introduce pressure drops in the flow due to fluid resistance and inertance in the pipe. Assuming a circular cross-section for the pipes, the

equations relating the pressure drop in the pipes can be written as

$$(P_1 - P_{11}) = \frac{R}{a} Q_1 + I \frac{dQ_1}{dt} \quad (6)$$

$$(P_{22} - P_2) = \frac{R}{a} Q_2 + I \frac{dQ_2}{dt} \quad (7)$$

where R is the coefficient of resistance in the pipes and I is the fluid inertance in the pipes.

The set of equations governing the continuity characteristics in the hydraulic cylinder are given by

$$Q_1 = A \frac{dy}{dt} + \frac{1}{B} \left(\frac{V}{2} + Ay \right) \frac{dP_{11}}{dt} + C_L (P_{11} - P_{22}) \quad (8)$$

$$Q_2 = A \frac{dy}{dt} - \frac{1}{B} \left(\frac{V}{2} - Ay \right) \frac{dP_{22}}{dt} + C_L (P_{11} - P_{22}) \quad (9)$$

where in equations (8) and (9) a laminar leakage coefficient, C_L is assumed for the leakage flow past the cylinder piston. The equivalent volume V includes the total volume of the cylinder and the connecting pipes; $V = V_c + V_p \cdot B/B_p$.

Assuming a resilient coupling between the lever and the spool valve, the equation of motion of the spool valve can be written from the schematic diagram in Figure 2.

$$M_s \frac{d^2 x_2}{dt^2} + C_s \left(\frac{dx_2}{dt} - \frac{dx_3}{dt} \right) + K_s (x_2 - x_3) + F_f = F_\ell \quad (10)$$

where

$$F_\ell = K_\ell (x_1 - x_2) \quad (11)$$

and F_f , the flow force which always acts in a direction to close the valve ports can be written as

$$F_f = 0.43 W e [(P_s - P_e) - (P_1 - P_2)] \quad (12)$$

From the kinematic equation of the lever, the displacement x_1 can be expressed as

$$x_1 = \left(\frac{a_{22}}{a_{11}} \right) x \quad (13)$$

The equation characterizing the dynamic behaviour of the hydraulic piston is

$$M \frac{d^2 y}{dt^2} + C \frac{dy}{dt} + K_1 (y - z) = A (P_{11} - P_{22}) \quad (14)$$

where $M = M_p + M_f$; M_p is the mass of moving piston, and $M_f = 4\rho A^2/3a$, is the equivalent mass of liquid in the pipe referred to the cylinder.

The equation of motion for the angular displacement of the platform together with the load is given by

$$I_m \frac{d^2 \theta}{dt^2} + C_m \frac{d\theta}{dt} = K_1 r_1 (y - z) + K_s r_2 (x_2 - x_3) \quad (15)$$

where

$$x_3 = -\left(\frac{r_2}{r_1}\right)z \quad (16)$$

For mechanisms with large values of r_1 and r_2 (approx. 1-2m) and with small displacement z (approx. 3-4 cm), the kinematic relationship between z and θ can be expressed as

$$z = r_1 \theta \quad (17)$$

The foregoing set of equations (1)-(17) completely describes the mathematical representation of the hydro-mechanical shaker system.

STABILITY OF THE MECHANISM

An important constraint in hydro-mechanical shakers used as a drive for generating vibrational signals is to have a stable operation without any unbounded oscillations. It has been shown that design alterations made in hydro-mechanical systems has led into the sphere of dynamic instability [3,4,5]. Hence it is essential to establish the stability limits for the hydro-mechanical shaker so that the choice of mechanism parameters could be made without any fear of instability problem.

The non-linearities in the flow characteristics equations make the study of stability complex and hence in this paper these non-linear equations are linearized using Taylor's series for two variables and retaining terms up to the first order. Using this linearization the flow characteristic equations can be simplified as

$$Q_1 = C_e e - C_p P_1 \quad (18)$$

$$Q_2 = C_e e + C_p P_2 \quad (19)$$

where C_e and C_p are the flow gain and flow-pressure coefficients. In the steady-state condition the flows into and out of the hydraulic cylinder will be equal and in general therefore with symmetric valve porting

$$C_e = \frac{\partial Q_1}{\partial e} = -\frac{\partial Q_2}{\partial e}$$

and

$$C_p = \frac{\partial Q_1}{\partial P_1} = \frac{\partial Q_2}{\partial P_2}$$

In writing equations (18) and (19), it is assumed that there is no reverse flow in the valve ports and the operating point satisfies the condition $e > 0$. Now the rest of the equations (5-17) remain unchanged for the stability analysis except that the equations are considered to be the perturbed equations about the operating point with the corresponding perturbed parameters.

Now, adding equations (18) and (19)

gives

$$Q = C_e e - C_p P \quad (20)$$

Combining equations (8) and (9), it can be written as

$$A \frac{dy}{dt} + \frac{V}{2B} \frac{d\beta}{dt} + 2C_L \beta = Q \quad (21)$$

where

$$2\beta = P_{11} - P_{22}$$

Adding equations (6) and (7) and combining with equation (20) gives

$$I \frac{dQ}{dt} + \left(\frac{R}{a} + \frac{1}{C_p}\right)Q - \frac{C_e}{C_p}e + \beta = 0 \quad (22)$$

The steady-state flow forces in the spool valve given by the equation (12) can be simplified by using the tangents to the flow characteristic curve at the point of system equilibrium and can be expressed as

$$F_f = H \cdot Q \quad (23)$$

where

$$H = 0.43 W \sqrt{2P} / k$$

Equations (5), (10), (11), (13) and (23) can be combined and after simplification can be expressed as

$$M_s \frac{d^2 e}{dt^2} + M_s \frac{d^2 x_3}{dt^2} + C_s \frac{de}{dt} + (K_s + K_L)e + HQ + K_L x_3 = \left(\frac{K_L a_2}{a_1}\right)x \quad (24)$$

$$\text{where } x = -\left(\frac{r_2}{r_1}\right)z$$

Substituting $2\beta = (P_{11} - P_{22})$ in equation (14) gives

$$M \frac{d^2 y}{dt^2} + C \frac{dy}{dt} + K_1 y - K_1 z = 2A\beta \quad (25)$$

Substituting equations (16) and (17) in (15) and rearranging gives

$$I_m \frac{d^2 z}{dt^2} + C_m \frac{dz}{dt} + K_1 r_1^2 z = K_1 r_1^2 y + K_s r_1 r_2 e \quad (26)$$

Hence for stability analysis, equations (21) to (26) completely describe the linearized mathematical model of the mechanism. For zero-input stability, substitute the input lever displacement $x = 0$ and assume that the solution of this system of homogeneous linear equations will be in the form $[X] = [\tau]e^{\lambda t}$, where $[X]$ is a vector of variables; $[X]^T = [z, y, e, Q, p, x_3]$ and $[\tau]$ is a vector of constants. Now the characteristic equation will take the form of a determinant equation as given below:

$$\det \begin{bmatrix} \lambda^2 I_m + \lambda C_m + K_1 r_1^2 & -K_1 r_1^2 & -K_s r_1 r_2 & 0 & 0 & 0 \\ -K_1 & \lambda^2 M + \lambda C + K_1 & 0 & 0 & -2A & 0 \\ 0 & 0 & \lambda^2 M_s + \lambda C_s + K_s + K_\ell & H & 0 & \lambda^2 M_s + K_\ell \\ 0 & 0 & -C_e / C_p & \lambda I + R/a + 1/C_p & 1 & 0 \\ 0 & \lambda A & 0 & -1 & \lambda V/2B + 2C_\ell & 0 \\ r_2/r_1 & 0 & 0 & 0 & 0 & +1 \end{bmatrix} = 0 \quad (27)$$

Evaluating the determinant and arranging the terms according to the powers of λ , the characteristic equation can be expressed as a sixth-order polynomial with the coefficients as functions of design parameters.

When the mechanism has rigid connections, the stiffnesses K_ℓ and K_1 becomes infinity and the characteristic equation (27) reduces to the form

$$\alpha_1 \lambda^4 + \alpha_2 \lambda^3 + \alpha_3 \lambda^2 + \alpha_4 \lambda + \alpha_5 = 0 \quad (28)$$

where the coefficients α 's are defined as

$$\alpha_1 = I_m I V/2B$$

$$\alpha_2 = (I_m \hat{\alpha} + C_m I)V/2B$$

$$\alpha_3 = I_m + (C_m \hat{\alpha} + K_s r_2^2 I)V/2B + 2r_1^2 A^2 I$$

$$\alpha_4 = C_m + (K_s r_2^2 V/2B + 2r_1^2 A^2) \hat{\alpha}$$

$$\alpha_5 = K_s r_2^2 + 2r_1 r_2 A C_e / C_p$$

$$\text{and } \hat{\alpha} = (R/a + 1/C_p)$$

Using the Routh-Hurwitz stability criterion [6] in equation (28), the absolute stability is given by the condition

$$\frac{\alpha_4}{\alpha_2} [\alpha_3 - \alpha_1 \alpha_4 / \alpha_2] > \alpha_5 \quad (29)$$

Substituting the coefficients of equation (28) into equation (29) gives

$$\frac{C_p}{C_e} > \left[\frac{V_t + \frac{V_p}{B_p} B}{2 B A} \right] \cdot \frac{r_2}{r_1} \quad (30)$$

The above inequality relationship gives the stability condition for the hydro-mechanical shaker system considered in this paper. Since this stability condition gives the limiting value of the valve characteristic, C_p/C_e , as a function of the mechanism parameters and the geometry of the connecting pipes, it aids to a great extent in the selection of a valve or in the design of the mechanism. It can be seen that the fluid inertance and the flow resistance due to

the connecting pipes have no influence on the stability of the mechanism. However, the size of the connecting pipes and their elasticity influence the stability of the mechanism. For a hydro-mechanical shaker used in vibration testing [7,8] and having parameters as in Table 2, the stability regions for variations in the geometry of the connecting pipes are calculated and are shown in Figure 3.

FREQUENCY RESPONSE OF THE HYDRO-MECHANICAL SHAKER SYSTEM

In analyzing the frequency response, the first step is to find the open loop frequency response of the mechanism when the housing of the control valve is disconnected from the platform. In the presence of a harmonic input displacement of the lever, the set of equations (1) to (17) describing the motion of the hydro-mechanical drive can be used for the frequency response analysis. The non-linear flow characteristic equations raise the major problem in determining the frequency characteristics. To overcome this difficulty, the linearized model of the flow characteristic equations in the stability analysis can be used. However, this linearized model has a major disadvantage when used for frequency analysis because of the fact that the coefficients of the linearized equation changes all the time during a cycle of events, and to evaluate a realistic mathematical model is very difficult. Hence in this paper, instead of linearizing the non-linear flow equations, they are expressed as a power series and the procedure is as follows:

Combining equations (1-4) and rearranging, the average flow Q can be expressed as

$$Q = k e p^{\frac{1}{2}} \left[1 - \frac{p}{p_c} \cdot \frac{e}{|e|} \right]^{\frac{1}{2}} \quad (31)$$

The above equation can be expanded binomially and the flow Q which includes the first two terms in the expansion is shown in Figure 4. However, for large values of p , which occur in vibration rigs with heavy loads, the mechanism

operates in a region as shown in Figure 4. For this operating state, the flow equation can be written as

$$Q = k e P^{\frac{1}{2}} - k |e| p / P^{\frac{1}{2}} \quad (32)$$

Since the fluid resonance due to the valve dynamics is only secondary in comparison with the resonance associated with the hydraulic cylinder, the control valve dynamics and the influence of the connecting pipes are considered to be negligible. Also, in this analysis the stiffness K_k of the contact spring of the lever is assumed to be infinite. Hence, substituting $P_{11} = P_1$, $P_{22} = P_2$ and $x_1 = x_2$ and neglecting equations (6) and (7), the following set of equations can be formulated for the open loop system:

By combining equations (8) and (9) and substituting equation (32) gives

$$A \frac{dy}{dt} + \frac{V}{2B} \frac{dp}{dt} + 2C_k p = k e P^{\frac{1}{2}} - k |e| p / P^{\frac{1}{2}} \quad (33)$$

$$\text{where } e = \frac{a_{22}}{a_{11}} x \quad (34)$$

Rearranging equation (14) gives

$$M \frac{d^2 y}{dt^2} + C \frac{dy}{dt} + K_1 (y - z) = 2A p \quad (35)$$

Combining equations (15) and (17) gives

$$I_m \frac{d^2 z}{dt^2} + C_m \frac{dz}{dt} + K_1 r_1^2 z = K_1 r_1^2 y \quad (36)$$

By combining equations (33-36) and rearranging, gives

$$a_1 \frac{d^5 z}{dt^5} + [a_2 + a_3 |x|] \frac{d^4 z}{dt^4} + [a_4 + a_5 |x|] \frac{d^3 z}{dt^3} + [a_6 + a_7 |x|] \frac{d^2 z}{dt^2} + [a_8 + a_9 |x|] \frac{dz}{dt} = a_{10} x \quad (37)$$

where

$$a_1 = V d_1 / 2B$$

$$a_2 = V d_2 / 2B + 2C_k d_1$$

$$a_3 = i k d_1 / P^{\frac{1}{2}}$$

$$a_4 = A I_m / K_1 r_1^2 + V d_3 / 2B + 2C_k d_2$$

$$a_5 = i k d_2 / P^{\frac{1}{2}}$$

$$a_6 = A C_m / K_1 r_1^2 + V d_4 / 2B + 2C_k d_3$$

$$a_7 = i k d_3 / P^{\frac{1}{2}}$$

$$a_8 = A + 2C_k d_4$$

$$a_9 = i k d_4 / P^{\frac{1}{2}}$$

$$a_{10} = i k P^{\frac{1}{2}}$$

$$d_1 = I_m M / 2K_1 r_1^2 A$$

$$d_2 = (C_m M + I_m C) / 2K_1 r_1^2 A$$

$$d_3 = (M K_1 r_1^2 + C_m C + I_m K_1) / 2K_1 r_1^2 A$$

and

$$d_4 = (C r_1^2 + C_m) / 2r_1^2 A$$

The non-linear differential equation (37) expresses the open-loop characteristics of the hydro-mechanical drive. In order to obtain an analytical expression for the open-loop frequency characteristics, a linearization of the non-linearities are carried out based on Duffing's linearization method [9]. Appendix 1 describes the procedure in predicting approximate open loop response using Duffing's method. The open-loop amplitude ratio and phase angle for sinusoidal input, derived in Appendix 1, are given by

$$\frac{\hat{z}}{\hat{x}} = \frac{-C_3 \sin \phi}{C_1 + C_2 \hat{x} + C_4 \hat{x} \sin 2\phi + C_5 \hat{x} \cos 2\phi} \quad (39)$$

and

$$\phi = \arctan \left[\frac{C_1 + (C_2 + C_5) \hat{x}}{C_6 - (C_4 - C_7) \hat{x}} \right] + \pi \quad (40)$$

where $\frac{\hat{z}}{\hat{x}}$ = open-loop amplitude ratio, (output amplitude/input amplitude)

$$C_1 = a_1 \omega^5 - a_4 \omega^3 + a_8 \omega$$

$$C_2 = \frac{2}{\pi} [a_9 \omega - a_5 \omega^3]$$

$$C_3 = -a_{10}$$

$$C_4 = \frac{2}{3\pi} [a_3 \omega^4 - a_7 \omega^2] \quad (41)$$

$$C_5 = \frac{2}{3\pi} [a_5 \omega^3 - a_9 \omega]$$

$$C_6 = a_2 \omega^4 - a_6 \omega^2$$

$$C_7 = 3C_4$$

The term π is added in equation (40) to reflect that z and x are measured in opposite directions.

For a closed-loop hydro-mechanical drive having a rigid connection between the spool valve and platform, the initial system of equations (32) - (36) remains the same except for changes in the equation of the spool displacement. For a closed-loop drive, the spool valve displacement equation (34) becomes

$$e = \frac{a_{22}}{a_{11}} x - \frac{r_2}{r_1} z$$

Hence using the above equation and the open-loop transfer function, the closed-loop transfer function can be written as

$$G_c(j\omega) = \frac{G_0(j\omega)}{1 + G_0(j\omega) \cdot i_1} \quad (42)$$

where $i_1 = r_2/r_1$

and $G_0(j\omega)$ is the open-loop transfer function given by

$$G_0(j\omega) = \frac{\hat{z}}{\hat{x}} e^{-j\phi(\omega)}$$

From equation (42), the frequency characteristics of a closed-loop hydro-mechanical drive can be determined by the known frequency characteristics of an open-loop hydro-mechanical drive.

Rewriting the equation (42), the amplitude ratio and the phase angle against frequency for the closed-loop mechanism can be written as

$$|G_c(j\omega)| = \frac{i\hat{z}/\hat{x}}{[1 + 2i i_1 \cos\phi(\omega)/\hat{x} + (2 i_1/\hat{x})^2]^{1/2}}$$

$$G_c(j\omega) = -\phi(\omega) + \arctan \left[\frac{\hat{z} i_1 \sin\phi(\omega)/\hat{x}}{1 + 2 i_1 \cos\phi(\omega)/\hat{x}} \right]$$

where \hat{z}/\hat{x} and $\phi(\omega)$ are as given in equations (39) and (40)

RESULTS AND DISCUSSION

Using the expressions derived for open- and closed-loop frequency response characteristics, the plots of the amplitude ratio and phase angle against frequency, are drawn for values of $B = 145$ and 1450 N/cm^2 and are as shown in Figures 5 to 8. It can be seen from the amplitude plots that the natural frequency of the hydro-mechanical system increases as the values of B_p increases. Further, the closed-loop amplitude ratio remains almost a constant over the frequency range from D.C. to a frequency below the natural frequency. This frequency range is the actual operating range of the hydro-mechanical vibration rig.

In order to estimate the error involved in using the Duffing's linearization method, the non-linear equations characterizing the dynamic behaviour of the hydro-mechanical shaker system were solved using a digital computer. These results were superposed on the closed-loop amplitude ratio against frequency plots (Figures 6 and 8) for the input amplitudes of $\hat{x} = 0.05$ and 0.2 cm . From these results, it can be seen that good correlation exists in obtaining frequency response characteristics using the Duffing's linearization method.

The expressions derived for the frequency response characteristics based on the Duffing's method are simple and

straightforward in calculating the frequency characteristics of hydro-mechanical shakers. Further, the linearization method avoids any repeated, time-consuming digital computer solution of non-linear system of differential equations for every value of ω , \hat{x} and B_p . Based on the above facts, the formulae deduced from the Duffing's linearization method can be recommended for the calculation of frequency characteristics of hydro-mechanical shaker systems.

CONCLUSIONS

An analytical study on the stability and frequency response of hydro-mechanical shakers used for generating vibrational signals to drive a vibration rig is presented. The system of equations that characterize the behaviour of the shaker takes into account: a) oil flow characteristics in the cylinder, connecting pipes and across the valve orifices; b) dynamic behaviour of the control valve and the action of flow forces; and c) dynamic behaviour of the vibrating platform. Based on the above features, the analytical expression for stability are derived using the linearized flow characteristic equations. The stability condition gives the limiting value of the valve characteristic, C_p/C_e , as a function of the shaker parameters and the geometry of the connecting pipes. The results indicate that the fluid inertia and the flow resistance due to the connecting pipes have no influence on the stability of the shaker system. However, the size of the connecting pipes and their elasticity influence the stability of the shaker.

This paper also presents an analytical expression for calculating the amplitude ratio (output/input) and phase angle against frequency for both open- and closed-loop response of hydro-mechanical shaker systems. The formulae for the frequency response characteristics are derived based on the Duffing's linearization method. Major advantages of this method are its simplicity and its use in avoiding any tedious time-consuming digital computer solution of non-linear system of differential equations.

The frequency response characteristics of the hydro-mechanical shaker system calculated using the method outlined in this paper are found to have good agreement with the results obtained using direct digital computer solution of differential equations. The formulae for the frequency response and stability criterion derived respectively can be directly used by personnel in vibration testing to select and/or specify the

hydro-mechanical shaker which best meets a given set of requirements.

ACKNOWLEDGMENTS

The present work is a part of the research program for the developing techniques for analysis and design of hydro-mechanical systems in vibration environment. The support of the National Research Council of Canada, Grant No. A3685, and the Formation de Chercheurs et d'Action Concertée, of the Government of Quebec, Grant No. 042-110, is acknowledged.

REFERENCES

- (1) Random Vibration Seminar Course Notes by MB Electronics.
- (2) Harpur, N.F., "Some Design Considerations of Hydraulic Servos of Jack Types", Proceedings of Conference on Hydraulic Servo-mechanisms, Institution of Mechanical Engineers, London, 1953.
- (3) Chiappulini, R., "Sur la stabilité dynamique des hydro-copiers avec retroaction et appui de faible rigidité", Annals of the C.I.R.P., Vol. 15, 1967, pp. 129-135.
- (4) Sankar, S. and Osman, M.O.M., "On the Dynamic Accuracy of Machine-Tool Hydraulic Copying Systems", Trans. ASME, Journal of Engineering for Industry, Vol. 96, Series B, No. 2, May 1974, pp. 518-524.
- (5) Zeleny, J., "Stability of Hydraulic Copying-Systems", Czechoslovak Heavy Industry, No. 1, 1955.
- (6) Shinnars, S.M., "Modern Control System Theory and Application", Addison-Wesley, Inc., California, 1972.
- (7) Vavilov, A.A. and Solodovnikov, A.I., "Experimental Determination of Frequency Characteristics of Automatic Systems", Gosenergoizdat, 1963.
- (8) Gudilkin, Yu. I., "Frequency Characteristics of a hydraulic Drive with a Restrictor", Russian Engineering Journal, Vol. 11, No. 4, 1973, pp. 35-39.
- (9) Stoker, J.J., "Nonlinear Vibrations in Mechanical and Electrical Systems", Interscience Publishers, Inc., New York, 1950.

APPENDIX I

The first approximation required for solving the non-linear differential equation (37) using Duffing's method is to assume that the output response is sinusoidal for harmonic inputs. That is for

$$x = \hat{x} \sin(\omega t + \phi) \quad (A.1)$$

The output is given by

$$z = \hat{z} \sin(\omega t) \quad (A.2)$$

By Fourier analysis, $|x|$ can be written as

$$|x| = |\hat{x} \sin(\omega t + \phi)| \approx \frac{2}{\pi} \hat{x} [1 - \frac{2}{3} \cos 2(\omega t + \phi)] \quad (A.3)$$

Substituting equations (A.1 - A.3) in equation (37) and rearranging gives

$$\begin{aligned} [C_1 \hat{z} + C_2 \hat{x} \hat{z} + C_3 \hat{x} \sin \phi + C_4 \hat{x} \hat{z} \sin 2\phi \\ + C_5 \hat{x} \hat{z} \cos 2\phi] \cos \omega t + [C_6 \hat{z} + C_7 \hat{x} \hat{z} \\ + C_3 \hat{x} \cos \phi + C_4 \hat{x} \hat{z} \cos 2\phi - C_5 \hat{x} \hat{z} \sin 2\phi] \\ \sin \omega t + \text{terms associated with} \\ \sin(3\omega t + 2\phi) \text{ and } \cos(3\omega t + 2\phi) = 0 \end{aligned} \quad (A.4)$$

The coefficient C_1, \dots, C_7 are defined in equation (41).

In equation (A.4) the coefficients associated with $\cos \omega t$ and $\sin \omega t$ must be equal to zero. Hence

$$\begin{aligned} C_1 \hat{z} + C_2 \hat{x} \hat{z} + C_3 \hat{x} \sin \phi + C_4 \hat{x} \hat{z} \sin 2\phi + \\ + C_5 \hat{x} \hat{z} \cos 2\phi = 0 \end{aligned} \quad (A.5)$$

$$\begin{aligned} C_6 \hat{z} + C_7 \hat{x} \hat{z} + C_3 \hat{x} \cos \phi + C_4 \hat{x} \hat{z} \cos 2\phi \\ - C_5 \hat{x} \hat{z} \sin 2\phi = 0 \end{aligned} \quad (A.6)$$

From equations (A.5) and (A.6) the unknowns \hat{z} and ϕ can be solved to give

$$\frac{\hat{z}}{\hat{x}} = \frac{-C_3 \sin \phi}{C_1 + C_2 \hat{x} + C_4 \hat{x} \sin 2\phi + C_5 \hat{x} \cos 2\phi} \quad (A.7)$$

and

$$\tan \phi = \frac{C_1 + (C_2 + C_5) \hat{x}}{C_6 - (C_4 - C_7) \hat{x}} \quad (A.8)$$

The equations (A.7) and (A.8) give the analytical expressions for the open-loop amplitude ratio and phase shift of the hydro-mechanical drive.

NONENCLATURE

A	effective cross-sectional area of piston; cm^2	K_s	stiffness of spring between valve spool and body; N/cm^2
a	effective cross-sectional area of connecting pipes; cm^2	k	$C_d W [2/\rho]^{1/2}$; $\text{cm/sec.N}^{1/2}$
$a_{1,2,2}$	linear dimensions of the lever; cm	L	total stroke of piston; cm
B	bulk modulus of elasticity of fluid; N/cm^2	ℓ	total length of connecting pipes; cm
B_p	bulk modulus of elasticity of the connecting pipes and fluid inside; N/cm^2	M	$M_p + M_f$; total moving mass referred to the cylinder; Kg
C	viscous damping coefficient between piston and cylinder; N.sec/cm	M_f	mass of fluid in the pipe referred to the cylinder; Kg
C_d	coefficient of discharge; dimensionless	M_p	Mass of piston; Kg
C_e	slope of valve flow - valve opening curve; $\text{cm}^3/\text{sec.cm}$	M_s	mass of spool valve; Kg
C_ℓ	laminar leakage coefficient; $\text{cm}^5/\text{N.sec.}$	$P_{1,2}$	Pressures in the valve ports; N/cm^2
C_m	damping coefficient at the pivot in vibration rig; N.sec./cm	$P_{11,22}$	pressures in the cylinder chambers; N/cm^2
C_p	slope of valve flow - pressure drop curve; $\text{cm}^5/\text{sec.N}$	P	$\frac{P_s - P_e}{2}$; N/cm^2
C_s	viscous damping coefficient in spool valve; N.sec./cm	$P_{s,e}$	supply and exhaust pressures; N/cm^2
d	diameter of the connecting pipes; cm	p	$\frac{P_1 - P_2}{2}$; N/cm^2
e	valve error; cm	\hat{p}	$\frac{P_{11} - P_{12}}{2}$; N/cm^2
F_f	flow force on valve; N	$Q_{1,2}$	flow into and out of cylinder chambers; $\text{cm}^3/\text{sec.}$
F_ℓ	restoring force of lever contact spring; N	Q	$\frac{Q_1 + Q_2}{2}$; $\text{cm}^3/\text{sec.}$
I	fluid inertance in the pipes; $\text{N.sec.}^2/\text{cm}^5$	R	fluid resistance in pipes; N.sec./cm^3
I_m	mass moment of inertia of the platform and the load; N.cm.sec^2	$r_{1,2}$	linear dimensions of the platform; cm
i	$a_{2,2}/a_{1,1}$; dimensionless	t	time; sec.
i_1	r_2/r_1 ; dimensionless	V	$V_t + V_p B/B_p$; equivalent volume referred to the cylinder; cm^3
j	$\sqrt{-1}$	V_t	total volume of cylinder; cm^3
K	stiffness of spring between cylinder and platform; N/cm^2	V_p	total volume of connecting pipes; cm^3
K	stiffness of spring between lever and valve; N/cm^2	W	width of valve port; cm
		x	input displacement; cm
		$x_{1,2,3}$	displacements referred in Figure 2; cm
		\hat{x}	amplitude of harmonic input displacement; cm
		y	absolute displacement of piston; cm

z	absolute displacement of platform; cm	ρ	mass density of fluid; kg/cm ³
\hat{z}	amplitude of harmonic output displacement; cm	ϕ	phase angle between input and open-loop output; rad.
θ	angular displacement of platform; rad.	ω	frequency; rad./sec.

TABLE 1

Comparison of Electro-hydraulic and Electro-Dynamic Drives for Vibration Rigs [1]

Load = 3400 N

Acceleration = 20 g

Frequency = 25-250 Hz

Description	Electro-hydraulic Drive	Electro-Dynamic Drive
HYDRAULIC POWER SUPPLY		
size	1.5 x 2.1m x 1.2m (high)	
weight	4.45 x 10 ⁴ N	
input power	1.30 kva	
POWER AMPLIFIER (servo valve)		
size	164 cm ³	1.8m x 2.4m x 2.1m (high)
weight	890 N	6.25 x 10 ⁴ N
input power	hydraulic power supply	200 kva
ACTUATOR		
size	0.3m x 0.3m x 0.3m (high)	1.5m x 2.7m x 1.5m (high)
weight	1335 N	13.4 x 10 ⁵ N
APPROXIMATE COST	\$75,000.	\$120,000.

TABLE 2

System Parameters of a Hydro-Mechanical Shaker

$A = 80 \text{ cm}^2$	$I_m = 1176 \text{ N.m.s}^2$	$P_e = 0$
$B = 1.5 \times 10^3 \text{ N/cm}^2$	$K_1 = 9.8 \times 10^3 \text{ N/cm}$	$r_1 = 100 \text{ cm}$
$B_p = 14.5 \times 10^2 \text{ N/cm}^2$	$l = 100 \text{ cm}$	$r_2 = 100 \text{ cm}$
$d = 1.5 \text{ cm}$	$L = 10 \text{ cm}$	$W = 4.4 \text{ cm}$
$i = a_2/a_1 = 0.34 \text{ cm}$	$P_s = 294 \text{ N/cm}^2$	

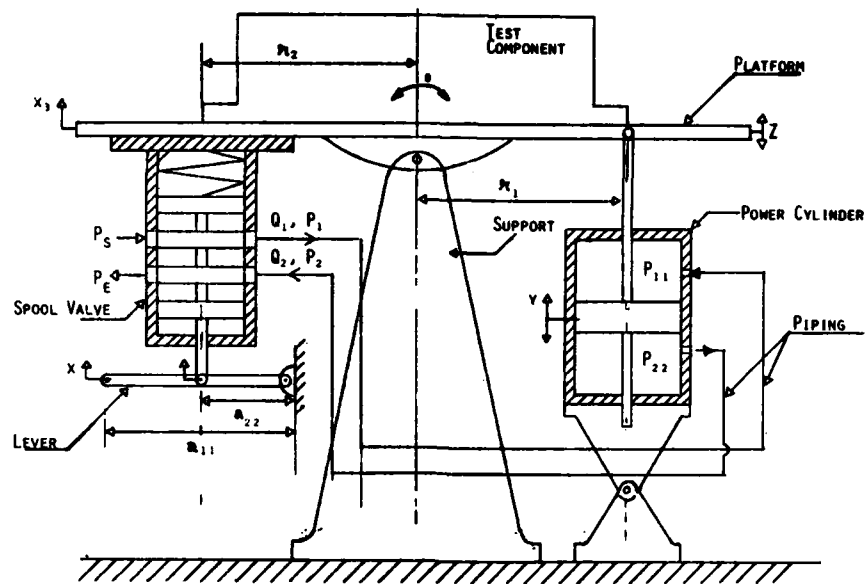


Figure 1. Schematic Diagram of a Hydro-Mechanical Shaker System

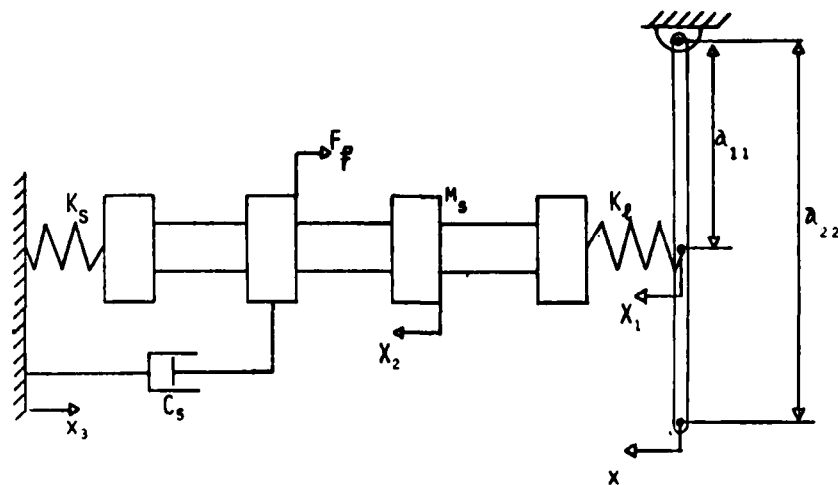


Figure 2. Schematic Diagram of Spool Valve-Lever System

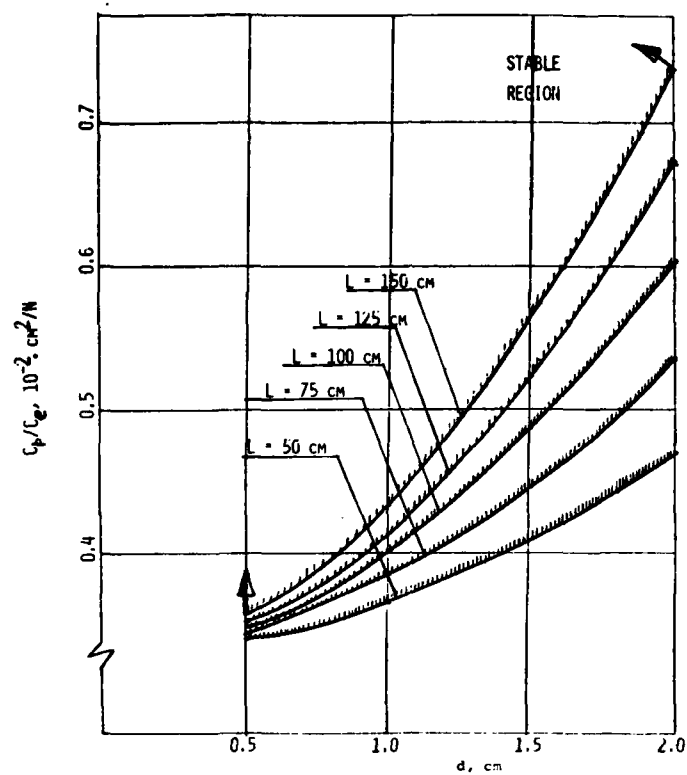


Figure 3. Stability Regions for Hydro-Mechanical Shaker Systems

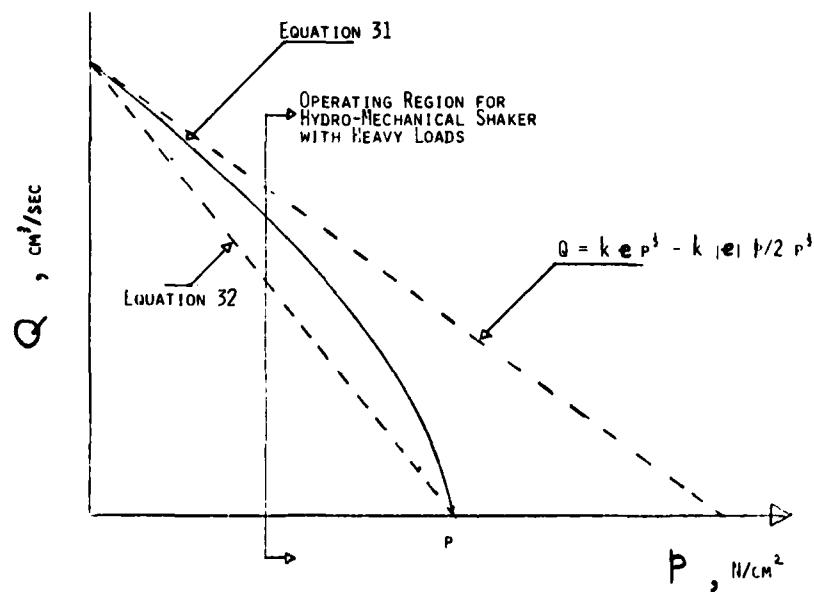


Figure 4. Flow Characteristic of Spool Valve

$\hat{x} = 0.005$ $\hat{x} = 0.05$ $\hat{x} = 0.15$
 $\hat{x} = 0.01$ $\hat{x} = 0.1$ $\hat{x} = 0.2$

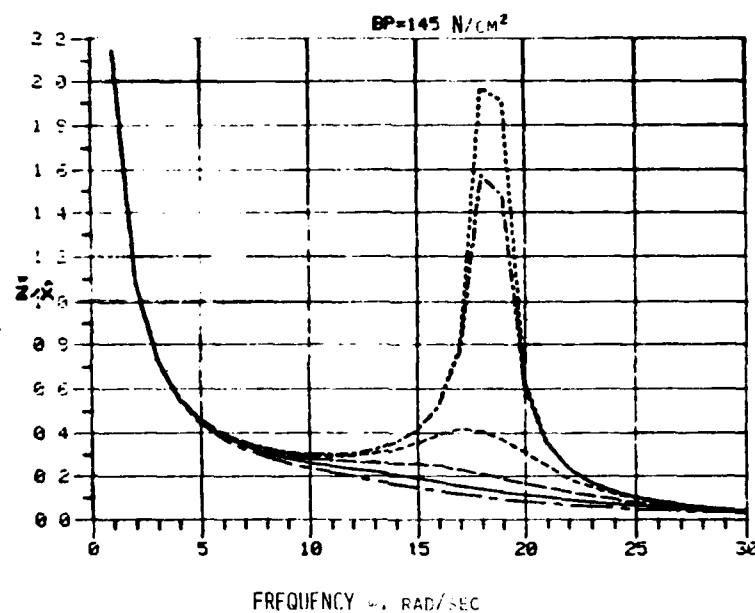


Figure 5a. Open-Loop Amplitude Ratio VS Frequency

$\hat{x} = 0.005$ $\hat{x} = 0.05$ $\hat{x} = 0.15$
 $\hat{x} = 0.01$ $\hat{x} = 0.1$ $\hat{x} = 0.20$

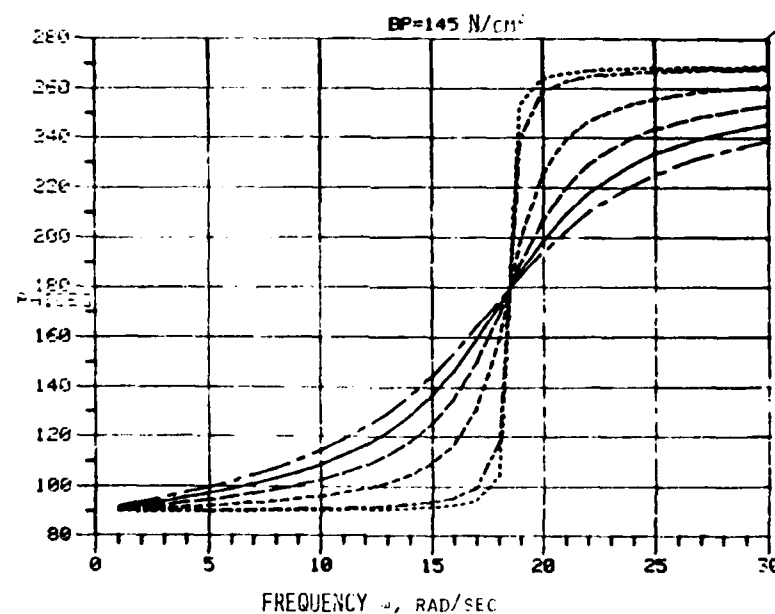


Figure 5b. Open-Loop Phase Angle VS Frequency

$\hat{x} = 0.005$ $\hat{x} = 0.05$ $\hat{x} = 0.15$
 $\hat{x} = 0.01$ $\hat{x} = 0.1$ $\hat{x} = 0.2$
 ○ Digital Computer Result; $\hat{x} = 0.05$ □ Digital Computer Result; $\hat{x} = 0.2$

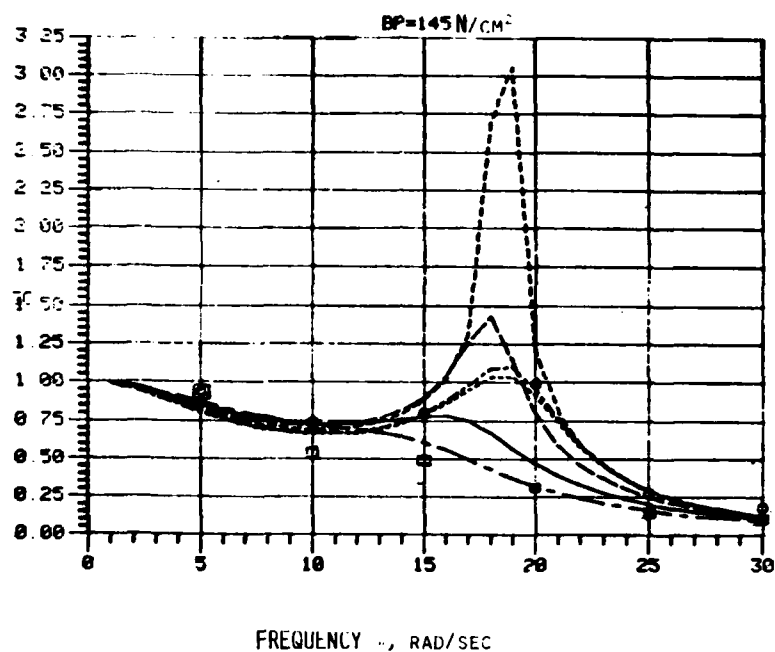


Figure 6a. Closed-Loop Amplitude Ratio VS Frequency

$\hat{x} = 0.005$ $\hat{x} = 0.05$ $\hat{x} = 0.15$
 $\hat{x} = 0.01$ $\hat{x} = 0.1$ $\hat{x} = 0.2$

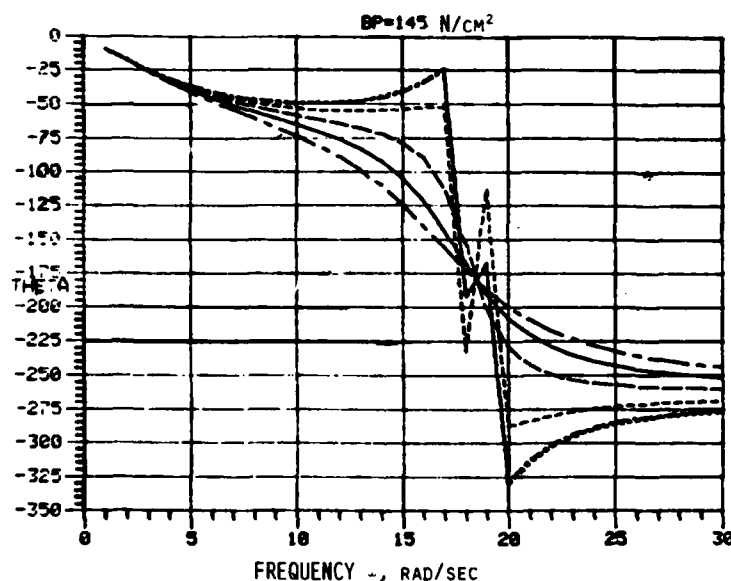


Figure 6b. Closed-Loop Phase Angle VS Frequency

$\hat{x} = 0.005$ $\hat{x} = 0.05$ $\hat{x} = 0.15$
 $\hat{x} = 0.01$ $\hat{x} = 0.1$ $\hat{x} = 0.2$

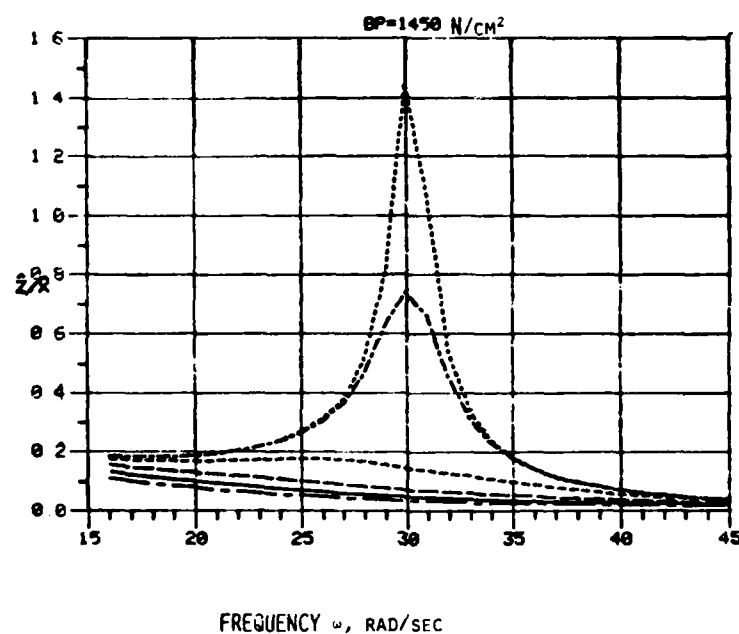


Figure 7a. Open-Loop Amplitude Ratio VS Frequency

$\hat{x} = 0.005$ $\hat{x} = 0.05$ $\hat{x} = 0.15$
 $\hat{x} = 0.01$ $\hat{x} = 0.1$ $\hat{x} = 0.20$

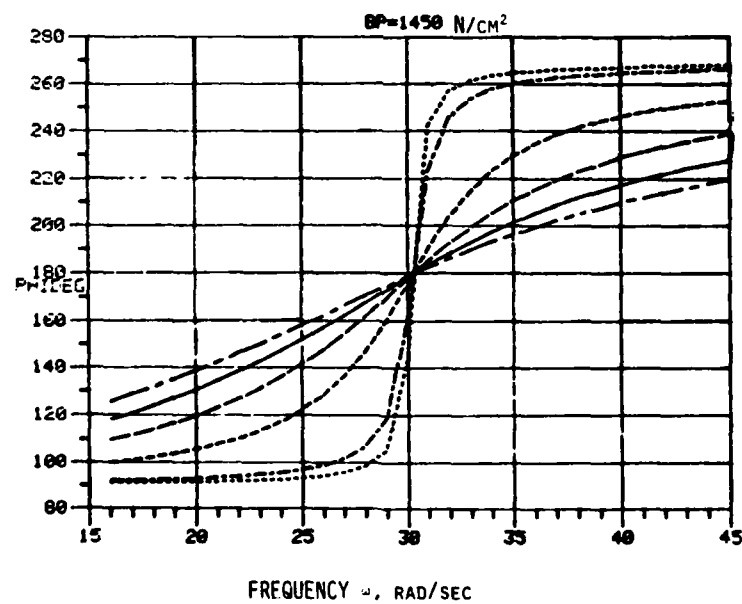


Figure 7b. Open-Loop Phase Angle VS Frequency

$\hat{x} = 0.005$ $\hat{x} = 0.05$ $\hat{x} = 0.15$
 $\hat{x} = 0.01$ $\hat{x} = 0.1$ $\hat{x} = 0.20$
 ○ Digital Computer Result; $\hat{x} = 0.05$ □ Digital Computer Result; $\hat{x} = 0.2$

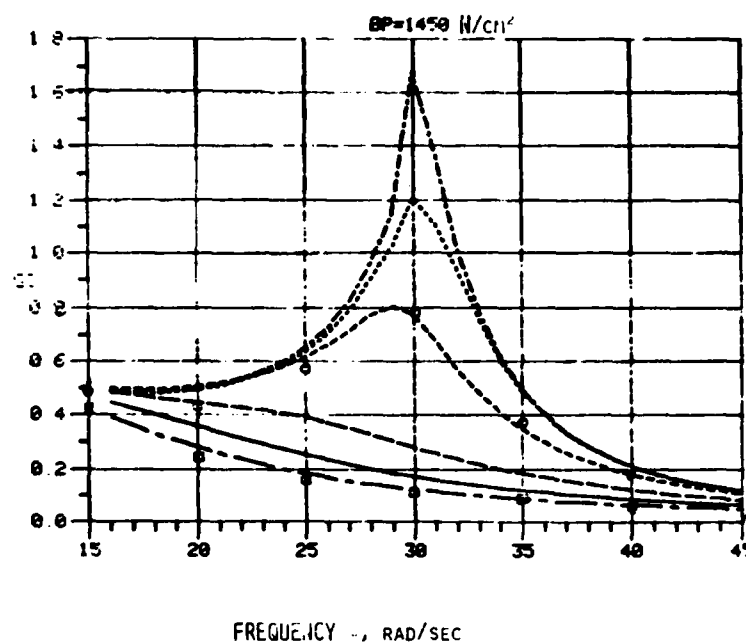


Figure 8a. Closed-Loop Amplitude Ratio VS Frequency

$\hat{x} = 0.005$ $\hat{x} = 0.005$ $\hat{x} = 0.15$
 $\hat{x} = 0.01$ $\hat{x} = 0.1$ $\hat{x} = 0.20$

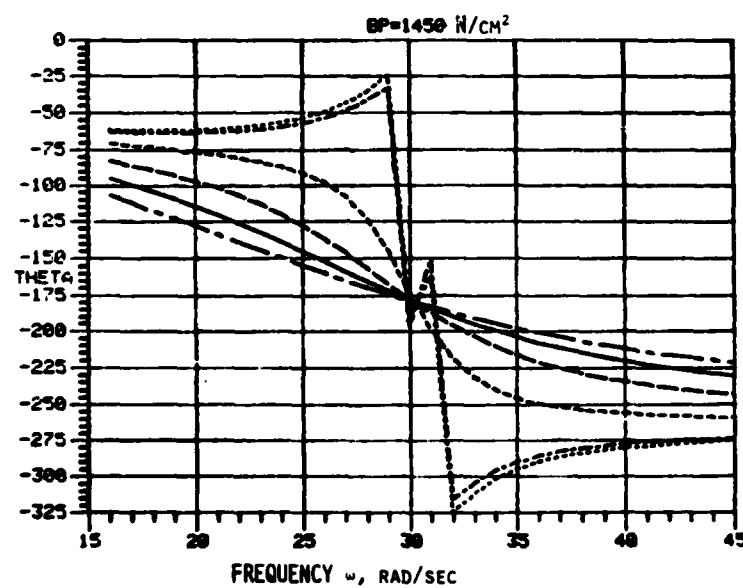


Figure 8b. Closed-Loop Phase Angle VS Frequency

MIL-STD-781C RANDOM RELIABILITY TESTING
PERFORMED BY USING ACOUSTIC COUPLING

S.M. Landre
Harris Corporation, Electronic Systems Division
Melbourne, Florida

This paper describes an approach for performing random vibration during reliability testing by using an acoustic coupled shaker system. The new Revision C to MIL-STD-781 is requiring either random or sine vibration during temperature cycling, depending on the equipment specification. The requirement to subject some test items to random vibration instead of sine vibration creates demands for inexpensive replacement equipment capable of performing the new tests.

INTRODUCTION

Currently available replacement shaker systems such as electrodynamic and mechanical, capable of performing random vibration, are costly and/or inaccurate. Electrodynamic shaker systems can easily meet both random or sine vibration test requirements, except their great cost generally prohibits their application. Although mechanical shaker systems are less expensive than electrodynamic systems, they are quite inaccurate and are unable to produce the desired response at all frequencies. The development of an inexpensive and accurate random motion shaker system would greatly simplify the performance of MIL-STD-781C reliability testing, requiring random vibration.

The acoustic coupled shaker system, described in this paper, employs four (4) basic components; a speaker, a flat plate fixture, a hi-fi amplifier and a hi-fi tape recorder capable of playing a tape loop. A digital random vibration control system is initially used to generate the desired random noise signal which is amplified and reproduced through the speaker as sound energy. This sound energy is transmitted to the fixture through a coupling medium, producing random motion on the fixture. When the random noise from the digital random vibration control system is equalized and the fixture response is within the desired

tolerance, the amplified signal is recorded on a tape loop. This recorded signal can then be played back at any time to run its particular random vibration profile on the acoustic coupled shaker, without further need of a random vibration control system.

This paper also describes the laboratory experiments performed on an acoustic coupled shaker model to evaluate its performance and potential.

NEW REVISION C TO MIL-STD-781

The C revision to MIL-STD-781 has a much more demanding vibration requirement than did the previous B revision. Where applicable, the B revision only required sine vibration at a $2.2 \text{ g} \pm 10\%$ peak acceleration level at a non-resonant frequency between 20 and 60 Hz. For every hour of operating time, the equipment is vibrated for 10 minutes. The vibration requirement of Revision C is dependant on equipment usage and its expected environment. The purpose of this requirement is to subject the equipment to a vibration exposure similar in all respects to what the equipment will see in the field. Vibration will consist of either sine or random over a bandwidth from 4 to 2000 Hz for a short to continuous time period.

ACOUSTIC COUPLED (a/c) SHAKER SYSTEM OPERATION

The a/c shaker system was designed to be simple and inexpensive. Figure 1 shows a block diagram of the basic equipment comprising the a/c shaker system.

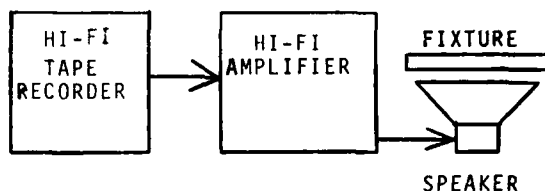


Figure 1
Acoustic Coupled Shaker System.

A pre-recorded tape loop of a random noise signal is played on the hi-fi tape recorder, amplified through the hi-fi amplifier and reproduced as sound energy through the speaker. The fixture is excited by the sound energy, consequently producing random motion. Initially, however, the taped random signal must be recorded while the a/c shaker is running at the desired vibration level under a simulated test item load condition. This is accomplished by using a digital random vibration control system, an analog filter bank or a peak and notch system to generate the random noise signal capable of producing the desired spectrum on the a/c shaker. Once recorded, the random signal can be played back any time to run its particular random vibration profile on the individual a/c shaker setup. This means that the taped random signal is only good for the conditions it was recorded under, i.e., the test item's weight and the fixture/speaker assembly. To run higher levels on the same test item or to run vibration on a different test item would require the recording of a new tape for the new requirements.

Companies who do not have the equipment required to generate a tape loop can subcontract the recording portion of the tape loop to a company with the appropriate facilities.

MODEL DESCRIPTION

A 30.5 cm (12 in.) Utah speaker, power capability of 60 watts RMS, was used to produce random noise which was then coupled to the fixture. The fixture was suspended over the top of the speaker by four springs, each of which had one end attached to a movable bracket. Threaded rods, attached at the speaker's mounting holes, were used to hold each of the four movable brackets in place by securing each with two nuts. See Figures 2 and 3. With this configuration, the fixture's height could easily be adjusted to meet with a given test requirement and/or load condition.

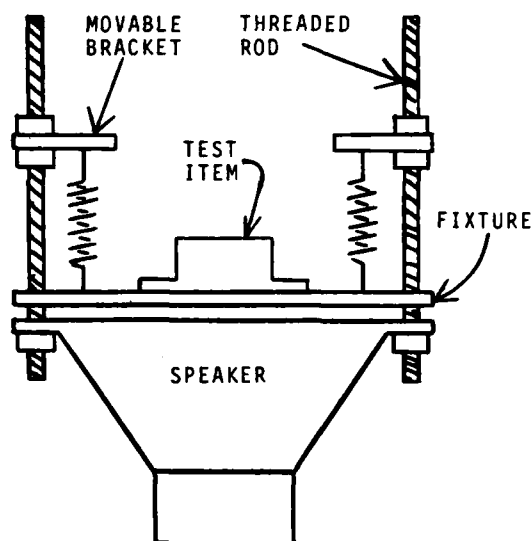


Figure 2
Schematic Diagram of a/c Shaker.

Air was used as the coupling medium between the speaker and fixture for the experiments described in this paper. A liquid coupling medium was considered but no experimental data was obtained because it would require a more complicated shaker configuration.

One possible way of using a liquid coupling medium, is illustrated in Figure 4. This system employs an under water speaker submerged in a liquid filled cylinder. The fixture is suspended on top of the liquid by springs and is attached to the cylinder walls by a thin elastic membrane, allowing the fixture to vibrate freely in the vertical plane.

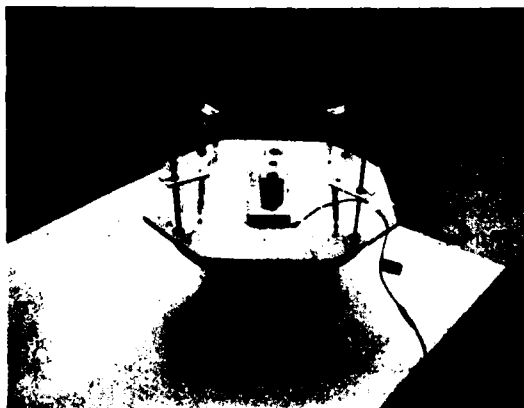


Figure 3
Photograph of a/c Shaker Model.

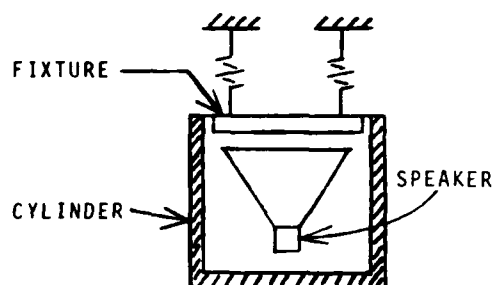


FIGURE 4
Schematic Diagram of an a/c Shaker using a Liquid Coupling Medium.

The amplifier used to amplify the random noise signal between the computer and a/c shaker, was a McIntosh Model MC75 with a power rating of 75 watts. Almost full gain was required, at all times, to run the a/c shaker at the test levels.

DATA ACQUISITION AND ANALYSIS

A 1923 Time Series System (Time/Data PDP 11/15) mini computer was used to run random vibration on the a/c shaker. Figure 5 shows a block diagram of the a/c shaker test setup.

A piezoelectric accelerometer was mounted to the fixture, next to the simulated loads, to control and monitor vibration levels during the testing.

The monitor accelerometer signal was analyzed from 20 to 2000 Hz using a bandwidth resolution of 20 Hz. Tolerance limits for the monitor response were set at ± 6 dB. Data in this paper is presented as X-Y plots of power spectral density (g^2/Hz) versus frequency (Hz).

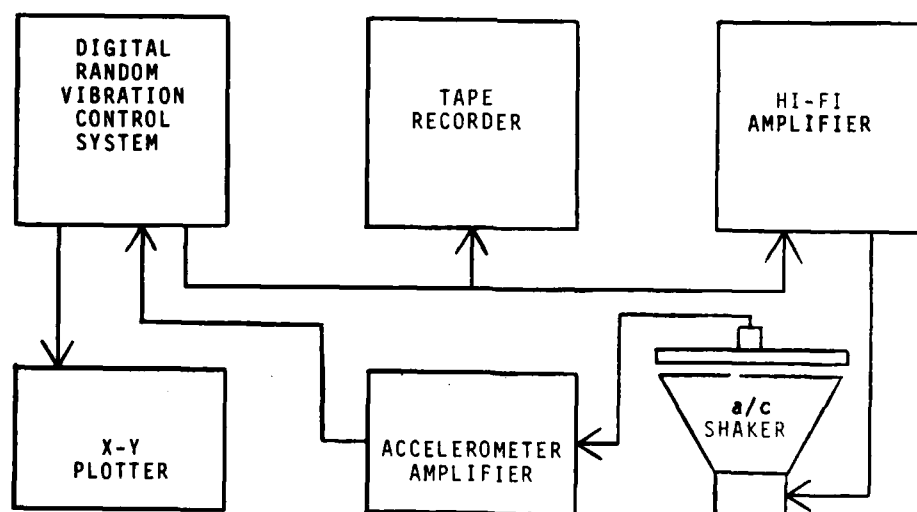


Figure 5
Acoustic Coupled Shaker Test Setup.

TEST DATA

Various tests were performed on the a/c shaker model to evaluate its performance and potential. These tests include vibrating the a/c shaker at different levels, running vibration on different loads and evaluating the recording of a random noise signal of a particular spectrum. Unless otherwise stated, all of the tests were run to meet the $0.01 \text{ g}^2/\text{Hz}$ power spectrum density level.

Different fixture materials were evaluated to determine which one would provide the stiffest structure for its shape and size. Fixture materials used were plywood, epoxy coated plywood, aluminum and plexiglass. All of the fixtures were cut to the same octagonal shape, and were tested with a 454 gram load. The uncoated 6.3 mm (.25 in.) plywood fixture, weighing 300 grams (.66 lbs), had a better response than the other three fixtures. As a result, the plywood fixture was used in the performance of all the other tests.

To determine the optimum coupling gap (the distance between the fixture and the speaker) a series of three vibration tests were run at different gaps, keeping all other variables constant. Steel springs, having an average spring constant of 263 grams/cm (1.47 lb/in.) were used to support the fixture which had a 454 gram (1.0 lb) load mounted to it. Figures 6, 7, and 8 show the vibration level on the fixture at gaps of 0.0, 3.2 and 6.4 mm (0.0, 0.125 and 0.25 in.), respectively. The figures indicate that as the gap is increased, the low frequency from 20 to 200 Hz gradually drops out of spec, yet the high frequency response seems to flatten above 300 Hz.

One series of tests was conducted to find out what vibration levels the a/c shaker model was capable of running. These tests were run at a gap of 0.0 mm and fixture loading of 1000 grams (2.2 lb). The springs used in the previous test were also used for this test. Once assembled, the only change made to the a/c shaker system while performing the tests, was to reprogram the digital random vibration control system to run higher vibration levels. Figures 9, 10 and 11 show the a/c shakers response, while controlling at a 0.005, 0.01 and 0.02 g^2/Hz level, respectively. The figures indicate that the highest attainable vibration level of the a/c shaker model which comes close to meeting the $\pm 6 \text{ dB}$ tolerance is the $0.01 \text{ g}^2/\text{Hz}$ level.

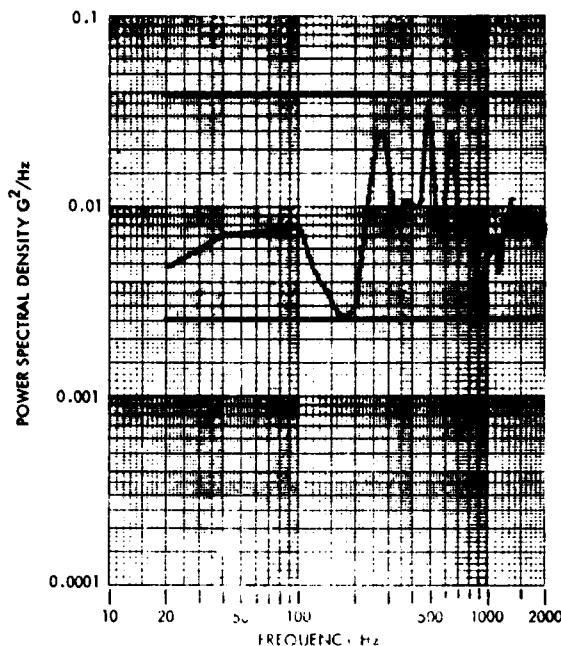


FIGURE 6

Fixture vibration level at a gap of 0.0mm and 454 gram load.

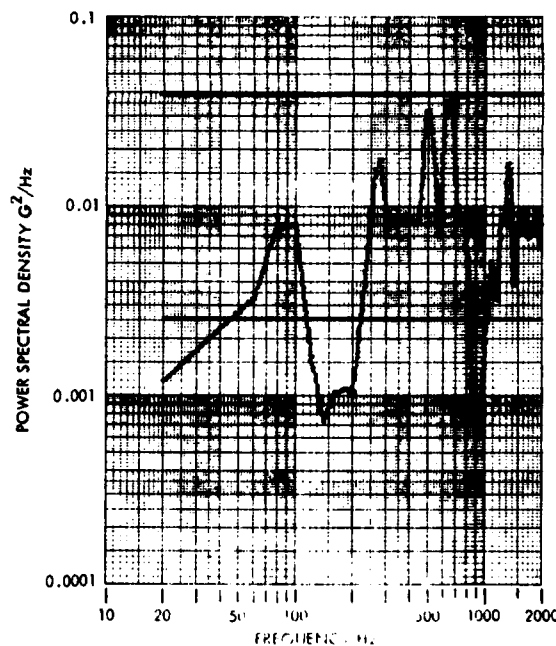


FIGURE 7

Fixture vibration level at a gap of 3.2 mm and 454 gram load.

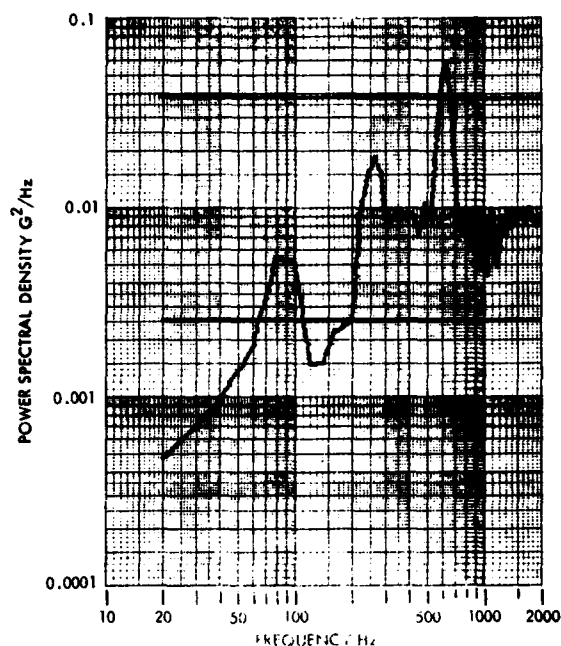


FIGURE 8

Fixture vibration level at a gap of 6.4 mm and 454 gram load.

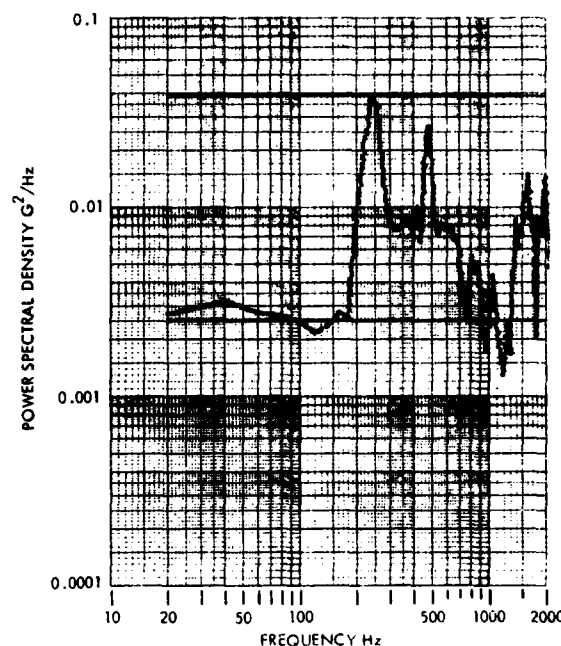


FIGURE 10

Shakers response while being controlled at a $0.01 \text{ g}^2/\text{Hz}$ level.

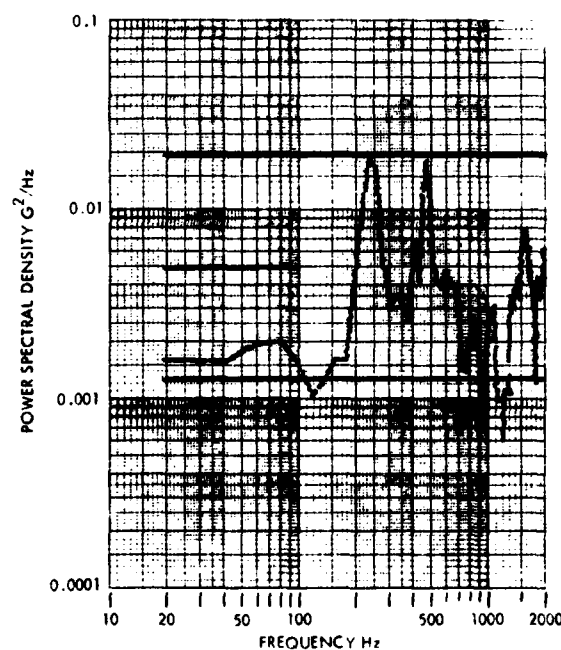


FIGURE 9

Shakers response while being controlled at a $0.005 \text{ g}^2/\text{Hz}$ level

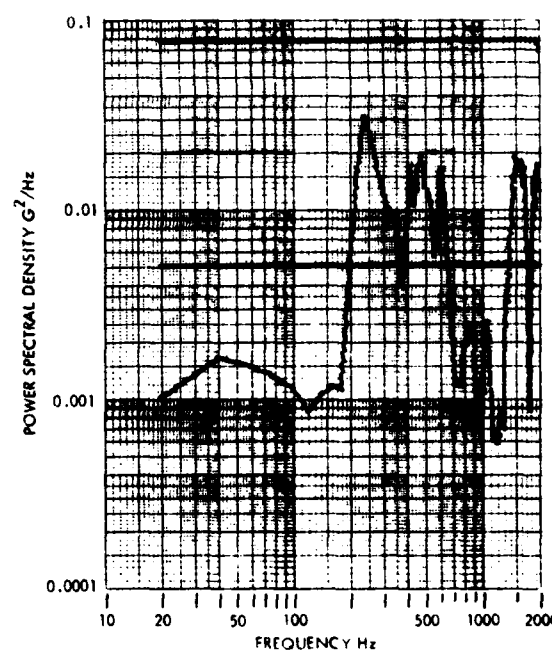


FIGURE 11

Shakers response while being controlled at a $0.02 \text{ g}^2/\text{Hz}$ level.

The a/c shaker model was tested under different load conditions to see what it was capable of vibrating. Figures 12, 13, 14 and 15 show the vibration levels of the shaker under load conditions of 0.18, 0.82, 1.54 and 4.63 Kg (0.4, 1.8, 3.4 and 10.2 lb),

respectively. The figures indicate that the a/c shaker is capable of vibrating the various test loads above 150 Hz, but is unable to keep the low frequency in spec, for 3 of the heavier loads below 150 Hz.

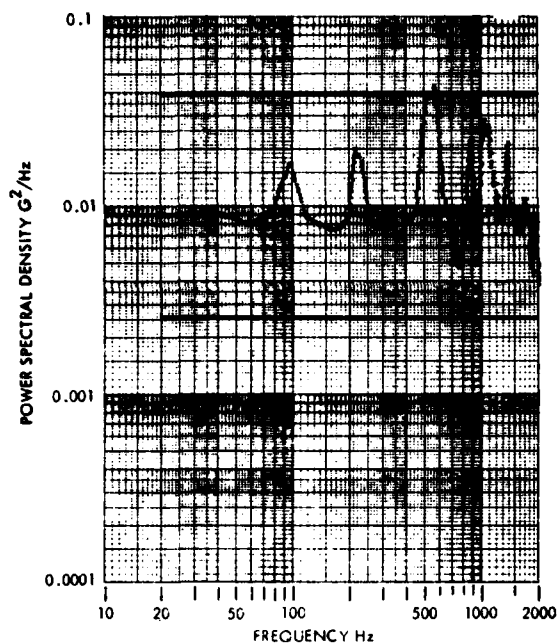


FIGURE 12

Shaker vibration level under a 0.18 Kg load.

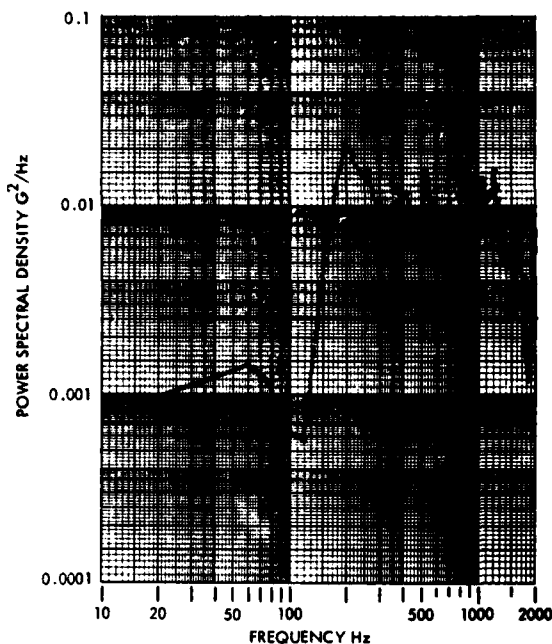


FIGURE 14

Shaker vibration level under a 1.54 Kg load.

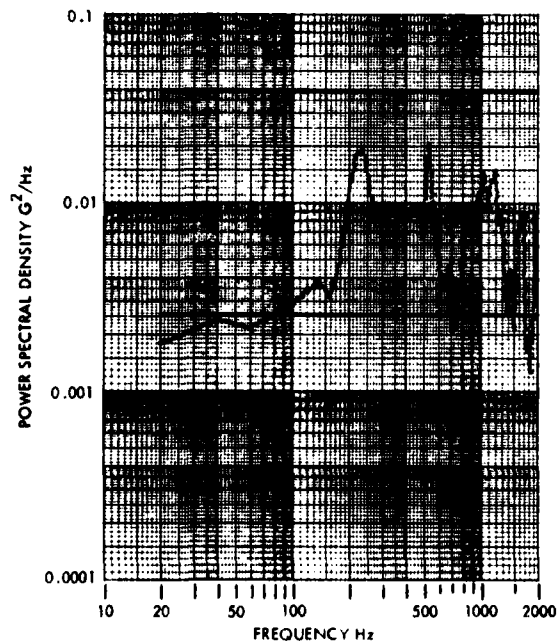


FIGURE 13

Shaker vibration level under a 0.82 Kg load.

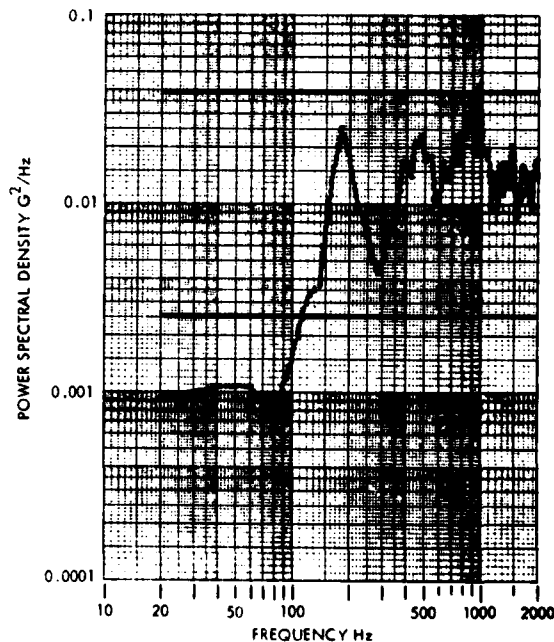


FIGURE 15

Shaker vibration level under a 4.63 Kg load.

While the a/c shaker was being vibrated under a 454 gram (1.0 lb) load, and after being equalized, the random vibration control signal was directly recorded for 4 minutes. The recorded signal was then played back to run the a/c shaker. The a/c shaker's vibration level, while being controlled live and from the recording, was then compared. Figures 16 and 17 show the shaker's response to the live control

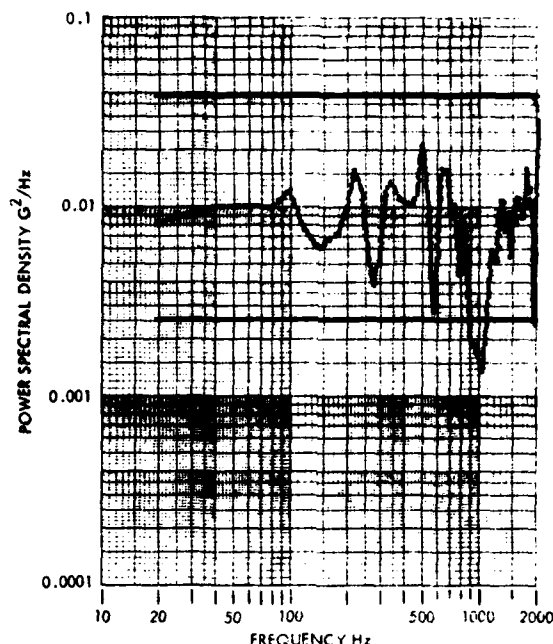


Figure 16

Shakers response to a live control signal under a 454 gram load.

FIXTURE DESIGN CONSIDERATIONS

Obviously, the resonant frequency of the fixture/spring assembly must be well below 20 Hz, preferably around 1.0 Hz. The fixture should be resonant free to 2000 Hz and be as light as possible to handle heavy loads. Also, the standing wave phenomenon must be considered in setting the speaker/fixture spacing.

CONCLUSIONS

The a/c shaker system offers a great potential as inexpensive replacement equipment capable of running random vibration for MIL-STD-781C.

The experiments performed on the a/c shaker model showed that:

1. The fixture/speaker gap must be as small as possible.

signal and the recorded control signal, respectively. The figures indicate that the low frequency was not able to be successfully reproduced from the recorded tape, from 20 to 80 Hz. This is typical of most direct recording tape recorders. The higher frequency seems to be accurately reproduced, except for some minor level fluctuations.

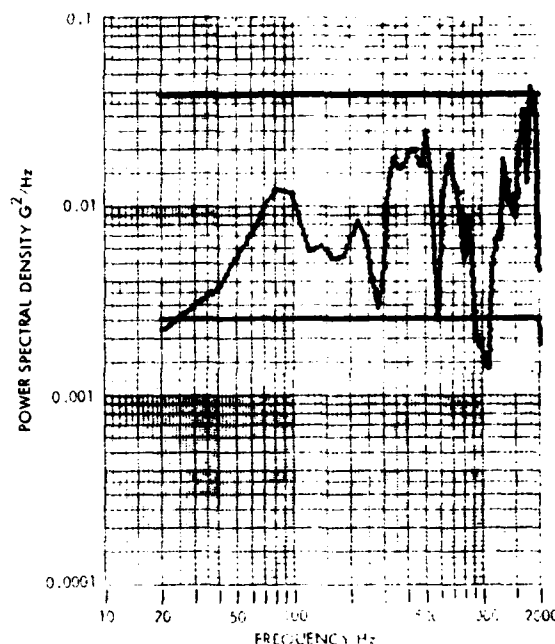


FIGURE 17

Shakers response to a recorded control signal under a 454 gram load.

2. The 60 watt model was only capable of running a 0.01 g²/Hz level, within a ± 6 dB tolerance.
3. The a/c shaker model was capable of vibrating up to a 4.63 Kg load, quite successfully above 150 Hz.
4. A taped control signal was capable of accurately reproducing the original spectrum, from 80 to 2000 Hz.

Spectrum flatness was excellent and far surpassed mechanical shaker systems. The major advantages to this system are low cost, excellent spectrum reproduction, and utilization of an inexpensive hi-fi tape recorder to drive the shaker rather than an equalization system. Also, since the acoustic coupled shaker system is mostly composed of hi-fi equipment, replacement parts would be readily available at any hi-fi dealer.

All testing was done under standard ambient conditions. As a result, there is no information, at this time, about the effect of temperature variations on the a/c shaker systems operation.

REFERENCES

- (1) Klass, P.J. "Reliability Test Procedure Changes Set". Aviation Week and Space Technology, (April 19, 1976), 62-63
- (2) MIL-STD-781B - Reliability Tests: Exponential Distribution, 15 November 1967.
- (3) MIL-STD-781C - Reliability Design Qualification and Production Acceptance Tests: Exponential Distribution, 21 October 1977.

CONSERVATISM IN RANDOM VIBRATION ANALYSIS AND TESTING

Thomas L. Paez
Applied Mechanics Division III 1284
Sandia Laboratories
Albuquerque, NM 87115

This study investigates conservatism in random vibration testing. It shows that some common spectral density estimators have an approximately normal sampling probability distribution. Based on this fact, the study proposes some measures of confidence in specified test levels. The study describes a technique for finding the probability that a test is more severe than the field environment from which it was derived. A mean square structural response criterion is used.

The results of this study show that a laboratory random vibration test is most likely to fail when the structure being tested has lightly damped, low frequency modes, and when the test duration is short.

INTRODUCTION

In structural analysis and testing it is common to measure physical inputs, such as base motions in the field, and then simulate these inputs in a laboratory experiment in order to test the adequacy of structural systems and their components. When the field inputs are deterministic, they can be approximately reproduced in the laboratory. In this case, uncertainties arise in measurement of the signal, control of the test, structural configuration differences between the laboratory and the field, and other sources. In order to assure conservatism of a deterministic test, the input is usually increased by a factor above the measured input. When the field input is a stationary random process, we do not reproduce the measured signal since it is simply one realization drawn from an infinite family of possible inputs. Instead, we characterize the input by estimating some of its parameters, most commonly, its mean and spectral density. (Spectral density is a measure of the mean-square characteristics of a random process in the frequency domain.) Then we test our structure in the laboratory by subjecting it to a random environment with a spectral density which is derived from that spectral density estimated from the field signal. Usually, the test spectral density is an envelope of the field-estimated spectral density. This is where the problem of test conservatism arises. We want to specify a test spectral density which is higher than that based on the field measurement in order to avoid undertest problems

associated with the inherent randomness of the situation. Yet we do not want to specify a test spectral density which is so high that we grossly overtest the structure or component of interest. The problem is that since the field environment is random, the spectral density estimate is a realization of a random variable. Since the test environment is random, the "apparent spectral density" which is realized during the short period of a test is also a realization of a random variable. In order to make it unlikely that the actual field environment is higher than the actual test environment, we would like to determine how much greater than the estimated field spectral density the test spectral density must be.

The objective of this analysis is to determine how great an envelope spectral density should be used in a test. The analysis describes some indices of the conservatism of a random vibration test and pays particular attention to spectral density levels at the modal frequencies of a complex structure. The analysis also describes a confidence criterion and a mean-square factor-of-conservatism criterion. Finally it describes a method for finding the probability of an undertest.

Several factors bear on the exactness and completeness of the analysis performed here. First, all those factors which cause uncertainty in a deterministic analysis also affect a probabilistic analysis in addition to the inherent signal randomness. We treat only that uncertainty arising from inherent randomness.

Second, the assumption is made that the signals of interest have a normal (Gaussian) probability distribution. Though this is usually the case for field signals, the assumption is not always exactly correct. The laboratory test input generally has an approximately normal distribution. Third, the spectral density estimators analyzed here are only valid for ergodic random processes. We assume that all processes considered are ergodic.

At the end of this analysis a numerical example applies some of the proposed measures of conservatism to an actual case. Specifically, these measures are applied to a test which has been specified for the Global Positioning System-Y Sensor. This is a satellite component which will be subjected to a random vibration environment during liftoff on an Atlas F booster rocket. The study discusses the effects caused by modification and refinement of the input spectral density.

ESTIMATION OF SPECTRAL DENSITY

In the analysis of stationary random signals it is usually assumed that the signal under consideration is one of many possible realizations of a random process, and that the signal comes from a source with a constant spectral density. One purpose of signal analysis is to estimate the underlying spectral density. Since the source is random, the portion of signal we measure is random, and any function of the signal is random. Therefore, any estimate we make of the spectral density which is based on a measurement of the signal is a realization of a random variable; an estimate of the underlying spectral density which is made from a finite duration measured signal might be called the "apparent spectral density" of the measured signal. There are various methods of spectral density estimation; two of these are summarized below.

The spectral density, $S(f)$, is a measure of the mean-square characteristics of a signal as a function of frequency. Therefore, one method of spectral density estimation is based on an

estimate of the mean-square value of a random process in intervals of its frequency range. This is the analog approach to spectral density estimation; the estimate is obtained as follows. The analog signal of duration T , $x(t)$, (or a digitized form of it) is band pass filtered with a filter of unit height, center frequency, f_c , and pass band, B , to obtain $x_p(t, f_c, B)$. This is done using analog equipment in the case of an analog signal or on a digital computer when the signal is digitized. The operation is represented as follows:

$$x_p(t, f_c, B) = F^{-1} (X(f, T) H(f)) \quad (1)$$

where

$$H(f) = \begin{cases} 1, & f_c - .5B \leq f \leq f_c + .5B \\ 0 & \text{elsewhere} \end{cases}$$

$X(f, T)$ is the finite Fourier transform of $x(t)$ on the interval $(0, T)$, and $F^{-1}(\cdot)$ represents the operation of inverse Fourier transformation. This filtered signal is then squared, integrated on $(0, T)$ and multiplied by T^{-1} to obtain an estimate of the mean square of that component of the random signal with power in the frequency range $(f_c - .5B, f_c + .5B)$.

Denoting the mean-square estimate by $\sigma^2(f_c, B, T)$ we have

$$\sigma^2(f_c, B, T) = T^{-1} \int_0^T x_p^2(t, f_c, B) dt. \quad (2)$$

The spectral density estimate is obtained by dividing the mean-square estimate by B .

$$\hat{s}(f_c) = B^{-1} \sigma^2(f_c, B, T) \quad (3)$$

The analog spectral density estimator depends on the filter bandwidth, B , and measurement duration, T . Figure 1 shows in block diagram how the spectral density estimate is obtained.

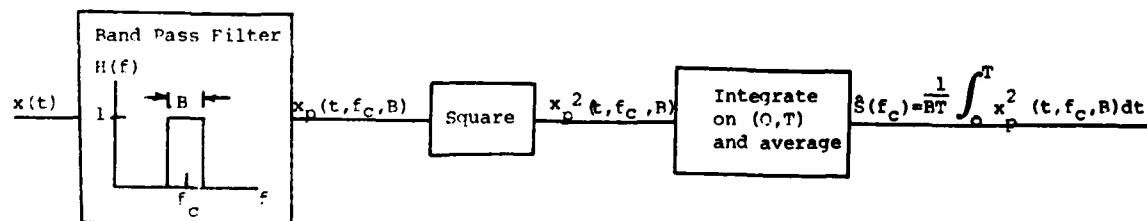


Figure 1. Block Diagram for Computation of Analog Spectral Density Estimate

This estimate of the spectral density has been shown to be consistent in the statistical sense¹ (i.e., The estimate converges to the underlying value as $T \rightarrow \infty$), and to have normalized mean-square error, $\epsilon^2 = (BT)^{-1}$. The quantity ϵ is an index of the magnitude of random variation of the estimate from the underlying value. When ϵ is small, the probability distribution of the estimate is closely concentrated about the underlying spectral density value. This estimate improves, in one sense, as B and/or T are increased; however, it has been shown that the bias error (systematic error) in the estimate increases approximately as B^2 . This estimate provides the average spectral density in the frequency band B , centered at f_c . Newland² states that empirical studies have shown that this estimator has a chi-square distribution. Particularly,

$k\hat{S}(f_c) S^{-1}(f_c)$ is chi-square with k degrees of freedom, denoted χ_k^2 , where $k = 2BT$, and $S(f_c)$ is the underlying (unknown) spectral density at frequency, f_c . Here χ_k^2 is known as the sampling distribution of the estimator. Note that $\hat{S}(f_c)$ should be thought of as a random variable as long as we consider $x(t)$ to be a random process. When a particular realization of the random process is used in the above equations, then the numerical estimate of spectral density can be thought of as a realization of the spectral density estimate random variable.

Another method of spectral density estimation is based on a definition of spectral density. Spectral density can be written as

$$S(f) = \lim_{T \rightarrow \infty} \frac{2}{T} E \left[|X(f, T)|^2 \right] \quad (4)$$

i.e., spectral density is the limit of a function of the finite Fourier transform of the random signal as the signal duration becomes infinite. This equation is used in the following way to form a spectral density estimate. A digitized form of the signal is used, x_i $i = 1, \dots, n$, where Δt is the digitization interval and $T = n\Delta t$ is the signal duration. The periodogram of this signal is formed

$$C(f_k) = \frac{2}{T} |X(f_k, T)|^2, \quad k=0, \dots, \frac{n}{2}, \quad (5)$$

where

$$f_k = k\Delta f$$

$$f = \frac{1}{T} = \frac{1}{n\Delta t}$$

and $X(f_k, T)$ is the discrete finite Fourier transform of x_i . This periodogram is an unsmoothed estimate of spectral density; i.e., it is an estimate which is not consistent in the statistical sense. To smooth this estimate and make it consistent, we can average disjoint collections of adjacent periodogram estimates

in groups of j . We obtain

$$\hat{S}(f_c) = j^{-1} \sum_{f_k \in (f_c - .5B, f_c + .5B)} C(f_k) \quad (6)$$

where $B = j\Delta f = jT^{-1}$ is the frequency interval of the smoothed estimate. Another way to arrive at a spectral density estimate which is nearly the same as that in Equation 6 is as follows. Divide the time signal into j equal segments and form a periodogram from each segment.

$$C_m(f_k) = \frac{2}{Tj-1} |X_m(f, Tj^{-1})|^2 \quad \begin{matrix} k=0, \dots, \frac{n}{2j} \\ m=1, \dots, j \end{matrix} \quad (7)$$

$$\Delta f_j = \frac{1}{Tj-1} = \frac{1}{n\Delta t j-1}.$$

The subscript "m" refers to a particular segment of signal. Each point on each periodogram is an unsmoothed spectral density estimate. To obtain a smoothed spectral density estimator, we average the "j" periodograms.

$$\hat{S}(f_k) = j^{-1} \sum_{m=1}^j C_m(f_k) \quad k=0, \dots, \frac{n}{2j}. \quad (8)$$

Here again, $\hat{S}(f)$ should be thought of as a random variable when x_i is considered as a random process; when particular values of x_i are used, the numerical value of $S(f)$ is a realization of the spectral density estimate random variable.

The two approaches shown here are nearly equivalent (Ref. 1). In both cases, the averaging causes the estimates to be consistent in a statistical sense. This general technique is known as the digital approach to spectral density estimation. The normalized mean-square error is $\epsilon^2 = (BT)^{-1}$ as it was in the analog case, where $B = j\Delta f$ and j is the averaging constant used above. It can be shown (Ref. 1) that this estimate has a chi-square distribution; in particular, $2j\hat{S}(f) S^{-1}(f)$ is χ_{2j}^2 .

This is an exact parallel to the analog case since $2j = 2BT = k$.

The central limit theorem in probability states that the distribution of a sum of a large number "n" of independent random variables approaches the normal distribution as n becomes large. Since the distribution of χ_n^2 is the distribution of the sum of the squares of n independent normal random variables, this distribution approaches the normal distribution as n becomes large. In fact, the distribution of χ_n^2 is practically indistinguishable from a normal distribution, with mean $\mu = n$ and variance $\sigma^2 = 2n$, when $n \geq 30$. From above, we know that

the sampling distribution for the analog spectral density estimator is X_k^2 , with $k = 2BT$. (This is also true in the discrete case.) We also know that $\epsilon^2 = (BT)^{-1}$. Therefore, $k \geq 30$ implies $\epsilon \leq .26$. Thus, when the spectral density estimate is formed in one of the above described ways and the measured data and estimate are such that $\epsilon \leq .26$, the probability distribution of the quantity $k\hat{S}(f) S^{-1}(f)$ is normal with mean k and variance $2k$. Since k and $S(f)$ are constants and since $k = 2\epsilon^{-2}$, the sampling distribution of the spectral density estimator, $\hat{S}(f)$, is normal with mean $S(f)$ and variance $\epsilon^2 S^2(f)$. Recall that ϵ is a normalized measure of the possible error in an estimate. In order to keep the error low, data is collected and the frequency bands are chosen so that ϵ is usually lower than 0.15. Therefore, the sampling distributions of our spectral density estimates are usually normal. Figure 2 is a graph of $\epsilon = (BT)^{-1/2}$ vs. B for various values of T . This shows the value of BT required to keep ϵ at or below an arbitrary level.

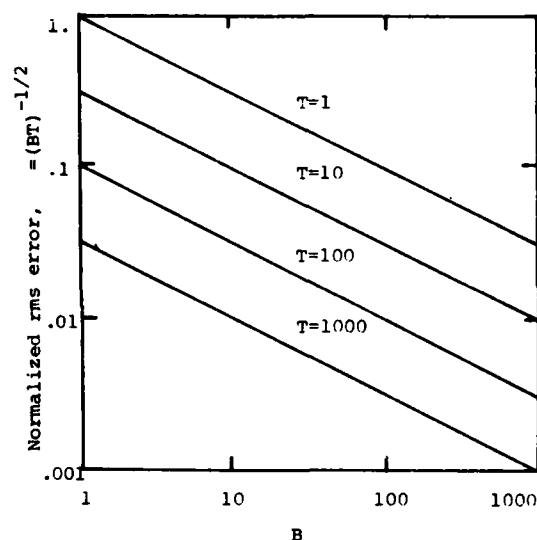


Figure 2. Normalized rms Error

As mentioned earlier $\hat{S}(f_c)$ is a random variable and $S(f)$ is a constant; however, we do not know $S(f)$ and we can form an estimate $\hat{S}(f_c)$ which is a realization of the random variable $\hat{S}(f_c)$. Further, we have the probability distribution of $k\hat{S}(f) S^{-1}(f_c)$. In fact, this describes the random behavior of $\hat{S}(f_c)$, but in confidence analysis we turn this around. We say that our knowledge of the probability distribution of $k\hat{S}(f_c) S^{-1}(f_c)$ can be used as a measure of our confidence that the underlying

spectral density $S(f_c)$ is within some range of the estimated spectral density $\hat{S}(f_c)$. We usually speak in terms of confidence intervals, and when $\epsilon \leq .26$, we can write

$$C(k\hat{S}(f_c) S^{-1}(f_c) \leq q) = C(S(f_c) \geq kq^{-1} \hat{S}(f_c)) = \Phi\left(\frac{q-k}{\sqrt{2k}}\right) \quad (9)$$

where $C(a \leq b)$ can be read as our confidence that a is equal to or less than b , and $\Phi(\cdot)$ is the cumulative probability distribution function of a standardized normal random variable. If we could refer to $S(f_c)$ as a random variable (it is actually a constant by our initial assumption) we would say that $S^{-1}(f_c)$ has a normal distribution. We are interested in expressing our confidence that $S(f_c)$ exceeds $\hat{S}(f_c)$ by some number of multiples of the normalized root mean-square error, ϵ ; i.e., we want to find $C(S(f_c) \geq \hat{S}(f_c) (1 + N\epsilon))$. Using Equation 9 we set $kq^{-1} = 1 + N\epsilon$ and note that $k = 2\epsilon^{-2}$ to obtain

$$C(S(f_c) \geq \hat{S}(f_c) (1 + N\epsilon)) = \Phi\left(-\frac{N}{1 + N\epsilon}\right) \quad (10)$$

This equation is plotted for various values of ϵ in Figure 3. This relation can be altered to show that

$$C(S(f_c) \leq \hat{S}(f_c) (1 + N\epsilon)) = \Phi\left(\frac{N}{1 + N\epsilon}\right) \quad (11)$$

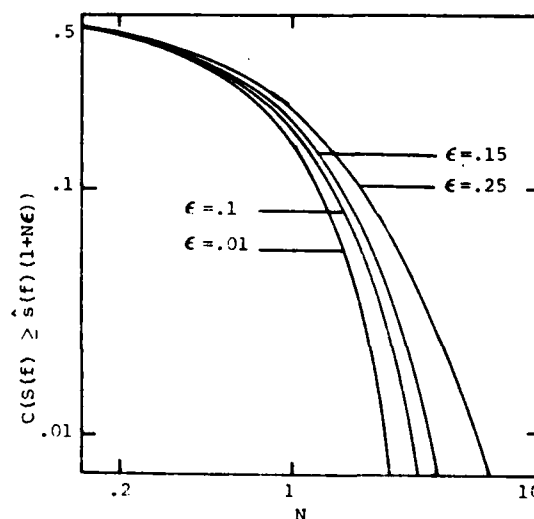


Figure 3. Confidence Levels for Exceedance of Sample Spectral Density of Normal Random Process

In all cases where ϵ is reasonably small, the confidence of Equation 10 approaches zero very rapidly as N increases.

APPARENT SPECTRAL DENSITY OF GENERATED SIGNALS, DISTRIBUTION OF SPECTRAL DENSITY ESTIMATOR NEAR NATURAL FREQUENCY OF STRUCTURE

In the same sense that a spectral density estimated from field data is random, the apparent spectral density estimated from data measured over the duration of a random vibration test is also random; specifically, the estimated spectral density is the realization of a random variable. In the case of a test, however, we know the underlying spectral density value. It is simply the specified test spectral density value. If we denote this quantity $S_t(f)$ and if we denote the apparent spectral density based on the realized test signal $\hat{S}_t(f)$, then we can say that $\hat{S}_t(f)$ has a normal distribution with mean $S_t(f)$, and variance $\epsilon^2 S_t^2(f)$. Here $\epsilon^2 = BT^{-1}$ where T is test duration and B is the frequency interval at which spectral density is estimated.

Since the apparent field and test spectral densities are random, so are the apparent spectral densities and variances of the responses excited by the field and test environments. The response of a single-degree-of-freedom (SDF) system, or a mode in a complex system, depends on the spectral density of the input in the frequency range near the natural frequency of the system. Particularly, the mean-square characteristics of the response of a SDF system depend on the average input spectral density in the frequency band $\pi\zeta f_n$ which is centered at f_n , where ζ is the damping factor and f_n is the natural frequency of the SDF system. (Note that $\pi\zeta f_n$ is the frequency bandwidth which, when multiplied by the peak height of the spectral density curve for the response of a SDF system, yields the correct mean-square response value.) Because of this dependence of the response-mean-square characteristics on the input spectral density near f_n in the band $\pi\zeta f_n$, we choose, in this study, to look at input spectral density variation over the band of frequencies $B = \pi\zeta f_n$. The normalized mean-square error becomes $\epsilon^2 = (\pi\zeta f_n T)^{-1}$. Therefore, the mean-square variability of apparent spectral density in the frequency range of interest is an inverse function of natural frequency, damping factor, and test duration. The probability distribution of the average spectral density estimate, $\hat{S}(f_n)$, over the frequency band $\pi\zeta f_n$ is still normally distributed; it has mean $S(f_n)$ and variance $S^2(f_n) (\pi\zeta f_n T)^{-1}$. T is the duration of the field environment. The apparent spectral

density of a test, $\hat{S}_t(f_n)$, is also normally distributed with mean $S_t(f_n)$ and variance $S_t^2(f_n) (\pi\zeta f_n T)^{-1}$. T is the test duration. Figure 4 is a graph of $\epsilon = (\pi\zeta f_n T)^{-1/2}$ vs. ν for various values of c . When we take ν to be either f_n or ζ or T , and we take c to be the product of the remaining two variables, Figure 4 shows how much normalized variation in apparent spectral density can be expected as a function of the variable represented by ν , when the product of the remaining two variables is specified as c . For example, the normalized rms error, ϵ , varies with $\nu = f_n$ according to the curve marked $C=10$ when $\zeta T=10$. This shows that the sample variability tends to increase as f_n decreases. The results presented here assume $\zeta f_n T \gg 1$. (Since we later assume that ζ is small, we actually require that $f_n T \gg 1$.)

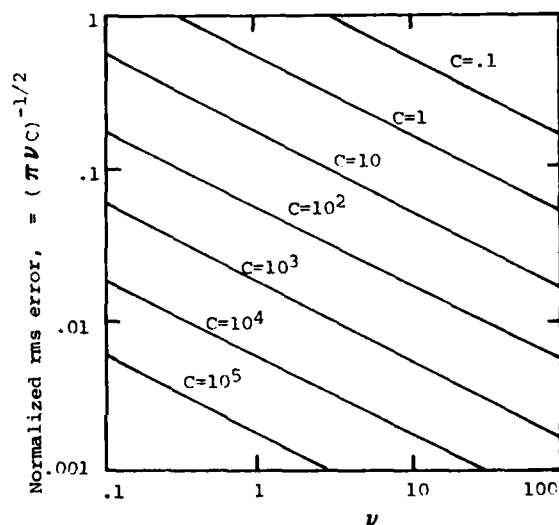


Figure 4. Normalized rms Error

CONSERVATISM OF STRUCTURAL RANDOM VIBRATION TESTS

The structural response of a lightly damped system can be expressed using a modal approach. When this is done, and the system has modal frequencies in the frequency range where the input has power, the average input spectral densities at the modal frequencies of the structure are the most important factors in determining the stationary response of the structure. In connection with the modal representation of structural response we can discuss the conservatism of a random vibration test in two ways. First, we can consider the conservatism involved in setting spectral density envelope levels based on estimated spectral density levels. In this case, we use a confidence analysis approach and concentrate on the test envelope levels at

the modal frequencies. Second, once we have defined a test level, we can consider the conservatism of a test in light of the random variability involved in running a test and the random variability involved in the realization of an actual environment. Particularly, we can compute the probability that a field environment excites a more severe response than a test environment. Here we use information on the sampling probability distribution of the spectral density estimators.

Let us define a system as follows. It is elastic, lightly damped, and has m modes of vibration in the frequency range of interest. Its natural frequencies are f_i , $i = 1, \dots, m$; its modal damping factors are ζ_i , $i = 1, \dots, m$; the elements of its diagonal structural mass matrix are m_i , $i = 1, \dots, m$. It has normal modal vectors u_i , $i = 1, \dots, m$. Test conservatism at a given mode with regard to specification of the input can be measured in the following ways. First, our confidence that the underlying spectral density is lower than the test spectral density at each mode is

$$C(S(f_i) \leq S_t(f_i)) = \Phi\left(\frac{N_i}{1 + N_i \epsilon_i}\right), \quad i = 1, \dots, m, \quad (12)$$

where

$$\epsilon_i = (\pi \zeta_i f_i T)^{-1/2}$$

$$N_i = \epsilon_i^{-1} \left(S_t(f_i) (\hat{s}(f_i))^{-1} - 1 \right)$$

T is the duration of the environmental measurement, and $\hat{s}(f_i)$ refers to the average of a specific numerical estimate of spectral density over the band of frequencies $(f_i(1 - .5\pi\zeta_i), f_i(1 + .5\pi\zeta_i))$. This equation is based on Equation 11. Figure 3 can be used in connection with the above relations to help in choosing a suitable value for $S_t(f_i)$. Another measure of test conservatism at each mode is obtained as follows.

Let the expected factor of conservatism at i^{th} mode, $Q(f_i)$, denote the ratio of the test spectral density level, $S_t(f_i)$, to the average input spectral density level, $S(f_i)$, where the average is taken over the frequency band $\pi\zeta_i f_i$. This is approximated as follows:

$$Q(f_i) = S_t(f_i) (\hat{s}(f_i))^{-1}, \quad i = 1, \dots, m \quad (13)$$

This is an average factor of overtest at mode i in a mean-square sense. A root-mean-square (rms) factor of overtest is obtained from $Q^{1/2}(f_i)$.

Consider all modes of the response jointly. If the bandwidths associated with the individual modes do not overlap, then the average input spectral density estimators in those bandwidths are independent. In this case, the product of the confidences that the underlying spectral density levels do not exceed the test levels is a measure of our confidence in the overall test. Call this product C_s ; we have

$$C_s = \prod_{i=1}^m C(S(f_i) \leq S_t(f_i)) \quad (14)$$

A geometric mean confidence that no individual underlying spectral density exceeds its corresponding test spectral density level is defined as

$$C_g = C_s^{1/m} \quad (15)$$

The arithmetic average confidence for all modes is

$$C_a = m^{-1} \sum_{i=1}^m C(S(f_i) \leq S_t(f_i)) \quad (16)$$

The average overtest for all modes is

$$Q_a = m^{-1} \sum_{i=1}^m Q(f_i) \quad (17)$$

In the above formulas no particular importance is attached to any specific response mode. However, the expression for response at a point on a structure, in terms of modal responses, shows that different modes usually predominate in contributing to the response at different points on the structure. The matrix of modal vectors quantitatively describes the participation of the various modes in the response at a point. To reflect the degree of participation in the point response by the modes, in a normalized sense, we define normalized participation factors.

$$v_{ij} = \frac{u_{ij}}{\sum_{j=1}^m u_{ij}} \quad (18)$$

where u_{ij} is the i^{th} row j^{th} column element of the modal matrix u which is formed by assembling normal mode vectors. The v_{ij} 's are normalized in the sense that $\sum_j v_{ij} = 1$. It has been assumed that there are m measurement points on the structure where output may be observed. The weighted average confidence that no underlying spectral density at any modal frequency surpasses a corresponding test spectral density at a point i on the structure is

$$C_{wa(i)} = \sum_{j=1}^m v_{ij} C(S(f_j) \leq S_t(f_j)) \quad i=1, \dots, m. \quad (19)$$

The weighted average factor of conservatism of the test at point i on the structure is

$$Q_{wa}(i) = \sum_{j=1}^m v_{ij} Q(f_j) \quad i = 1, \dots, m \quad (20)$$

This is an approximate mean-square test factor of conservatism where those modes contributing most heavily to the response at point i are given the greatest weight. An rms factor of conservatism is $Q_{wa}(i)^{1/2}$.

Once a test input spectral density has been specified, a test can be run, and even though any measure of the expected factor of conservatism should be greater than unity, a particular test response can always turn out to be unconservative with respect to the field input, in one sense or another, because of the fact that both inputs are random. We are well prepared to assess the probability that a particular test is unconservative, in a mean square sense, since we know the sampling distribution for apparent spectral density and further, since it is normal. Denote the vector of structural responses at the m points on the structure by $\{y\}$ and let $\{\eta\}$ be the m component vector of modal responses. The modal matrix relates these two vectors as follows

$$\{y\} = [u] \{\eta\} \quad (21)$$

The j -th element of $\{y\}$ can be expressed

$$y_j = \sum_i u_{ji} \eta_i \quad j = 1, \dots, m \quad (22)$$

Based on this expression the autocorrelation function of the response y_j is found to be

$$R_{y_j}(\tau) = E\{y_j(t) y_j(t + \tau)\} \\ = \sum_i \sum_k u_{ji} u_{jk} R_{\eta_i \eta_k}(\tau) \quad j = 1, \dots, m \quad (23)$$

where $R_{\eta_i \eta_k}(\tau)$ is the crosscorrelation between the modal responses $\eta_i(t)$ and $\eta_k(t + \tau)$. When

the structural response modes are widely separated, the modal responses have little cross-correlation and we can write approximately

$$R_{y_j}(\tau) \cong \sum_i u_{ji}^2 R_{\eta_i}(\tau) \quad j = 1, \dots, m \quad (24)$$

where $R_{\eta_i}(\tau)$ is the autocorrelation of the modal response, $\eta_i(t)$. Fourier transforming this expression yields an approximate relation between the spectral densities of the modal responses and the structural response, y_j .

$$S_{y_j}(f) \cong \sum_i u_{ji}^2 S_{\eta_i}(f) \quad i = 1, \dots, m \quad (25)$$

But the spectral density of each modal response is that of an SDF system, f modes are widely separated, and the approximate mean-square response in each mode is easily computed.² (The mean structural response is assumed zero.) The mean-square response of the structure at point j is the integral of the spectral density at point j over all frequencies and, in modal terms can be written approximately

$$\sigma_{y_j}^2 = \sum_i u_{ji}^2 \frac{\pi f_i \alpha_i S(f_i)}{2 \zeta_i} \quad j = 1, \dots, m \quad (26)$$

where \ddot{y}_j is the acceleration response at point j on the structure, and $\alpha_i = [u_{ik} m_k]^2$ is a

quantity obtained in the modal analysis of a base excited structure which indicates how strongly mode i is excited by the base input. Using this formula, the apparent, or estimated, mean-square response at point j on the structure excited by the field and test inputs, respectively, can be written

$$\sigma_{y_j, f}^2 = \sum_i u_{ji}^2 \frac{\pi f_i \alpha_i S(f_i)}{2 \zeta_i} \quad j = 1, \dots, m \quad (27)$$

and

$$\sigma_{y_j, t}^2 = \sum_i u_{ji}^2 \frac{\pi f_i \alpha_i S_t(f_i)}{2 \zeta_i} \quad j = 1, \dots, m \quad (28)$$

where the subscript f refers to "field" and t refers to "test," and T is the duration of the field or test input. (These are assumed equal in this analysis.) Since $\hat{S}(f_i)$ and $\hat{S}_t(f_i)$ are normally distributed random variables,

$\sigma_{y_j, f}^2$ and $\sigma_{y_j, t}^2$ are normally distributed

random variables. An undertest occurs at point j on the structure, in one sense, if the field-mean-square structural response $\sigma_{y_j, f}^2$ is

greater than the test-mean-square structural response, $\sigma_{y_j, t}^2$. Since these are normal random

variables a linear combination of them is a normal random variable. Let $A_j = \sigma_{y_j, t}^2 - \sigma_{y_j, f}^2$.

The random variable A_j has mean μ_{A_j} and variance $\sigma_{A_j}^2$. The chance of an undertest is

$$P(A_j \leq 0) = \Phi\left(\frac{-\mu_{A_j}}{\sigma_{A_j}}\right) \quad j = 1, \dots, m \quad (29)$$

where $\Phi(\cdot)$ is the cumulative probability distribution function of a standardized normal random variable and

$$\mu_{A_j} = \sum_i \frac{\pi f_i \alpha_i}{2 \zeta_i} (S_t(f_i) - \hat{S}(f_i)), \quad j=1, \dots, m$$

and

$$\sigma_{A_j}^2 = \sum_i \frac{\pi u_{ji} f_i \alpha_i}{4 \zeta_i^3 T} (S_t^2(f_i) + (\hat{S}(f_i))^2). \quad (30)$$

(Recall that $\hat{S}(f_i)$ is normally distributed with mean $S(f_i)$ and variance $\epsilon^2 S^2(f_i)$, and $\hat{S}_t(f_i)$ is normally distributed with mean $S_t(f_i)$ and variance $\epsilon^2 S_t^2(f_i)$, where $\epsilon^2 = (\pi \zeta_i f_i T)^{-1}$.) These equations are approximate since it has been assumed that $S(f_i)$ can be represented by $\hat{S}(f_i)$ in the frequency band $(f_i(1 - .5\pi\zeta_i), f_i(1 + .5\pi\zeta_i))$. We assume that $S_t(f_i)$ will always be chosen greater than $\hat{S}(f_i)$, i.e., μ_{A_j} is greater than zero.

We can draw several conclusions regarding the chance of an undertest from Equations 29 and 30. When μ_{A_j}/σ_{A_j} is large, the chance of an undertest is small, and as μ_{A_j}/σ_{A_j} decreases,

the chance of an undertest increases. Therefore, those variations in ζ_i , f_i , and T which tend to cause the ratio μ_{A_j}/σ_{A_j} to increase will cause the probability of conservatism of a test to increase. Let the ratio μ_{A_j}/σ_{A_j} be denoted

R. We can examine the variation of R with respect to its individual parameters, T , ζ_i , and f_i , by taking the partial derivative of R with respect to these parameters. When this derivative is positive, R increases with respect to the parameter, thus increasing the probability of conservatism of a test. The α_i 's are always taken as constants. For the purpose of analyzing the variation of R with respect to T , note that μ_{A_j} does not vary with T , and σ_{A_j} varies as $T^{-1/2}$. Therefore, we can write

$$R = CT^{1/2}, \quad (31)$$

where C is taken to be a positive constant. The derivative of R with respect to T is

$$\frac{\partial R}{\partial T} = \frac{1}{2} CT^{-1/2}. \quad (32)$$

This is positive for all positive T, indicating that the probability of test conservatism, in a mean-square sense, increases with increasing T.

Next let us analyze the variation of R with respect to damping in the k^{th} mode, ζ_k . Note that the component terms of μ_{A_j} vary as ζ_i^{-1} and the terms of $\sigma_{A_j}^2$ vary as ζ_i^{-3} . We can write

$$R = \frac{\sum_i a_i / \zeta_i}{\left[\sum_j b_j / \zeta_j^3 \right]^{1/2}} \quad (33)$$

where all terms in μ_{A_j} and σ_{A_j} which do not depend on the damping terms are accounted for in the positive constants a_i and b_j . To determine the variation of R with respect to the k^{th} mode damping term, we differentiate R with respect to ζ_k .

$$\frac{\partial R}{\partial \zeta_k} = \frac{-a_k / \zeta_k^2}{\left[\sum_j b_j / \zeta_j^3 \right]^{1/2}} + \frac{3}{2} \frac{b_k}{\zeta_k^4} \frac{\left[\sum_i a_i / \zeta_i \right]}{\left[\sum_j b_j / \zeta_j^3 \right]^{3/2}}. \quad (34)$$

The change in R is positive when ζ_k is increased if the following inequality is satisfied

$$\frac{2}{3} \frac{a_k \zeta_k^2}{b_k} < \frac{\sum_i a_i / \zeta_i}{\sum_j b_j / \zeta_j^3}. \quad (35)$$

This was obtained by setting the right side of Equation 34 greater than zero. This can be rewritten

$$\frac{2}{3} \frac{a_k / \zeta_k}{b_k / \zeta_k^3} < \frac{\sum_i a_i / \zeta_i}{\sum_j b_j / \zeta_j^3}. \quad (36)$$

Ignoring the two-thirds factor on the left side, we see that the numerator of the left side is

the k^{th} term of μ_{A_j} , and the denominator is the k^{th} term of $\sigma_{A_j}^2$. The numerator of the right

side is the average or mean of the individual component terms which constitute μ_{A_j} , and the

denominator is the mean of the terms which constitute $\sigma_{A_j}^2$. In practice, only direct

computations with the terms a_i , b_i , ζ_i , $i = 1, \dots, m$, will tell us whether Inequality 36 holds and $\partial R / \partial \zeta_k > 0$. When it does not, then

$\partial R / \partial \zeta_k < 0$. In fact, we could construct an example in which the inequality does not hold at $m-1$ modes. However, because of the two-thirds factor, the inequality will tend to hold most of the time if the factors are not chosen to specifically prevent this. This assumes that the terms a_k/ζ_k and b_k/ζ_k^3 are approximately as likely to be above their means as below. When the distributions of the components a_i/ζ_i and b_j/ζ_j^3 tighten about their means, the Inequality 36 will tend to hold more often because any given term in the sum, for example, a_k/ζ_k , will tend to be close to the mean, $m^{-1} \sum_i a_i/\zeta_i$. A strong positive correlation between the factors a_i/ζ_i and b_j/ζ_j^3 will also

tend to make Inequality 36 hold more often because a positive correlation will tend to diminish the random variation of the left side of Inequality 36. It is clear that when there is only one mode, the Inequality 36 is always correct because of the two-thirds factor. The result of this part of the analysis shows that R , and the probability of test conservatism, tend to increase with increases in modal damping. In other words, the probability of mean-square test conservatism tends to increase with modal damping.

The analysis of the variation of R with respect to f_k closely follows that given above. Initially, let us assume that $S_t(f_i)$ and $\hat{s}(f_i)$ are approximately constants in the neighborhood of f_i . Then we can write

$$R = \frac{\sum_i a_i f_i}{\left[\sum_j b_j f_j \right]^{1/2}}, \quad (37)$$

where the a_i and b_j account for all the factors in Equation 30 besides the modal frequencies. The change in R with respect to a change in the k^{th} modal frequency is determined by taking the partial derivative of R with respect to f_k .

$$\frac{\partial R}{\partial f_k} = \frac{a_k}{\sum_j [b_j f_j]^{1/2}} - \frac{b_k}{2} \frac{\sum_i a_i f_i}{\left[\sum_j b_j f_j \right]^{3/2}}. \quad (38)$$

This is greater than zero when

$$\frac{a_k}{b_k} > \frac{\sum_i a_i f_i}{\sum_j b_j f_j}. \quad (39)$$

This inequality can be rewritten

$$\frac{a_k f_k}{b_k f_k} > \frac{m^{-1} \sum_i a_i f_i}{m^{-1} \sum_j b_j f_j}. \quad (40)$$

When this inequality holds, $\partial R / \partial f_k > 0$. When it does not, $\partial R / \partial f_k < 0$. Disregarding the factor of two on the left side, the numerator of the left side is the k^{th} component of μ_{A_j} , and the denominator is the k^{th} component of $\sigma_{A_j}^2$. The numerator of the right side is the average of all the components of μ_{A_j} , and the denominator is the average of all the components of $\sigma_{A_j}^2$. Only specific values of a_i , b_i and f_i

can be used to determine whether or not the inequality holds. And, as before, an example can be constructed in which Inequality 40 does not hold at all modes but one. However, because of the factor of two, the inequality should tend to hold most of the time if the factors are not chosen to specifically prevent this. When the factors $a_i f_i$ and $b_j f_j$ are closely concentrated about their means and when they are positively correlated with one another, the Inequality 40 will tend to hold a greater percentage of the time. When there is only one mode, the inequality is always true. This part of the analysis shows that R and the probability of test conservatism usually tend to increase with modal frequency when $S_t(f_i)$ and $\hat{s}(f_i)$ are constant near f_i . This assumption of constancy is usually quite accurate in the case $S_t(f_i)$ since it is often specified to be a constant, or at most, varies gradually (compared to $\hat{s}(f_i)$) in the neighborhood of f_i . However, $\hat{s}(f_i)$ may vary rapidly in the neighborhood of f_i . In particular, since the structure or component which we are testing has a mode at f_i , motion of the structure or component in the field may influence the shape of the input or attachment point spectral density. We would usually expect to find a trough in $\hat{s}(f_i)$ when this occurs. Therefore, let us consider the case where $\hat{s}'(f_i) = 0$, $\hat{s}''(f_i) \neq 0$. Now we express R as

$$R = \frac{\sum_i a_i f_i (C_1 - \hat{s}(f_i))}{\left[\sum_j b_j f_j (C_2 + \hat{s}^2(f_j)) \right]^{1/2}}. \quad (41)$$

Taking the partial derivative of R with respect to f_k results in

$$\frac{\partial R}{\partial \epsilon_k} = \frac{a_k (c_1 - \hat{s}(\epsilon_k))}{\left[\sum_j b_j \epsilon_j (c_2 + \hat{s}^2(\epsilon_j)) \right]^{1/2}} - \frac{b_k}{2} \frac{\sum_i a_i \epsilon_i (c_1 - \hat{s}(\epsilon_i))}{\left[\sum_j b_j \epsilon_j (c_2 + \hat{s}^2(\epsilon_j)) \right]^{3/2}} (c_2 + \hat{s}^2(\epsilon_k)). \quad (42)$$

where advantage has been taken of the fact that $\hat{s}'(f_i) = 0$. But this expression is the same as Equation 38 if we identify a_k in Equation 38 with $a_k (c_1 - \hat{s}(f_k))$ from above, and b_k in Equation 38 with $b_k (c_2 + \hat{s}^2(f_k))$ from above. Therefore, the conclusions drawn above apply also to the case where $S_t(f_i)$ is a constant and $\hat{s}'(f_i) = 0$, $\hat{s}''(f_i) \neq 0$. That is, R and the probability of a conservative test increase as the modal frequencies of the structure we are testing increase.

It should be emphasized here that Equation 29 provides only an approximation of the probability of an undertest since the estimated spectral density $\hat{s}(f_i)$ is used in place of the underlying field spectral density $S(f_i)$. When $\hat{s}(f_i) < S(f_i)$, then $S_r(f_i) - \hat{s}(f_i) > S_t(f_i) - S(f_i)$ and $S_t^2(f_i) + \hat{s}^2(f_i) < S_t^2(f_i) + S^2(f_i)$. As seen from Equation 30, this condition makes our estimate of μ_{A_j} / σ_{A_j} greater

than it should be. This is what we would expect, since when we estimate a value of $\hat{s}(f_i)$ in the field which is "lower than average," and then specify a test spectral density at that frequency, the test appears to be more conservative than it really is. We cannot avoid this since the only information available is the estimated spectral density values. A corresponding set of comments apply when $\hat{s}(f_i) > S(f_i)$. One factor which tends to make Equation 29 a good approximation is that roughly half the spectral density estimates will be low and half will be high, on the average, since the probability distribution of apparent spectral density is normal. In fact, the number of estimates lower than average is random and is governed by a binomial probability distribution. Roughly speaking, the effects on μ_{A_j} and σ_{A_j} of those estimates, $\hat{s}(f_i)$, which are high will tend to cancel the effects of those estimates, $\hat{s}(f_i)$, which are low; this can be seen from Equation 30.

NUMERICAL EXAMPLE

The Global Positioning System (GPS) will be

lifted into earth orbit on an Atlas "F" booster rocket. The system will be subjected to shock, quasi-static acceleration and random vibration. We assume, conservatively, that the random vibration will have a duration of three minutes. The random vibration is induced by acoustic noise, and the noise spectrum has been measured on previous flights. The input noise spectrum is smooth. To determine random vibration qualification levels, a mass mockup of the GPS was subjected to the acoustic noise in a laboratory test, and attachment point accelerations were measured on components. Attachment point spectral densities were estimated, and these were enveloped and specified as random vibration qualification levels. One particular component, the GPS Y Sensor, will be analyzed in this example. The attachment point acceleration spectral density of the GPS Y Sensor is shown in Figure 5. It reflects mean-square contributions to the input motion over a broad band of frequencies. This spectral density was estimated at frequency intervals of 6.4 Hz with a BT constant of 180. Therefore, the measurement duration was approximately 28 seconds. The

normalized root-mean-square error is $(180)^{-1/2} = .0745$. The rapid variation in the spectral density estimate and changes in the estimate by factors greater than two, in light of the smoothness of the acoustic input, lead to the conclusion that most of the peaks reflect vibration modes of the overall GPS system rather than random error. The heavy black line shown in Figure 5 is the envelope of the attachment point spectral density which was initially suggested as a test input qualification level spectral density. The conservatism of this test level with respect to the estimated spectral density level is estimated below.

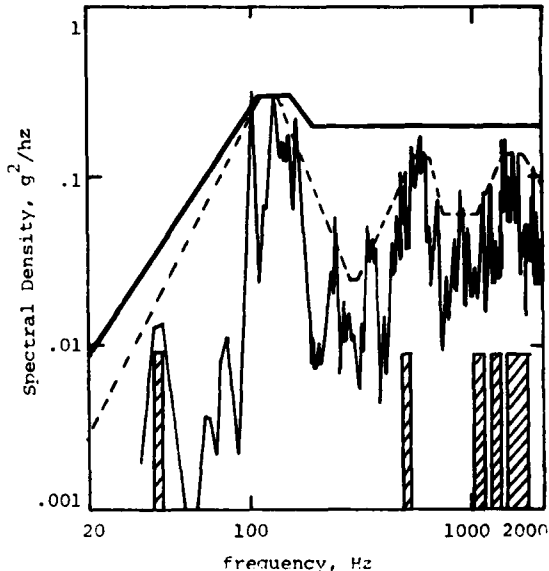


Figure 5. Field, Test, and Alternate Test Spectral Densities. Frequency Bands of First Five Modes are Shown

A sketch of the Y sensor is shown at the bottom of Table I. It consists of a sunshade which is attached to a lens housing via a flexible fiberglass sunshade spacer. The lens housing is attached to the electronics package at two points with stiff elements. An experimental modal analysis was performed on the Y sensor. Table I summarizes the results of the modal analysis. Modal frequencies, dampings, and shapes are included. The effective bandwidths of the first five modes are shown as shaded bars in Figure 5.

the formula following Equation 12 and are given in Table II. Finally, the confidences that the underlying spectral density values at the modes are listed in Table II. The product of the modal confidences was taken, and it is approximately

$$C_s = 1 - 2.29 \times 10^{-15}$$

Its geometric mean is

$$C_g = C_s^{1/5} = 1 - .46 \times 10^{-15}$$

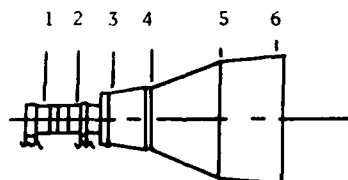
TABLE I

Global Positioning System Y Sensor Modal Characteristics

Mode Number		Frequency (Hz)	Damping Factor (%)			
1		37.8	4.67			
2		505.0	1.81			
3		1040.5	3.24			
4		1247.7	3.55			
5		1534.2	7.39			
6		2195.2	4.76			

Mode Shapes (Not Normalized)							
Mode Number		1	2	3	4	5	6
Accelerometer Number (Positions shown below)	1	7.88	1.49	2.98	9.72	0.22	0.19
	2	0.51	1.79	6.69	6.58	0.36	0.30
	3	1.41	9.62	11.06	5.74	1.14	4.22
	4	5.13	17.15	1.16	2.01	0.31	0.85
	5	19.11	8.01	0.55	1.30	0.09	0.48
	6	19.06	21.60	5.88	2.64	0.15	0.63

Accelerometer Locations on GPS Y Sensor



The measures of test conservatism defined in Equations 12 through 20 were computed for the system under consideration for the test specified in Figure 5. Table II lists modal frequency bands, the average estimated spectral density levels, and the test spectral density levels at each mode. The normalized root-mean-square errors, ϵ , are computed using the formula following Equation 12 at each modal frequency, and these are listed in Table II. Next, the approximate expected factors of conservatism, $Q(f_i)$, are computed at each mode from Equation 13, and the rms values are also computed. These are listed in Table II. The values of N at each mode are calculated from

The arithmetic average confidence for all modes is

$$C_a = 1 - .46 \times 10^{-15}$$

The average factor of conservatism for all modes is

$$Q_a = 3.45$$

A measure of rms factor of conservatism is the square root of this

$$Q_a^{1/2} = 1.86$$

Table II lists the normalized participation factors at three points on the structure. Specific structure locations are shown in the figure at the bottom of Table I. The weighted average modal confidences at structural locations 2, 5, and 6 were computed using Equation 19 and are

$$C_{wa(2)} = 1 - .07 \times 10^{-15} ,$$

$$C_{wa(5)} = 1 - 1.51 \times 10^{-15} ,$$

$$C_{wa(6)} = 1 - .88 \times 10^{-15} .$$

The weighted average factors of conservatism of the test at the same three points on the structure were also computed and are given below.

$$Q_{wa(2)} = 4.24$$

$$Q_{wa(5)} = 2.90$$

$$Q_{wa(6)} = 3.21$$

These results show that, according to this criterion, the structure is most greatly overtested at point 2 on the structure; the reason for this is that the response at point 2 is dominated by the modes at whose frequency the test conservatism is greatest. All our measures of confidence that the underlying spectral density is lower than the test spectral density are practically unity. This implies that expected factors of conservatism on the order of 3.0, which are associated with normalized rms errors on the order of .02, result in practical certainty of conservative tests.

In order to see how test conservatism varies numerically with test level, consider the specified test spectral density given by the dashed line in Figure 5. The measures of conservatism of this test were computed and are summarized in Table III and below. In Table III the average estimated spectral density levels are repeated, and the test spectral density levels at the modal frequencies are given. The normalized rms errors are repeated, and the average factors of conservatism and rms factors of conservatism are given. The modal values of N_i were computed and are listed in Table III.

TABLE II

Mode Number	1	2	3	4	5
(Mode number six deleted since input not characterized at that frequency)					
Modal frequency bands (Hz)	5.55	28.65	105.84	139.22	357.29
Average Estimated Spectral Density (g^2/Hz)	.013	.065	.040	.050	.080
Test Spectral Density (g^2/Hz)	.035	.200	.200	.200	.200
Normalized rms error $\epsilon = (\pi^2 f_i T)^{-1/2}$.080	.035	.018	.016	.010
Average factor of conservatism $Q(f_i)$	2.69	3.08	5.00	4.00	2.50
$Q^{1/2}(f_i)$	1.64	1.74	2.24	2.0	1.58
$N = \epsilon^{-1} \left[\frac{S_t(f_i)}{\hat{S}(f_i)} - 1 \right]$	21.1	59.4	222.2	187.5	150.0
$* \phi \left(\frac{N}{1 + N\epsilon} \right)$	$1 - 2.29 \times 10^{-15}$	$1 - 3.27 \times 10^{-83}$	1	1	1
u_{2j}	.032	.112	.420	.413	.023
u_{5j}	.658	.276	.019	.045	.003
u_{6j}	.386	.438	.119	.054	.003

*Numbers closer than $1 - 1 \times 10^{-99}$ to unity are given as 1.

From these, the modal confidence levels were found. The product of modal confidences is approximately

$$C_s = 1 - 4.05 \times 10^{-15}$$

The geometric and arithmetic means are approximately equal and are

$$C_g = C_a = 1 - .81 \times 10^{-5}$$

The average factor of conservatism for all modes is

$$Q_a = 1.67$$

The rms of the average factor of conservatism is

$$Q_a^{1/2} = 1.29$$

Using the normalized participation factors of Table II, we find the weighted average confidences at structural locations 2, 5, and 6.

$$C_{wa(2)} = 1 - .13 \times 10^{-5}$$

$$C_{wa(5)} = 1 - 2.68 \times 10^{-5}$$

$$C_{wa(6)} = 1 - 1.57 \times 10^{-5}$$

The weighted average factors of conservatism are formed as before.

$$Q_{wa(2)} = 1.76$$

$$Q_{wa(5)} = 1.51$$

$$Q_{wa(6)} = 1.54$$

Again, the high measures of confidence and weighted average factor of conservatism show that structure point 2 is most greatly over-tested, though the factor is not as great as before. The facts that the weighted average confidence levels are so near unity and the dashed line spectral density in Figure 5 is such a "close" envelope of the field data imply that it would be very difficult to reasonably specify a test which does not result in very nearly unit confidence in test conservatism. The reason for this is that in specifying a test the analyst must allow for slight shifts in modal frequency, nonlinear variation of damping with response level, and the presence of very lightly damped narrow bandwidth modes; and, therefore, he cannot reasonably specify a test which is a smoothed average of the field spectral density.

The test conservatism criterion of Equation 29 was not applied in this problem since the mode shapes provided by the modal test are not normal modes. Moreover, the test considered here has a duration 6.4 times as long as the measurement duration. Therefore, rms variability in running the test is $(6.4)^{-1/2} = 0.40$ times the measurement rms variability.

Test inputs for the y sensor in other directions are available, but they are not as severe as that shown in Figure 4; therefore, they were omitted from this analysis. The realism of using a base input to qualify a component which is part of a structure which is acoustically excited was not examined. To the extent that the component motion is forced by base input, the test is realistic. Input which the component receives other than through the base will tend to augment or diminish the base excited response. The response of flexible structural components will tend to have lower high frequency response components when excited by base input.

The results of this numerical example show that the GPS y sensor is conservatively tested when it is subjected to a random vibration test with spectral density given by the solid line envelope of Figure 5.

CONCLUSION AND SUMMARY

In this study we show that the probability distributions of three common spectral density estimators are usually normal. We used this fact to simplify calculations on several estimators of the conservatism of random vibration tests.

We measured random vibration test conservatism in several ways for lightly damped structural systems. Both confidence that field spectral density levels are lower than test spectral density levels and expected factor of conservatism were estimated at the individual structural modes. We averaged these modal confidences and factors of conservatism and also computed weighted averages to reflect varying degrees of modal participation at various structural locations. Through a typical numerical example we found that the normalized rms error of a spectral density estimate should usually be quite small over the frequency bandwidth of a structural mode. Therefore, any measure of confidence in a particular test should usually be quite near unity for any specified test spectral density which is an envelope of the estimated field spectral density, even when the envelope is a close one. For a given structure and test, those influences which tend to cause $\epsilon = (\pi^2 f_1 f)^{-1/2}$ to be large tend to diminish our confidence in the conservatism of a test; i.e., lightly damped, low frequency modes, and short duration tests tend to be associated with diminished confidence in test conservatism.

TABLE III

Mode Number	1	2	3	4	5
Average Estimated Spectral Density (g^2/Hz)	.013	.065	.040	.050	.080
Test Spectral Density (g^2/Hz)	.019	.100	.060	.105	.140
Normalized rms error = $\sum_i f_i T)^{-1/2}$.080	.035	.018	.016	.010
Average factor of conservatism, $Q(f_i)$	1.46	.154	1.50	2.1	1.75
$Q^{1/2}(f_i)$	1.21	1.24	1.22	1.45	1.32
$N = \epsilon^{-1} \left[\frac{S_t(f_i)}{\hat{s}(f_i)} - 1 \right]$	5.75	15.43	27.78	68.75	75.000
$\phi\left(\frac{N}{1 + N\epsilon}\right)$	$1 - 4.07 \times 10^{-5}$	$1 - 6.29 \times 10^{-24}$	1	1	1

We also approximated the probability of test failure based on a criterion of mean square structural response as a function of structural modal parameters, apparent field spectral density and specified test spectral density. Though no numerical example was worked, we expect that for typical tests the probabilities of test failure estimated using Equations 29 and 30 should be very small, particularly for systems containing several high frequency modes. The probability of failure of a test at a single mode can be higher, particularly when a lightly damped, low frequency mode tested over a short time duration is considered. This agrees with the previous results.

The various measures of test conservatism given in this study require different amounts of structural information. When modal frequencies and bandwidths are known, we can use Equations 12 through 17 to specify test spectral density levels such that the test confidence and mean-square factor of overtest are acceptable. If, in addition, we know the structural mode shapes, Equations 18 through 20, can be used to find our weighted average confidence in a test and weighted average factor of conservatism of a test at a point on the structure. Finally, if all modal information is known, then the probability of test conservatism in a mean-square structural response sense can be computed.

REFERENCES

1. J. S. Bendat and S. G. Piersol, Random Data: Analysis and Measurement Procedure, Wiley Interscience, New York.
2. D. E. Newland, An Introduction to Random Vibration and Spectral Analysis, Langman, London and New York, 1975.

INCANDESCENT LAMP LIFE UNDER RANDOM VIBRATION

Clark J. Beck, Jr.
Boeing Aerospace Company
Seattle, Washington

Several sets of incandescent lamps were subjected to random vibration in order to generate a curve of lamp life versus vibration level. The vibration levels were varied from 0.02 G^2/Hz to 1.6 G^2/Hz . Each set of lamps was vibrated until all lamps failed or for a maximum time of 2-1/2 hours. The tests were conducted with lamps energized and not energized. The test results show that average operational life of a lamp under random vibration differs significantly from lamp rated life.

INTRODUCTION

Subminiature incandescent lamps are used extensively in aircraft avionics. The lamps illuminate function switches and provide digital readouts for the crew. High reliability and long life are important lamp characteristics since lamp failures impair the crews ability to operate and receive information from the avionics. Vibration is known to shorten lamp life. Therefore, the vibration environment is an important consideration when designing avionics which contain incandescent lamps. However, quantitative data on lamp life under vibration is limited. What data exists is usually based on sinusoidal vibration. Lamp life under random vibration is needed for design evaluation since random vibration is characteristic of jet aircraft. This paper presents an evaluation of lamp life under random vibration.

The paper was written as the result of lamp failures observed during random vibration testing on an avionics control panel designed for use on the B-1 aircraft. Extensive testing was accomplished following the failures to define the failure mode, develop a design modification and determine lamp life as a function of random vibration level. A description of the test procedures and test results are discussed in the following paragraphs.

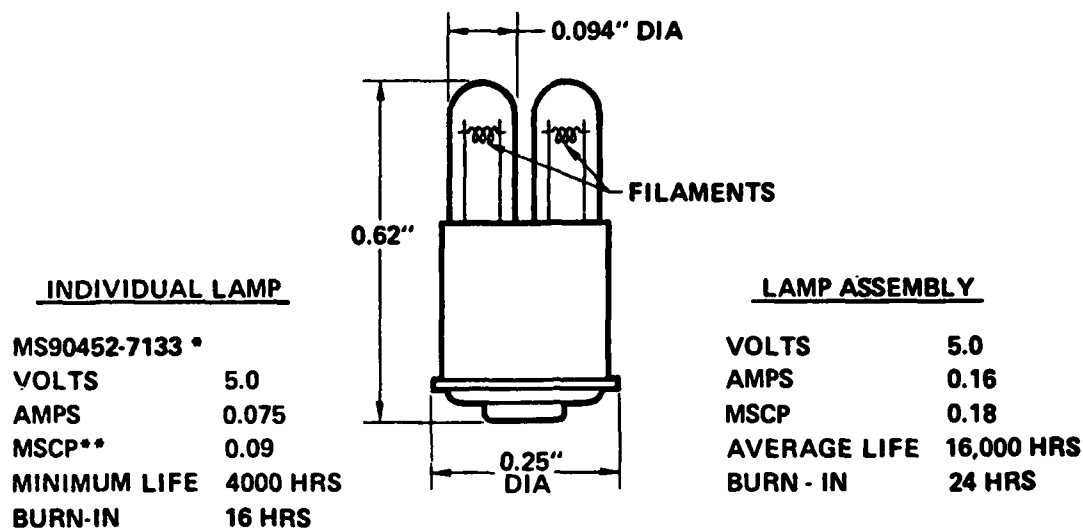
Information relative to subminiature lamp characteristics, vibration design guides and test methods are presented to provide the reader with background to better understand the test results. Conclusions relative to lamp life under random vibration and the design of avionics to enhance lamp life are presented.

LAMP DESCRIPTION

The lamp assemblies used during the vibration tests are described in Figure 1. Note that the lamp assembly contains two single filament bulbs. The lamp assemblies had been qualified to the MIL-STD-202 vibration and shock tests described in Table 1.

AVIONICS PANEL TEST

The avionics panel shown in Figure 2 was subjected to the vibration test described in Table 2. The square pushbuttons on the panel face contain 29 of the twin filament lamps described in Figure 1. The lamps illuminate the pushbutton legends. The lamps were illuminated during the vibration test. The test progressed through the X axis sine test, and Y axis sine test without any lamp failures. During the Y axis



* MILITARY STANDARD, INCANDESCENT LAMP, T $\frac{1}{4}$ BULB
 ** MEAN SPHERICAL CANDLEPOWER

Fig. 1 - Lamp Description

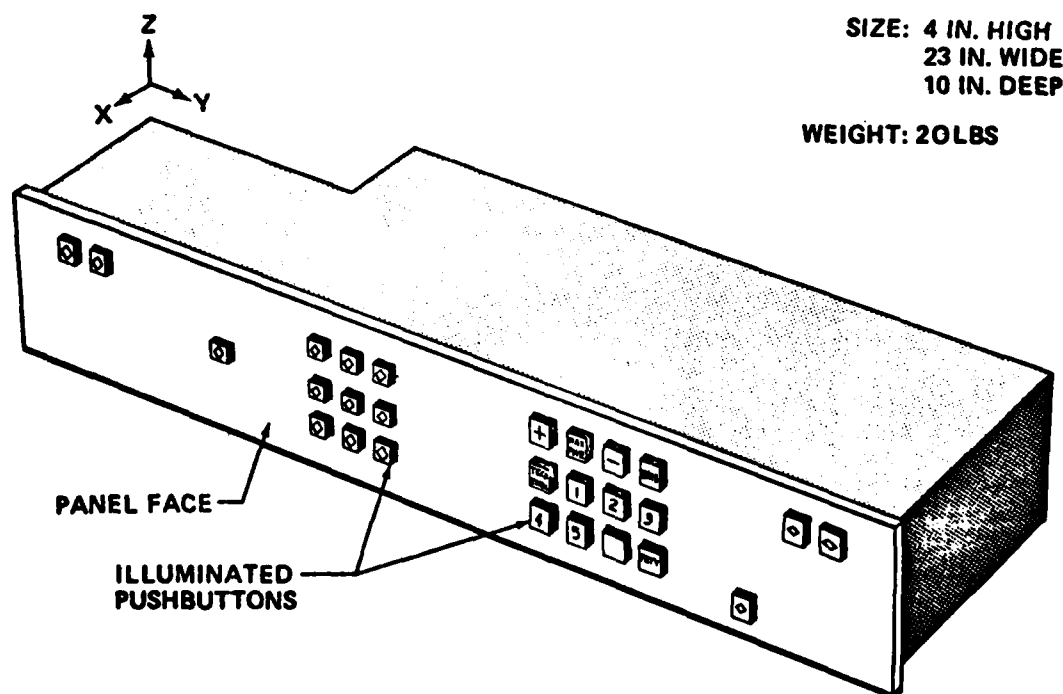


Fig. 2 - Avionics Panel

TABLE 1
Lamp Qualification Tests

MIL - STD - 202 VIBRATION
10 TO 55 HZ @ 0.06 IN DOUBLE AMPLITUDE
SINE SWEEP @ 5 OCTAVES/MINUTE
3 AXES
2 HOURS/AXIS
MIL - STD - 202 SHOCK
100 G TERMINAL PEAK SAWTOOTH
6 MILLISECONDS
3 AXES
6 SHOCKS/AXIS

TABLE 2
Avionics Panel Test

SINE VIBRATION
5 TO 10 HZ @ 0.2 IN DOUBLE AMPLITUDE
10 TO 100 HZ @ + - 1 G
SINE SWEEP @ 1 OCTAVE/MINUTE
3 AXES
90 MINUTES/AXIS
RANDOM VIBRATION
20 TO 300 HZ @ + 3 DB/OCTAVE
300 TO 1000 HZ @ 0.02 G²/HZ
1000 TO 2000 HZ @ -6 DB/OCTAVE
3 AXES
30 MINUTES/AXIS

random vibration test 6 of the 29 lamp assemblies failed*, 2 additional filaments failed and temporary loss of illumination was observed at 4 locations. Figure 3 indicates the locations of the failures and anomalies and the time at which they occurred. The failed lamps were replaced and testing was completed in the Z axis without any lamp failures. As a result of the lamp failures a series of tests were conducted to investigate the cause of the failure and to establish a design modification to preclude the failures.

PRELIMINARY LAMP TESTS

Following the avionics panel test, sine and random vibration tests were conducted to determine the resonant frequencies of the lamp filaments and to obtain an evaluation of lamp life under random vibration. The sine tests were run on 3 lamp assemblies to determine the filament resonant frequencies. Resonant frequencies were noted visually during a sinusoidal sweep from 5 to 2000 Hz. The applied vibration input varied from 2g to 10g as required to observe resonant response. Vibration was applied along 3 axes. Tests were conducted with cold lamp filaments and with hot filaments. The

*Lamp assembly failure or filament failure is defined as inability of the lamp or filament to illuminate.

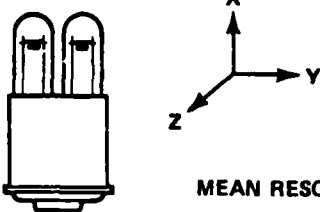
test results are tabulated in Table 3. Resonant frequencies with hot filaments were difficult to detect because of small response amplitudes.

Random vibration tests were conducted on ten lamp assemblies to determine the damage potential associated with random vibration level and filament condition (hot and cold). Vibration was applied in two axes at maximum levels of 0.02 g²/Hz and 0.2 g²/Hz. The random vibration spectra shape is described in Table 2. Testing was conducted for 30 minutes in each axis. For the first hour of testing the lamps were on (hot filaments). The last hour of testing was conducted with cold filaments (lamps off). The test results are shown in Table 4.

The lamp test results indicate that filament resonances occur over a broad frequency range (300 to 1600 Hz) and that lamp failures can be expected at vibration levels somewhere between 0.02 g²/Hz and 0.2 g²/Hz. These findings prompted the establishment of additional testing on the avionics panel to determine panel resonant frequencies and panel vibration levels.

An interesting phenomena observed during testing was that of reheat. A lamp would increase in brightness, go out and then come back on. This phenomena is the result of adjacent coils of the filament shorting, breaking and then "rehooking" or "rehealing" during

TABLE 3
Filament Resonances



MS 90452-7133 LAMP

RESPONSE/INPUT > 25 (COLD)
RESPONSE/INPUT ~ 5 (HOT)

MEAN RESONANT FREQUENCY = 980HZ (COLD)

LAMP ASSY	FILAMENT		RESONANT FREQUENCY ~ Hz		
			X AXIS	Y AXIS	Z AXIS
1	1	COLD	910, 1605	545, 910, 1600	300, 900, 1600
	2		950, 1605	540, 950, 1600	315, 910, 1600
2	1		640, 1040	650, 1075	640, 1075
	2		860	-	860, 1450
3	1		-	745, 1325	745
	2		-	640, 1200	640
1	1	HOT	-	-	800
	2		-	-	875, 1535
2	1		-	-	660
	2		-	-	840
3	1		-	-	680, 1200
	2		-	998	540

TABLE 4
Filament Failures - Random Vibration

MS 90452-7133 LAMP
10 LAMP ASSEMBLIES
(20 FILAMENTS)

TEST SEQUENCE /CONDITIONS

FILAMENT FAILURES

AXIS

LEVEL
(G2/Hz)

TIME
(MIN)

FILAMENT

Y

0.02

30

HOT

NONE

Z

↓

30

HOT

NONE

Y

↓

30

COLD

NONE

Z

↓

30

COLD

NONE

Y

0.2

30

HOT

NONE

Z

↓

30

HOT

2

Y

↓

30

COLD

8

Z

↓

30

COLD

TOTALS

4 HRS

10 FAILURES

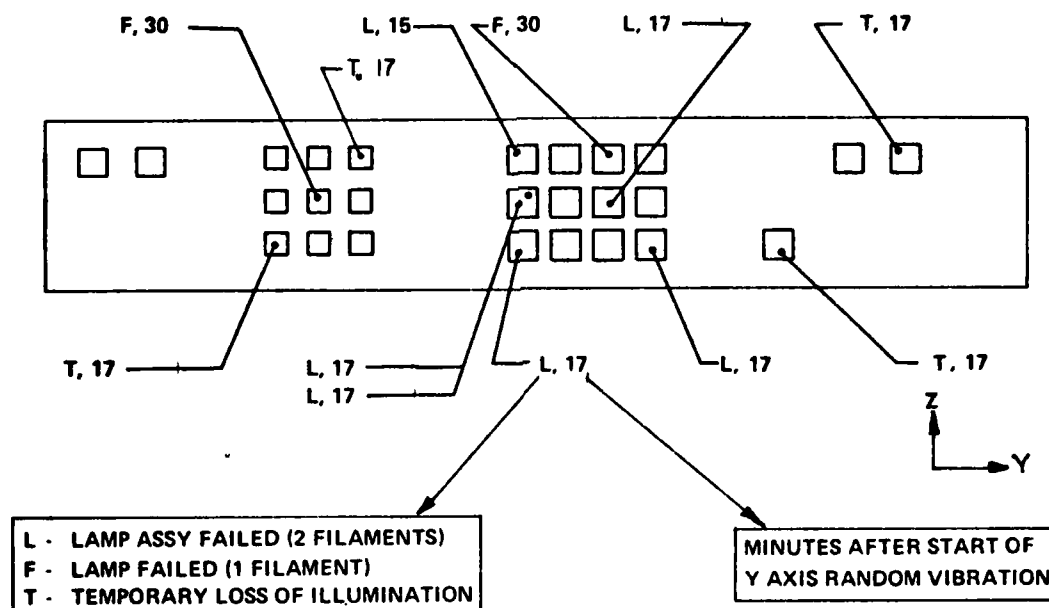


Fig. 3 - Avionics Panel Lamp Failures

vibratory motion. Reference [1] also describes this phenomena occurring on 31 out of 46 test lamps.

AVIONICS PANEL EXPLORATORY TESTS

A series of exploratory vibration tests were conducted on the avionics panel to determine panel resonant frequencies and the vibration levels near the lamp assemblies. The first test used the avionics panel as a test specimen. The test specimen was instrumented as shown in Figure 4. The panel was subjected to random vibration in 3 axes at the levels described in Table 2. The vibration response of the push-button switches was recorded during the test and analyzed to produce acceleration power spectral density curves. The frequency and magnitude of the three highest peaks from each curve were noted. The response magnitude was divided by the magnitude of the vibration input to the avionics panel at the frequency of the response peak. The square root of this ratio provided an estimate of the panel resonance quality factor (Q). A plot of Q versus resonant frequency for the avionics panel is shown in Figure 5.

Several tests were run using a test specimen which simulated the panel face in the vicinity of the 12 pushbuttons array (see Figure 4). The simulator

was used to develop a panel face modification. The modification which was developed consisted of reducing the panel thickness, eliminating panel stiffeners near the switches, modifying switch cutouts in the panel and lowering the torque requirements for the switch mounting screws. The modifications resulted in reduced panel resonant frequencies and Q values as shown on Figure 6.

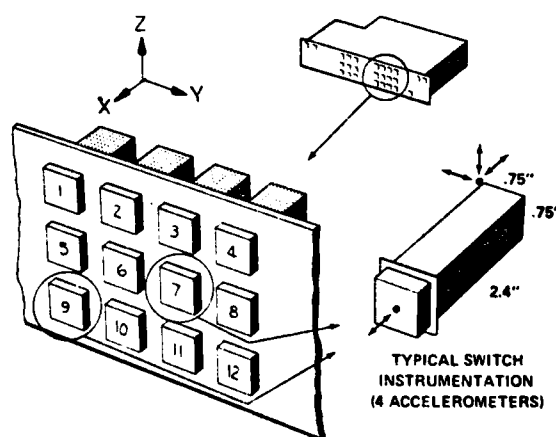


Fig. 4 - Instrumentation

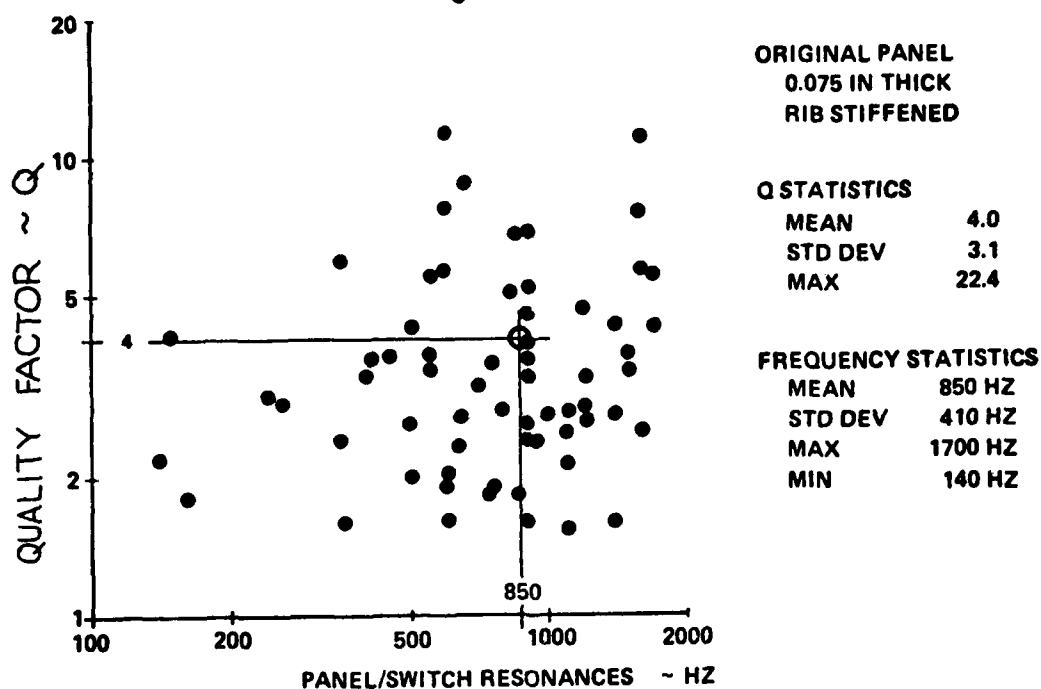


Fig. 5 - Avionics Panel Vibration Response

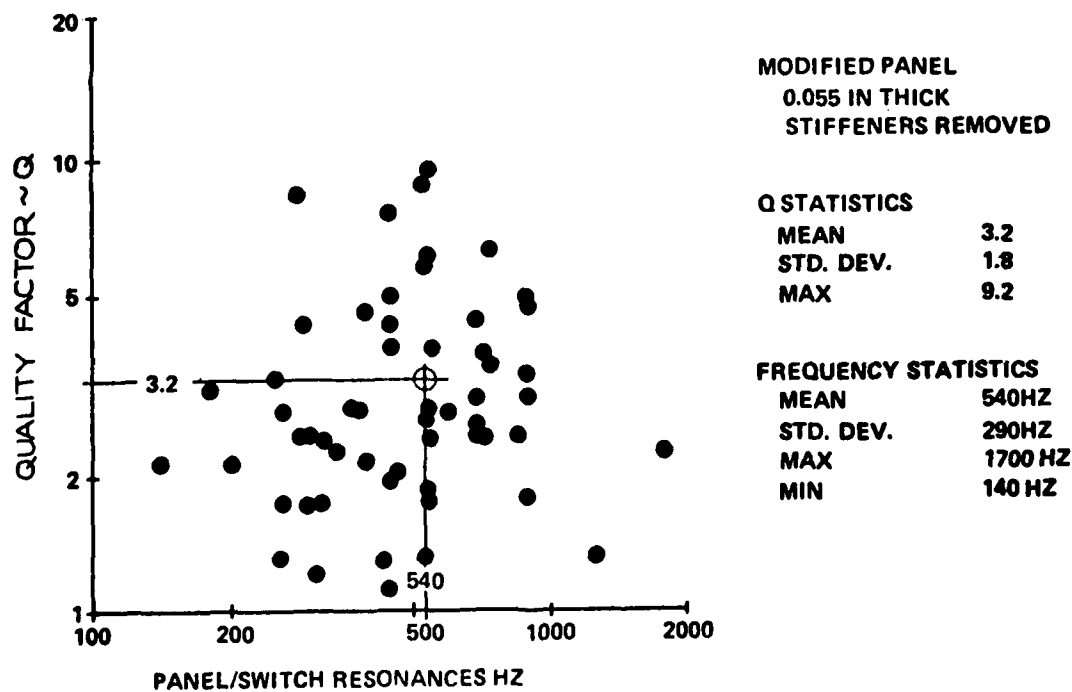


Fig. 6 - Modified Panel Vibration Response

The modified panel dynamics are an improvement over the original panel characteristics for two reasons. First, the mean frequency of the modified panel is less than the original panel resulting in a larger separation between panel resonances and lamp filament resonances (980 Hz). Second, the mean Q for the modified panel is less than the Q for the original panel. These differences can be seen by comparing the mean values of Figures 5 and 6. Figure 7 contains a comparison of measured vibration spectra which also illustrates differences in panel dynamic characteristics.

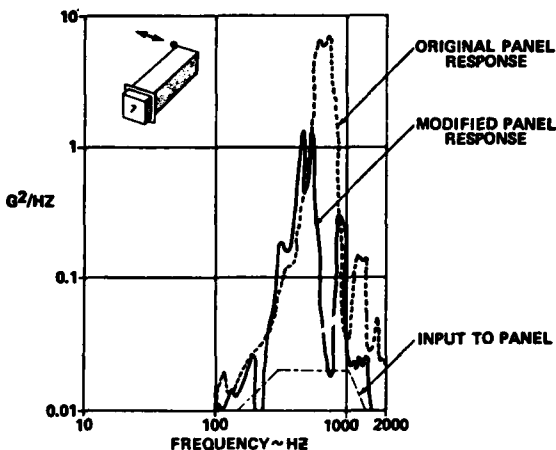


Fig. 7 - Vibration Comparison

The effectiveness of the modification was demonstrated by subjecting the modified panel to the random vibration test described in Table 2. Twenty-four lamp assemblies (48 filaments) were installed in the panel. Only 6 of the 48 filaments (12.5%) had failed at the completion of the 1-1/2 hour test. There were no lamp assembly failures (both filaments failed). Comparing the modified panel filament failures with the failures noted during the original panel test (13 filament failures out of 28 filaments or 46.4%), a 34% decrease in failures is evident.

During the first avionics panel test all of the lamp filament failures occurred in the Y axis (see Figure 3). These test results indicated that the panel vibration response in the Y direction was greater than the response in the X and Z directions. A comparison

of the in-axis response data revealed that this was the case as evidenced by a comparison of the data in Table 5.

TABLE 5
In-Axis Vibration Response

AXIS	QUALITY FACTOR - Q		
	MEAN	MEAN + STD. DEVIATION	MAXIMUM
Y	6.0	12.8	22.4
Z	4.6	6.8	7.7
X	3.8	4.9	5.4

ADDITIONAL LAMP TESTS

The avionics panel tests demonstrated that lamp filament failures can be significantly reduced by modifying the dynamic characteristics of the panel. However, neither the panel tests nor the preliminary lamp tests provided sufficient data to determine lamp filament life as a function of random vibration level. Therefore, 50 lamp assemblies were subjected to a range of random vibration levels to determine the life/level relationship.

The 50 lamps were subjected to the vibration tests described in Table 6. The lamp assemblies were tested in groups of 10 thereby exposing 20 filaments to each test level. All lamps were new at the start of each test except for test number 6. Each lamp was assigned a serial number and photographed prior to the test.

TABLE 6
Lamp Random Vibration Tests


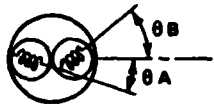
				
TEST	LAMP ASSY S/N	TEST LEVEL (G ² /HZ)	TEST DURATION (MIN)	FILAMENT CONDITION
1	0001 - 0010	1.8	150	COLD
2	0011 - 0020	0.8	150	COLD
3	0021 - 0030	0.2	150	COLD
4	0031 - 0040	0.05	150	COLD
5	0041 - 0050	0.8	150	HOT
6	0031 - 0040	0.2	(40) (150)	COLD HOT

TABLE 7
Lamp Life Data Sheet

		VIBRATION LEVEL - 1.6 G ² /HZ FILAMENTS - COLD																			
		<div style="display: flex; align-items: center; justify-content: space-between;"><div>VIBRATION DIRECTION</div><div></div></div>																			
		FILAMENT CONDITION ● OK X FAILED ○ VERY BRIGHT																			
LAMP S/N	θ	INSPECTION TIME - MINUTES																			
		1	2	4	8	10	15	20	30	40	50	60	70	80	90	100	110	120	130	140	150
0001	A 45	●	●	○	○	○	○	○	○	○	○	○	○	○	○	○	○	○	○	○	○
	B 30	●	●	●	X	●	●	X	X	X	X	X	X	X	X	X	X	X	X	X	X
0002	A 70	●	●	●	●	X	●	X	X	X	X	X	X	X	X	X	X	X	X	X	X
	B 70	●	●	●	●	●	●	●	●	●	●	●	●	●	●	●	●	●	X	X	X
0003	A 25	●	●	●	●	●	●	●	X	X	X	X	X	X	X	X	X	X	X	X	X
	B 5	●	●	●	●	●	●	●	●	●	●	●	●	●	●	●	●	●	X	X	X
0004	A 60	●	●	●	●	●	●	●	X	X	X	X	X	X	X	X	X	X	X	X	X
	B 45	●	●	●	●	●	●	●	●	●	●	●	●	●	●	●	●	●	●	X	X
0005	A 80	X	●	○	●	X	X	X	X	X	X	X	X	X	X	X	X	X	X	X	X
	B 5	●	●	●	●	●	●	●	●	●	●	●	●	●	●	●	●	●	●	●	●
0006	A 45	X	X	X	X	X	X	X	X	X	X	X	X	X	X	X	X	X	X	X	X
	B 60	X	X	X	X	X	●	X	X	X	X	X	X	X	X	X	X	X	X	X	X
0007	A 45	●	●	●	X	X	X	X	X	X	X	X	X	X	X	X	X	X	X	X	X
	B 45	X	X	X	X	X	X	X	X	X	X	X	X	X	X	X	X	X	X	X	X
0008	A 20	●	●	●	●	●	●	●	●	●	●	●	X	X	X	X	X	X	X	X	X
	B 75	●	●	●	●	●	●	●	X	X	X	X	X	X	X	X	X	X	X	X	X
0009	A 0	●	●	●	●	●	●	●	●	●	●	●	●	●	●	●	●	●	●	●	●
	B 0	●	●	●	●	●	●	●	●	●	●	●	●	●	X	X	X	X	X	●	●
0010	A 5	●	●	●	●	●	●	●	X	X	X	X	X	X	X	X	X	X	X	X	X
	B 30	●	●	●	●	●	X	X	X	X	X	X	X	X	X	X	X	X	X	X	X

The ten lamp assemblies were hard mounted to the vibration test fixture and the alignment of each filament was noted relative to the direction of vibration excitation. No attempt was made to maintain a specified angle between the filament and the direction of vibration. Vibration excitation was applied perpendicular to the long axis of the assembly as shown in Table 6. During the test the lamps were checked periodically for failed filaments. When the filaments were tested cold the test was stopped and the lamps were energized to check for failures. The inspection periods were the following: 1 minute, 2 minutes, 4 minutes, 8 minutes, 10 minutes, 15 minutes, 20 minutes, and 10 minute intervals thereafter until the end of the test. The test was terminated after 150 minutes. The condition of each filament was recorded after each inspection period. One of the data recording sheets is shown in Table 7. Note in Table 7

that some of the filaments fail and subsequently are capable of illumination. This is probably the result of reheal.

The results of the vibration tests were used to determine the average lamp life and the average filament life. Average life as commonly defined in the lamp industry is the time required for 50% of the lamps to fail. The average life results are tabulated in Table 8. The lamp filament failure time is plotted versus vibration level in Figure 9 to indicate the time spread of the failures. Note that the data trend shown in Figure 9 is similar to the trend exhibited by a metal fatigue curve (S-N curve).

Observation of filament resonant response during the preliminary lamp tests indicated that filament response amplitude is a function of filament orientation relative to vibration

TABLE 8
Average Life

MS 90452 - 7133 LAMP			
VIBRATION LEVEL (G ² /HZ)	FILAMENT CONDITION	*AVERAGE LIFE (MINUTES)	
		FILAMENT	LAMP ASSEMBLY
1.8	COLD	30	130
0.8	COLD	30	>180
0.8	HOT	30	70
0.2	COLD	>180	>180
0.2	HOT	>180	>180
0.05	COLD	>180	>180
*TIME FOR 50% FAILURE			

direction. Maximum response appeared to occur when the direction of vibration was perpendicular to the long axis of the filament. The results from the 50 lamp test are presented in Figure 10 to show the variation of filament time to failure as a function of filament orientation. A power curve was fitted to the data to determine the time/orientation relationship. The curve

shown in Figure 10 indicates that time-to-failure decreases as the angle between the filament longitudinal axis and vibration direction approaches 90°.

APPLICATION OF LAMP LIFE/VIBRATION CURVE

Using the failure trend curve shown in Figure 9 an estimate of the time for 50% filament failure was made for the original avionics panel. The estimate was made as follows:

1. The Q value of panel response in the Y axis was selected as 6.0 (see Table 5).
2. The vibration level on the panel was determined.

$$Q^2 \times \text{input vibration}$$

$$= (6.0)^2 \times 0.02 \text{ g}^2/\text{Hz}$$

$$= 0.72 \text{ g}^2/\text{Hz}$$
3. The Figure 9 trend curve was used to determine that the estimated time for 50% of the filaments to fail at 0.72 g²/Hz is about 50 minutes.

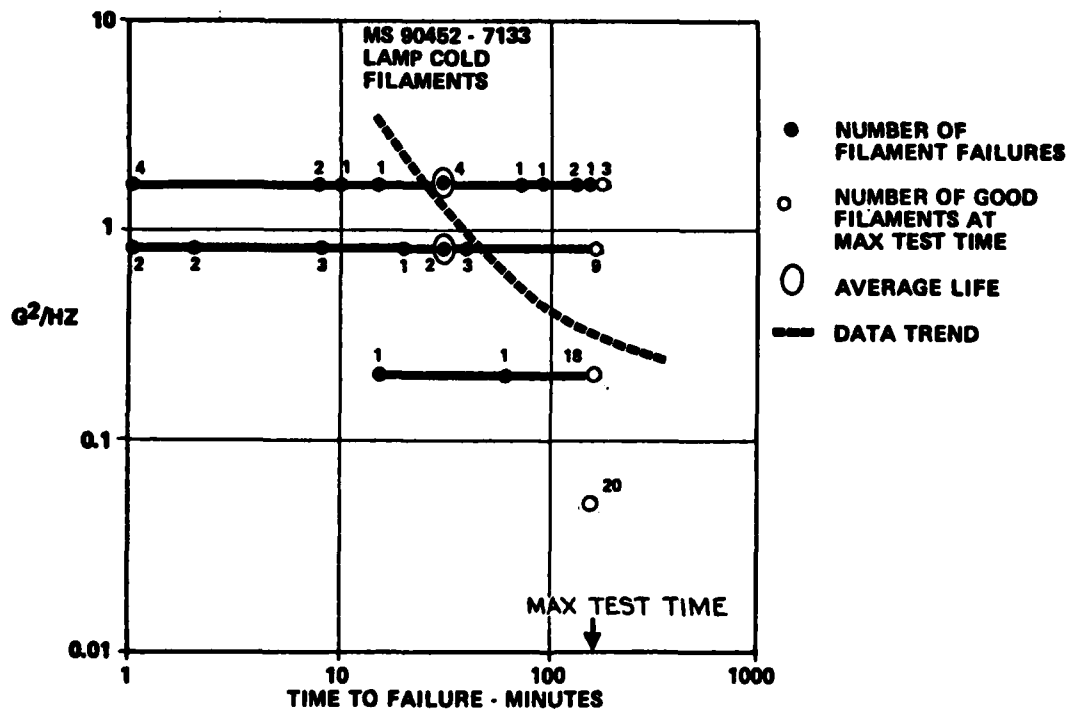


Fig. 9 - Failure Time vs. Vibration Level

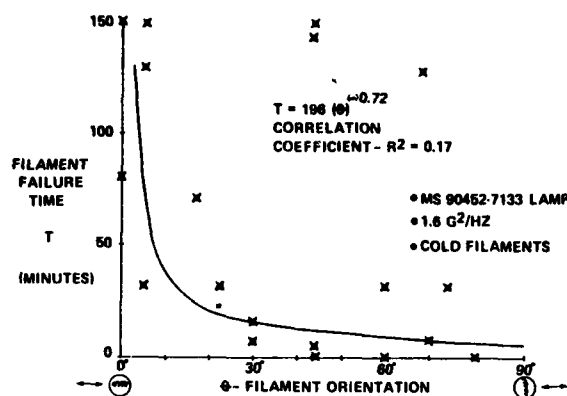


Fig. 10 - Filament Orientation

During the original panel test 13 out of 28 filaments (46.4%) failed during 30 minutes of testing in the Y axis.

LAMP LIFE COMPARISONS

Lamp life ratings as stated in lamp catalogs are generally determined mathematically as the point at which the filament wire weight has been reduced by ten percent, reference [2]. The life rating is confirmed thru laboratory testing. However, lamp life is substantially shortened when a lamp is subjected to vibration and shock environments. The effect of sine vibration and shock on lamp life is illustrated by the comparisons shown in Table 9. The lamps used to generate the data in Table 9 were chosen because of their general usage and due to their vulnerability to shock and vibration.

LAMP DESIGN GUIDES

Lamp manufacturers suggest the following guidelines for use of sub-miniature lamps in shock and vibration environments [2, 4 and 5].

- Use lower voltage (5 to 6 volt) non-anchored filament lamps rather than high voltage anchored types.

TABLE 9
Vibration and Shock Effects

LIFE TEST CONDITIONS	LAMP NO. 327		LAMP NO. 387	
	LIFE (HRS)	% RATED	LIFE (HRS)	% RATED
LIFE RATING (90% FILAMENT WEIGHT)	7,000	100	25,000	100
INTERMITTENT VIBRATION 125 HRS AC AGING MIL-STD-202 VIBRATION(2)	1,250(1)	18	1,350 ⁽¹⁾	5
INTERMITTENT VIBRATION 500 HRS DC AGING MIL-STD-202 VIBRATION	1,500(1)	21	3,000 ⁽¹⁾	12
INTERMITTENT SHOCK 500 HRS AC AGING MIL-STD-202 SHOCK(3)	2,250(1)	32	3,000 ⁽¹⁾	12
(1) 50% OF TEST SPECIMENS FAILED (2) 10 TO 55 HZ @ 0.06 IN DA, 3 AXES, 2 HRS/AXIS (3) 100 G @ 6 MS, 3 AXES, 6 SHOCKS/AXIS (4) DATA FROM CHICAGO MINIATURE LAMP REPORT, REF.[3]				

- Derate lamps to the lowest practical filament temperatures.
- Maintain current through the filament to keep it from becoming brittle when the lamp is not providing illumination.
- Provide shock and vibration isolation whenever possible.

SUMMARY

The lamp life test results discussed in this paper apply to subminiature tungsten filament lamps designated as MS90452-7133. The 7133 lamp is considered to be a relatively rugged lamp suitable for use in shock and vibration environments. Conclusions resulting from these tests are the following:

- Average lamp filament life (time required for 50% of filaments to fail) is about 30 minutes at random vibration levels in the order of $1.0 \text{ g}^2/\text{Hz}$. Average lamp life (2 filaments) is greater than 60 minutes.
- Average filament life is similar for hot or cold filaments.
- The range of filament life is large, i.e., 1 minute to more than 150 minutes at random vibration levels in the order of $1.0 \text{ g}^2/\text{Hz}$.
- When filament failure time is plotted versus vibration level the resulting curve has the characteristics of a metal S-N curve.
- MIL-STD-202 shock and sine vibration are commonly used to qualify lamps for shock and vibration. Qualification of a lamp to the MIL-STD-202 tests indicates that a lamp is suitable for use in dynamic environments. The tests do not reveal information regarding the lamp life under random vibration commonly encountered in service.
- Lamp filament resonant frequencies occur over a wide frequency range, 300 to 1600 Hz for #7133 lamps. Q factors associated with resonance are in the order of 25 and 5 for cold and hot filaments, respectively. The wide resonant frequency range and high Q values make the lamps vulnerable to damage by structural resonances.

- Significant numbers of lamp failures can occur in avionics panels with input vibration levels as low as $0.02 \text{ g}^2/\text{Hz}$.
- Avionics panels can be designed to minimize coincidence between lamp and panel resonances and to increase panel damping thereby minimizing lamp failures.
- The design of avionics panels which contain incandescent lamps should consider the adverse affect of random vibration on lamp life. The vibration effects can be evaluated using test techniques described in this paper.

REFERENCES

1. Jennings, G. and Schmerda, J; Vibration and Life Test Report, 3% Rhenium/97% Tungsten Lamps; General Motors, Corp.; AC Electronics; May 1966.
2. Chicago Miniature Lamp Works Catalog CMT-3A, Subminiature Lamps, Chicago, Ill.
3. Lamp Comparison and Evaluation of the Industry Standards No. 327 and No. 387 Subminiature Lamps, Chicago Miniature Lamp Works, Chicago, Ill.
4. Subminiature Lamps Catalog, Illuminated Products, Inc., Los Angeles, Calif.
5. Guennewig, J.T.; "Avionics Application of Incandescent Digital Readouts"; Electro-Optical Systems Design; May 1977.

INSTRUMENTATION

ANGULAR VIBRATION MEASUREMENT TECHNIQUES

P. Wayne Whaley and Michael W. Obal
Air Force Flight Dynamics Laboratory
Wright-Patterson AFB, Ohio 45433

The angular and linear vibratory response of aircraft structures affects airborne electro-optical packages. In order to design these systems with acceptable pointing accuracies and sufficient subsystem mirror alignments, knowledge of the angular responses of aircraft structures is important. Thus, it is necessary to be able to measure angular vibrations of aircraft structures in order to describe optical package disturbances. Six angular vibration sensors were encountered in a literature survey and are evaluated in light of the above requirements. In addition, experience with differential angular vibration measurement using conventional accelerometers is presented and evaluated. These results indicate a strong need to develop a good, reliable, miniature angular vibration sensor for airborne measurements.

INTRODUCTION

The design and operation of airborne electro-optical systems requires a knowledge of the angular vibration response characteristics of aircraft structures. Previous efforts in analyzing aircraft angular vibration have been based on the idea that the angular vibration may be predicted, or estimated from the known linear vibration environment [1]. Although this concept avoids the requirement for collecting a broad base of aircraft angular vibration data for prediction purposes, data are still required to provide validation of such an analytical prediction scheme. The current lack of suitable angular vibration transducers makes even this task difficult to attain at present. The purpose of this paper is to survey existing angular vibration sensors or measurement techniques and discuss their applicability to airborne angular vibration measurements from 0-1000 Hz and from $1-20 \times 10^{-6}$ rad.

The primary design goal in airborne electro-optical systems is to provide acceptable pointing accuracies and subsystem mirror alignments. The angular response of the aircraft structure seriously impedes these goals. The characteristics of an angular sensor should therefore enable the measurement of that response and also survive the airborne measurement environment. The sensor should be small enough so that the local response of the structure is not affected by its presence, and still

be capable of measuring angles in the 10^{-6} rad range. The transducer must be capable of measuring broadband signals (0-1000 Hz) and it must be an inertial sensing device. Six devices which can measure angular vibrations were encountered during a literature survey. These are: rate gyroscopes, an angular differentiating accelerometer, magnetohydrodynamic angular rate sensor, a rotary variable differential transformer, a seismic angular vibration transducer, and an angular velocity vibrometer. Their applications will be discussed in light of the above requirements. A technique for measuring angular vibration using conventional accelerometers will also be discussed. This technique provides a reliable and effective way to measure angular vibration until a suitable angular sensor can be developed.

Rate Gyroscopes

One of the most common angular sensors is the rate gyroscope. Fig. 1 shows a schematic of a rate gyroscope and demonstrates the principle of its operation [2]. The momentum of a wheel spinning about the x-axis requires torque in order to rotate about the y-axis. The electrical output of the sensor is proportional to the torque about the z-axis.

The transfer function of the rate gyroscope indicates that the sensor is useful below the natural frequency of the system. Most commercially available rate gyroscopes have natural frequencies of 20 Hz to 50 Hz and are

able to measure angles of about 10^{-3} rad.

Angular Differentiating Accelerometer (ADA)

The operating principle of this ADA is a small torsional pendulum which transmits inertial motion to a tachometer. A schematic of an ADA and its transfer function is shown in Fig. 2 [3]. The transfer function indicates that the ADA must operate above its natural frequency where its output is proportional to angular velocity. Thus, most ADA designs attempt to force the natural frequency as low as possible for maximum bandwidth. When the case of the ADA moves relative to the flywheel, the tachometer will sense the relative motion between flywheel and case and provide an output electrical signal proportional to that velocity.

As shown by the transfer function in Fig. 2, compared to a rate gyroscope, the ADA is a high frequency device. A typical commercially available ADA has a bandwidth of 2-20 kHz, but requires an elevated operating temperature of 48.8°C (120°F) to maintain the damping fluid at its prescribed viscosity. This requires a heat sink in the ADA design which makes most ADAs quite bulky. The size of the ADA causes the structural response characteristics to be affected by its mass. Therefore, data collected with ADAs should be used with caution and they should be attached to major structural members.

Magnetohydrodynamic (MHD) Angular Rate Sensor

The MHD rate sensor operates on the principle of a toroid of liquid metal in a magnetic field rather than depending on the momentum of a spinning wheel [4]. The magnetohydrodynamic principle used here refers to the process of voltage induced by an angular acceleration about an axis normal to the plane of a toroid of liquid metal moving in a magnetic field. Fig. 3 shows a schematic of the angular accelerometer component of the MHD and the theory of its operation.

The basic design of the MHD sensor consists of a ring of liquid metal sandwiched between a magnet and case. The liquid metal is in contact with a spool of conducting material which surrounds a toroidal tape wound core. When an angular rate is applied to the input axis, the motion produces an oscillation of the magnetic field with respect to the liquid metal. This relative motion generates a voltage between the liquid metal and conductive spool. A cutaway drawing of a typical MHD sensor is shown in Fig. 4.

The frequency range of this MHD is approximately 0-100 Hz, and recent laboratory and flight tests indicate that it is capable of measuring angular vibration as low as 10^{-5} rad. However, the MHD failed during the flight tests and should be evaluated further before being used on additional flight tests [5].

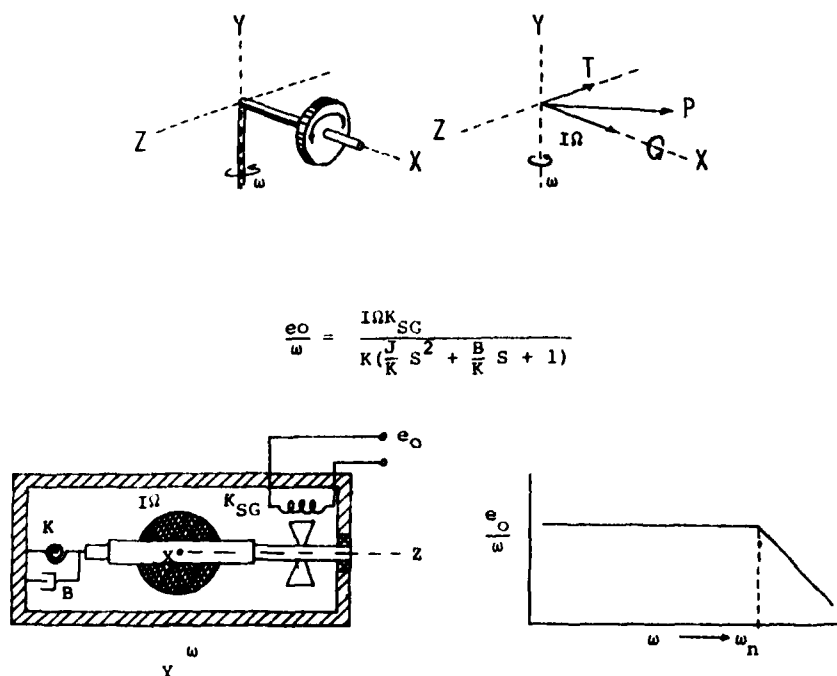


Fig. 1 - Schematic and theory of operation of the rate gyroscope.

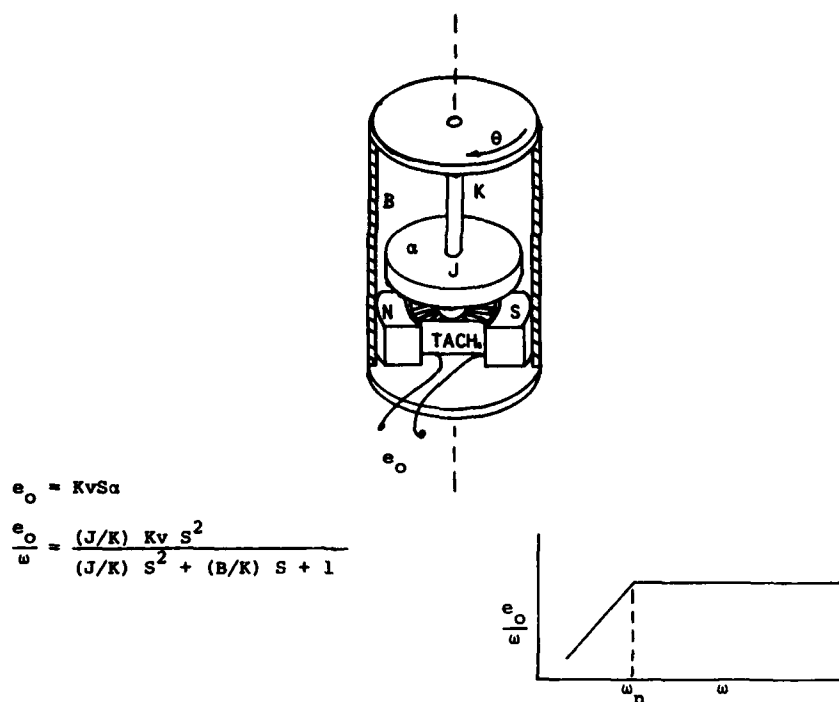


Fig. 2 - Schematic and theory of operation of the angular differentiating accelerometer (ADA).

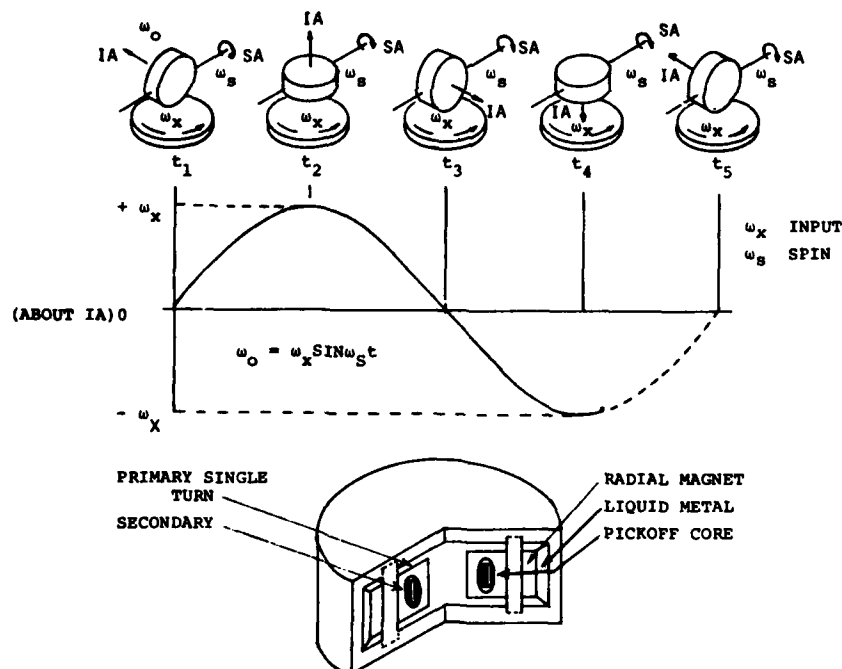


Fig. 3 - Schematic and theory of operation of the angular accelerometer component of the magnetohydrodynamic angular rate sensor.

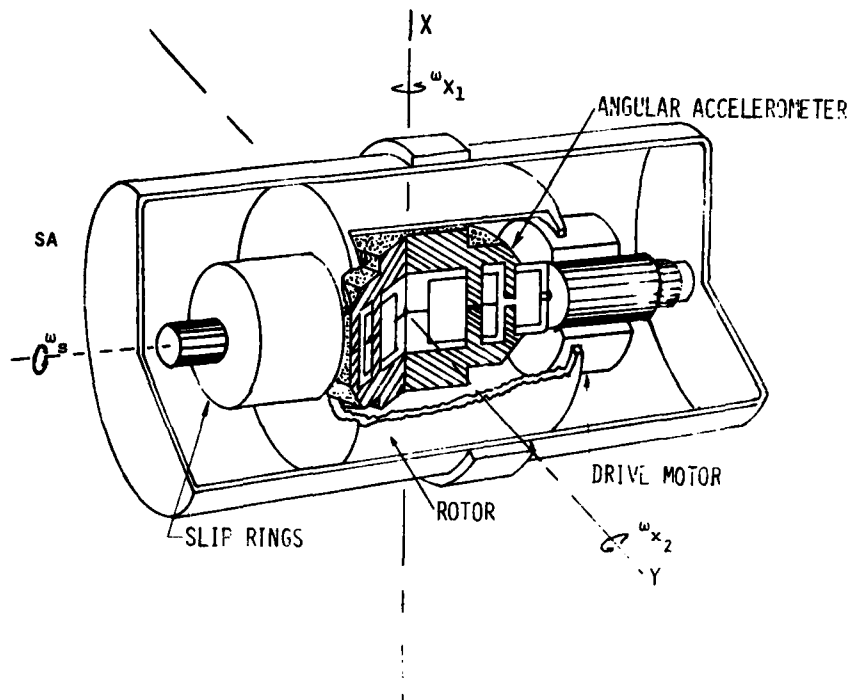


Fig. 4 - Schematic of the magnetohydrodynamic angular rate sensor.

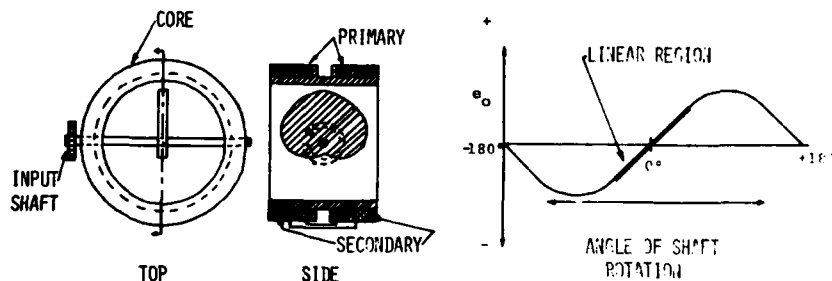


Fig. 5 - Schematic and theory of operation of the rotary variable differential transformer

Rotary Variable Differential Transformer (RVDT)

The operating principle of the variable differential transformer is the electrically sensed position of an iron core relative to a set of electrical windings. The shape of the iron core in its relation to this set of electrical windings dictates whether linear or angular measurements are to be made. The RVDT is basically a cardioid shaped rotor of mag-

netic material inside a symmetrically wound coil as shown in Fig. 5 [6]. The rotor shape produces a highly linear output within a specified range of rotation. The linear range of the RVDT is ± 696 rad and it can operate in a continuously rotating mode. There are no known commercially available RVDT sensors that can measure microradian angular displacements over the desired frequency range.

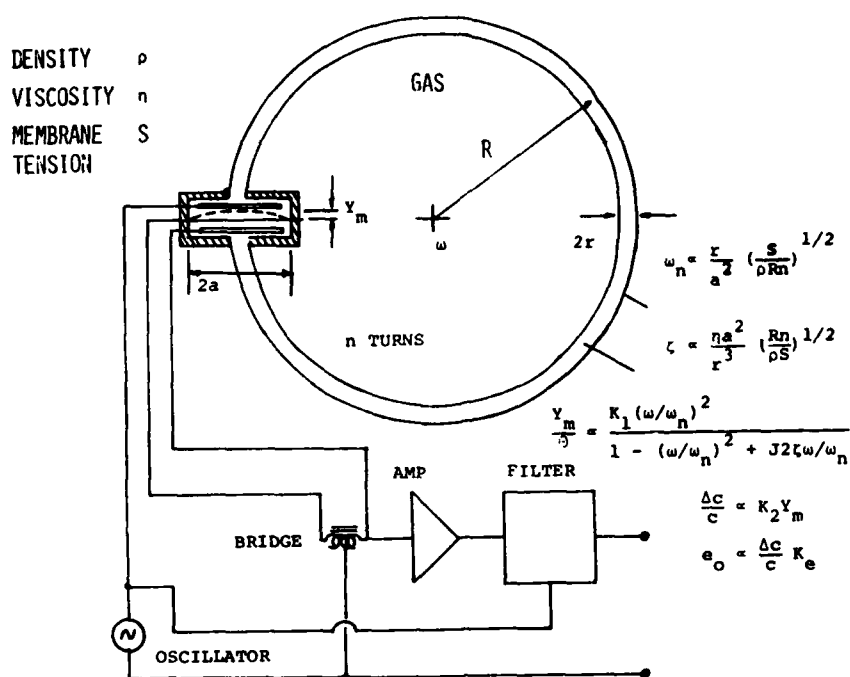


Fig. 6 - Schematic and theory of operation of the seismic gas angular sensor.

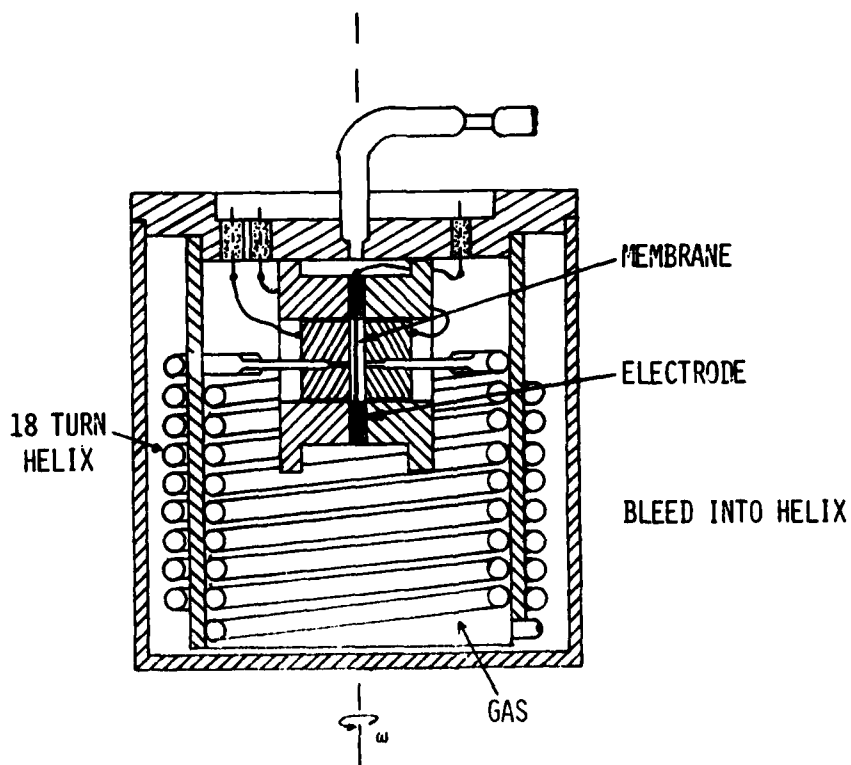


Fig. 7 - Cross section of the seismic gas angular sensor.

Seismic Gas Rotor Angular Vibration Transducer

The seismic gas transducer uses a helical column of gas as a seismic rotary mass [7]. Fig. 6 shows a schematic of the seismic gas transducer which consists of a helical tube of gas connected at the ends to a chamber and separated by a thin membrane. When the tube is displaced, the gas presses against a thin membrane which is located between two capacitive plates. This displacement causes a differential capacitive charge which is converted to a voltage.

Fig. 7 shows a cross-section of a typical seismic gas transducer. This device operates at ± 174 rad and from 2-20 Hz. The natural frequency of this device depends on the mass of the gas column, stiffness of the membrane, and column resonances in the gas. This device could utilize liquid to increase its frequency range, but would then be very temperature sensitive. This transducer fails to satisfy the 10^{-6} rad sensitivity requirement.

Angular Velocity Vibrometer

An angular velocity vibrometer is based on the coriolis effect of combined translational and rotational masses [8]. The coriolis effect is generated by rectilinear motion of two half-wave bars which is perpendicular

to the angular axis. Supporting piezoelectric crystals at the ends of the vibrating bars sense the coriolis accelerations. For constant rectilinear periodic motions the output is proportional only to angular motion.

Fig. 8 is a drawing based on the Soviet patent statement. Although no performance specifications were found for this device, repeated use of the word resonance in the patent indicates that it operates only within a specified frequency range. In addition, the forces required to drive the half-wave bars limit the upper frequency.

None of the devices reviewed here satisfy all the requirements for an acceptable angular sensor. The device which comes closest is the ADA, and it is anticipated that continued use of the ADA will be required, especially if the ADA can be miniaturized. In order to measure aircraft angular vibrations until such devices become available, a technique using conventional accelerometers has been developed. Experience gained by applying this technique to collect flight data will be reported and discussions concerning assessments of reliability of the angular vibration data will be given.

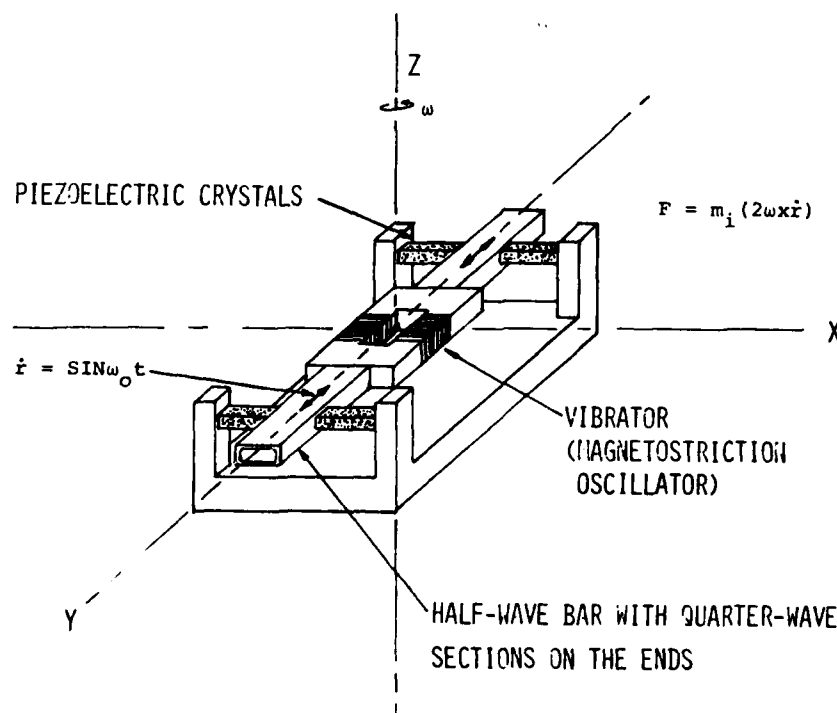


Fig. 8 - Schematic of an angular velocity vibrometer based on coriolis accelerations.

USE OF CONVENTIONAL ACCELEROMETERS

Background

Angular vibration may be measured using linear accelerometers by placing them some distance apart, subtracting the outputs and dividing the difference by the separation distance between the two accelerometers as shown in Fig. 9. The separation distance is a primary consideration when using this technique and it inherently has an upper limit and a lower limit. The theory suggests that the accelerometers should be placed as close together as possible to approach the true angular response of the structure. However, when the accelerometers are too close to each other the difference signal will become contaminated with noise at low frequencies [9]. Therefore, the lower limit on separation distance between the accelerometers depends primarily on their noise floor.

Since the angle approximated by the accelerometer differencing technique is proportional to the inverse of the separation distance, the greater the separation distance, the better the low frequency sensitivity. However, the upper limit for separation distance is affected by the flexural error between the accelerometers. This flexural error is dependent upon the upper frequency desired and is defined in terms of the vibratory wavelength of the structure [9]. By considering the speed of a bending traveling wave it is possible to define a wavelength, which is a function of frequency and structural properties. In this manner it is possible to establish an upper limit of separation distance consistent with the desired upper frequency range to be measured.

The low frequency measurement capabilities of differential accelerometers have been studied in detail and are based on the following equation [9].

$$\theta = \frac{\Delta y}{\Delta x} \quad (1)$$

θ = desired angular vibration magnitude

Δy = differential displacement

Δx = separation distance

For accelerometers, Eq.(1) may be rewritten as

$$\frac{\Delta \ddot{y}}{\Delta x} = \omega^2 \theta \quad (2)$$

where ω is frequency in radians/second. Multiplying Eq.(2) by Δx , one gets

$$\Delta \ddot{y} = \omega^2 \Delta x \theta \quad (3)$$

From Eq.(3) the dependence of $\Delta \ddot{y}$ on ω^2 , Δx , and θ may be seen. At a given x and desired θ , as ω decreases, $\Delta \ddot{y}$ falls below the noise

floor of the accelerometers. The frequency where that happens depends on Δx and θ . For measurement of large θ the frequency where $\Delta \ddot{y}$ disappears into accelerometer noise will be low. The important idea which Eq.(3) indicates, however, is that the larger the Δx , the lower the frequency where $\Delta \ddot{y}$ disappears into the instrument noise. Therefore Δx should be chosen as large as possible, subject to flexural error constraints in order to give good low frequency measurements.

Conversely, the separation distance should be chosen as small as possible in order to have acceptable flexural error at higher frequencies. This idea can best be visualized by considering an analogy from acoustics. For acoustical systems, lumped parameter models give acceptable results whenever the system physical dimensions are less than 1/4 of the wavelength at the upper frequency end. Converting this analogy to the problem at hand, one might say that whenever the separation distance is less than 1/4 of the wavelength of the traveling wave of the structure, the differential angle is a close approximation to the true angle.

To summarize, measurements of angular vibration can be made using conventional accelerometers by carefully choosing separation distance. The lower limit for separation distance is chosen based on acceptable low frequency signal-to-noise ratio and the upper limit is chosen based on acceptable high frequency flexural error.

Experience With Differential Angular Vibration Measurements

Angular vibration was measured on two different types of aircraft, a fighter and a helicopter, using differential accelerometers. Evaluation of those results are difficult because there are no accurate angular sensors with which to compare. Evaluation of differential angular measurements can proceed, however, by comparing the measurements one gets with different separation distances.

Angular vibration was measured on a fighter, using two separation distances as shown in Fig. 10. Preliminary calculations on the structural components of transducer locations according to Ref. [9] showed that frequencies from 40 Hz to 4000 Hz could be measured with acceptable accuracy. If the upper frequency flexural error is low, halving the separation distance should change the upper frequency response shape very little and the lowest frequency which can be successfully measured should be increased only slightly. However, the two separation distances were not about the same point on the aircraft. The measurements were taken from three colinear accelerometers and the two differential angles are for the outer two accelerometers in one case, and one of the outer accelerometers with the

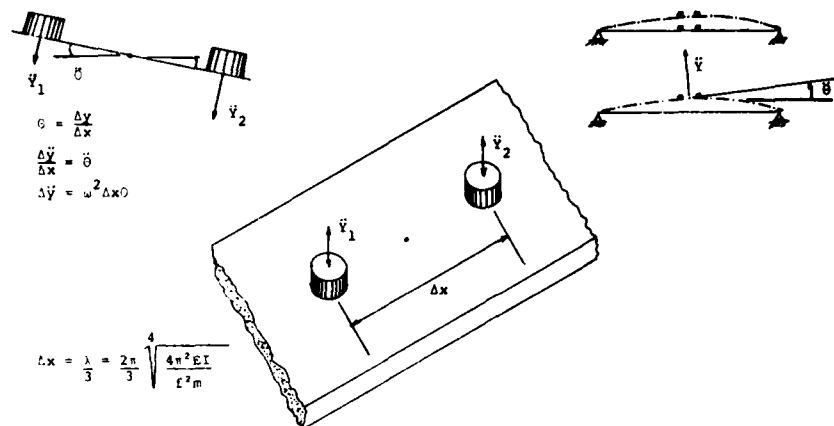


Fig. 9 - Linear accelerometer differential method angular vibration measurement.

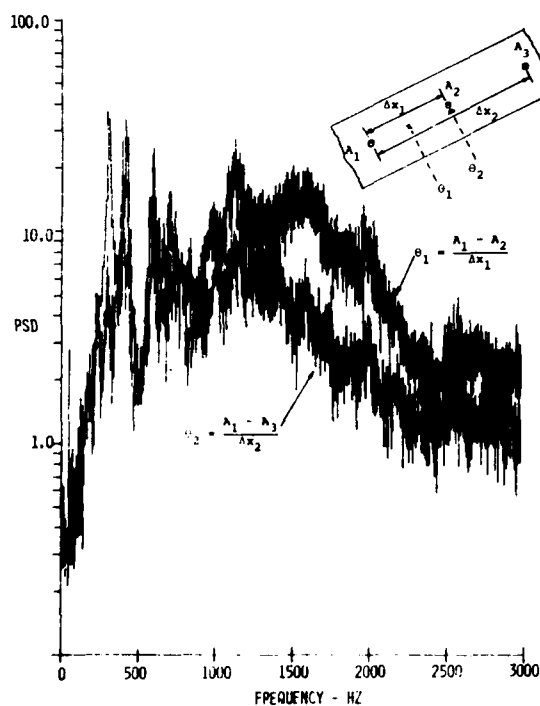


Fig. 10 - Angular vibration data obtained using differential accelerometers, two different separation distances, $\Delta x_1, \Delta x_2$ - fighter aircraft.

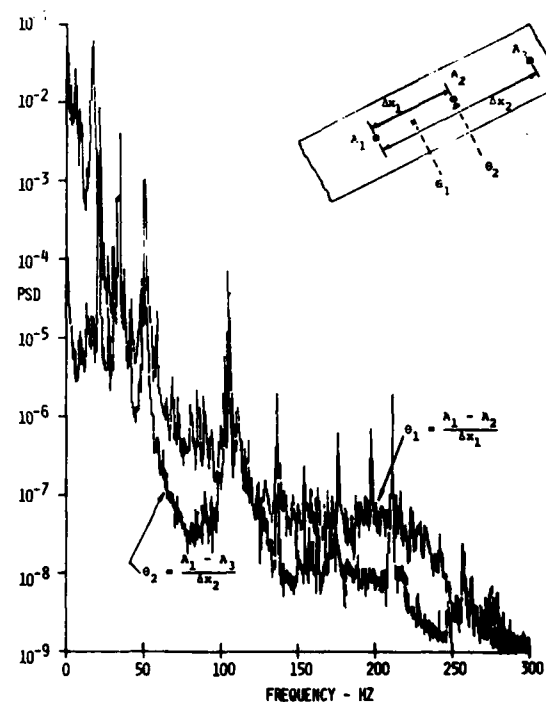


Fig. 11 - Angular vibration data obtained using differential accelerometers, two different separation distances, $\Delta x_1, \Delta x_2$ - helicopter.

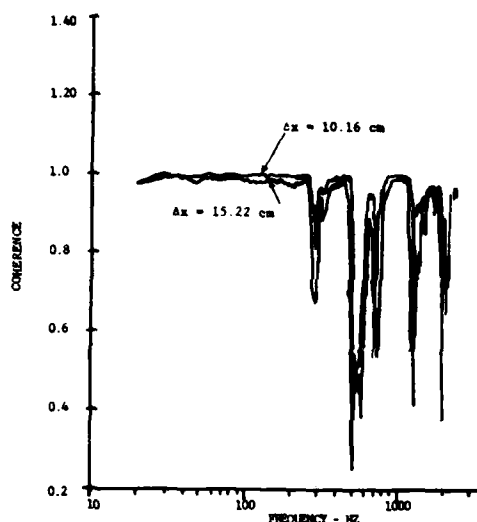


Fig. 12 - Coherence functions between two accelerometers attached to an experimental beam for two different separation distances.

center accelerometer in the other case. Fig. 10 shows good agreement between the two signals at frequencies greater than 100 Hz. Below 40 Hz the signal is essentially instrument noise.

Angular vibration was also measured on a helicopter using differential accelerometers with results for two separation distances given in Fig. 11. Preliminary calculations on the local structure around the transducer location indicated that vibrations at frequencies from 0.7 Hz to 200 Hz could be accurately measured. However, the two angular signals in Fig. 11 had the same problem as those of Fig. 10 in that they were not at the same point on the structure due to the colinear orientation of three accelerometers. Good agreement between the two spectrum shapes is indicated up to 250 Hz, but above this frequency the shapes deviate, indicating flexural error. (See Fig. 11). These results compare well with the preliminary calculations which yielded an upper frequency limit of 200 Hz.

Figs. 9 and 10 show that angular measurements using differential accelerometers can be successful. The two angular levels for both cases agree well in spectrum shape and the frequency limits indicated by the preliminary calculations were supported by the data. This apparent success does not imply that there is no longer any need for good, miniature angular vibration sensors, however. The efforts required to collect detailed structural information used in computing the separation distances frequently involves getting information from the Air Logistics Center servicing the aircraft

and is usually quite time consuming. There is still a very distinct need for acceptable angular vibration sensors.

COHERENCE FUNCTIONS AND DIFFERENTIAL ANGULAR VIBRATION MEASUREMENTS

In using differential accelerometers to measure angular vibration, there must be a continuing search for methods which can be used to evaluate the results. It has been suggested that the coherence function could be used for this purpose. The idea is that when there is flexure between two accelerometers used in measuring angular vibration, such flexure can be determined from the coherence. If that is true then one can always tell over which frequency range differential angular vibration data is acceptable without having to compute the upper separation distance limit from structural properties.

The coherence function may be used to: (1) detect linear relationships between excitations at two different locations, (2) detect structural transmission paths, and (3) predict errors in frequency response function estimates [10]. In addition, when the coherence is computed between two accelerometers it can be used to determine global and local modes. Coherence was calculated for two accelerometers attached to a simply supported beam excited with broad band random noise at mid span.

The coherence function for two random processes x and y is defined as [11].

$$\gamma_{xy} = \frac{|S_{xy}(\omega)|^2}{S_{xx}(\omega) S_{yy}(\omega)} \quad (4)$$

$S_{xy}(\omega)$ is the Cross-Power Spectral Density (PSD) between x and y

$S_{xx}(\omega)$ is the PSD at x

$S_{yy}(\omega)$ is the PSD at y

For the simply supported beam, the output PSD is

$$S_{xy}(\omega) = H(x, \omega) H^*(y, \omega) S_i$$

$H(x, \omega)$ is the beam frequency response function at x

S_i is the forcing function PSD

Therefore the coherence is

$$\gamma = \frac{[H(x, \omega) H^*(y, \omega) H(y, \omega) H^*(x, \omega)]}{[H(x, \omega) H^*(x, \omega) H(y, \omega) H^*(y, \omega)]} = 1. \quad (5)$$

Eq.(5) reveals that the displacements are fully correlated, independent of separation distance.

As verification of this, the coherence for an experimental simply supported beam under broadband excitation was measured and is shown in Fig. 12. The coherence of Fig. 12 shows deviations from the theoretical value of one only at the resonant frequencies, independent of separation distance. In fact, Fig. 12 reveals no distinct relationship between coherence and separation distance. The coherence function is identically one, deviating at resonance in Fig. 12 perhaps because of the finite bandwidth used in computing the Fast Fourier Transform.

CONCLUSIONS

Good aircraft angular vibration data are essential to the effective design and operation of aircraft optical packages. Of the six angular vibration sensors encountered during literature survey, only the ADA meets the requirements for angular vibration measurement. The ADA still has a serious limitation, however, in that its size renders its use on stiffened panels or other secondary structure questionable. The fact that the ADA is so bulky means that it can only be used with confidence on major structural components.

Differential accelerometers for measuring angular vibrations were used on two aircraft. The analysis consisted of measuring angular vibrations using two different separation distances and comparing the results. Agreement was sufficiently close to support the validity of differential angular vibration measurement. The coherence function was evaluated as a potential check for differential angular vibration measurement. There is still a distinct need for a miniature, sensitive, broadband angular vibration sensor.

REFERENCES

1. Lee, J. and P. W. Whaley, "Prediction of the Angular Vibration of Aircraft Structures," Journal of Sound and Vibration, Vol 49, no 4, pp 541-549, Dec 1976.
2. Canfield, E. B., Electromechanical Control Systems and Devices, John Wiley, 1965.
3. Sher, L., Angular Effects on a Telescope System, AFWL-TR-72-202, Feb 1973.
4. Honeywell, GG2500 Magnetohydrodynamic (MHD) Two-Axis Rate Sensor, A Technical Description, April 1974.
5. Whaley, P. W., and P. G. Bolds, "Test Report on Vibration Survey of the CH-3E Helicopter For the SAR-Retrans Guidance Test Program," AFFDL/FBG 77-1, May 1977.
6. Van der Linden, J. C., and H. A. Mensink, "Linear and Angular Position Measurement of Aircraft Components," AGARD-AG-160, Vol 8.
7. MacDonald, W. R., and D. W. Cole, "A Seismic Angular Vibration Transducer Employing a Gas Rotor," Royal Aircraft Establishment, RAE-TM-IR-128.
8. Dubrovin, G. N., S. P., Krasilnikov, "Angular Velocity Vibrometer," FTD-HT-23-2113-71 (June 1972). Edited translation of USSR Patent 250475 Pl-2, by Rene E. Convelle.
9. Whaley, P. W., and M. W. Obal "Measurement of Angular Vibration Using Conventional Accelerometers" Shock & Vibration Bulletin, No 47, pt 3, Sept 1977.
10. Gray, C. L., and A. G. Piersol, Methods for Applying Measured Data to Vibration and Acoustic Problems, AFFDL-TR-65-60, June 1965.
11. Bendat, J. S., and A. G. Piersol, Random Data Analysis and Measurement Procedures, New York 1971.

Discussion

Voice: You seem to have the biggest difference between θ_1 and θ_2 . What is the significance of that?

Mr. Obal: We measured the angular motion on a cargo deck and we have to assume the moment of inertia for a cargo deck on an aircraft. That is the hardest thing in this technique; you have to figure an average cross-sectional moment of inertia bending to get the traveling wave of the structure and I would primarily consider this difference to be the fact that we are measuring two different points on the structure.

Mr. Silver (Westinghouse): We are curious as to your experience with the use of coherence on the acceleration measurements. It looks like it would be a pretty powerful device to eliminate noise floor content.

Mr. Obal: That is a very good question. We are also looking at the angular coherence between two different points on a structure. That has really lead us to a dead end street. We talked to Julius Bendat about that since he is big on partial coherence theory; but given a frequency response function of structure, computing the coherence by dividing the cross PSD by the auto PSD squared hasn't shown us much. We have looked at separation distances on a simply supported beam between four inches and forty two inches and the coherence plots came out to be the same. The theory and the experimental data don't seem to show that that is a good approach, but we are doing it and we will continue to do it until we find a better way. We don't say this is the best technique; but since we don't have a small angular sensor we will have to use something else until industry develops one because we need an angular vibration data base. We need this data base to solve these problems and to check out our analytical prediction capabilities. We are considering finite elements for the low frequencies and statistical energy analysis for the high frequencies. I guess this is almost a plea to industry to give us a good angular broadband sensor capable of measuring down to less than 20 microradians.

Voice: Why does the sensor have to have the capability of measuring such small angles?

Mr. Obal: That is because of the accuracies that they would like in their electro-optical systems.

HIGH FREQUENCY GROUND VIBRATION MEASUREMENT

H. Nolle
Monash University
Clayton, Victoria, Australia

Recently interest has focused on ground transmitted vibration and noise from sources related to human activity such as mining and tunnelling work, as well as traffic and industrial plant operations. The disturbance thus generated contains low and high frequency Fourier components, and accurate measurement of the vibration requires recording of the signal free from harmonic distortion in the frequency range of interest.

This paper reviews the basic requirements for vibration transducer-to-ground coupling to ensure linear measuring *system* response. Results are presented of field tests of a range of different designs for ground attachments, and recommendations are made for procedures of ground attachment installation in different type soils and rock formations.

The techniques described are demonstrated with reference to some of the results of vibration surveys of three different railway track installations.

INTRODUCTION

The earliest application of ground vibration measurement appears to have occurred in the investigation of seismological and geophysical phenomena. These phenomena manifest themselves as low frequency displacements, mainly below 10 Hz, which can be recorded on instruments resting on a smooth surface that is connected to the ground mass. More recently, growing interest has focused on ground transmitted vibration and noise from sources related to human activity such as mining, quarrying and tunnelling work, as well as traffic and industrial plant operations. Measurements of such sources are made with the objective of establishing local vibration levels and ground transmission characteristics. The latter type disturbances usually - but not always - are of a transient or impactive (shock wave) character and contain low and high frequency Fourier components*. Accurate measurement of such signals requires recording free from harmonic distortion in the frequency range of interest. In this regard high frequency ground vibration measurements have

suffered less from limitations in transducer design than from unexpected - and often unknown - transducer to ground coupling effects. Current vibration transducer technology has virtually eliminated the problems associated with poor frequency response, sensitivity and linearity. On the other hand, the lack of definition of the impedance of the ground mass immediately surrounding the transducer in a field installation may render the measuring *system* frequency response characteristics unknown, which in turn has an equally debilitating effect on the measured data and any results of a subsequent data analysis.

This paper reviews the basic requirements for ground coupling to ensure linear measuring *system* response. Results are presented of field tests of a range of designs for ground attachments, and recommendations are made for procedures of ground attachment installation in different type soils and rock formations.

THE COUPLING PROBLEM

The evolution of ground surface vibration measuring instruments dates back to the beginning of the 19th century [1]. The earliest technologically significant devices were of the pendulum type, which recorded relative movement between the ground and a seismic mass of the instrument. These were

* The dividing line between "low" and "high" frequency is quite arbitrary, but, for practical reasons, may be put at about 30 Hz or the lower limit of the audio-frequency range.

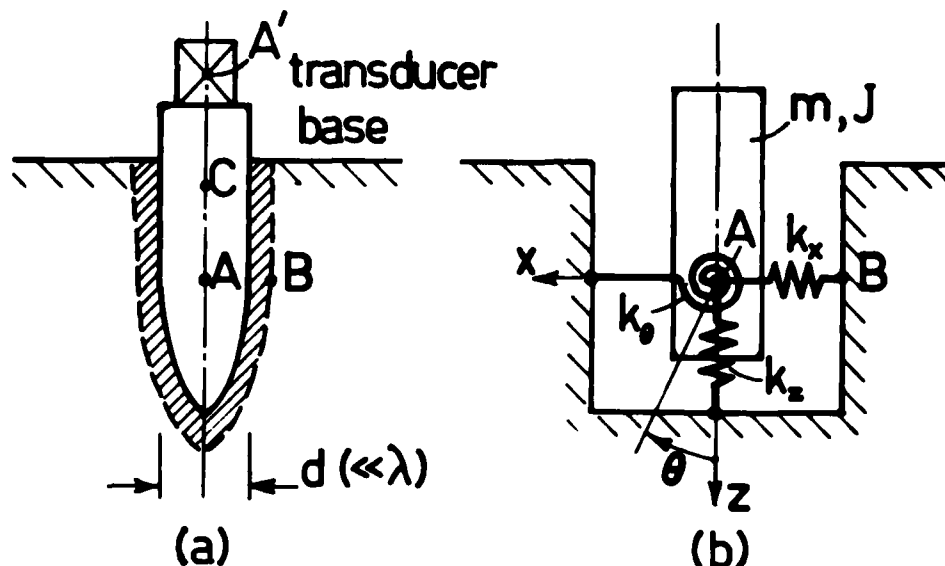


Fig. 1 (a) - Transducer and base installation
(b) - Dynamical model of (a)

complex fragile mechanical assemblages, sensitive to the environment, and little reliable information is on hand of their dynamic performance characteristics. Over a number of years these instruments have been supplanted by the compact, portable and simpler to use electro-mechanical transducer.

For proper operation the transducer and its casing should move in phase with and at the same amplitude of the ground particles immediately surrounding the transducer base. Fig. 1 (a) shows schematically a typical surface installation where the transducer casing is fixed to a rigid base which provides the mechanical coupling member to the ground. The base may take the form of a steel spike which is driven into the ground; however, use of such a device is not always possible and alternative techniques are then used. Point B, Fig. 1 (a), designates a particle of the undisturbed ground mass, whereas A is the origin of a coordinate system (x, z, θ) defining the motion of the base. Since A', the centre of sensitivity of the transducer, is usually above ground level, points A and A' do not coincide. The shaded area of ground shown between A and B represents a thin layer of the disturbed ground medium whose motion may be different from that at point B.

Assuming that the mass and stiffness properties are axi-symmetrical with respect to the z axis, the dynamic behaviour of the transducer-base assembly may be modelled as a rigid mass on elastic support, as shown in Fig. 1 (b). The model parameters are defined as follows:-

m = mass of transducer, base and equivalent mass of the surrounding

ground; centre of gravity at C ;

J = mass moment of inertia of m about an axis through A, normal to the xz plane;

$k_{x,y}$ = effective linear translational spring constants of disturbed ground layer ($k_x = k_y$) ;

k_θ = effective linear torsional spring constant of disturbed ground layer.

Whereas reasonably accurate estimates are possible for m and J , the stiffness parameters are affected by base geometry, soil properties and the technique of installation and it would hardly be possible to calculate reliable values for $k_{x,y}$ and k_θ . The base has three significant degrees of freedom and hence three natural frequencies of interest: two of these correspond to translational-rocking modes and one to an uncoupled mode in the vertical direction. Of these the lower of the rocking mode frequencies and the vertical mode frequency determine the frequency limits of linear system response.

For all practical purposes the typical dimension of the installation, d , is much smaller than the wave length of the ground vibration, λ , and the motion of the undisturbed ground at points A and B is in phase and of the same amplitude. Ideally, with the measuring system installed, points A and B should respond similarly, which is possible only when $k_{x,y}$ and k_θ are both infinite. As a result of intrusion through the ground surface layer the elastic properties of the ground around the base are modified, and

$k_{x,y}$ and k_g assume unknown finite values.

The need to reduce signal harmonic distortion resulting from inadequate ground coupling has been recognized previously. Warburton [4] reported an apparent transducer sensitivity to variations in mass m . Johnson [2] and Awojobi and Sobayo [3] suggest the method of "density matching" in which the average density of m is matched to that of the soil, and the transducer and protective casing is buried below ground level; the latter method has also been used by Kamperman [6], Balachandra and Malthan [7] and probably others. However, there is no documented evidence of the benefits derived by this technique. Moreover, the model of Fig. 1 (b) suggests, for best frequency response, the following base design criteria:

- (i) least values for m and J ;
- (ii) centre of gravity of m at A ; and
- (iii) a base-soil interface geometry and method of installation that give the highest $k_{x,y}$ and k_g ,

of which (i) and (iii) are in conflict with the density matching idea.

A factor that has not been taken into account in the model, but one that exerts a marked influence on the base frequency response, is the damping of the system. In a real installation the total damping is the resultant of material damping, frictional effects - largely at the interface - and geometrical damping. The latter constitutes a frequency dependent energy loss due to momentum transfer in the form of elastic waves radiated from the base into the ground mass. It has been shown theoretically [5] that for an infinite half-space this damping varies with the mode of oscillation and the mass ratio of the system. The mass ratio is a non-dimensional parameter, defined as $m/\rho l^3$, where ρ is the density of the ground and l is a characteristic dimension of the base. Quite generally, the smaller this ratio, the greater the damping effect; thus for lightly constructed bases the theory predicts a higher damping ratio which may approach, and in some cases exceed, critical damping. This has in fact been confirmed in some of the tests reported below.

BASE DESIGN AND PROCEDURES FOR INSTALLATION

The major difficulty of determining analytical natural frequencies of the base installation is the uncertainty of the values $k_{x,y}$ and k_g . Ground installations are affected by soil inhomogeneities, layering and nonlinearity effects for which the upper ground surface layers are notorious. Frequently access is possible only to areas where the ground has been previously disturbed or filled. In such cases and in cases where base installation causes fracture or crumbling of the medium no meaningful values can be assigned

to the elastic parameters and the system dynamic behaviour can be predicted by empirical methods only. To this end a series of base designs was tested for their ability to give undistorted signal transmission to as high an exciting frequency as possible. Relevant design data are shown in Fig. 2. The bases are all of steel, monolithic or welded; bolted or screwed joints not being recommended. Designs No.1 to 7 shown are bases of the "spike" type, having different effective densities, lengths and cross sections. Designs 8 and 9 are welded steel constructions having several prongs joined to a rigid base plate, whereas No.10 is a capped steel tube construction bonded to the ground mass by non-shrink grout. This latter principle has been applied successfully in mine blast vibration measurements [8]. In those tests a 4" Plexiglas cylinder was epoxied into the rock mass, forming the accelerometer base. Investigation of the base response showed that resonance was encountered, though at a quite high frequency (possibly at 10 kHz). This could possibly have been avoided had the plastic material been replaced by a steel base. While minimum mass is one of the design criteria, the bases have to possess the rigidity and the structural integrity to resist, without distortion, the rigours of being driven into the ground. In this regard particular caution should be exercised to protect and preserve the trueness of the mounting surface for the transducer.











The suitability of the different design bases has been assessed in conjunction with the type of ground surface layer in which the base is installed. This may be categorized in the following five classes:-

- (a) sand, silt, cohesionless soil;
- (b) fine sand/clay mixtures, cohesive soils, loamy sand, stiff clay;
- (c) soft weathered rock, mudstone, soft sandstone;
- (d) fine particle soils with dispersions of rocks and coarse gravel or aggregates (fills or natural mixes);
- (e) hard rock.

Testing experience with the various designs of Fig. 2 has shown that each class represents its own installation problems which have to be dealt with in different ways. Accordingly, a summary of the findings and recommendations relating to installation procedure are given in Table 1.

FREQUENCY RESPONSE TESTS

Dynamic tests were performed under field conditions to measure the natural frequencies of the base in the lower of the rocking modes and in the vertical mode. The base was excited using an electrodynamic exciter coupled to a point 10 mm above the top surface of the base. The total mass of the transducer, adapters and

											
Base Design No.		1	2	3	4	5	6	7	8	9	10
Heavy clay	H	+300	+360	+620	-660	+420	-780	-820	-620	+250	
	V	-580	-800	-660	-700	-800	-940	-650	-450	-520	
Sandy loam	H	-180	+ 80* -140	-260	+ 60* -180	-140	+110* -180	+ 75** -180	-160	+100	
	V	-180	-180* -320	-130	-190* -220	-140	-230* -300	-150** -230	-180	-140	
Sand (wet)	H						- 80		- 65		
Sand + loam mix H (dry, hard)						+400 +170+ +110+					
Mudstone	H										-1500
	V										>2000

* Top 125 mm above ground
 ** Top 100 mm above ground

+ Bond damaged (see Fig. 4)
 ++ Bond badly damaged

Fig. 2 - Linear frequency response limits (± 3 dB points) of various base designs in different ground. H and V designate response to horizontal and vertical forcing respectively. Construction details for bases are (dimensions are in mm):

1. 10 x 50 dia. top plate, 5 x 150 long tapered plate welded to form + section.
2. As per 1 above, 300 long.
3. 50 dia. x 150 long solid cone.
4. 50 dia. x 300 long solid cone.
5. As per 3 above, hollow.
6. As per 4 above, hollow.
7. 40 x 230 long, parallel hollow cylinder.
8. 10 x 115 square top plate, 5 x 40 x 150 T section legs.
9. 15 x 100 dia. top plate, 12 dia. x 65 legs on 80 P.C.D.
10. 20 dia. x 180 long capped tube in non-shrink grout.

TABLE 1
Recommended Procedures for Transducer Base Installation

Ground Class	Likely Problems	Recommended Method for Installation
(a)	Method of soil excavation and burial of transducer box unreliable. Impact of hammer-driven peg shatters bond. Cohesion of soil insufficient to support "spike" type base.	Use lightweight, maximum taper peg, No. 6 base. If cohesion insufficient (e.g. as in dry sand), use No. 8 base. Where no foothold can be established, cast slab of sand and epoxy mixture on formed depression in ground surface; glue on 6 mm steel base.
(b)	Hard (dry, cracked) clay subject to fracture and loss of bond; peg "bounce" damages bond.	In soft (wet) clay use parallel or slightly tapered peg of 230 mm maximum length. In hard clay use tapered peg of length not greater than depth of penetration. If formation too hard to penetrate, use method (c).
(c)	Too hard for driving peg; damage to peg; fissuring of rock; peg "bounce" damages bond. Too soft for expanding bolt anchorage.	Use masonry drill, brush clean walls of hole and vacuum clean, grout steel peg with non-shrink grout (design No. 10).
(d)	As for (a). Impact of point of peg on rock/gravel shatters bond. Damage to peg.	If rocks cannot be avoided, carefully excavate between rocks and use method (c), without drilling. Alternatively, use last of methods (a).
(e)	Formation too hard for penetration other than by rock drilling.	Use masonry drill and fit base plate with expanding bolt anchor, or use method (c). If rock face is dry and smooth, use epoxy glued 6 mm steel base.

force link was approximately 0.35 kg. Vertical or rocking mode excitation was applied in slow sine-sweep tests using a constant force amplitude. The line of action of the force was directed through point A' (Fig. 1), either vertically or horizontally.

For a second order linear system the acceleration response curve follows, starting at the low frequency end, an asymptote sloping at 40 dB/decade, then rises steeply to reach resonance (if damping ratio is low), and thereafter falls to approach a second asymptote which is a constant level line. An idealized response curve of this kind is shown in Fig. 3. The lower curve in the Figure shows the corresponding response of a highly damped system.

For comparison, a selection of response curves from the field tests is given in Fig. 4. From the shape of some of these it is apparent that in some tests damping ratios of the order of 1, or greater, were obtained. When the damping is high, deviation from the 40 dB/decade line is seen to be negative, i.e. transmissibility never rises above 1 but simply diminishes with increasing applied frequency.

The frequencies at which deviation from true linear response first reaches ± 3 dB are given in Fig. 2, the \pm signs indicating whether the response rises above or falls below that expected.

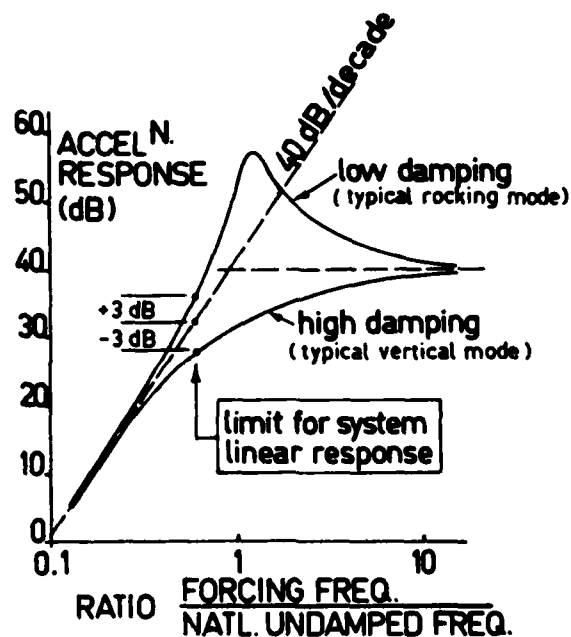
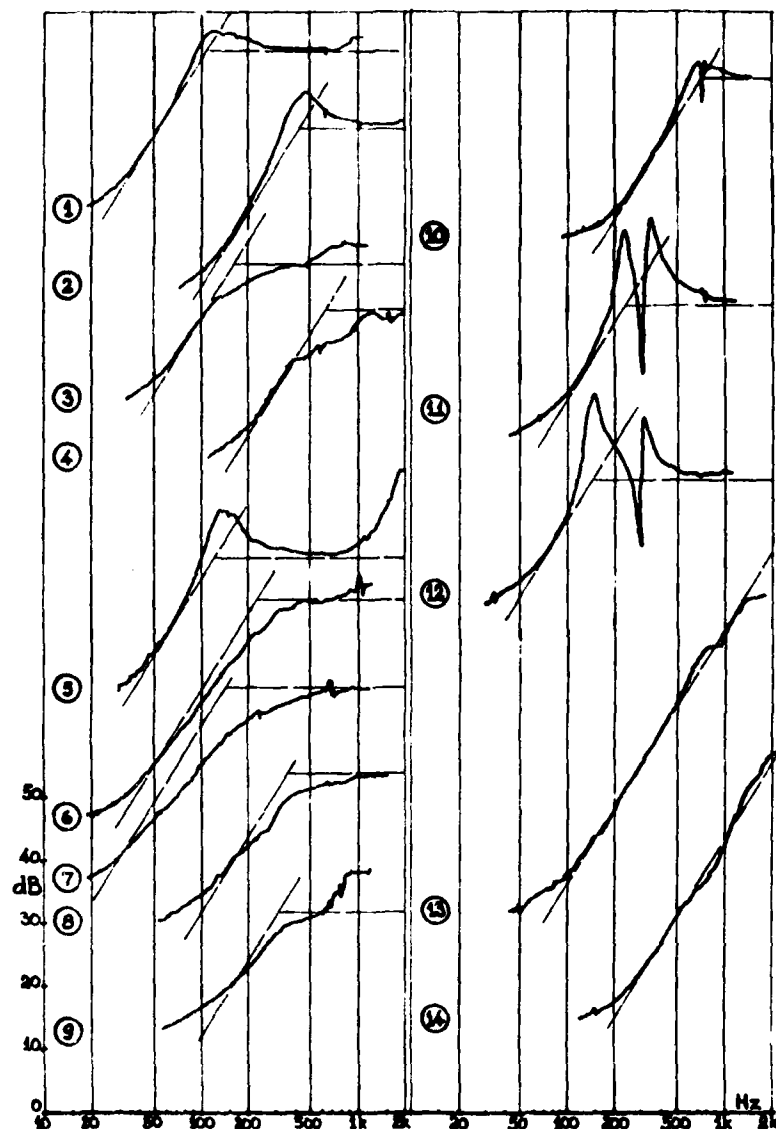


Fig. 3 - Response of linear 2nd order system to harmonic force excitation



Graph No.	Base No.	Direction of Force	Type of Ground	Remarks
1	9	H	Sandy loam	Typical lawn topsoil; ground wet.
2	9	H	Heavy clay	Wet (drying out, shrinking).
3	9	V	Sandy loam	As for graph 1.
4	9	V	Heavy clay	As for graph 2.
5	6	H	Sandy loam	Top of base 125 mm above ground.
6	6	H	Sandy loam	Base fully in ground.
7	6	H	Wet sand	
8	6	V	Sandy loam	Top of base 125 mm above ground.
9	6	V	Sandy loam	Base fully in ground.
10	5	H	Sand + loam	Dry, hard sand + loam mix; good bond, ground slightly cracked.
11	5	H	Sand + loam	As for graph 10; bond damaged by lateral hammer blow applied to base.
12	5	H	Sand + loam	As for graph 10; bond badly damaged.
13	10	H	Mudstone	
14	10	V	Mudstone	

Fig. 4 - Typical acceleration vs. frequency curves for different ground conditions

DISCUSSION OF RESULTS

For almost all of the base-ground combinations tested the system transmissibility was found to be most sensitive to frequency under horizontal forcing. The first rocking mode natural frequency could, in most cases, be identified from the peak in the response curve. This was not the case with vertical mode oscillation which appeared to be heavily damped, there being no clearly defined maximum. Similarly, the combination of the effect of damping and the apparently high value of the second rocking mode frequency precluded identification of the latter.

The frequencies given in Fig. 2 show the limits of linearity, within ± 3 dB, of the system response. These frequencies provide a fair basis for comparative assessment of the various designs; but the final choice of base design for a critical application would need to be made taking into account ground conditions and the desired degree of damping (i.e. whether error of measurement is preferred to be +ve or -ve). The general trend observed from the tests in all soils was that damping in the vertical mode is significantly greater than in the rocking mode. In the former case the deviation from linear response was always -ve, whereas in the rocking mode the damping varied depending on the base design and condition of installation. Thus the multi-pronged designs (Nos. 8 and 9) have a characteristically high damping whereas the shorter pegs and pegs rising above ground surface have the lowest system damping. The high damping of the vertical mode is believed to be due to slip at the peg-soil interface. On theoretical grounds, there is also supportive evidence that the vertical mode oscillation is subject to greatest geometrical damping [5, p.199].

Of particular importance to good frequency response were found to be two parameters. One is the taper of the peg; the tapers used in the test series are zero for design No. 7, 1:22 in the case of the 300 mm circular cross-section pegs (Nos. 4 and 6), and 1:10 for the 150 mm circular cross-section pegs (Nos. 3 and 5). For cohesionless and dry, brittle soils the taper used should be a maximum that still permits driving the peg without bounce or deep cracking of the soil. In heavy wet, shrinking (drying) clay increasing the taper does not seem to have the same beneficial effect.

The other parameter is the depth of the driven peg. The cantilever effect of the unsupported mass above ground level of an incompletely driven peg is most detrimental to good frequency response. This is visible from the results of Fig. 2 for some of the pegs in sandy loam. It follows that the length of the peg should be made no greater than the depth to which the peg can be driven.

However, the principle of using maximum taper and maximum depth drive was found to have

its limits in that too much taper and/or too forceful driving will cause loss of bond or fracture of the ground, particularly around the upper part of the peg. The effect of this is shown in the data for the 150 mm peg in a dry, hard sand and loam mix. The fully driven peg in slightly cracked sand gives linear response to 400 Hz. With slightly damaged and badly damaged bond the corresponding frequency for this peg reduces to 170 Hz and 110 Hz, respectively (see also Fig. 4). In general, the effect on the limiting frequency of loss of bond around the upper part of the peg is similar to that of the cantilevered part of an incompletely driven peg.

The purpose of the taper is, of course, to generate a higher contact pressure at the peg-soil interface, hence increase the values of the parameters $k_{x,y}$ and k_{θ} . By comparison, the role of the effective density of the base (defined by parameter m) appeared to be a relatively minor one, to the extent that it became obscured by the random, unavoidable variations in bond effectiveness in the series of field installations tested.

These findings are in general agreement with the conclusions of Balachandra et al. [7], drawn from their experimental and analytical work on ground motion measurement in vertical boreholes. Though different to this work - in respect of mode of excitation of the system (detonation above ground surface, hence impulsive) and positioning of the accelerometer (subterranean) - Balachandra's experiments revealed that good interface bond between the borehole grout and the free-field medium is the primary requirement for ensuring the fidelity of acceleration measurement. Moreover, it was observed that mismatch in the impedances of the borehole grout and the free-field material could be tolerated if a *non-slip* interface can be maintained between them.

APPLICATION TO TRAFFIC-INDUCED VIBRATION MEASUREMENT

The techniques described in this paper are now demonstrated with reference to some of the results of vibration surveys of three different railway track installations. The main source of ground vibration from transit train operations is the rolling impact at the wheel-rail interface. In the frequency spectrum so generated identification of the various frequency components is based on accurate data of vibration at the rail, the supporting track and the subgrade in the vicinity of the track centre line. From this a picture may be built up of the vibration near field, and the effectiveness of the various structural components of a track system may be assessed for their ability to limit vibration at the source and to control transmission of vibration to the surroundings. However, the highest demands in fidelity of signal reproduction arise in ground-borne noise studies. Thus

sound radiated from free surfaces excited by ground-transmitted vibration may have a significant spectrum extending to 800 Hz and above.

The major features of the three different design concepts for the tracks are depicted in Fig. 6. Design (a) is a conventional ballasted track on subgrade, with spiked rails on timber sleepers; (b) incorporates resiliently supported concrete sleepers set in a continuous reinforced concrete slab cast on subgrade. The rails are secured to the sleepers by a resilient direct fixation fastener system. The design (c) is based on the 'floating slab' concept and features heavy concrete slabs on natural rubber isolators. The rails are elastically mounted on the slabs by means of direct fixation fasteners.

A quantitative evaluation of the vibration performance of these systems necessitates accurate measurements of vibration of the ground mass surrounding the track. Following an assessment of the ground conditions and the requirements in respect of frequency response of the measuring system, design No. 10, Fig. 2, was chosen for all ground vibration measurements. Additional accelerometers were installed on the rail support system to monitor track component vibration levels.

As the train passes a point on or near the track a vibration pulse is generated at that point. The instantaneous strength of the pulse varies with the approach and departure of each car bogie. Such a pulse, measured at the rail head, sleeper, concrete slab and the ground at some distance from the track centre is shown in Fig. 5. These records refer to design (b), Fig. 6, but substantially similar pulse profiles are obtained from the other two track designs.

The vibration levels are total signal strength (RMS), shown on a dB scale, unreferenced. The 14 bogies of the seven cars of the train may be seen to generate 14 major peaks of differing intensity which is characteristic of the particular bogie of the train. Reproducibility of the results is demonstrated in graph (C) where the records for tests 15 and 27 refer to different runs of the same train in the same direction. The quality of reproducibility further suggests the possibility of vibration "signature" analysis as a technique for monitoring some aspects of bogie performance and soundness of mechanical condition of the wheels.

The spectral content of the ground vibration at points 5 m from the respective track centre lines is shown in Fig. 6. These spectra confirm the existence of significant ground vibration components up to at least the 500 Hz octave band, and have been used in a vibration performance evaluation of the three track designs.

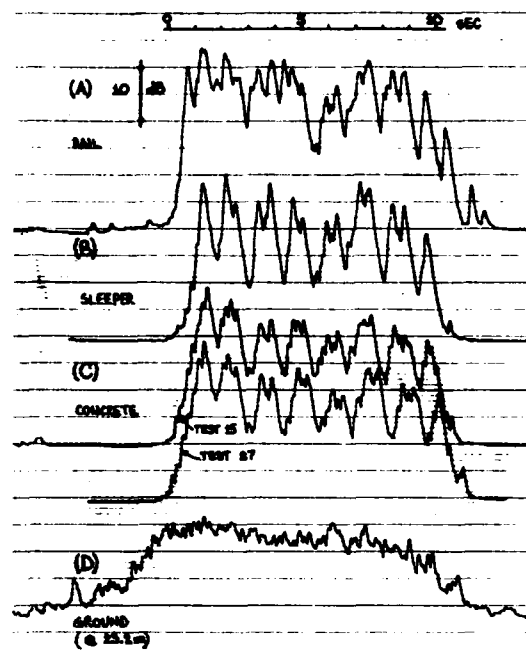


Fig. 5 - Acceleration pulse from train pass measured on resiliently supported track. Tests 15 and 27 refer to the same train travelling in the same direction.

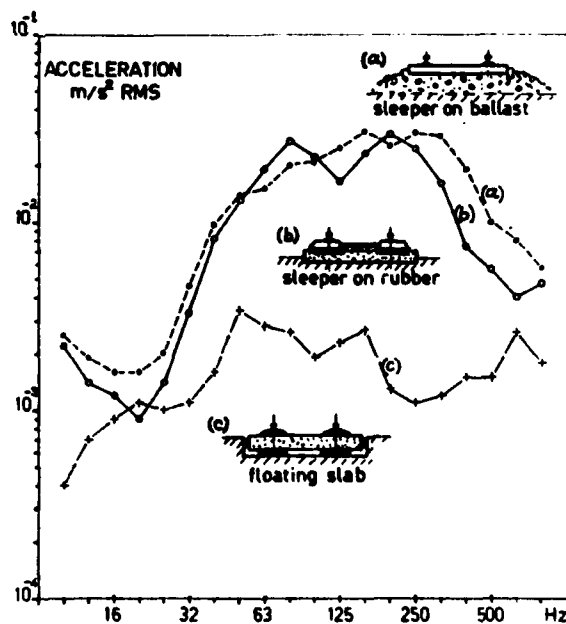


Fig. 6 - $1/3$ -octave spectrum of ground acceleration in the range 8 Hz to 800 Hz centre frequencies. Measurements refer to a position 5 m from the track centre line.

CONCLUSIONS

It has been shown that high frequency ground vibration measurements may be subject to errors caused by inadequate dynamic coupling of the transducer to the ground. A range of designs for transducer bases has been field tested in different soils and their performance is evaluated. The results of these tests suggest that the base response is satisfactorily modelled by a linear 2nd order spring-mass system.

Recommendations based on the writer's experience are given for base installation in different soils and rock. The final choice for method rests with the field engineer, however, in view of the wide fluctuation of soil properties and site conditions which may affect the vibration measurement.

The results of tests in cohesionless soils have indicated a need for further development of the technique to improve both quality and *reliability* of the measured data.

REFERENCES

1. J. WARTNABY. Seismology: Historical Survey and Catalogue, Her Majesty's Stationery Office, London, 1957.

Discussion

Mr. Ramboz (National Bureau of Standards): The material from which these were made appear to be a cast iron or steel, is that correct?

Mr. Nolle: All installations were made of steel. We used welded machined installations. We do not recommend bolted or screwed joints. They always lead to problems.

Mr. Ramboz: Are there any advantages to using a lighter material such as the harder aluminum alloys or perhaps beryllium?

Mr. Nolle: I suppose you can go to extremes, but I don't think it is necessary. We found in tests with the solid and hollow spikes of circular cross section that there wasn't very much difference between the two. Yes, you are quite right, in theory we should make the mass as small as possible. But once you have designed what might be termed a light weight construction you should concentrate on installation and this is where the problem lies.

Mr. Ramboz: Has any thought been given to the possible use of impedance techniques to try to optimize these?

2. C.F. JOHNSON. Coupling Small Vibration Gauges to Soil, Seismological Soc. of Amer., Eastern Section, Earthquake Notes, v.33, 1962, pp 40-47.
3. A.O. AWOJOBI and O.A. SOBAYO. Ground Vibrations due to Seismic Detonation in Oil Exploration, Earthquake Engineering and Structural Dynamics, v.3, pp 171-181, 1974.
4. G.B. WARBURTON. Transmission of Vibrations, Proc. Symp. Vibration in Civil Engineering, London, April 1965, Butterworths, London, 1966, pp 43-59.
5. F.E. RICHART, J.R. HALL, and R.D. WOODS. Vibrations of Soils and Foundations, Prentice-Hall, Inc., Englewood Cliffs, 1970.
6. G.W. KAMPERMAN. Vibration Isolation Effectiveness of Inertia Pads Resting on Soil, Jnl. Spacecraft and Rockets, v.2, n.2, 1965, pp 182-186.
7. M.B. BALACHANDRA and J.A. MALTHAN. Grout-Soil Interaction and Ground-Motion Measurement, The Shock and Vibration Bull., n.47, pt.3, Sept. 1977, pp 117-125.
8. J.J. OLSON, R.A. DICK, J.L. CONDON, A.D. HENDRICKSON, and D.E. FOGELSON. Mine Roof Vibrations from Underground Blasts, Report No. 7330, U.S. Dept. of the Interior, Bureau of Mines, Washington, 1970.

Mr. Nolle: Again, I would say that in theory you could use this. The problem is that we know very little if anything about the properties of the ground, especially the thin layer surrounding the spike, and I feel from experience that it is very hard to establish this data. The only thing you can do is to instrument the system and test it because there is no way to get the mechanical impedance data and use it to calculate the system response.

Mr. Ramboz: Either for optimization of your pads or for computing transmissibility across the soil through your interface?

Mr. Nolle: Well the optimum conditions that I have stated in my summary are that you should minimize the mass and the moment of inertia and you should lower the center of gravity to the point "A", which was the elastic center of support so that you in effect remove the rocking or the rotational motion from the system. But you can appreciate the problem, you can't go below ground level, it is very difficult to go below ground level so you always have an extended structure which is usually cantilevered.

THE RECIPROCITY CALIBRATION OF VIBRATION STANDARDS
OVER AN EXTENDED FREQUENCY RANGE

R. R. Bouche
Bouche Laboratories
Sun Valley, California

Reciprocity calibrations are performed at various frequencies up to 10,000 Hz using an air-bearing shaker with a built-in primary standard accelerometer. The shaker is used for sensitivity and frequency response calibrations on other accelerometers and velocity pickups in the range of 10 Hz to 10,000 Hz and up to 50,000 Hz for resonance frequency calibrations.

INTRODUCTION

Early reciprocity calibrations were performed on individual velocity pickups by Trent (1) and London (2). This was followed by the Levy and Bouche (3) paper on the reciprocity calibration of a velocity pickup built into a shaker. This paper included the development of the reciprocity theory. Later Bouche (4) developed a weighted least squares theory for processing the data to improve the calibration accuracy.

Bouche and Ensor (5, 6) converted the theory of the reciprocity calibration from velocity pickups to accelerometers attached to an electrodynamic shaker. This theory was a simplification of the previously published papers (3, 4), because these reciprocity calibrations were limited to the single frequency of 100 Hz.

Most reciprocity calibrations have been performed on an accelerometer attached externally to the armature of a shaker. Improved accuracy of the reciprocity calibrations is achieved by using an accelerometer built permanently into the shaker. This improvement actually comes from the design of the primary accelerometer standard built into the shaker to achieve very high resonance frequencies both in the standard accelerometer and also in the armature of the shaker. The characteristics of this high frequency shaker are described in reference (7). The purpose of this paper is to describe the reciprocity calibration at

frequencies to 10,000 Hz. This is an absolute calibration method. Its traceability to the National Bureau of Standards is accomplished through measurements of mass, frequency, transfer admittance and voltage ratio. The reciprocity calibration eliminates the need to perform comparison calibrations to demonstrate the accuracy and traceability of primary vibration standards.

The comparison calibration method (8) is used extensively to calibrate test accelerometers, velocity pickups and other vibration instruments in everyday use in various testing and calibration laboratories. The reciprocity calibrations are intended mostly for the primary vibration standard prior to using it for performing the comparison calibrations. The reciprocity calibration on the primary vibration standard should be performed about once each year. This practice enables each calibration laboratory to maintain a history on its standard to demonstrate that no significant changes occur in the acceleration sensitivity.

PRIMARY STANDARD AND SHAKER

The primary vibration standard consists of a piezoelectric accelerometer built into a beryllium alloy shaker armature.

The resonance frequency of the beryllium alloy armature including the driver coil is approximately 50,000 Hz. Experience in using this shaker indicates the presence of another resonance

frequency at approximately 80,000 Hz. It is expected that this is the resonance frequency of the accelerometer built into the armature. The shaker armature is guided in an air-bearing based upon a shaker designed with a ceramic armature, Dimoff (9). The mass of the armature is supported by three rubber O-rings. The purpose of the air-bearing is to virtually eliminate transverse motion and acceleration waveform distortion when using the shaker at frequencies from 10 Hz to 10,000 Hz. The absence of acceleration waveform distortion is also due to the high resonance frequencies of the beryllium alloy armature. Another characteristic of this armature is that it provides a shaker capability for measuring the resonance frequencies of test accelerometers up to 50,000 Hz (10). These performance characteristics and design features of the shaker provide a primary vibration standard which makes it practical to perform accurate reciprocity calibrations at virtually any frequency of interest to 10,000 Hz.

RECIPROCITY CALIBRATION EQUATIONS

The sensitivity of a velocity standard is derived in reference (3). Simply by making use of the relationships for sinusoidal velocity and acceleration and the acceleration of gravity results in the following equation for the sensitivity of an accelerometer standard.

$$S_a = 2635 \left[\sqrt{\frac{J_R}{J_T}} + Q \sqrt{\frac{J_R}{J_T}} \right] \quad (1)$$

where

- S_a = sensitivity of the primary accelerometer standard, mV/g
- J = transfer admittance intercept (the intercept of the plot of mass/transfer admittance ratio, lbf/mho (N/mho) where transfer admittance ratio is the driver coil current/primary accelerometer voltage output, and mass refers to ten 20 to 200 gram values used for the reciprocity calibration.
- Q = slope of the plot of the mass/transfer admittance ratio, mho.
- R = voltage ratio, voltage output of accelerometer standard divided by the voltage output of the shaker coil when the shaker is driven by a second beryllium alloy shaker armature and the first driver coil is open circuit.

- j = the 90° vector, $\sqrt{-1}$
- f = frequency at which the transfer admittance and voltage ratio are measured, Hz.
- W = mass of test accelerometer subsequently attached to the primary vibration standard shaker during comparison calibrations, lbm(kg).

At most of the calibration frequencies the phase angle for the transfer admittance ratio is 0° and, for the voltage ratio it is 90°. A phase meter is used to measure the angles and verify these values. Variation from these values occurs at the higher calibration frequencies above 5,000 Hz and also below 50 Hz due to the effects of the resonances. Particularly at frequencies near and above 5,000 Hz it is necessary to separate the transfer admittance ratio into its real and imaginary parts. Both the intercept and slope of the real and imaginary parts of J are determined from the following equations based upon the weighted least squares procedure developed in reference (4). At lower frequencies it is only necessary to determine the real part of J since the imaginary part of J and slope Q have negligibly small values.

$$J_R = 0.0420408 \sum n^2 Y_{nr} - 0.1138536 \sum n^2 W_n Y_{nr} \quad (2)$$

$$J_i = -0.0420408 \sum n^2 Y_{ni} + 0.1138536 \sum n^2 W_n Y_{ni} \quad (3)$$

$$Q_R = -0.1138536 \sum n^2 Y_{nr} + 0.3286387 \sum n^2 W_n Y_{nr} \quad (4)$$

$$Q_i = 0.1138536 \sum n^2 Y_{ni} - 0.3286387 \sum n^2 W_n Y_{ni} \quad (5)$$

where

- n = integers from 1 to 10 corresponding to the number of masses used during the transfer admittance measurements
- W_n = mass values expressed in English units, lbm corresponding to mass values ranging from 20 to 200 grams
- Y_{nr} = real part of the mass divided by the difference of the transfer admittance measured with the mass attached minus the transfer admittance measured with the mass not attached to the shaker
- Y_{ni} = imaginary part of the mass divided by the difference of the

transfer admittance measured with the mass attached minus the transfer admittance measured with the mass not attached to the shaker.

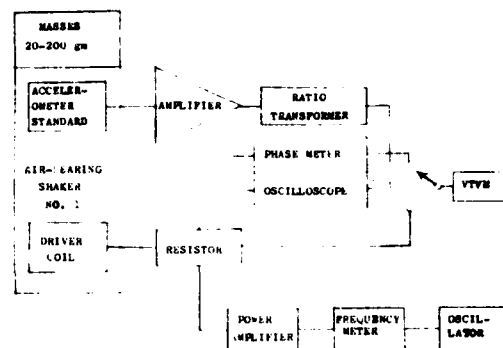
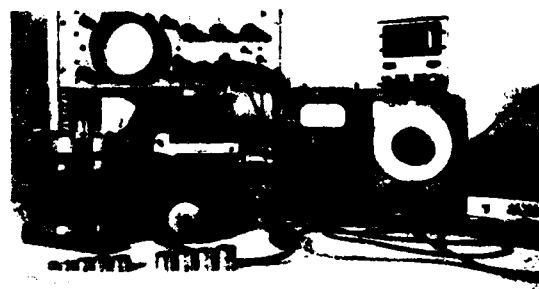
The equations described above use English units of pounds for mass because these are based upon previously published papers (3,4) using English units. However the final reciprocity calibration results are given in units of grams for the mass of test accelerometers attached to the shaker when performing comparison calibrations.

RECIPROCITY CALIBRATION PROCEDURE

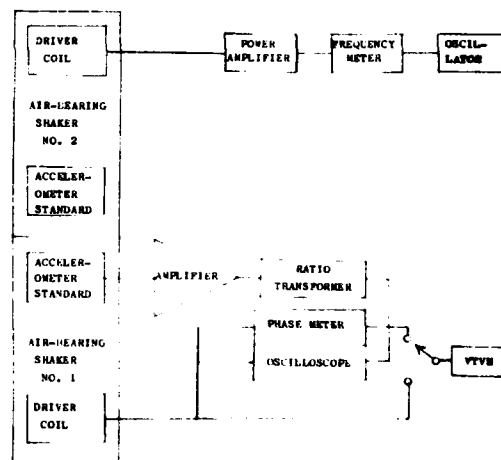
The reciprocity calibration procedure consists of making the transfer admittance and voltage ratio measurements using the instruments illustrated in Fig. 1(a) and (b). These instruments include an audio oscillator, power amplifier, air-bearing primary vibration standard - shaker, voltage ratio transformer, phase meter, vacuum tube voltmeter, frequency meter and oscilloscope. During the transfer admittance ratio measurements a precision 1-ohm resistor is put in series with the driver coil of the shaker. Prior to performing the reciprocity calibration, the ten masses in equal increments from 20 to 200 grams are sealed on a scale balance. The calibration is performed with the charge amplifier used as a system with the primary standard accelerometer. The frequency meter is used to measure and maintain the frequency at the desired values when making both the transfer admittance and voltage ratio measurements.

Consider the calibration at 1,000 Hz for example. It is performed by connecting the ratio transformer across the output of the accelerometer amplifier and adjusting the transformer until its output exactly equals the output across the 1-ohm precision resistor as indicated by a reading on the vacuum tube voltmeter. This measurement is repeated with each of the 10 masses attached to the armature of the shaker and also with no mass attached. These transfer admittance measurements are repeated at each of 10 different calibration frequencies from about 30 Hz to 10,000 Hz.

The calibration setup is changed to measure the voltage ratio. Care is taken to make use of the frequency meter to measure the voltage ratio at the same frequency at which the transfer admittance measurements are made. A special fixture is used to align the armature of two air-bearing shakers.



(a)



(b)

Fig. 1 (a) Photograph and block diagram used for making the transfer admittance measurements, (b) block diagram used for making the voltage ratio measurements.

The stator of one of the shakers is set aside so that the two armatures, rigidly connected together, are guided by the air-bearing stator of the other shaker. The driver coil of the shaker on which the transfer admittance measurements are made is now virtually open circuit. Both the outputs of this driver coil and the output of the ratio transformer connected to the accelerometer amplifier are sequentially connected to the vacuum tube voltmeter until both of the outputs are equal. The output of the ratio transformer is made equal to the output of the driver coil by making adjustments to the dial settings on the transformer.

At 1,000 Hz and most other calibration frequencies it is necessary only to determine the real part of the transfer admittance intercept as described by equation (2). It is necessary to determine the difference between the transfer admittance measured with each mass and with no mass attached to the armature and to multiply the inverse of this difference by the mass used, by the square of the mass used and by the square of the integer as indicated by the terms in equation (2). At higher frequencies such as 5,000 Hz, 8,000 Hz and 10,000 Hz it is necessary to separate the transfer admittance measurements into the real and imaginary parts and perform the computations as indicated in equations (2), (3), (4) and (5).

RECIPROCITY CALIBRATION RESULTS

In addition to performing the computations in accordance with these equations it is useful to plot the results at some of the frequencies as indicated in Figs. 2 and 3.

Fig. 2 shows that the mass/transfer admittance ratio is virtually constant for all masses used when performing the calibrations at most frequencies including 1,000 Hz. At the higher frequencies such as 10,000 Hz Fig. 3, there is a slope for the plot of mass/transfer admittance ratio for both the real and imaginary parts of these measurements. Both the real and imaginary parts of the mass/transfer admittance difference are used to determine the real and imaginary parts of the intercept J and slope λ as indicated by equations (2), (3), (4) and (5). The real and imaginary parts of J and λ are combined and then used in equation (1).

The voltage ratio measurements are given in Fig. 4. It is important that the phase angle be close to 90° throughout the calibration frequency

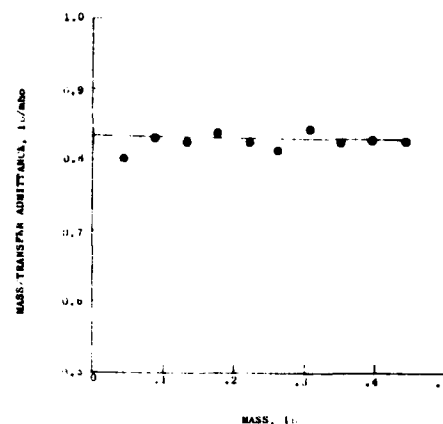


Fig. 2 Results of ratio of weight to transfer admittance difference at 1,000 Hz.

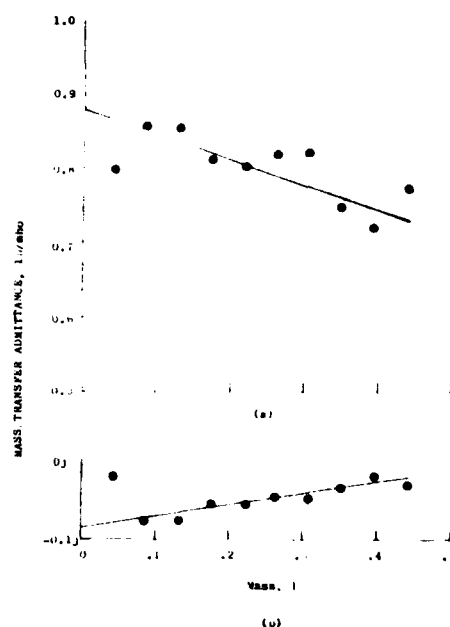


Fig. 3 (a) Real and (b) imaginary parts of ratio of weight to transfer admittance difference at 10,000 Hz.

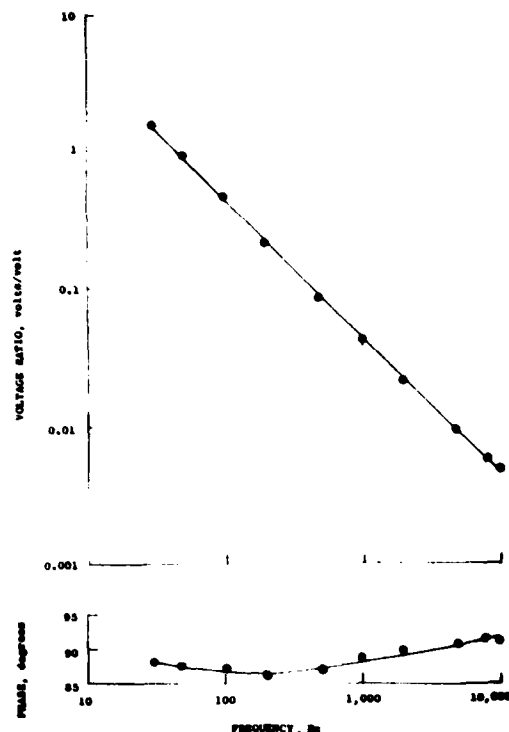


Fig. 4 Magnitude and phase angle results of voltage ratio measurements.

range to 10,000 Hz. Using a shaker designed so this phase angle is close to 90° makes it possible to maintain small calibration errors. This is accomplished by using the calibration shaker having a resonance frequency near 50,000 Hz.

PRIMARY STANDARD SENSITIVITY

The sensitivity of the primary vibration accelerometer standard is plotted in Fig. 5. Each sensitivity plotted is obtained by performing the reciprocity calibration. There are different values for the sensitivity at frequencies of 5,000 Hz and above depending upon the mass of the test accelerometers to be attached subsequently when performing comparison calibrations. These different sensitivities vary by only about 1 to 4 percent depending upon frequency and mass of the test accelerometer. It is expected that the decrease in sensitivity with mass of the test accelerometer is the result of relative motion between the accelerometer built into the armature and the motion of the mounting surface to which test accelerometers are

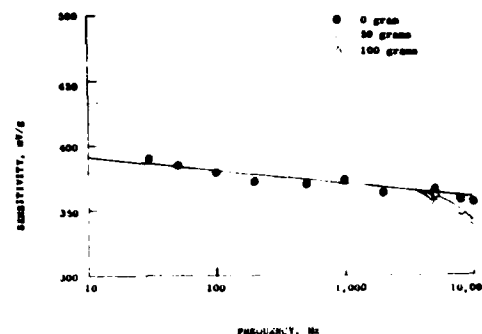


Fig. 5 Sensitivity of a primary vibration standard determined by the reciprocity method at frequencies to 10,000 Hz.

attached. This variation of sensitivity is one of the important results of the reciprocity calibration. Other techniques for determining the change in sensitivity as a function of test accelerometer mass are difficult to perform with reasonable accuracy. The sensitivities indicated in Fig. 5 show a decrease of somewhat less than 1 percent for each octave increase in frequency. This decrease in sensitivity is characteristic of accelerometers made with lead zirconate titanate ceramics. Other ceramic materials, also used in the air-bearing vibration standard shakers, have a smaller change in sensitivity with frequency. Although the frequency characteristics is improved with these other materials, the sensitivity has a much smaller value. Good calibration results are obtained when using different piezoelectric materials to build the accelerometer into the armature of the primary vibration standard shaker.

The use of the reciprocity calibration method is limited at frequencies below 30 Hz depending upon the stiffness of the suspension used to support the dead weight of the shaker armature. Accordingly, it is desirable to use the absolute optical method (8) at these low frequencies. However, if it proves desirable to perform reciprocity calibrations at these very low frequencies it would merely be necessary to install rubber O-rings having a smaller stiffness.

RECIPROCITY CALIBRATION ACCURACY

The analysis of calibration errors in the Table is similar to that given previously (5, 6). The root sum of the squares of the individual

Table - Reciprocity Calibration Errors in Determining the Sensitivity of Primary Vibration Standards with an Air-Bearing Shaker

Measurement	Errors at 100 Hz - 2,000 Hz	Errors at <100 Hz >2,000 Hz
	percent	percent
Mass	0.05	0.05
Transfer Admittance Intercept	0.2	1.0
Voltage Ratio	0.2	1.0
Distortion	0.1	0.3
Frequency	0.05	0.05
Accelerometer Effects, Transverse Sensitivity, Strain, Temperature, etc.	0.2	0.2
Amplifier Effects, Gain, Stability, Source Capacitance, etc.	0.3	0.3
Estimated Error*	0.5	1.5

*Determined from the square root of the sum of the squares of the individual errors.

Measurement errors is 0.5 percent at calibration frequencies in the range from 100 Hz to 2,000 Hz. The uncertainty increases at other frequencies with a RSS error of 1.5 percent. These small reciprocity calibration errors are due primarily to the performance characteristics of the primary vibration standard shaker. The high resonance frequencies of the shaker account for the accuracy during the transfer admittance and voltage ratio measurements at high frequencies. Other factors contributing to the accuracy include the absence of transverse motion and waveform distortion. It is necessary to have these shaker performance characteristics in order to achieve reciprocity calibration errors comparable to the errors in the primary standard accelerometer and charge amplifier.

SUMMARY

The work on performing reciprocity calibrations on primary vibration standards cover almost an uninterrupted period of twenty-five years. During that time the improvements made were primarily in changing from a velocity pickup standard to a piezoelectric accelerometer standard and, most importantly, by improving the performance characteristics of the calibration shakers. These improvements have extended the frequency range for performing reciprocity calibrations with reasonably small errors. The air-bearing primary standard-shaker is suitable for performing accurate reciprocity

calibrations to 10,000 Hz. These calibrations should be performed prior to using the vibration standard-shaker to perform comparison calibrations on various test accelerometers, velocity pickups and other vibration measuring instruments. In addition to performing these comparison calibrations, the standard shaker is used to determine resonance frequencies up to 50,000 Hz on test accelerometers.

REFERENCES

1. H. M. Trent, "The Absolute Calibration of Electromechanical Pickups," J. Appl. Mech., 15:49-52 (1948).
2. A. London, "The Absolute Calibration of Vibration Pickups," NBS Tech. News Bull. 32:8-10 (1948).
3. S. Levy, and R. R. Bouche, "Calibration of Vibration Pickups by the Reciprocity Method," J. Res. NBS, 57 (4):227-243 (1956).
4. R. R. Bouche, "Development of Standards for the Measurement of Vibratory Motion," Univ. of Maryland Ph.D. Thesis (Dec. 12, 1958).
5. R. R. Bouche, and L. C. Ensor, "Use of Reciprocity Calibrated Accelerometer Standards for Performing Routine Laboratory Comparison Calibrations," Shock and Vibration Bull. 34(4):21-29(1965).
6. R. R. Bouche, and L. C. Ensor, "Accelerometer Calibration with Reciprocity Vibration Standards," Measurements and Data 4(4):84-89 (July/Aug 1970).
7. R. R. Bouche, "High Frequency Shaker for Accurate Accelerometer Calibrations," Journal of Environmental Sciences, 13 (3): 10-15, (July/Aug 1970).
8. Anon, "American Standard Methods for the Calibration of Shock and Vibration Pickups," American National Standards Institute, S2.2-1959:39(1959).
9. T. Dimoff, "Electrodynamic Vibration Standard with a Ceramic Moving Element," Journal of Acoustical Society of America, 40 (3):671-676 (1966).
10. R. R. Bouche, "A Practical Application of Accelerometer Calibrations" The Shock and Vibration Bulletin 41(3):1-9(1970).

Discussion

Mr. Ramboz (National Bureau of Standards):

Reciprocity remains one of two common ways of calibrating pickups particularly at the higher frequencies. The other method is an optical method using an optical interferometer. Those are the basically two accepted ways of doing this work so I think it is important that this work is carried on and extended to higher frequencies. I would like to criticize one statement that was made. It says other published papers describe the reciprocity calibration of piezoelectric standards only at 100 hz. Ray, I assume you are talking about other papers that you have published. The literature is full of National Bureau of Standards papers and of course your work on reciprocity at many other frequencies. I would like to emphasize that calibration at the higher frequencies by reciprocity is extremely difficult and great care has to be taken; those of you who have delved into reciprocity know it is full of gremlins and many pitfalls. We have developed other reciprocity methods besides this and as a result of that it has become necessary to distinguish one method from another. In honor of the developers of this particular method that Ray has discussed, we call it the Bouche-Lettie method and this has been identified in the literature. Other methods are the par balanced and the three mass methods. There are two more being discussed. I think the area of reciprocity is indeed alive and is moving very slowly forward.

A NON-CONTACTING BETA BACKSCATTER
GAGE FOR EXPLOSIVE QUANTITY MEASUREMENT

P. B. Higgins, F. H. Mathews, R. A. Benahm
Sandia Laboratories
Albuquerque, New Mexico

A non-contacting method of measuring the quantity of light-initiable explosive previously applied to a surface is described. Design parameters, calibration procedures and field results are given for a beta backscatter gage which measures the areal density of a layer of the primary explosive, silver acetylide-silver nitrate (SASN), on a carbon or aluminum sub-surface. The "radiation patterns" produced by the gage using three different beta source geometries were determined and their relative merits are discussed.

INTRODUCTION

Impulse loading delivered to a structure as a result of radiation-induced blowoff can be simulated by spray painting areas of interest on the structure's surface with a light-initiable explosive, then detonating the explosive with a flash of intense light⁽¹⁾. Since impulse is a function of areal density of the explosive coating⁽²⁾, a desired impulse profile can be produced by varying the amount of explosive applied to different portions of the structure. Because this application employs silver acetylide-silver nitrate (SASN), a sensitive primary explosive, all operations involving significant quantities of explosive are performed by remote control.

For several years we have measured areal density of the deposited SASN with the aid of small Kovar coupons of known weight. As illustrated in Fig. 1, the coupons are mounted on thin magnets which in turn are glued to the test surface prior to application of the explosive. At any time during or after the spray operation, the areal density of the explosive deposited on a coupon may be measured by temporarily removing the coupon from its magnetic holder and weighing it. This is done with master-slave manipulators using a remote read-out balance located in the spray booth. After subtracting the weight of the coupon, the net weight of explosive is divided by the known area of the coupon face to determine the areal density of the applied explosive. This measurement

deals directly with the physical parameters involved--mass and area--and has provided a means of predicting impulse generally within $\pm 10\%$ in the case of a single coupon measurement.

The following considerations have made the development of a supplementary method of measuring areal density worthwhile:

1. The coupon weighing approach is a limited sampling technique. The progress of a spray operation that may include several hundred passes of the spray head must be judged by weighing coupons from a limited number of predetermined locations which cannot be altered after the spray operation begins.

2. A good deal of operator skill is presently required to grasp a short coupon stem of 20 gage wire eight feet away with heavy-duty manipulators, pull the explosive-laden coupon cleanly from its magnetic holder, move the coupon several feet through a maze of rubber hoses loaded with circulating explosive to the weighing platform, release it for weighing, pick it up again and return it to the exact spot on the structure from which it came. All of this must be done without disturbing the fragile coating on the sprayed surface while viewing the proceedings through a hazy, foot-thick protective window. When multiplied by as many as 30 coupons and several measurements, this technique adds significantly to operator stress and the possibility of a mishap.

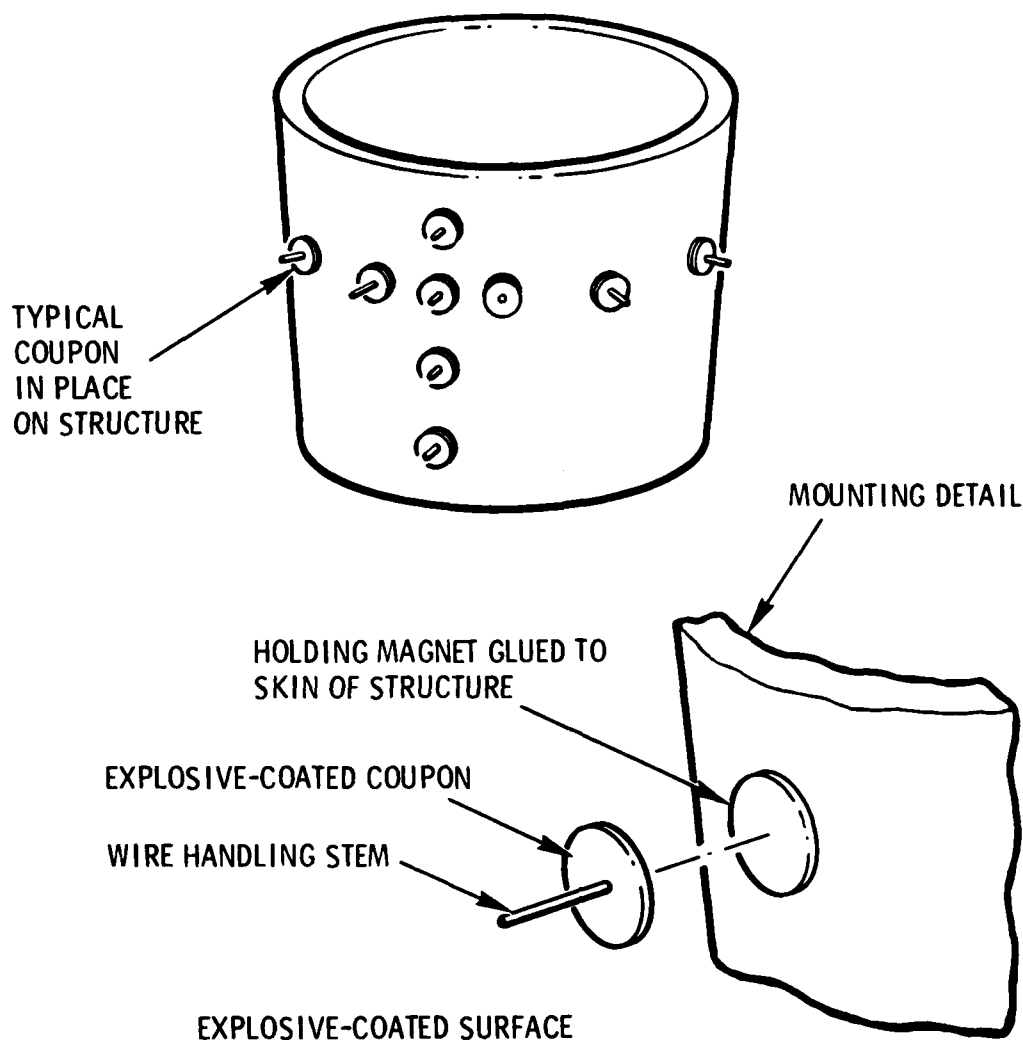


FIG. 1 TYPICAL COUPON APPLICATION

3. Another limitation of the coupon sampling method is the edge effect exhibited by the explosive on the periphery of the circular coupon. The magnet which holds each coupon in place also elevates it above the adjacent surface, leading to a non-uniform coating of explosive at the discontinuity, as shown in Fig. 2. A rather elaborate optical measurement is required to correct for this effect when the areal density of the explosive exceeds 50 mg/cm^2 .

BETA BACKSCATTER GAGE

Several non-contacting methods of measuring areal density of the SASN were considered as a means of overcoming the limitations of the coupon weighing method; the beta backscatter technique outlined in Fig. 3 was chosen.

Beta particles from the radioactive source radiate in all directions but are blocked from entering the detector

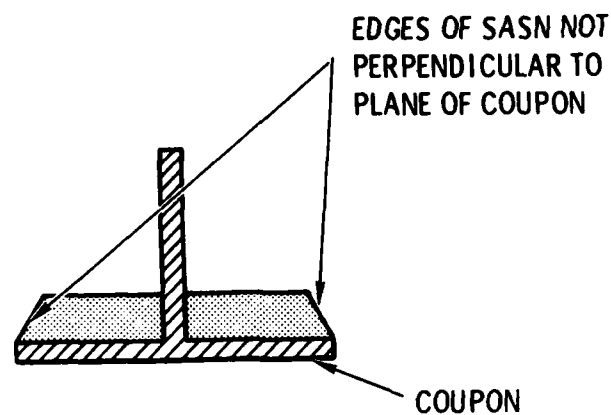


FIG. 2 EDGE EFFECT OF EXPLOSIVE
SPRAYED ON COUPON.

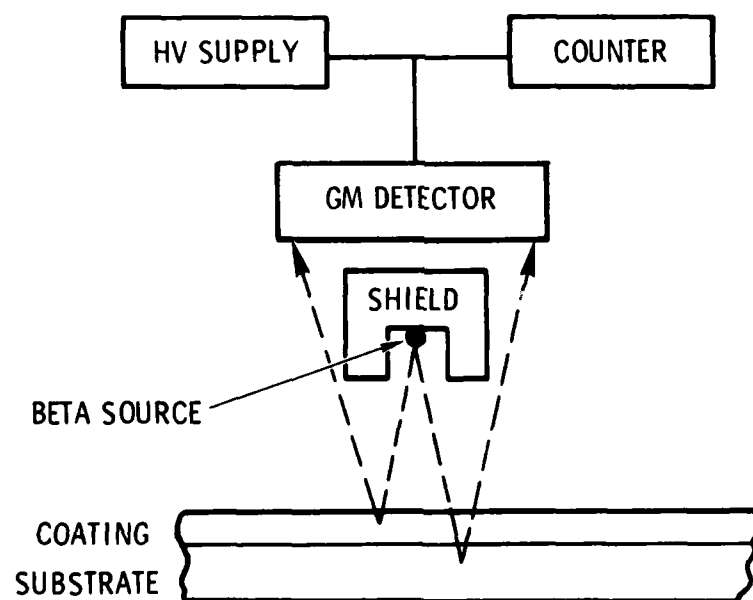


FIG. 3 PRINCIPLE OF BETA BACKSCATTER MEASUREMENT
(90° SOURCE).

directly by the indicated shield. Radiation reaching the coated surface will either pass through, be absorbed, or be backscattered. Backscatter measurements of the coating depend upon the coating being thin enough to pass a fraction of the beta particles and the substrate being of at least "critical" thickness, which prevents any significant amount of beta transmission. Under these conditions the particles backscattered to the detector will contain contributions from both the substrate and the coating. If the coating and the substrate compositions do not change and the geometry of the measurement remains fixed, then a change in the areal density of the coating will affect the amount of backscatter received by the detector and provide a measurement of areal density. These were sufficient conditions for our purpose, since impulse is predicted in terms of areal density; however, the more common use of the backscatter technique to measure thickness requires that the coating have a constant, or at least known, volumetric density.

A further requirement for successful backscatter measurements is that there be a significant difference in the atomic numbers of the substrate and coating materials. A difference of at least 15% is considered minimal and the attainable accuracy of the measurement increases as the difference becomes greater⁽³⁾. The relationship of atomic numbers of the materials used and the relative counts expected is shown in Fig. 4.

SYSTEM DESCRIPTION

The equipment layout used to spray and measure the quantity of sprayed explosive applied to a typical structure is shown in Fig. 5. The equipment is located in a spray booth isolated from the operating position by a laminated window of Lexan and Lucite.

The beta backscatter system (BBS) is diagrammed in Fig. 6. For clarity, the manually controlled vertical positioning equipment is not illustrated.

The Sensor Head is a motor-driven assembly consisting of a Strontium-Yttrium ($Sr^{90} + Y^{90}$) beta source, a "pancake" Geiger-Mueller (GM) detector, and an eddy-current sensing coil together with its associated electronics. Cables conduct control and data signals between the Sensor Head, Fig. 7, in the spray booth and the equipment rack in the control room.

The beta source is contained in the bottom of a 3.7 mm deep lead cup having

walls approximately 1.26 mm thick. The walls of the cup collimate the beta radiation to about a 90° solid angle. This arrangement provides adequate attenuation of direct radiation from source to detector when the cup is normal to the surface under measurement, as in the 90° source indicated in Fig. 3. Such is not the case for the 45° offset source shown in Fig. 6 and an extended "scoop" of lead foil was added to reduce the background count resulting from direct leakage into the detector.

The GM tube, an Eberline Model HP-210, receives particles backscattered from the sprayed surface being irradiated by the beta source. Each particle which penetrates the thin "window" of the GM tube ionizes the gas in the tube and causes current from the high voltage supply to flow. The resulting voltage spike causes the counter to register one count.

The eddy current coil is the heart of the horizontal position control system designed to hold the GM tube at a fixed distance from the sprayed surface being measured. Electrically, the coil is one arm of a rectifying resistance bridge powered by an RF source of approximately 6.5 MHz. The bridge is initially balanced with the outer edge of the beta source about 6.3 mm from the sprayed surface. Any movement of the surface which changes this so-called "lift-off" distance will unbalance the bridge by changing the effective impedance of the eddy current loop induced in the substrate (which must be conductive). The unbalance signal is amplified and drives the Sensor Head motor in the appropriate direction to correct the original change in lift-off distance. Response time of the position servo is not critical because of the relatively long time required to complete a backscatter measurement after the servo settles.

In addition to amplifying the bipolar signal from the position-sensing bridge, the electronics associated with the horizontal positioning system converts the control signal into a 3-phase drive current for the horizontal positioning pulse motor. A pulse motor was selected for Sensor Head positioning in anticipation of possible future computer control of the BBS.

BETA SOURCE DESIGN

The radiation from a decaying isotope follows the Poisson statistics⁽⁵⁾. Consequently, the standard deviation, SD, of the number of counts N logged on the counter in a fixed interval of time closely approximates the square root of N .

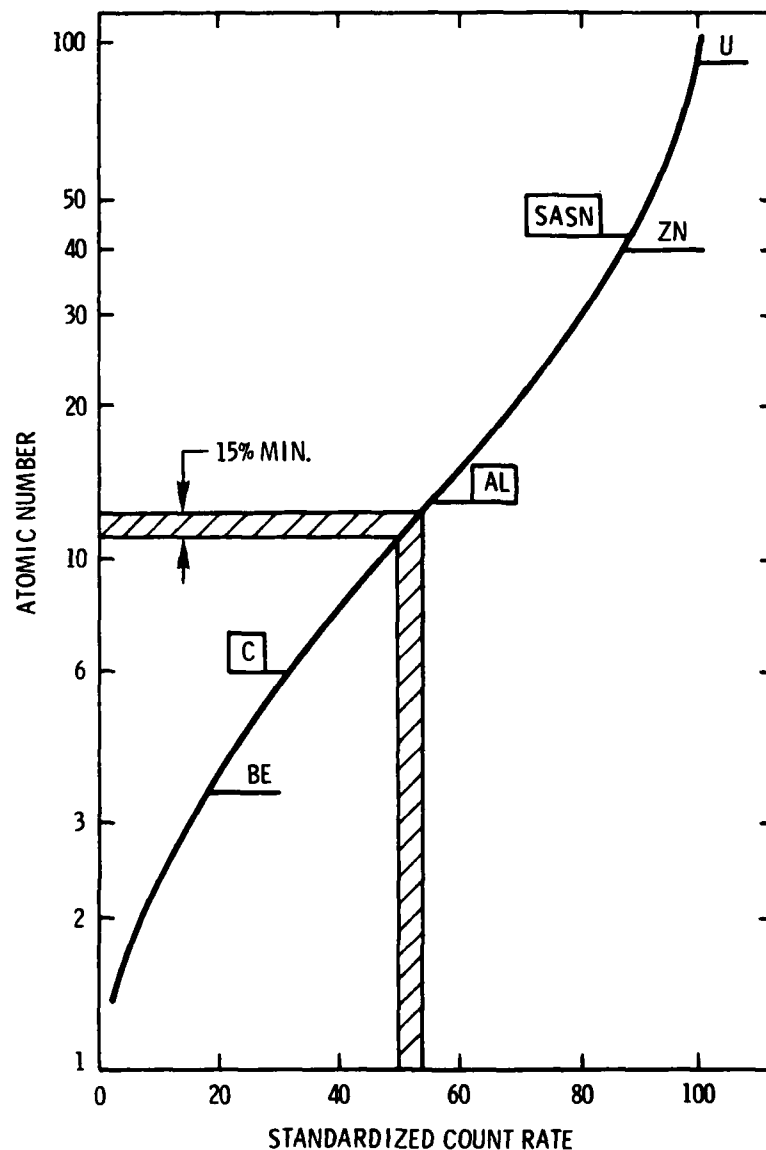


FIG.4 SATURATION BACKSCATTER AS A FUNCTION
OF ATOMIC NUMBER⁽⁴⁾

$$SD = N^{1/2} \quad (1)$$

and the true count will lie within $N \pm 2SD$ approximately 95% of the time.

Based on this statistical relationship, the probable error in areal density measurements due to the random beta radiation from a $Sr^{90} + Y^{90}$ source was calculated for a family of nominal coating/substrate values and tabulated in Table 1. A backscatter return factor of 0.1 was used for the carbon substrate,

a factor of 0.53 for the SASN coating⁽⁶⁾.

From the bottom row of the tabular data it is seen that an acceptable error of about $\pm 1.0 \text{ mg/cm}^2$ for the 2SD points at 30 mg/cm^2 requires a total detector count of about 25,000 counts.

The GM detector selected for our application has a specified "dead time", T_D , of 50 microseconds following such ionization of the tube by a beta

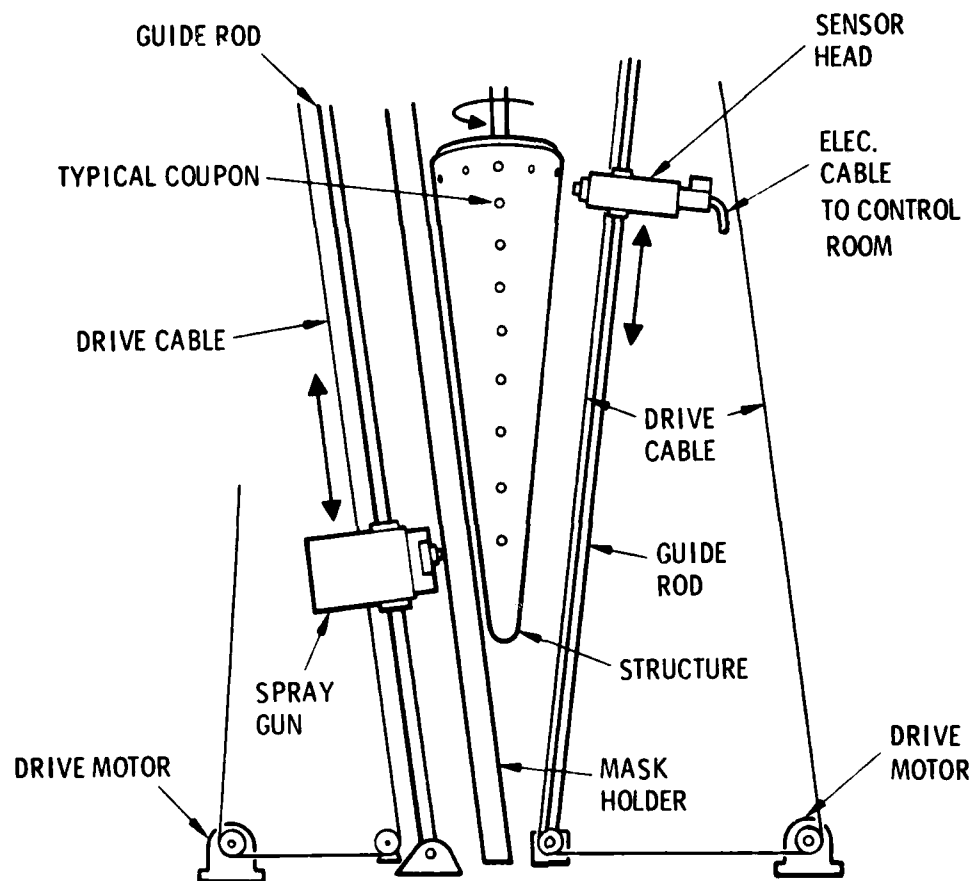


FIG. 5 SPRAY GUN & SENSOR HEAD SETUP

particle. During dead time, another particle entering the detector tube will not be detected. A calculated correction is made for this effect but, because the adjustment is based on a nominal recovery time subject to error, it is desirable to limit the dead time to no more than 10% of the total count interval, T . Solving

$$0.1T = T_0 N$$

$$\text{and } T = 50\mu\text{s/count} \times 25,000 \text{ counts}/0.1$$

$$T = 12.5 \text{ s}$$

The permissible count rate of the detector, I_D , becomes

$$\begin{aligned} I_D &= N / 0.1T \\ &= 25,000 / 12.5 \\ &= 2000 \text{ counts/s} \end{aligned} \quad (2)$$

The required activity of the source, I_s , to produce this count rate may be related

to the detector output, I_D , by the product of six multipliers, A_1 through A_6 , which represent absorption, reflection and divergence factors experienced by beta particles traveling from source to detector:

$$I_s = I_D (A_1 \times A_2 \dots A_6) \quad (3)$$

All multipliers exceed one except the one which represents "reflection" from the bottom of the source holding cup. The factor representing geometrical divergence is an order of magnitude greater than any other factor and dominates the equation. A detailed solution of Eq. 3 is beyond the scope of this paper, but the solution for the specified value of I_D is

$$I_s = 85\mu\text{curie.}$$

With an idea of the source requirements, $\text{Sr}^{90} + \text{Y}^{90}$ was selected for three reasons:

1. The penetration range of the beta particles from this isotope covered our anticipated usage.
2. The long half-life (28 years) of this source made the need for replacement unlikely.
3. The selected source was available in-house in a wide range of specific activities.

The actual source was fabricated at one of Sandia's radiation laboratories. Using the expected gage/source geometry, source activity was adjusted to provide the approximate count rate desired.

CALIBRATION

Calibration of the system began with the preparation of two sets of "standards". One set was produced by spraying 50 mm diameter patches of SASN on carbon substrate of greater than critical thickness (6.5 mm). The areal density of the deposited explosive was determined by carefully weighing coupons of known area sprayed at the same time. Because of their fragile and hazardous nature, these standards could not be used directly for long-term calibration of the BBS.

To provide long-term calibration of the system, another set of standards consisting of silver foils of different thicknesses thinly cemented to a 6.5 mm carbon substrate was built. When measured with the BBS under the same conditions as the SASN samples, the silver foil standards provide a set of correlation points which are expected to reveal any deterioration of gage performance over its useful life.

Before actual calibration of the gage with the standards, the optimum liftoff distance was established. For this purpose, the SASN standards were mounted in front of the beta source on a micrometer drive which permitted accurate variation of the liftoff distance. With the servo inoperative, the backscatter count for each of the SASN standards was recorded over a range of liftoff distances. The data is plotted in Fig. 8.

The peak of any one curve represents the optimum operating lift-off for a particular areal density because the measurement accuracy is maximum at that point and also because the counting error due to any small liftoff error will be least in the vicinity of the peak. A liftoff of 6.3 mm was selected for the

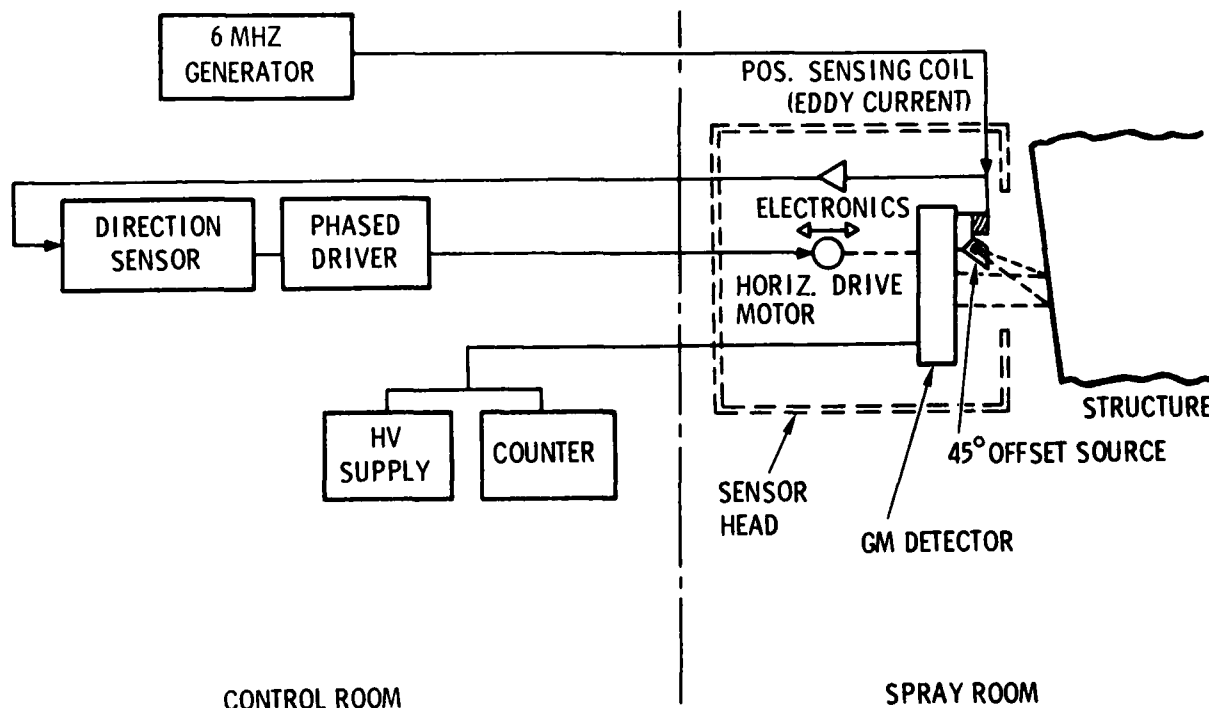


FIG. 6 SYSTEM BLOCK DIAGRAM

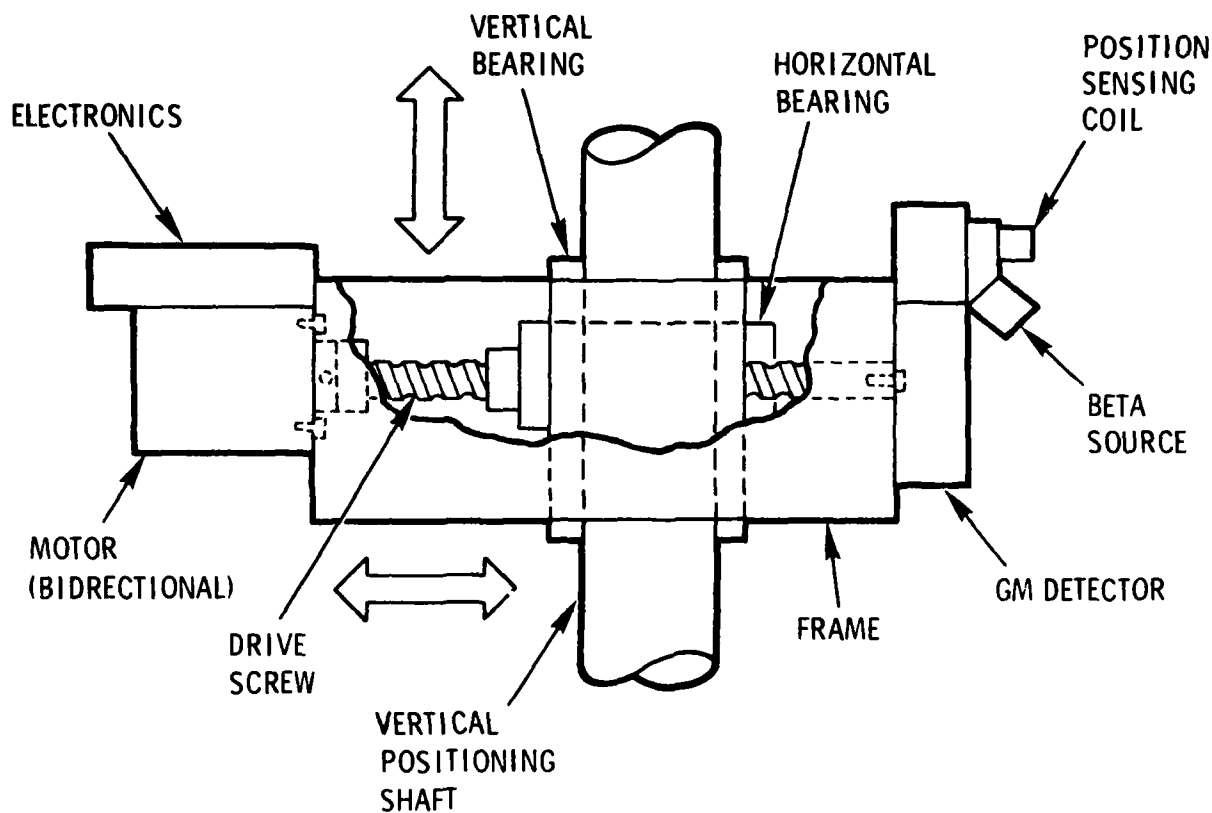


FIG. 7 SENSOR HEAD

NOMINAL			2 x STANDARD DEVIATION	
SUBSTRATE (CARBON)	COATING (SASN)			
COUNTS	COUNTS	AREAL DENSITY MG/CM ²	COUNTS	AREAL DENSITY MG/CM ²
1000	2340	30.0	± 97	+2.5 -2.8
2000	4680	↑ ↓	± 137	+1.8 -2.0
4000	9360		± 194	+1.2 -1.4
8000	18720		± 274	+ .8 -1.0

TABLE I: PREDICTED PERFORMANCE OF $\text{Sr}^{90} + \text{Y}^{90}$
AS A BETA BACKSCATTER SOURCE

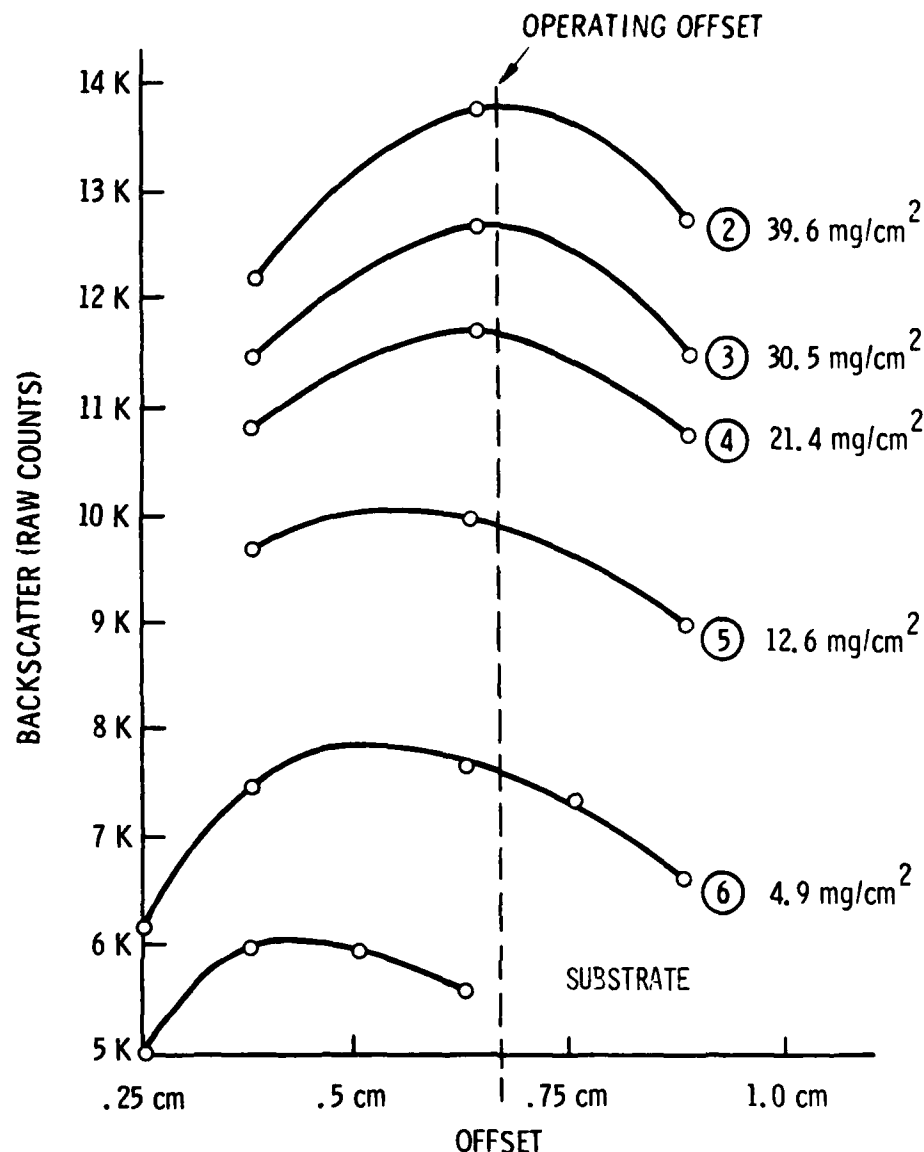


FIG. 8 VARIATION OF MAXIMUM BACKSCATTER WITH OFFSET AS A FUNCTION OF AREAL DENSITY (90° SOURCE).

90° source as a compromise distance which set the operating point at peak counts or near peak on the low slope side of the counts-vs-lift-off curve over the range of areal density covered by the sprayed standards.

Detector counts versus computed areal density of both SASN and silver foil standards are shown in Fig. 9. The excellent fit of straight lines through both sets of data plotted on semilog paper indicates the exponential relation of areal density to number of counts.

The corrected counts shown in Fig. 9 differ from the raw detector counts because of adjustments for decay of the S⁹⁰ + Y⁹⁰ source, dead time of the detector, and background count. The latter is recorded when no significant backscatter target is in front of the source.

APPLICATION

Initially, the BBS was used to supplement coupon measurements during development tests of a carbon-carbon re-entry vehicle (RV). The RV was 1.6 m

long and 0.46 m in diameter at the base and approximately conical in shape. A total of 30 coupons were mounted on the surface of the vehicle in a modified Cross of Lorraine configuration shown in Fig. 10.

The center of a "viewing area" for the BBS was defined by a vertical line through a coupon at a distance of 50 mm below the coupon. This procedure assured the same areal density of explosive on the viewing area and on the coupon, since the spray process was performed vertically and weight measurements of the vertical group of coupons verified that no significant variation of areal density existed along the length of the RV. This test utilized the 90° beta source, which mounts just about the entrance "window" in the center of the GM detector.

The 17 coupons at 10° intervals near the base were weighed periodically during the spray operation to assure the formation of the desired cosine impulse distribution over one-half the surface of the RV. Upon completion of the spraying, BBS measurements were made in the "viewing areas" and the two sets of data--explosive weight on the coupons and BBS count measurements--were entered into our computer for reduction to areal density. Both data sets are plotted in Fig. 11.

A maximum difference of about 5% of full scale is seen near position zero, with a considerably better average error at other positions.

Analysis of the rigid body data resulting from detonation of the explosive deposited on the RV led to an investigation of the response of the 90° beta

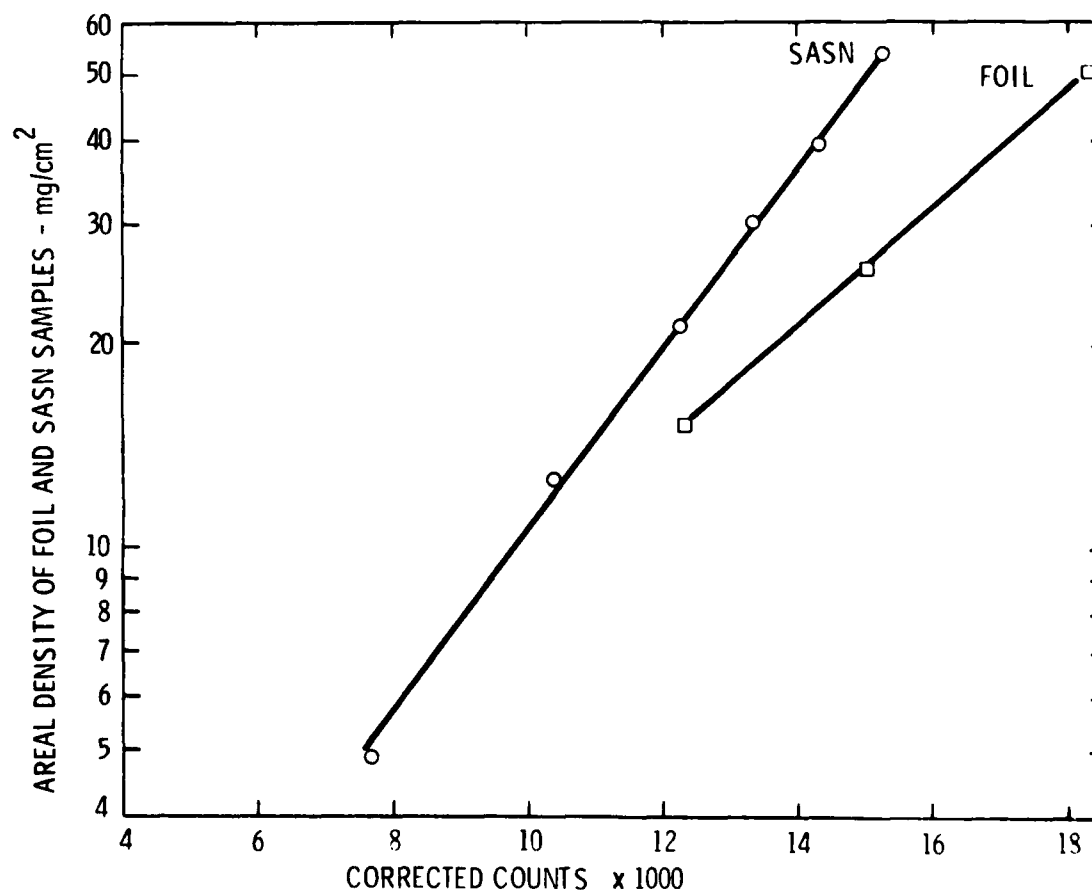


FIG. 9 BETA BACKSCATTER SYSTEM COUNTS CORRESPONDING TO WEIGHED SAMPLES

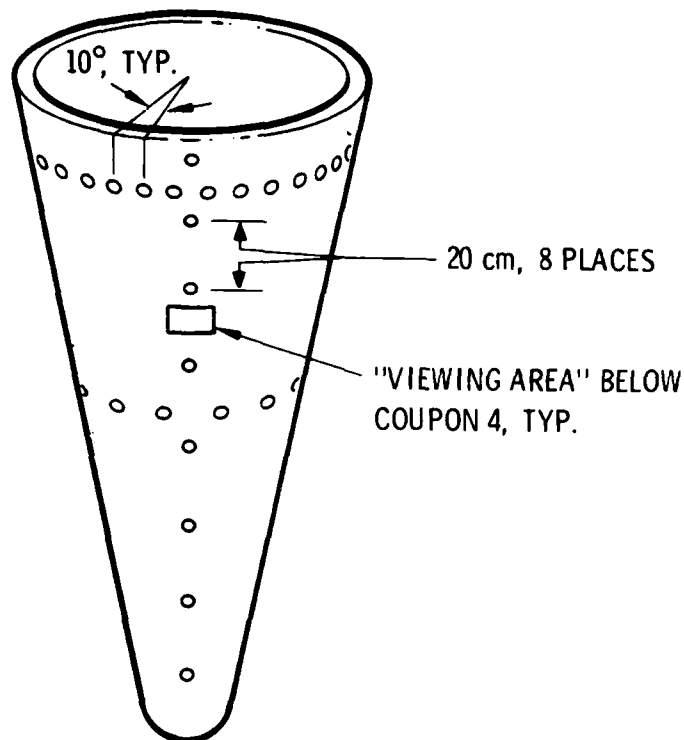


FIG. 10 COUPON AND VIEWING AREA LOCATIONS
ON REENTRY VEHICLE.

source to abrupt variations in areal density, a phenomena which occasionally occurs due to small misalignment of sprayer components. The experiment is diagrammed in Fig. 12.

A narrow 5.0 mm strip of silver foil 0.025 mm thick and 0.1 m long was glued to a 0.15 m by 0.2 m carbon flat, 13 mm thick. The beta source was centered over the foil and swept 20 mm either side of the foil in a direction normal to the length of the foil.

To eliminate the "cinder cone" response of the 90° mounting plotted in Fig. 12, the source was moved to the side of the detector and tilted 45°, as shown in Fig. 13. In order to reduce the resulting large increase in back-ground count, a lead shield in the form of a scoop was added in front of the source on the detector side. The indicated response shows the double peak structure to be absent.

A "final" modification consisted of adding a 4.3 mm diameter lead aperture in front of the 45° source. With this

additional collimation of the source and an offset distance of 3.2 mm, the somewhat "sharper" response shown in Fig. 14 was recorded, at a considerable price in number of counts. For accuracies consistent with the uncollimated source, it will be necessary to double either the measurement time or the source activity.

CONCLUSION

A self-positioning, non-contacting gage for remotely measuring the quantity of SASN explosive on a conductive carbon surface has been proven feasible. Based on calibration against weighed coupons from a flat sprayed sample, the accuracy of backscatter measurements on a surface having a 20 cm radius of curvature compared favorably to weighed coupon data when using a beta source centered over the detector and normal to the surface (90° source). Using a modified (45°) source, the ability of the gage to detect a common spray process anomaly--strip discontinuities in the explosive coating--was established experimentally.

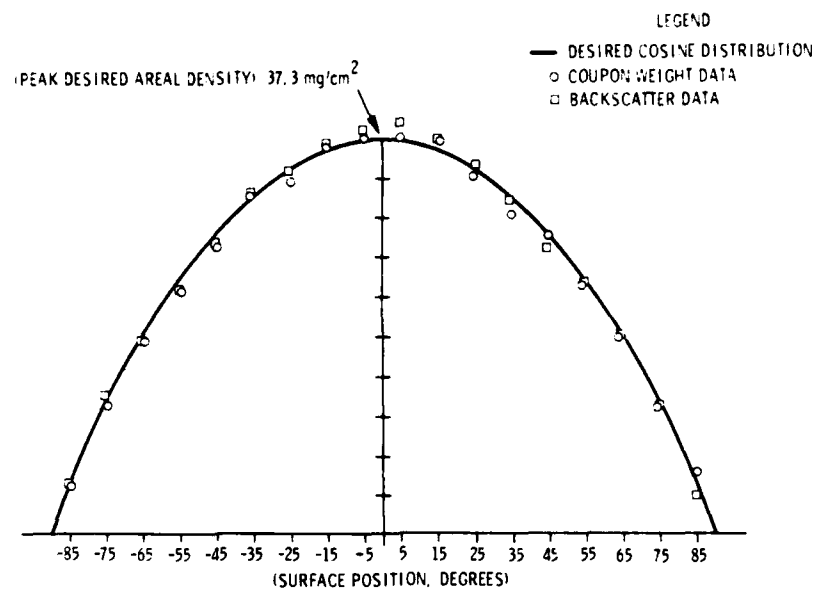


FIG. 11 WEIGHT-DERIVED AND BACKSCATTER-DERIVED AREAL DENSITY MEASUREMENTS COMPARED TO IDEAL COSINE

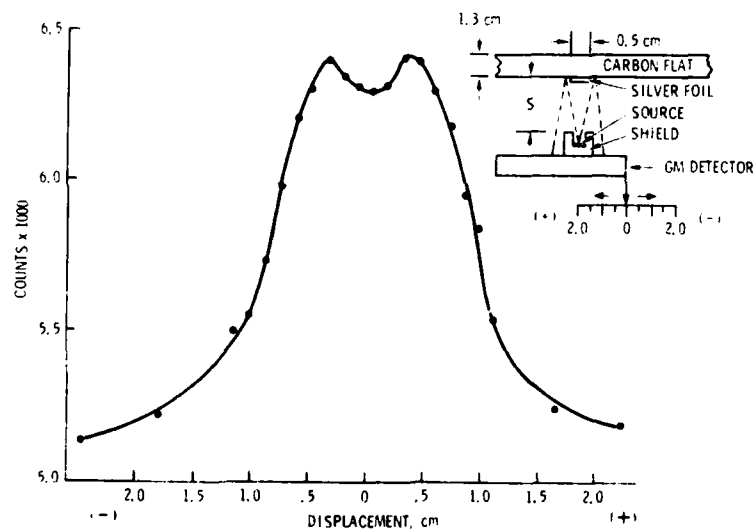


FIG. 12 BETA BACKSCATTER SYSTEM RESPONSE WITH 90° SOURCE
 $S = .63 \text{ cm}$

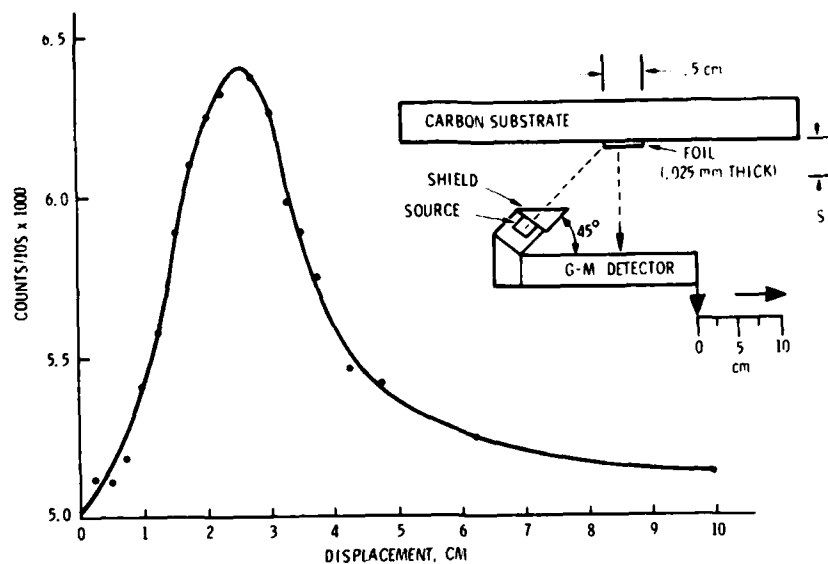


FIG. 13 BETA BACKSCATTER SYSTEM RESPONSE WITH 45° SOURCE. $S = .63$ cm

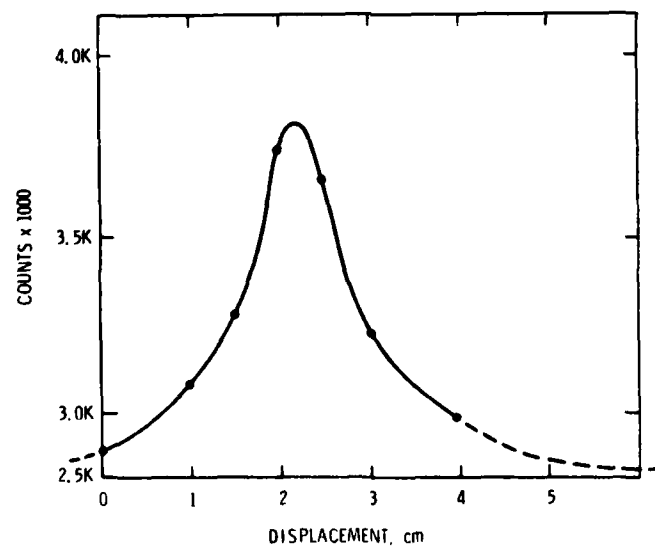


FIG. 14 BETA BACKSCATTER SYSTEM RESPONSE WITH 45°, COLLIMATED SOURCE, $S = 0.32$ cm.

ACKNOWLEDGEMENTS

The assistance of many persons was essential to the completion of the Beta Backscatter System. The authors would like to thank the personnel of the Sandia Environmental Health Department for preparing the $Sr^{90} + Y^{90}$ source. D. H. Shirey conceived and built the Sensor Head and several evaluation fixtures; B. Duggins was instrumental in providing much of the interface electronics; P. Wojick prepared the manuscript for publication.

REFERENCES

1. P. B. Higgins, "An Arc Source for Initiating Light-Sensitive Explosives," Shock and Vibration Bulletin 46, Part 3, p. 191.
2. R. A. Benham, F. H. Mathews, P. B. Higgins, "Application of Light-Initiated Explosive for Simulating X-Ray Blowoff Impulse Effects on a Full Scale Reentry Vehicle," Sandia Laboratories Report, SAND77-0266, April 1977.
3. Standard Method of Test for Coating Thickness by The Beta Backscattering Principle, B 567-72, Annual Book of ASTM Standards, May 30, 1972.
4. T. D. T. Latter, "Measuring Coating Thickness by the Beta-Backscatter Technique," Brit. J. of NDT, pp. 145-151, Sept. 1975.
5. E. G. Standord, et al, Progress in Applied Materials Research, Vol. 7, p. 145, London Hegwood Books.
6. H. B. Egerton (ed.), Non-Destructive Testing, p. 137, Oxford Univ. Press, London, Eng., 1969.

DATA ACQUISITION SYSTEMS FOR THE IMMEDIATE FUTURE

Josef F. Schneider
Civil Engineering Research Division
Air Force Weapons Laboratory
Kirtland AFB, NM

This paper addresses the acquisition problems with transient data in an extremely hostile environment. Digital techniques have recently become attractive due to rapid progress in semiconductor technology. However, FM systems cannot be ruled out. The most important feature of digital systems is the reduction of data uncertainties by an order of magnitude. Two digital systems are considered. One is the analog multiplex system that transmits data in real time. Analog-type recording is necessary. The other is a system that multiplexes on the digital side. Each channel has an A to D converter and memory, while transmission takes place after the test. The data is stored digitally and plotted for quick-look analysis without the need for precomputer data reduction. The presently used time-of-arrival data acquisition system is slow, ambiguous, and needs analog recording. A digital system will improve timing resolution by at least one order of magnitude and print the results on site. Application guides and formulae are given for all systems, and a comparison is presented which lists respective system merit parameters for similar data handling requirements. Recommendations favor the digital system but still leave room for improved FM systems.

1. INTRODUCTION

When choosing a data acquisition system in the not too distant past, the probability was very high that an FM multiplex would be selected. Today, with the advent of the microcomputer and the progress in A to D converter technology, the designer has a choice between an analog and a digital system. The criteria for the selection of a particular system have to be developed from the test instrumentation requirements. Although no simple rule can be provided for a selection, it is nevertheless possible to develop selection guidelines for general classes of acquisition systems. Although they are not restricted to special requirements, the systems discussed have evolved from the instrumentation of tests with several hundred sensors in an extremely hostile environment of short duration.

2. DESCRIPTION OF DATA ACQUISITION SYSTEMS

2.1 General

The systems described herein are of the state-of-the-art technology and constitute the arsenal to choose from for future instrumentation of large-scale, short-duration tests. The

requirement for the development of new systems is not new, only the technology to implement the solutions is new. Therefore, the venerated FM system has not become obsolete by the new technology of large-scale integration; on the contrary, it can be revived with this new technology by new component design and packaging.

The following list shows basic requirements for improving quality and cost-effectiveness of present data acquisition:

- a. Reduction in cable performance requirements
- b. Reduction in number of cables
- c. Reduction in noise and interference susceptibility
- d. Reduction in transmission bandwidth
- e. Increase in channel bandwidth
- f. Increase in dynamic range of the channel

g. Simplification of operation and maintenance

h. Standardization of sensor voltage output

The item under h is not a system feature but an interface requirement. The intention is to standardize all transducer outputs between 0 and 10V for unipolar transducers and between -5 and +5V for bipolar units. This can be accomplished by placing signal conditioners, including band-limiting filters, close to the transducer, preferably downhole.

Therefore, with the interface between the transducer and the acquisition system standardized, no special allowance has to be made for different sensors except, of course, for the consideration of channel bandwidth which determines largely what type of system will be used.

It is obvious that no one system exists that could satisfy all the requirements for improving the present systems. Therefore, one has to select for optimal performance. Cost-effectiveness should equally play a major role in the selection of a system.

A data acquisition system, for the purpose of this discussion, is defined as beginning at the transducer (signal conditioner) interface and containing the forward equipment, the cable, the receiver and/or controller (computer) and the recording device in the van, including optional quick-look equipment (see Fig. 1).

Signal conditioners are not included in this discussion because they are mostly transducer-oriented or even an integral part of the transducer system.

2.2 FM Systems

2.2.1 Present Systems

An example of an FM system, as presently used, is shown in Fig. 2. The low-level transducer output is transmitted through individual lines (several per transducer) to the van where the signal is conditioned, frequency-modulated, mixed with the other channels of the same system and recorded. A total system bandwidth of approximately 1 MHz is available in the recording system, which allows 10 to 20 channels with a bandwidth in the range of several kHz, depending on selection of system parameters.

2.2.2 Forward Systems

Improvement of the present systems is possible by putting the signal conditioner close to the transducer, which assures a high-level signal on the connecting cable; and putting the VCO's plus mixer in a forward location (e.g., splice bunker), which reduces the number of transmission cables to one wideband line and a telephone line for control (e.g., system calibration). This system is shown in Fig. 3. Whether the signal conditioner is in the transducer or in the splice bunker depends on the transducer requirement and the state-of-technology. Filters (F) have been added to the

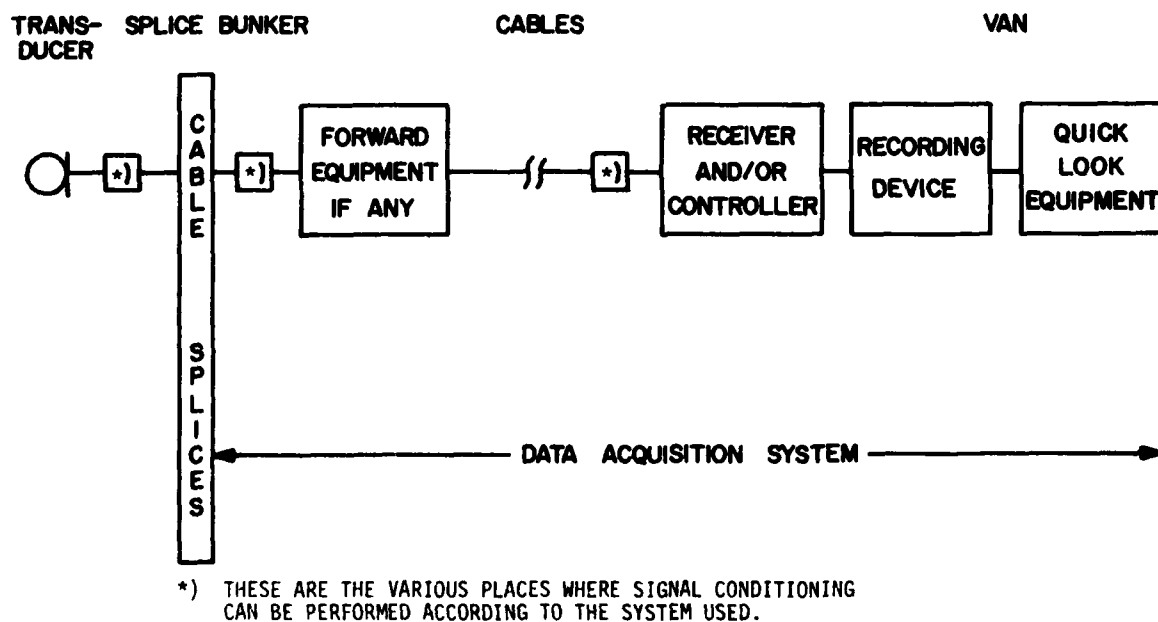
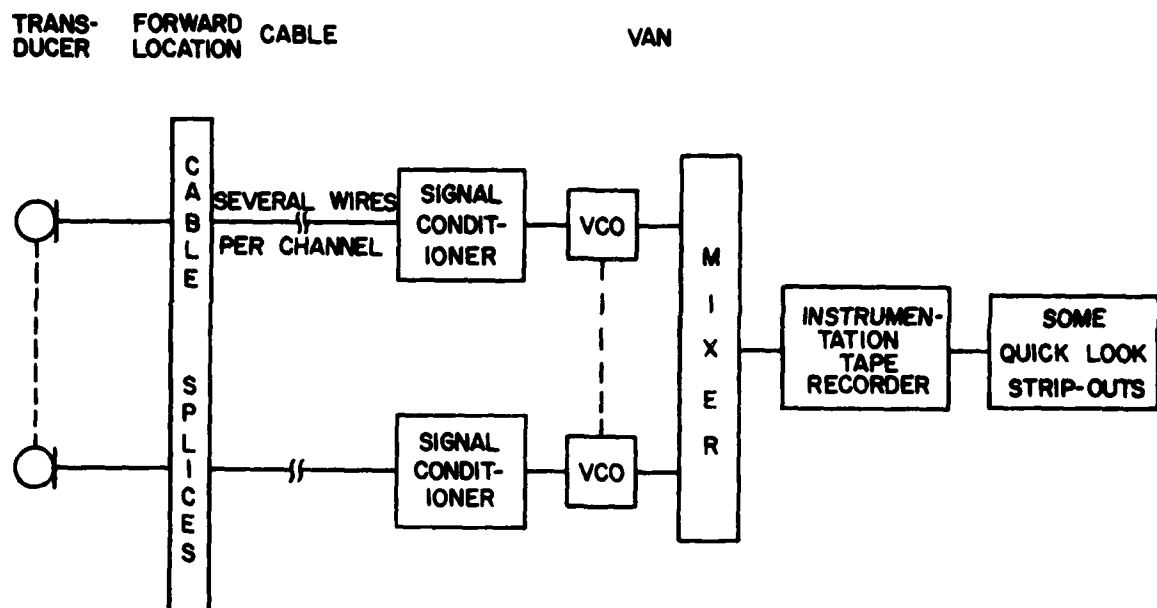


FIGURE 1. DEFINITION OF A SYSTEM



VCO = VOLTAGE-CONTROLLED OSCILLATOR

FIGURE 2. FM - SYSTEM PRESENTLY IN USE

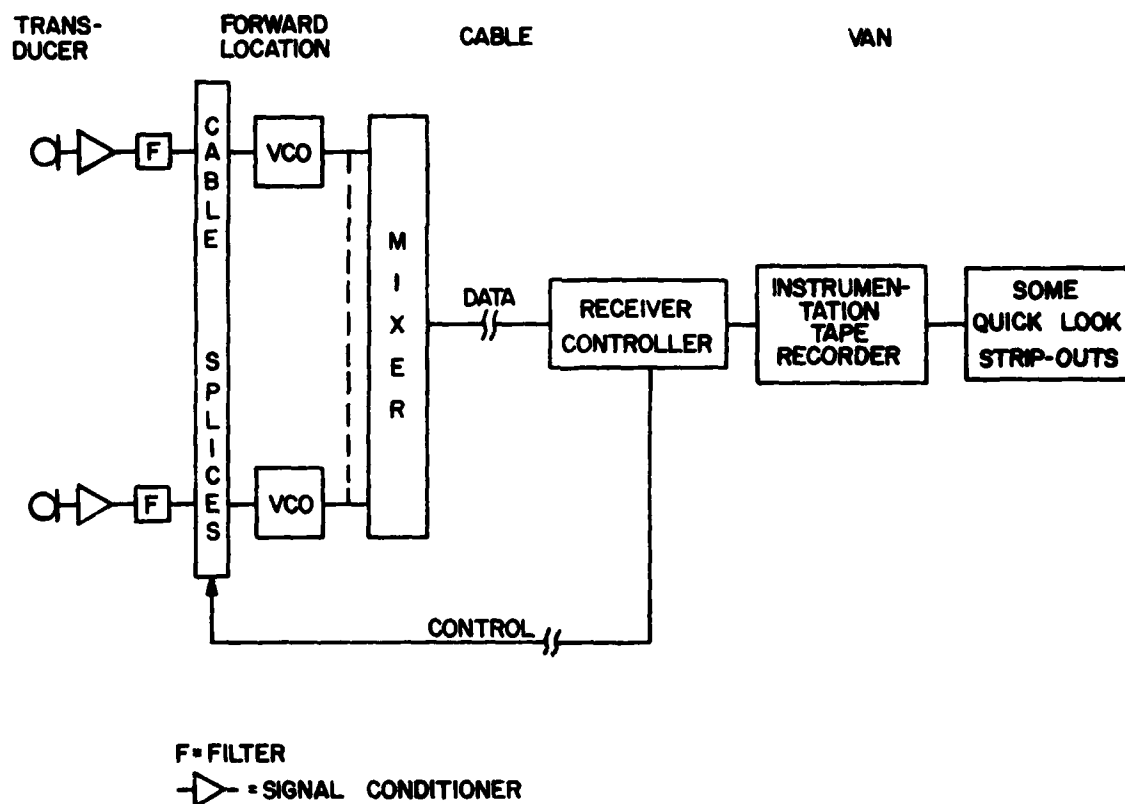


FIGURE 3. FORWARD FM SYSTEM

signal conditioner in order to limit the signal bandwidth to the bandwidth of the FM channel and thereby to avoid interchannel crosstalk in the telemetry link (in the past, these filters would have been far too costly and bulky). There is, however, one stringent requirement for this system; that is, the frequency stability of the VCO. It might not be possible, with the explosives in place, to go out to the forward location and adjust the VCO a few hours before the test. Therefore, a higher stability is necessary for this forward VCO than for conventional VCO's.

2.2.3 Accuracy

The data accuracy (amplitude uncertainty), given a perfect signal at the input to the system, is about 2% of full scale overall (i.e., including recording and reproducing on different machines) for a modulation index of 4 to 5, and deteriorates to approximately 5% for a modulation index of 2. Data reduction selects and demodulates channels from the composite FM signal and digitizes the data for subsequent computer use and quick-look display.

2.3 PCM Systems

2.3.1 General Features

In a PCM system, the data are transferred from the analog to the digital domain by the analog-to-digital conversion as a function of the acquisition system. This has the advantage of increasing the noise immunity of the resulting (PCM) signal almost 30 times over

that of an analog signal. Therefore, the proper place of the digitization is in a forward location in order to make use of this advantage. Two different versions of a PCM system are considered. Their outward difference is in the location of the multiplexer. Their application difference is in cost and signal bandwidth. For both versions a word (sample) length of 8 bits is considered adequate for two reasons: (1) the microprocessors that most likely will be used to control the operation have a standardized 8-bit word size, and (2) transducers usually are not better than 1% (if they are that good) and therefore a .2% digitization error does not materially add to the uncertainty of the data (the geometric total would be 1.02%).

Transducers with a higher dynamic range than 40 db would require more bits per word and a more complicated computer system (8-bit double precision, or 12- or 16-bit word size).

2.3.2 Analog Multiplex PCM

This system is depicted in Fig. 4. The multiplex function is performed in the analog domain, ahead of the digitization. A high bandwidth cable is necessary for transmission of the digitized (PCM) signal to the recording van. A wide bandwidth instrumentation recorder is necessary to record the PCM signal for further use.

The bandwidth available for one channel decreases as the number of channels to be accommodated in a given system increases because of the fixed sample rate and, therefore, fixed bandwidth of the multiplexed output.

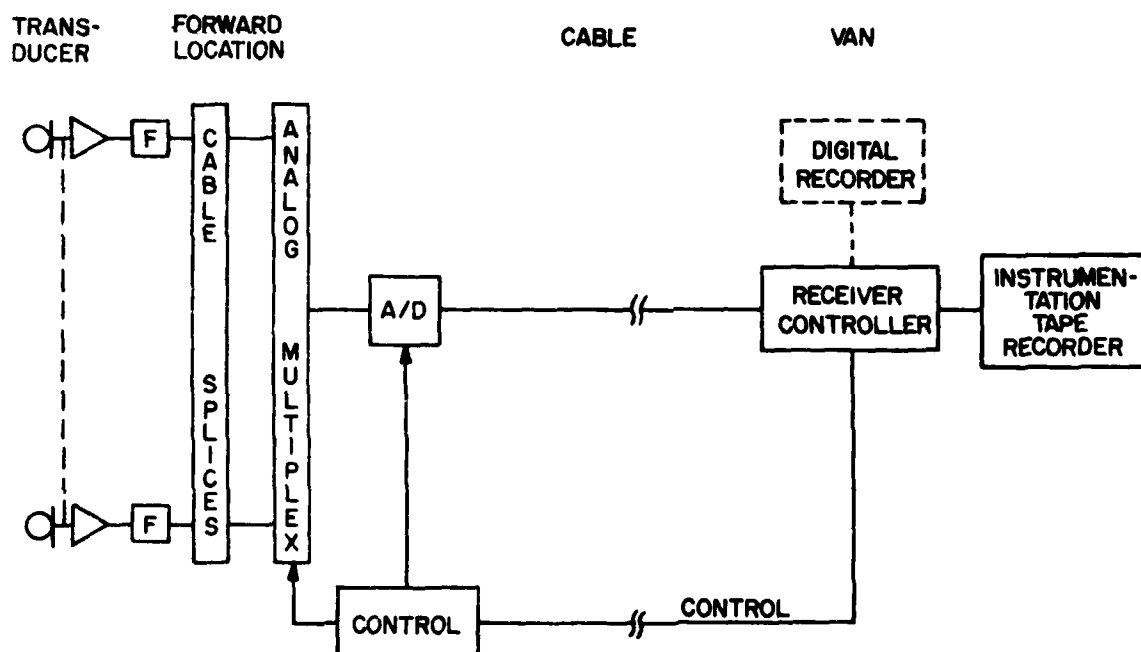


FIGURE 4. ANALOG MULTIPLEX PCM

Taking a 1 MHz cable bandwidth, 8-bit data words (plus some transmission format overhead), the maximum sampling frequency can almost be 200,000 samples per second. About 40 channels can be accommodated in a system, with a channel bandwidth of 1000 Hz. Only a handful of channels would be available for high frequency data (e.g., 10 kHz bandwidth for blast pressure measurements). On the other hand, this system provides continuous acquisition over a long period of time (as does an FM system). The control line can be a low bandwidth cable.

Signal amplitude uncertainty is typically a few tenths of a percent. The $\pm 1/2$ LSB (least significant bit) error of the digitization for an 8-bit system is $\pm 0.2\%$, and the analog components of the system (the multiplexer, and the sample and hold circuit) typically have a .1% error. Data reduction has to select and demodulate channels from the composite PCM signal for further computer use and also for the production of quick-look records.

2.3.3 Digital Multiplex PCM

As can be seen from Fig. 5, each channel now has its own A/D converter and adjacent

memory. Therefore, each channel can have the same high bandwidth regardless of the number of channels in the system. Using the sample rate of 200,000 for comparison, its bandwidth can be up to 50,000 Hz. The important feature, however, is that data transmission can take place after the event at a rate dictated by the quality of the cable. The control line can be of equal low quality. This system, however, works only when data with a definite trigger (e.g., fiducial at time zero) and rather short duration have to be acquired.

Amplitude uncertainty is even closer to $\pm 0.2\%$ because the only analog component left in the acquisition system is the sample and hold circuit, ahead of the analog-to-digital converter. The data window (duration of data to be acquired) is the number of samples the memory can hold divided by the sampling rate. Data reduction is not required for obtaining scaled and calibrated plots because they can be made at the test site directly.

2.4 Time-of-Arrival Systems

2.4.1 Event Data

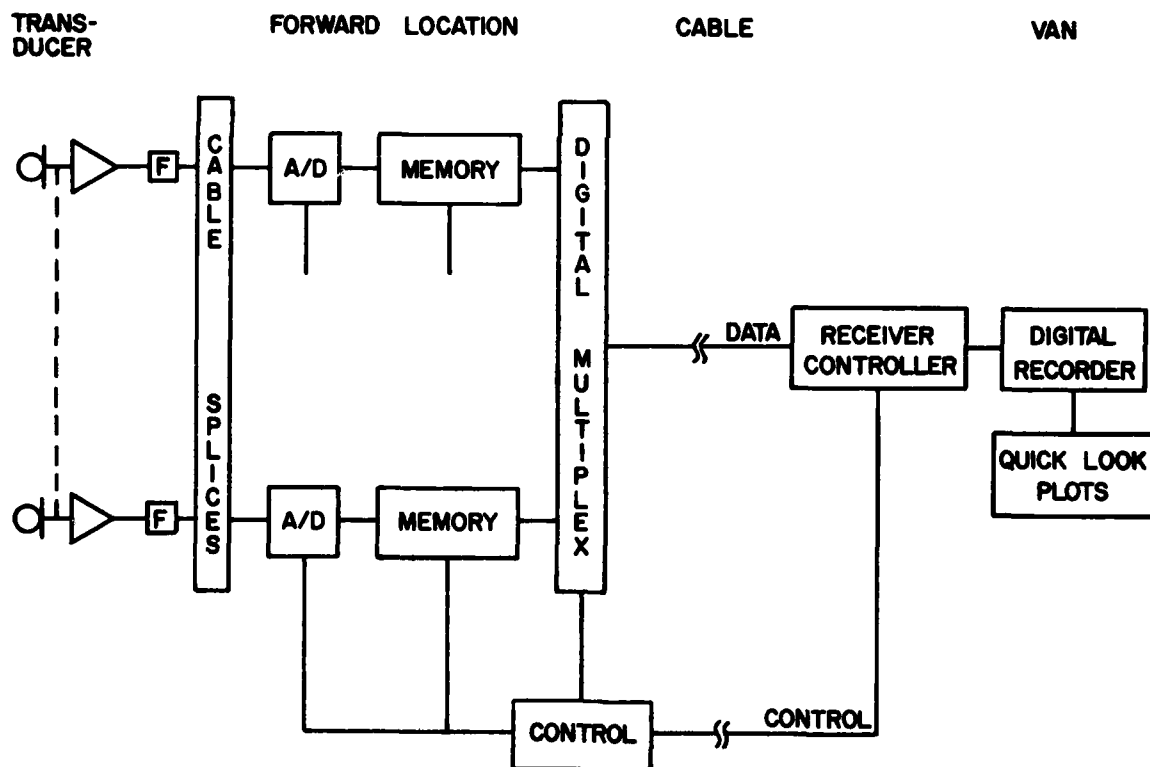


FIGURE 5. DIGITAL MULTIPLEX PCM

The systems described so far handle continuous or transient analog functions of time, as opposed to discrete functions of time. These are events whose arrival at certain stations is to be measured. Because of timing resolution requirements in the order of tenths of microseconds, long lines have to be avoided, analog magnetic tape recording is highly suspect, and the transmission cable has to have a high bandwidth.

2.4.2 An Analog System

The existing method uses magnetic tape for recording. Each measurement produces a pulse at the time of occurrence of an event whose amplitude identifies the measurement location. The pulses from eight measurements are multiplexed into one signal which is transmitted to the instrumentation van and recorded there, either direct or FM, one 8-station signal per track. Transmission bandwidth is 1 MHz (see Fig. 6) because recorders are usually run with 60 ips tape speed.

Data reduction consists of sampling these signals with 500,000 samples per second; i.e., with a 2 microsecond resolution, and reading the time difference between some point on the event pulse and the fiducial at $T = 0$. Timing accuracy is several microseconds at best.

2.4.3 A Digital System

Many of the shortcomings of the present system can be avoided if the time measurement is performed at a forward location, as shown in Fig. 7. Each channel has its own event counter that is started at the origin of test time (time zero) and stopped when the event arrives at the sensor. The accumulated time is read out after the test over the cable and printed. Data transmission time depends on cable quality rather than any other requirements. A control cable is not necessary when transceivers are used at the cable ends, as indicated in Fig. 7. Data reduction is not normally necessary because the printer output is the desired result. Timing resolutions of .1 microseconds can easily be

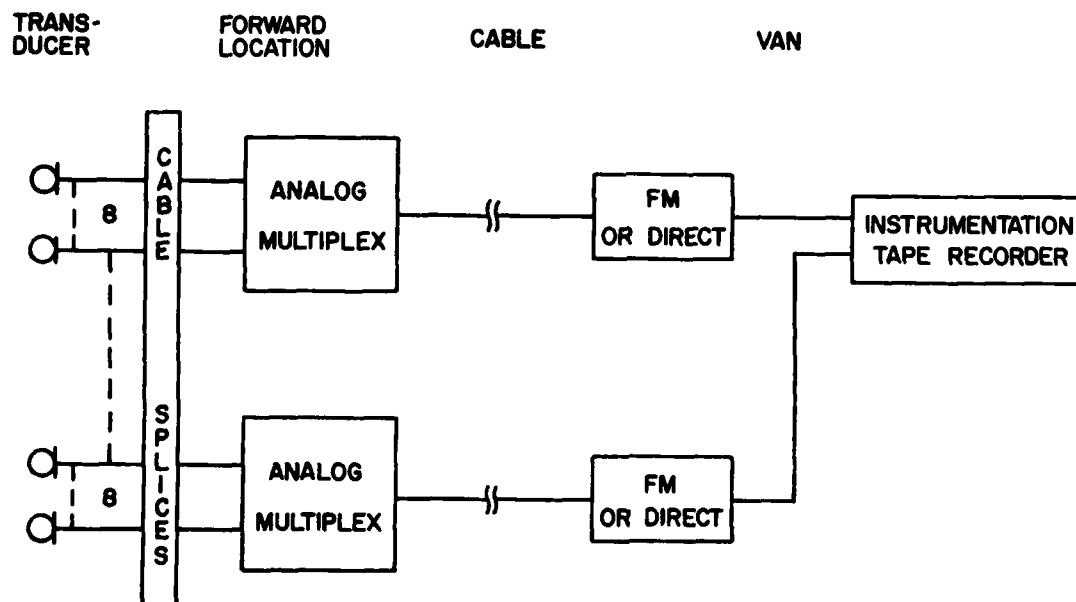


FIGURE 6. TIME-OF-ARRIVAL SYSTEM (ANALOG)

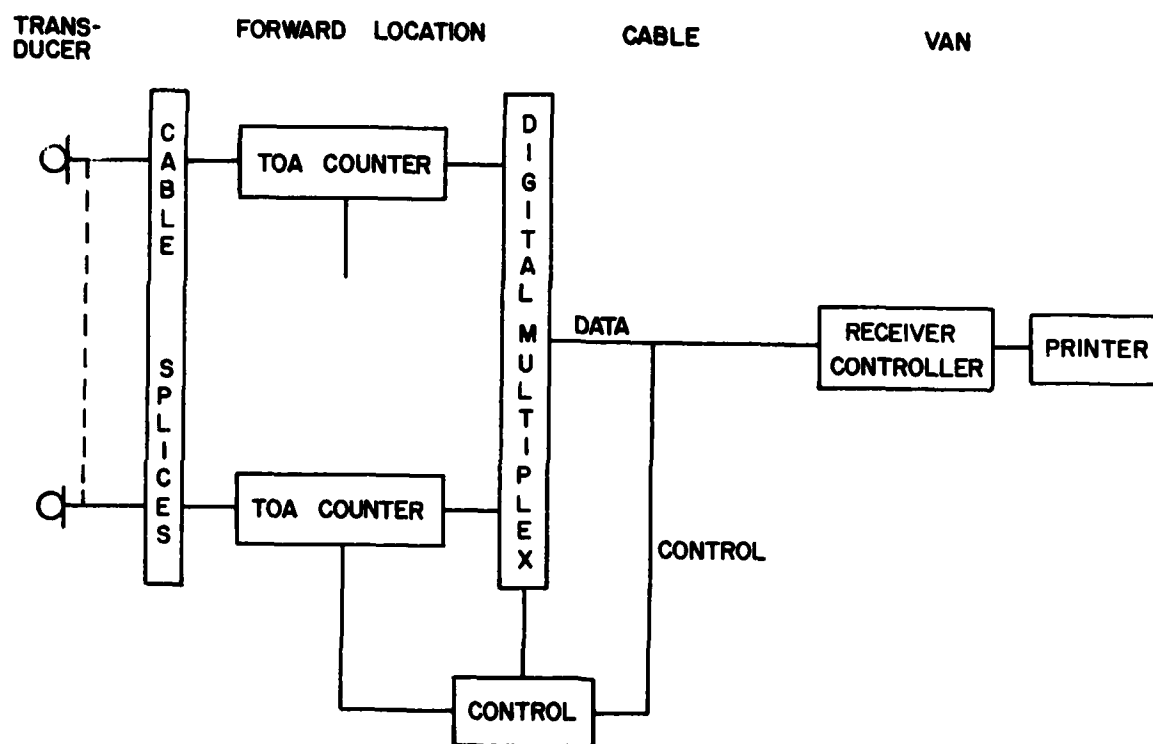


FIGURE 7. TIME OF ARRIVAL SYSTEM (DIGITAL)

provided with a 100 millisecond total time capability. Longer total times can be achieved at the expense of reduced resolution (e.g., 1 sec total with 1 microsecond resolution) or with the addition of more hardware.

3. SYSTEM PARAMETERS

3.1 Basis for Comparison

Before the respective systems can be compared to each other, the relationship between number of channels, channel bandwidth, and recording (or transmission) bandwidth of each system has to be defined. Then, a basis for comparison can be found. A conventional FM system for high bandwidth data usually covers about 1 MHz in the frequency spectrum. This figure will be used as the recording bandwidth, and therefore is also the transmission bandwidth that the cable has to be able to handle. An extrapolation to the often 2 MHz recording bandwidth for PCM systems can easily be made. Further, 8 bits per channel is considered standard for PCM systems, and 8 channels are presumed as the minimum number in any system. The latter figure again derives from convenient parameters of the FM system.

3.2 FM Systems

For the FM systems, the minimum recording bandwidths for a given number of channels is approximately:

$$\text{Recording B.W.} = \text{No. of Ch's} \times \text{Ch B.W.} \times \text{Dev. Rat.} \times 4 \times 1.1$$

Channel B.W. is the signal bandwidth; Dev. Rat. = deviation ratio = deviation from center frequency over signal bandwidth; the factor 4 includes \pm deviation and a guardband of a deviation width on each side; and the factor 1.1 stands for a 10% overhead (e.g., in FM a reference frequency is usually required to be added to the composite signal [1]). A second requirement is laid on the number of channels figure as follows:

$$\text{Deviation} \geq .01 \times \text{Center Frequency}$$

In the now usual case of constant bandwidth FM systems, given a 1 MHz (arbitrary) recording bandwidth, the number of channels for 10 KHz data could maximal be:

$$\text{No. of Ch's} = \frac{1000}{10 \times 2 \times 4 \times 1.1} = \frac{1000}{88} = 11$$

This(theoretical) maximum assumes the 1% deviation limit (calculated at 1 MHz) and a deviation ratio of 2 (the minimum ratio advisable for multiplexed FM systems). Data uncertainties in such a system are about 5%, especially in the higher frequency subcarriers. A good system should not deviate less than 4% and use a deviation ratio of 3 to 4 in order to approach data uncertainties of 2%. This would result in (again for 10 kHz data):

$$\text{No. of Ch's} = \frac{1000}{10 \times 4 \times 4 \times 1.1} = \frac{1000}{176} = 5$$

This seems low. Therefore, compromises are being struck; e.g., the guardband factor is reduced to 3.5, and a deviation ratio of 3 is used. A 10 kHz data bandwidth will then result in 3% deviation at the top of the spectrum.

$$\text{No. of Ch's} = \frac{1000}{10 \times 3 \times 3.5 \times 1.1} = \frac{1000}{115.5} = 8$$

This is a realistic figure which allows 10 kHz data B.W. and should result in approximately 3% data uncertainties overall.

The data uncertainties can only be given approximately because they depend on the deviation ratio which, in turn, depends on the data amplitude and frequency. Included in it is the degradation of the FM signal that is experienced in tape recording. (Measured uncertainties for existing FM systems are hard to come by and therefore unfortunately not available for this comparison.)

3.3 PCM Systems

3.3.1 Analog Multiplex

The recording (transmission) bandwidth for serial PCM systems with analog multiplex computes approximately as follows:

$$\text{Recording B.W.} = \frac{\text{No. of Ch's} \times \text{Ch B.W.} \times \text{No. of Bits} \times 4 \times 1/2}{1.1}$$

The number of bits determines the resolution of the data signal and is normally 8 or 10. The factor 4 guards against aliasing errors (this assumes prefiltering because the effectiveness of antialiasing results from the combination of this factor with the filter roll-off characteristic (see also Ref. [2]; e.g., for a 1% system, a 6-pole filter would keep the foldover error of a full-scale component within the uncertainty range, using a factor of 5). The factor 1/2 results from the recording mode (NRZ); for other modes, like Biphasic, this factor would be 1; and the factor 1.1 again allows for transmission format overhead in the serial PCM signal which consists mostly of synchronization bits and parity bits.

In order to compare with the FM systems, we use 8 channels and a recording bandwidth of 1 MHz. Using 8 bits a channel bandwidth of 7 kHz results for the same recording bandwidth. Frequently though, 10 bits are used; a guard factor of at least 5 is assumed; and a recording B.W. of 2 MHz (maximum) can be used on normal, nonmodified instrumentation recorders. The resulting channel B.W. would then be 9 kHz for an 8-channel complement.

Data uncertainty is a combination of the analog multiplex errors plus the digitization error. The former can be estimated to max .2%, and an 8-bit conversion results in $\pm 1/2$ LSB (least significant bit) error. This combines to less than .3% overall. Putting the multiplexer on the digital side for this real time PCM system would not change these relationships and therefore would be nonsense because now a separate A/D converter will be necessary for every channel.

3.3.2 Digital Multiplex

When, however, in addition to the A/D converter, a separate memory is attached to each channel and when the multiplexer is now moved to the digital side, an entirely new situation arises [3]. Transmission bandwidth is of no concern any more. Memory size determines how much data can be taken at any one time. Therefore, no real time transmission requirement exists. Transmission can take place any time after acquisition at any rate, but only data of limited duration can be acquired. The formula for channel B.W. is very simply:

$$\text{Ch B.W.} = \text{Memory Recording Rate} \times 4$$

The factor 4 is the guard against aliasing. Recording rate is measured in samples per second (= sample rate). The data duration computes as:

$$\text{Data Time} = \frac{\text{Memory Size}}{\text{Sample Rate}}$$

The number of channels in the system is determined by system design. Theoretically, there is no limit, but number and location of transducers will provide a limit and so will addressability; e.g., an 8-bit address can only reach 256 channels. Practical systems might have 30 to 60 channels.

Data uncertainty results mainly from the analog-to-digital conversion. The analog input can be held to .1%. The conversion contributes $\pm 1/2$ the least significant bit (LSB) which is approximately .2% for an 8-bit converter. This results in an uncertainty better than .25% overall.

3.4 Time-of-Arrival Systems

3.4.1 FM System

The measurement is not expressed in the amplitude of the signal (except for station

identification) but in the occurrence of the signal. This produces a pulse with an amplitude from zero volt to a predetermined level. Accurate absolute measurements are difficult because the pulses suffer various delays in the recording and/or telemetry channels before they can be detected. In addition, random jitter is contributed by the tape motion in the instrumentation recorder. Basic timing resolution is determined by data reduction capabilities which presently amount to 2 microseconds (for this system). All in all, absolute timing uncertainty better than several microseconds should be difficult to achieve.

The FM requirements are: The channel bandwidth should be as high as possible. Transmission bandwidth is limited by the recorder capability which is 500 kHz bandwidth in FM mode. Direct recording (2 MHz max) is also being used. The amplitude detection (station identification) is difficult and at times impossible. Because the pulses from some transducers are very narrow, the 2 microsecond sampling resolution is often not enough to reliably determine the amplitude of the pulse.

Stations can be triggered by all sorts of transients before the test and are then used up when the test comes along. The system cannot flag this condition.

3.4.2 Digital System

The transmission bandwidth is not of concern because it can be as low as the available cable dictates. This system has the same properties as the digital multiplex PCM system; i.e., short-duration measurements and forward resident memory for each channel. Resolution is typically .1 microsecond and accuracy should be several tenths of a microsecond. Total measurement capacity is 100 milliseconds, derived from specific test requirements.

Although the digital system is equally susceptible to noise interference on the measurement lines, it allows last-minute (count-down generated) reset of all channels. If a transient should still trigger a station before the arrival of the event, this measurement is flagged and the specific error is printed in line with the (false) results.

4. COMPARISON

4.1 Present FM Versus Forward FM

There is no question, considering cable cost, that the forward FM system is superior. The price to pay for the cable cost saved, however, is the need for higher stability of the forward VCO because it will not be as easy as with the present FM system to re-adjust the VCO's shortly before a test. Drift performance of the forward VCO's has not been obtained as yet. Another obvious consideration is that if the cable breaks, all channels of the forward system are lost; whereas, only specific

channels are lost due to cable breaks in the present configuration. Comparison of pertinent parameters is consolidated in Table 1. Signal-to-noise figure requirements are substantially different. Although these figures seem somewhat arbitrary, they are in the ball park and easy to remember. One very important column in terms of cost is the requirement for pre-computer data reduction; i.e., playback from analog tape, demodulation, analog-to-digital conversion, and system calibration.

4.2 FM Versus PCM (Digital Multiplex)

Again, the cable is a major factor in the comparison. Even though the forward FM system needs only one cable for transmission, it can handle only about a handful of channels and needs a wide bandwidth cable. Further, it is a real time system that is lost when the cable breaks.

The PCM system of the digital multiplex configuration can handle any number of channels, can use a low-grade cable (telephone quality), and is not out of commission when the cable breaks because the cable can be repaired before the transmission takes place. Another advantage is the wide bandwidth that every channel can have regardless of the number of channels (the FM spectrum range is limited, and the bandwidth per channel is inversely proportional to the number of channels in the system). Further, the permanent data record is in digital form, whereas the FM data are recorded on an analog instrumentation recorder. Pre-computer data reduction is not needed because digitization and system calibration are done in the field, thereby saving funds and time, especially when one considers that quick-look plots, scaled and calibrated, are available at the test site in a few hours after the test. Besides all these points, the system accuracy is by an order of magnitude higher than that of an FM system. Transmission line S/N requirements are very low due to the nature of the digital signal.

4.3 FM Versus PCM (Analog Multiplex)

System accuracy has the PCM advantage of low interference susceptibility, but everything else is like FM: A wide bandwidth cable is necessary and the channel bandwidth is inversely proportional to the number of channels in the system; also, costly and time-consuming pre-computer data reduction is necessary.

4.4 PCM (Analog Multiplex) Versus PCM (Digital Multiplex)

Main differences are the need for pre-computer data reduction and a wideband cable for the analog multiplex system, and its number of channels times data bandwidth limitation. With the digital multiplex system, data coverage is limited to the size of the channel memory.

TABLE 1
Comparison of System Parameters

	No. of Ch's	Data B.W.	Cable B.W.	No. of Cables	Recording	System Uncer- tainty	Trans- mission S/N Require.	Pre- Comp. Data Reduc.	Result Avail- able in	Per Channel Cost (\$)
Pres FM	8	10 kHz	10 kHz	8	Analog	> 2%	40 db	Yes	> 2 days	1000
New FM	8	1 J kHz	1 MHz	1	Analog	> 2%	20 db	Yes	> 2 days	600
PCM Analog Multiplex	8	7 kHz	1 MHz	1	Analog	< .3%	10 db	Yes	> 2 days	600
PCM Digital Multiplex	Any	20 kHz	100 Hz	1	Digital	< .2%	10 db	Not Needed	5 hrs	1000
Pres TOAS	8	500 kHz	500 kHz	1	Analog	~3 μ sec	20 db	Yes	> 2 days	500
New TOAS	Any	10 MHz	100 Hz	1	Printer	~.3 μ sec	10 db	Not Needed	1 hr	350

4.5 Analog and Digital TOA System

The digital system eliminates the need for the wideband cable of the present system due to the forward location of the acquisition operation and the memory-storage feature which is similar to the PCM system with digital multiplexing. Timing accuracy is improved by more than one order of magnitude. Also, station identification is completely assured because the channel number is automatically printed with the results. Again, the digital system does not need pre-computer data reduction. Its S/N transmission requirements are typically PCM, while the analog system which has to distinguish between two times four amplitudes in one multiplexed signal is more critical by at least a factor of 3.

4.6 Reliability

Without going into MTBF calculations, it is safe to say that analog circuits are generally more susceptible to deterioration than digital circuits due to drift that makes a system marginal long before fatal damage occurs. In terms of fatal damage, digital circuits may be only slightly better than their analog counterparts.

The need for analog instrumentation tape recorders in some systems decreases their reliability, while digital transmission over inexpensive lines should increase the reliability of these systems.

However, digital systems are generally more sophisticated than analog systems which tends to tilt the balance back in favor of the latter. Therefore, overall, it is difficult to find order of magnitude differences in reliability of the two types of systems.

Keep in mind that the reliability requirements on forward-placed or even transducer-integrated components are higher than for those with easy access for replacement.

4.7 Operability

The operation of a digital system is easier, simpler, and less cumbersome than that of an analog system. Analog systems need more setup, more rechecks, and usually cannot afford elaborate system exercises shortly before a test, whereas such operations can easily be automated in digital systems.

A digital system is set up once, and a complete system checkout can be performed any time without any more effort than initiating the procedure.

A complete checkout of an analog system involves the tape recorder and, therefore, pre-computer data reduction to obtain the result of a "dry run."

Other procedures, like system calibration, can also be automatically performed in digital systems during the execution of the test program.

5. PLACEMENT CONSIDERATIONS

Unless system accuracy is the overriding factor, there is a place for FM systems in the future. Based on cost-effectiveness, a forward FM system has merits in a location where only a few channels are clustered. When many more channels are clustered, but such that no unreasonably long transducer cables result, a PCM system is superior. However, for low data bandwidth, an FM system might still be more cost-effective than a PCM system with digital multiplex; but now competition comes from the PCM

system with analog multiplex which provides higher system accuracy than FM and is similarly cost-effective.

Similar considerations would seem to determine the use of the present or new time-of-arrival systems. However, the present system is so cumbersome to operate, so prone to system failures because of design shortcomings, and so time and cost consuming in pre-computer data reduction that it cannot be considered adequate any more.

6. SYSTEM COST

Excluding sensors and such labor-intensive costs as laying of cables, but including the cable themselves, the system cost is given on a per-channel basis for 1500 meters (5000 ft) of cable as a very rough estimate, just to provide an idea of the relative proportions. Keep in mind that the analog instrumentation recorder adds about \$200-300 per channel to the cost which is included. The cost of pre-computer data reduction however is not included, neither is the cost of waiting for the results of pre-computer operation (quick-look plots and digital tape). The times given in this column seem optimistic by the loudness of the complaints about this operation.

7. COST-EFFECTIVENESS

In choosing a system for a particular application, the cost per channel should not be the sole criterion. A system to be cost-effective should be chosen:

- a. First, to meet and not overly exceed the performance specifications, and then
- b. Has to have as low a cost figure as possible.

In evaluating the first requirement, one has also to investigate the value of certain performance features to the job at hand; e.g., what value does increased system automation have for an installation that has only a handful of channels. Without going into operations research and linear programming methods, it seems obvious that a system that best meets the requirements at the lowest price is a cost-effective system.

8. RECOMMENDATIONS

The present FM systems that use partially obsolescent equipment should gradually be phased out and replaced with forward FM systems (for which the feasibility of forward placement has to be established for a particular application) and/or with PCM systems with digital multiplex, and (for certain tests with lower frequency data) also with analog multiplex PCM systems.

The analog time-of-arrival system does not meet today's requirements and should be replaced by the digital system as soon as possible because of the increased system accuracy and the immediate availability of the results, without engaging precomputer data reduction. Detailed information on FM and PCM telemetry performance can be found in References [1, 2, and 4].

9. TECHNOLOGY TREND

The technology of large-scale integration of digital, as well as analog circuits and functions, leads to the prospect that all signal conditioning, filtering, analog-to-digital conversion, FM modulation, and line matching will eventually be integral with the transducer or as close to it as the environment allows. The first steps in this direction have been taken. Further steps depend on the availability of components, but low power consumption and reliability requirements will play a major role in how soon fully integrated transducers will be operable under field conditions.

REFERENCES

1. Myron H. Nichols and Lawrence L. Rauch, Radio Telemetry, John Wiley & Sons, New York, 1957.
2. Julius S. Bendat and Allan G. Piersol, Measurement and Analysis of Random Data, John Wiley & Sons, New York, 1966, pp. 278-282.
3. Josef F. Schneider and Allen L. Larson, "A PCM System for Forward Transient Data Acquisition," Proceedings of the 23rd International Instrumentation Symposium, 1977, pp. 525-530.
4. "Telemetry Standards," IRIG Document 106, Inter-Range Instrumentation Group, Range Commander's Council, White Sands Missile Range, NM.

LOADS AND ENVIRONMENTS

THE VIBRATION RESPONSE OF THE PHOENIX MISSILE IN THE F-14 AIRCRAFT CAPTIVE-FLIGHT ENVIRONMENT

MARSHA E. BURKE
Pacific Missile Test Center
Point Mugu, California

Vibration loads are an important cause of failures of air-launched missiles in the captive-flight environment. In order to reproduce these loads in testing it is first useful to understand the relationship between the induced vibration and the captive-flight parameters.

This paper investigates the vibration response characteristics of the PHOENIX missile on the F-14 aircraft in the captive-flight environment. Variations in vibration response with flight condition, mounting configuration, direction, and location along the length of the missile are examined. The conclusions drawn in this report add conformation to previous captive-flight vibration studies in establishing general correlations between captive-flight parameters and captive-flight vibration. The conclusions are: (1) vibration response in externally carried stores is directly proportional to dynamic pressure except in the transonic region where an increase in vibration occurs, (2) vibration response varies with platform configuration with an increase with additional externally carried stores in the flow field, (3) vibration response is most severe in the after section and in the vertical and lateral direction of the externally carried stores. The results of this paper are being used in the design of a laboratory captive-flight simulation. This simulation will be used to monitor the captive-flight reliability of new production and repaired PHOENIX missiles.

INTRODUCTION

Vibration of a PHOENIX missile was measured during the PHOENIX T-201/F-14 Flight Test Program conducted during January 1973 through July 1973 (reference 1), and during the PHOENIX/F-14 Captive-Flight Vibration Measurement Program conducted from September 1976 through July 1977.

Vibration was measured by means of a T-201 instrumented missile. The T-201 missile consists of a PHOENIX missile structure, with dummy internal units, which is dynamically representative of an actual missile. The warhead was replaced by a self-contained instrumentation system. This system was used to condition and record the outputs of the 10 accelerometers studied in this report. Figure 1 is a sketch of the missile showing the locations and orientations of the accelerometers. Accelerometers were mounted on major bulkheads. At missile positions 2 and 4, longitudinal vibration was not recorded.

An infinite number of flight conditions were available for analysis. The captive flights included steady state mach-altitude conditions with wing sweep varying from 0 degree to 68 degrees, accelerations, decelerations, left pedal sideslips, and right pedal sideslips. On the F-14 aircraft the

PHOENIX missile is carried on two aft fuselage stations, 4 and 5, two forward fuselage stations, 3 and 6, and two pylon stations, 1 and 8, as shown in figure 2. During these captive-flight programs, vibration was measured with T-201 carried on stations 5, 6, and 8. This report analyzes only data recorded at steady state mach-altitude conditions. Transient conditions were neglected because (with the exception of gunfire), they do not significantly affect vibration above 100 Hz and this combined with their small duration makes them an unimportant influence on missile mean-time-to-failure. Below is a list of the captive-flight variables studied:

Aircraft Configurations:	Configuration 1 consisting of:	Configuration 2 consisting of:
	6 PHOENIX	6 PHOENIX
	2 SIDEWINDER	
	2 fuel tanks	
Aircraft station:	5, 6, and 8	
Mach number:	0.47 to 1.73	
Altitude:	2,000 feet to 45,000 feet	
Position along length of missile:	1, 2, 3, and 4	
Direction:	vertical, lateral, longitudinal	

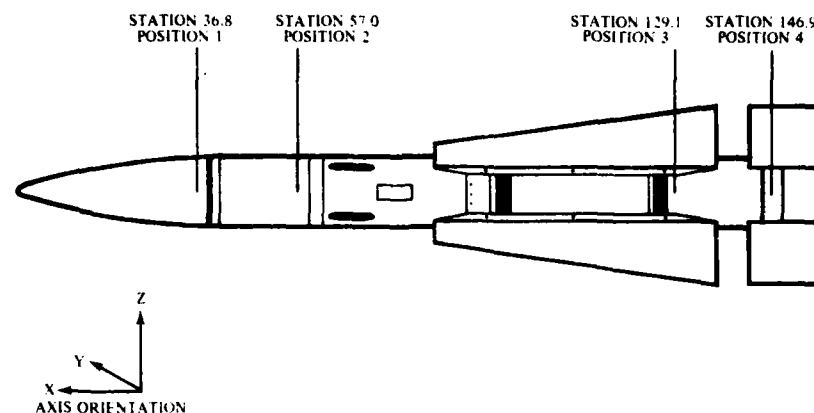


Figure 1. PHOENIX T-201 Environmental Measurements Missile

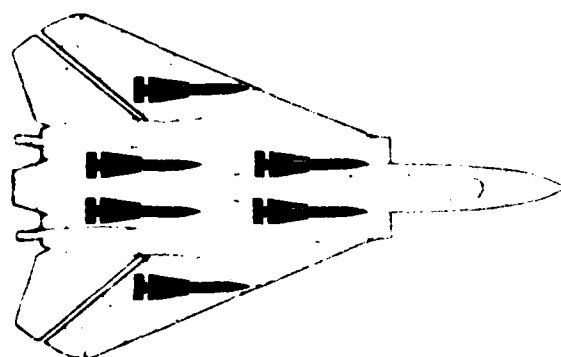


Figure 2. PHOENIX Missile Captive-Carry Stations on the F-14 Aircraft (As Seen From Above)

RESULTS

Variations With Flight Conditions

The major source of vibration in the captive-flight environment is aerodynamic boundary layer turbulence over the missile exterior surface (reference 2 and 3). Previous studies (reference 3 and 4) indicate that the rms value of the aerodynamic-noise-induced pressure fields and thus, the missile vibration produced by these pressure fields are approximately proportional to the flight dynamic pressure (q) for Mach numbers below 2. Earlier studies (reference 2), also suggest that increased vibration occurs in the transonic region. In the following section the captive-flight data will be analyzed to determine if the above described variations occur in the PHOENIX missile's vibration response.

In determining if PHOENIX vibration is proportional to q , the overall vibration level, over the frequency range 10 to 2560 hertz, for each flight condition was divided by the q for that condition. The "q-normalized" vibration levels were then plotted versus q . Data for each of the ten accelerometers was plotted separately for aircraft stations 5, 6, and 8. This was done to separate variations caused

by configuration, physical location and direction, which will be discussed later. The general trend of the "q-normalized" vibration level versus q plots was a horizontal band varying in width from approximately 15 to 60 percent depending on aircraft configuration and accelerometer location. This agrees with the theory that vibration response is linearly proportional to q . An example is shown in figure 3. The pylon station at the after portion of the missile showed an increase in the "q-normalized" vibration level for q s below 0.70 Mach number. This can be noted in figure 4. A less pronounced increase also was exhibited by flights on the forward fuselage station in the after portion of the missile.

The phenomenon of increased vibration in the transonic region was investigated by plotting "q-normalized" overall vibration levels versus Mach number. The results confirmed that there is an increase in the overall vibration level on all aircraft stations and for almost every measured position. An example is shown in figure 5. Note that the increased vibration occurs at Mach 0.88 and not at Mach 0.9 to 1.0. This is typical and is probably associated with local transonic flow in the neighborhood of the missile. This suggests that in the transonic region the linear relationship between vibration level and q has a higher proportionality constant than in the subsonic and supersonic regions. Table 1 shows the average "q-normalized" vibration levels for each station. The subsonic, transonic, and supersonic regions were defined as Mach numbers from 0.0 to 0.84, from 0.85 to 1.0, and from 1.0 to 1.7, respectively. The pylon station showed a decrease in "q-normalized" vibration level for Mach numbers higher than 1.3 by approximately a factor of 2. The forward fuselage station tended to show an increase in "q-normalized" vibration level for Mach numbers higher than 1.3 by a factor of approximately 1.4. Positions 2Z, 4Z, and 4Y when flown on the after fuselage station exhibited a constant decrease in "q-normalized" vibration level from Mach number 0.45 to 0.87 then a leveling off. Figure 6 shows an example of this phenomenon.

Up to this point, the overall vibration level has been analyzed for its relationship to q and Mach number with no mention of how the vibration spectrum varies with q

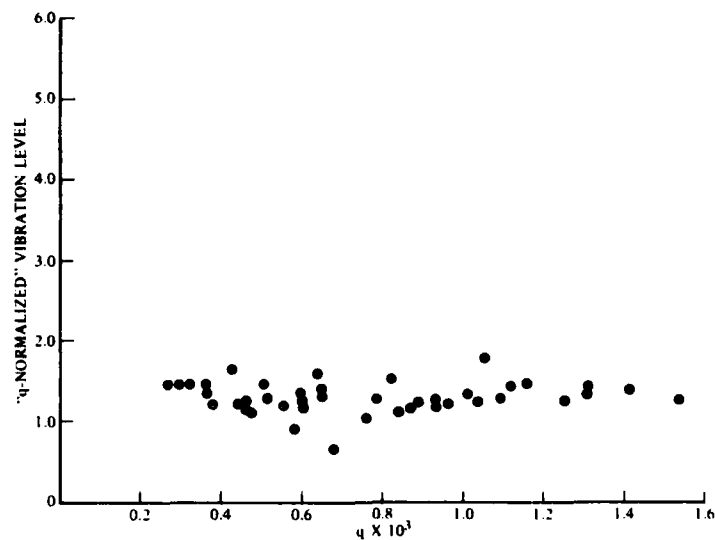


Figure 3. PHOENIX T-201 Missile "q-Normalized" Vibration Response Versus Dynamic Pressure (q) on Aircraft Station 6, Missile Position 2 in the Z Direction

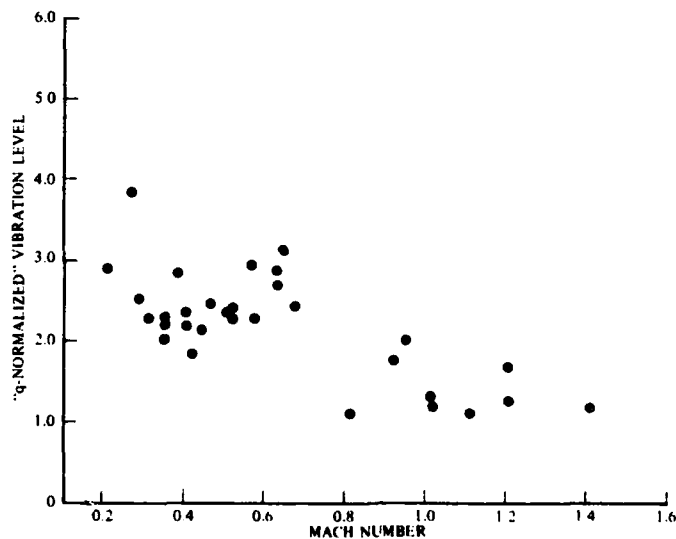


Figure 4. PHOENIX T-201 Missile "q-Normalized" Vibration Response Versus Mach Number on Aircraft Station 8, Missile Position 4 in the Y Direction

and Mach number. Fifteen captive-flight conditions were chosen for spectral analysis for each of the three stations 5, 6, and 8. Captive-flight conditions varied from Mach numbers of 0.68 to 1.60 and altitudes from 2,000 to 35,000 feet for this analysis. Power spectral density plots from 10 to 2560 hertz were made for each aircraft station and each accelerometer position. These were normalized with q and then plotted together to form an envelope. The envelopes varied from ± 2 to ± 5 db in width. Two examples are

shown in figures 7 and 8. The results revealed that the vibration spectrum does not vary with dynamic pressure or Mach number. However, there was an exception when the missile was carried on the after fuselage station, the front section of the missile, (positions 1 and 2), exhibited an increase in vibration energy in the 1200 to 2500 hertz range during transonic flights. Figure 9 is a comparison of a subsonic and a transonic power spectral density at missile position 2Y on the after fuselage station.

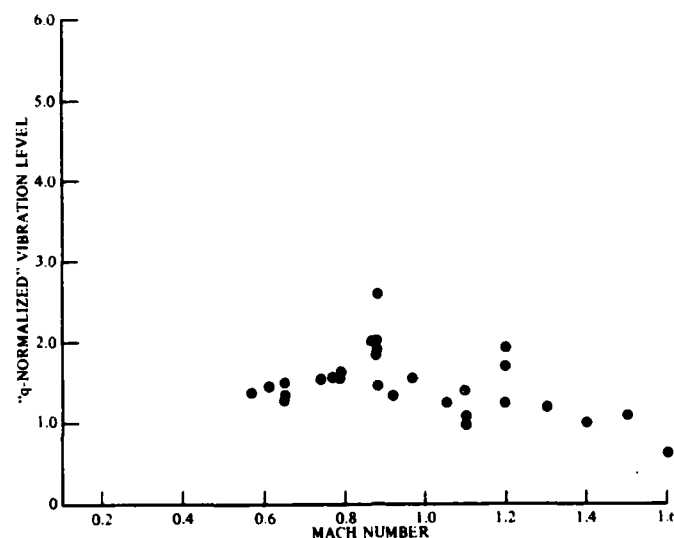


Figure 5. PHOENIX T-201 Missile "q-Normalized" Vibration Response Versus Mach Number on Aircraft Station 8, Missile Position 2 in the Y Direction

Table 1. PHOENIX T-201 Average "q-Normalized" Vibration Level for F-14 Aircraft Stations 5, 6, and 8

Aircraft Position	Station 5			Station 6			Station 8		
	Subsonic	Transonic	Supersonic	Subsonic	Transonic	Supersonic	Subsonic	Transonic	Supersonic
1Z	1.07	1.12	1.03	0.58	0.67	0.58	0.63	0.79	0.50
1Y	0.93	1.03	0.96	0.85	1.04	1.40	0.71	0.79	0.54
1X				0.65	0.55	0.49	0.52	0.56	0.37
2Z	1.86	1.97	1.56	1.19	1.28	1.41	1.29	1.59	1.21
2Y	1.92	2.94	2.60	1.44	1.58	1.79	1.44	1.83	1.36
3Z	5.60	5.52	5.70	3.18	3.64	3.73	4.04	5.33	3.08
3Y	3.71	3.91	3.71	2.26	2.58	2.30	2.34	2.75	1.94
3X				1.43	1.60	1.52	1.34	2.06	1.18
4Z	3.65	3.80	3.56	4.09	4.16	3.70	4.42	5.64	2.96
4Y	1.90	1.47	1.78	2.17	2.10	1.95	2.25	2.66	2.36

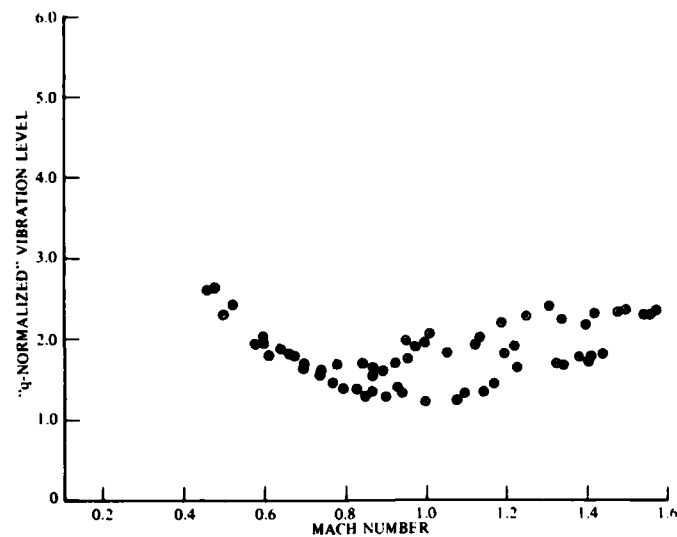


Figure 6. PHOENIX T-201 Missile "q-Normalized" Vibration Response Versus Mach Number on Aircraft Station 5, Missile Position 2 in the Z Direction

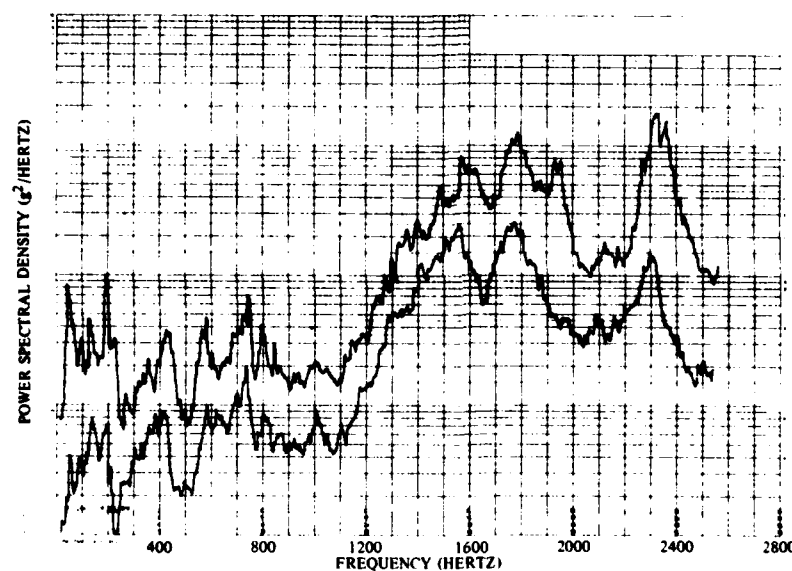


Figure 7. PHOENIX T-201 Missile Vibration Response Envelope on Aircraft Station 6, Missile Position 4 in the Z Direction

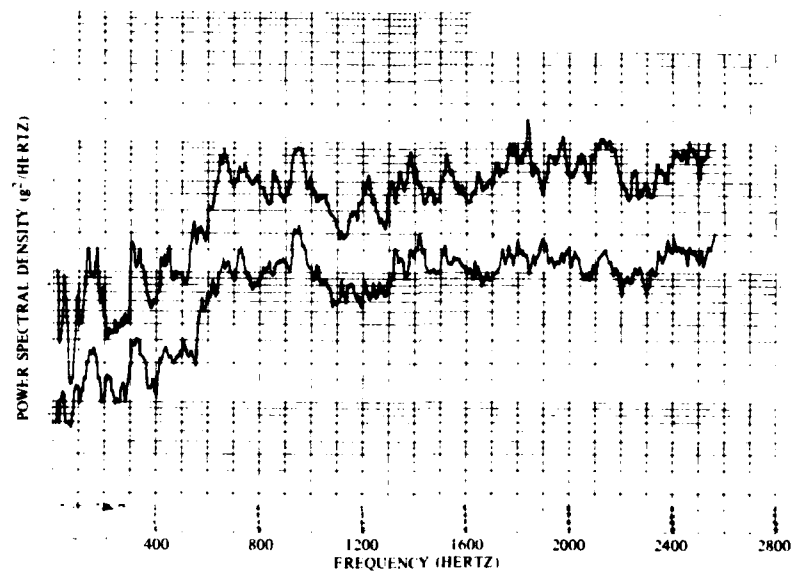


Figure 8. PHOENIX T-201 Missile Vibration Response
Envelope on Aircraft Station 6, Missile Position 3
in the Y Direction.

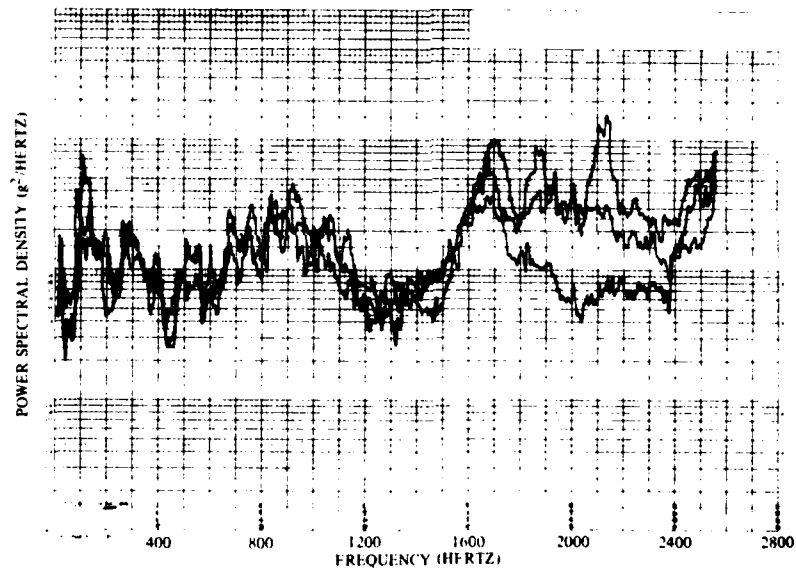


Figure 9. PHOENIX T-201 Missile Vibration Response
Envelope on Aircraft Station 5, Missile Position 2
in the Y Direction

Variations With Configuration

As stated earlier, the PHOENIX missile is captive carried on F-14 aircraft on six different aircraft stations. In addition to these possible configurations there are a variety of other externally carried stores that can be carried in conjunction with the PHOENIX missile. Figure 10 shows the two configurations used in collecting PHOENIX captive-carry data. Configuration One was realized by six PHOENIX missiles, two SIDEWINDER missiles and two 300 gallon tanks. This configuration was used in the PHOENIX T-201/F-14A Flight Test Program. Configuration Two, used in the PHOENIX/F-14 Captive-Flight Vibration Measurement Program, was that of six PHOENIX missiles. Vibration data from both programs was used in analyzing the after fuselage vibration. Analysis of the forward fuselage and the pylon stations was accomplished using data only from the first program. Data from the second program for these stations is not yet available.

In analyzing vibration on the after fuselage station, it was noted that data from the first captive-flight program tended to have a higher overall vibration level for the same flight conditions. This suggests that the configuration in the first captive-flight program produced increased vibration due to the increased aerodynamic boundary layer turbulence caused by the two 300 gallon (1135.6 liter) tanks. An example of this is shown in figure 11.

Ratios of the "q-normalized" vibration level averages for comparing the overall vibration levels produced on the different stations were calculated for each accelerometer position. These ratios are shown in table 2. Data for positions 1X and 3X were not available on the after fuselage station. Data was analyzed separately for subsonic, transonic, and supersonic regions to minimize variations caused by Mach number. The results show that the vibration on the after station is significantly more severe in most cases than vibration on the forward fuselage or pylon station.

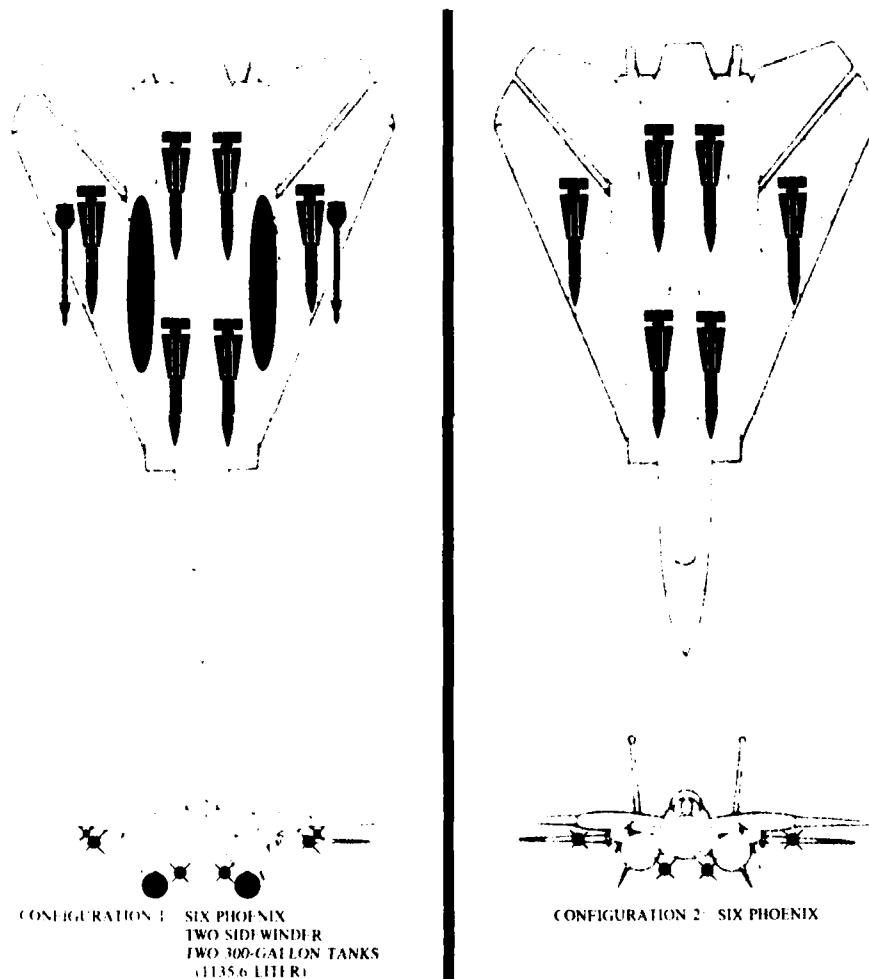


Figure 10. F-14 Aircraft Configurations As Seen From Above and Front

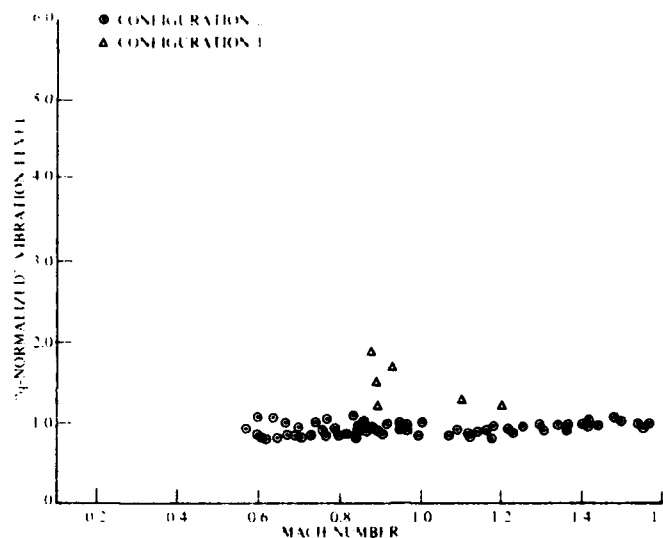


Figure 11. PHOENIX T-201 Missile "q-Normalized" Vibration Response Versus Mach Number on Aircraft Station 5, Missile Position 1 in the Y Direction

Table 2. Comparison of the Averaged "q-Normalized" Vibration Levels on F-14 Aircraft Stations 5, 6, and 8

Aircraft Position	Subsonic		Transonic		Supersonic	
	5/8	6/8	5/8	6/8	5/8	6/8
1Z	1.69	0.92	1.42	0.85	2.06	1.16
1Y	1.31	1.20	1.29	1.36	1.77	2.59
1X	--	1.25	--	0.98	--	1.32
2Z	1.44	0.92	1.25	0.72	1.28	1.17
2Y	1.33	1.00	1.61	0.86	1.91	1.32
3Z	1.39	0.79	1.04	0.68	1.85	1.21
3Y	1.59	0.97	1.42	0.94	1.91	1.19
3X	--	1.07	--	0.78	--	1.29
4Z	0.83	0.93	0.67	0.74	1.20	1.25
4Y	0.84	0.96	0.53	0.76	0.75	0.83

Vibration occurring on the forward fuselage or pylon station during subsonic and transonic are indistinguishable in overall level. In supersonic flight there is an increase in vibration level on the pylon station relative to forward fuselage station vibration.

Looking at power spectrum density (PSD) variations with configuration it was found that the PSD envelopes produced by all three stations coincided with the exception of the after fuselage station forward part of the missile transonic data as noted in the previous section.

Variations With Physical Location and Direction

Vibration measurements were made in the forward and after region of the missile along each of the orthogonal axes (vertical, lateral, and longitudinal) as shown in figure 2.

Vibration tests generally specify the application of excitation to the missile along these same orthogonal axes; therefore, it is of interest to determine variation in vibration level with location and direction. Overall vibration levels were found to be significantly more severe in the after region of the missile for each aircraft station. This holds true in each direction. Figures 12, 13, and 14 show the "q-normalized" vibration level averages (taken from table 1) plotted versus position along the missile's length for subsonic flight conditions. This variation with position probably reflects the build up of boundary layer turbulence along the missile and the greater coupling to this turbulence provided by the wings and control surfaces at the rear of the missile. Variation in vibration level versus direction were small in the forward region of the missile. The vibration level was higher in the after part of the missiles and the level varied with direction. The Z axis showed the highest level, followed by Y and X. This is shown in figures 12, 13, and 14.

DISCUSSION

Variations With Flight Condition

The PHOENIX missiles overall vibration response level suggests that vibration response is linearly proportional to q over the entire mach number - altitude regime. The only exception being the transonic region in which the overall vibration level was higher for the same q than for non-transonic flight. This indicates that a higher proportionality constant than in the subsonic and supersonic region is characteristic of the transonic region. While the overall vibration level was proportional to q , the spectral distribution of the vibration response produced in the missile was found to be independent of q and constant throughout the PHOENIX envelope. This was found to be true for each of the measured positions and directions on each of

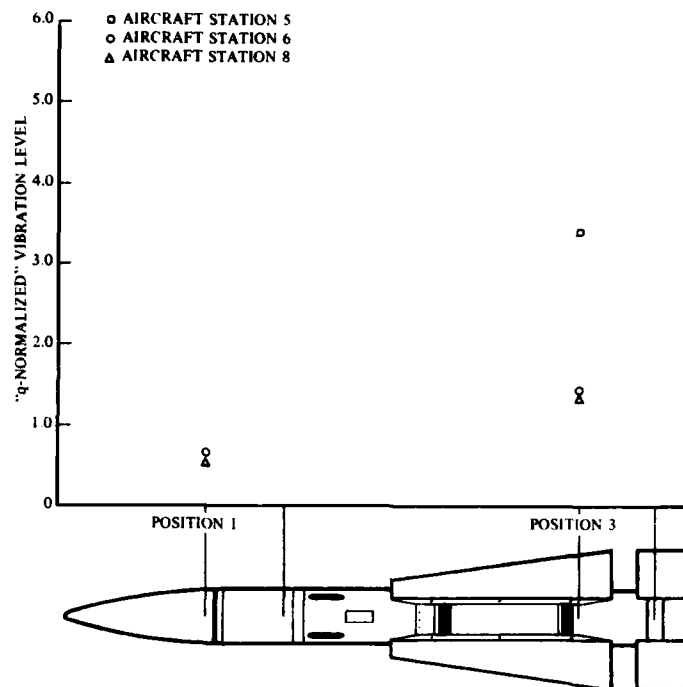


Figure 12. PHOENIX T-201 Missile "q-Normalized" Vibration Response for the Subsonic Captive Flight as Traversed Along the Length of the Missile in the X Direction

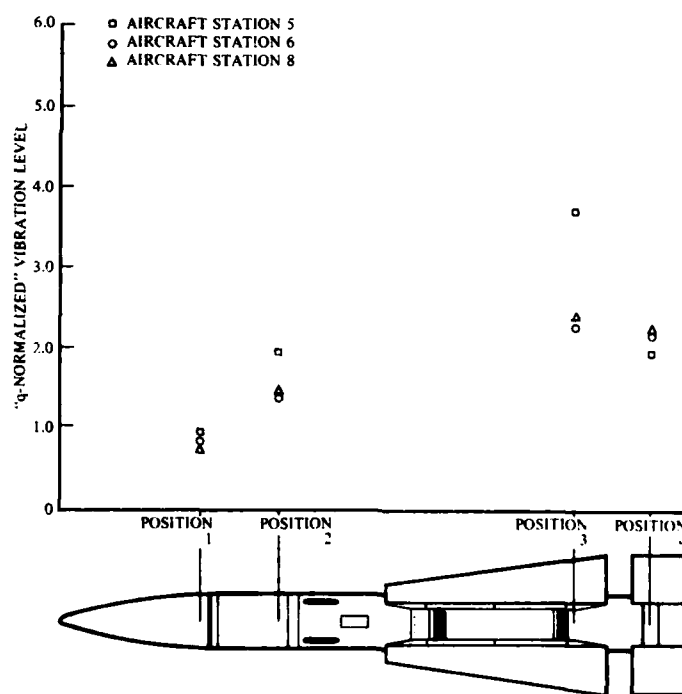


Figure 13. PHOENIX T-201 Missile "q-Normalized" Vibration Response for the Subsonic Captive Flight as Traversed Along the Length of the Missile in the Y Direction

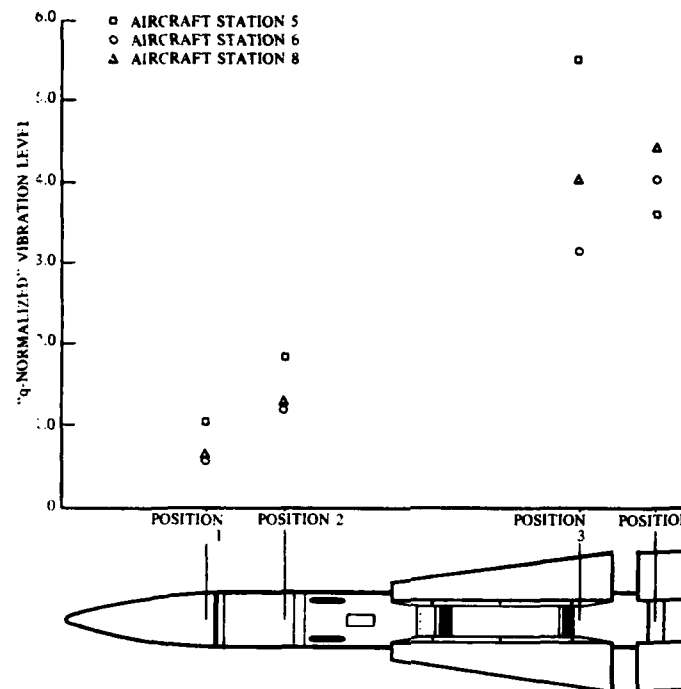


Figure 14. PHOENIX T-201 Missile "q-Normalized" Vibration Response for the Subsonic Captive Flight as Traversed Along the Length of the Missile in the Z Direction

the measured aircraft stations. This phenomenon along with the q proportional to vibration level greatly simplifies the design of captive-flight simulation tests. In testing, once a vibrational input that reproduces the missiles captive flight response is determined, all that is necessary to simulate the entire mach number altitude regime is to vary the level of the vibration input such that the overall vibration response increases proportionally to q and the response spectrum remains constant.

In general, the captive-flight measurements suggested that vibration response is linearly proportional to q . However, at some positions, there was a high degree of scatter; as much as ± 60 percent in one case. The cause of this scatter is not known. Perhaps there is another captive-flight variable that affected these accelerometers that is not yet recognized.

Variations With Configuration

In determining the dependence of vibration response on captive carry station, the forward fuselage and the pylon station data were found to be indistinguishable in terms of power spectral distribution and overall vibration level. Captive carry on the after fuselage station produced a higher overall vibration level and also displayed a more pronounced transonic effect. The transonic effect was in the form of an equal increase in energy over the entire range of frequency plus a pronounced increase in the 1200 to 2560 hertz range. The other two stations also exhibited the equal increase in energy over the entire range. The pres-

ence of other externally carried stores increased vibration response of the adjacent PHOENIX missile. The vibration response of missiles not adjacent to the additional stores showed no noticeable increase.

Variations With Physical Location and Direction

Concerning the distribution of vibration levels from one point to another along the missiles length, it was found that vibration in the after section was more severe than the forward section by a factor of 2.4. The vibration in the vertical direction is more severe than the lateral or longitudinal directions with vibration in the lateral more severe than the longitudinal.

CONCLUSIONS

This report studied the causes of variation in vibration response for externally carried stores. With the support of previous studies (reference(s) 2, 3, and 4) concerning externally carried stores, the following conclusions may be drawn concerning all externally carried stores:

1. Vibration responses in externally carried stores is directly proportional to dynamic pressure (except as modified by 2 below).
2. Vibration response in externally carried stores increases in the transonic region.

3. Vibration response varies with platform configuration with an increase occurring with additional externally carried stores in the flow field.

4. Vibration response tends to be more severe in the after section of externally captive carried stores.

5. Vibration response is more severe in the vertical and lateral directions than in the longitudinal direction in externally carried stores.

6. The relationship between the induced vibration and captive-flight parameters is not adequately understood.

With further analysis of this and other captive-flight data, the relationship between induced vibration and the captive-flight parameters will be more fully understood. Variations such as (1) the large scatter in vibration level that occurs at certain positions along the missile in certain directions, (2) the changes in vibration level at certain mach numbers and aircraft station, and (3) the changes in the frequency spectrum that occur during transonic flight only on specific aircraft stations and only in the forward part of the missile need to be explained. Understanding of these relationships will facilitate the improvement of captive-flight vibration predictions and simulation of the captive-flight environment for externally carried stores. The improvement will be accomplished because assumptions and compromises for the purpose of simplification will no longer have to be blindly made.

Discussion

Mr. Christo (Naval Underwater Systems Center): Why did the vibration level increase due to the presence of other external stores?

Miss Burke: Because there was more turbulence when there were other external carried stores in its vicinity.

Mr. Silver (Westinghouse): We are concerned about this: I think we need a lot more stress distribution type statements. We are concerned about the requirement for testing for long periods of time at insignificant stress levels. You have defined the very probable stress for a very large population. How does your work compare with the requirements of Method 514 in MIL-STD-810C for external store vibration tests? Do you think higher levels at the rear of the external store is largely the function of whether fins are present? MIL-STD-810C calls out factors for a smooth body at the rear of the vehicle versus a finned vehicle.

Miss Burke: I would imagine the vibration response in the rear is caused by the boundary layer build-up along the length of the missile and the fins are another surface on which the boundary layer acts. Yes I imagine that the fins do have a significant effect. In regard to your question about MIL-STD-810C, when we have actual captive flight measurement data we do not rely on MIL-STD-810C and that has

REFERENCES

1. Hughes Aircraft Company. "PHOENIX T-1/F-14A Flight Test Status Report." Aerospace Systems Division, Canoga Park, California, DM-73-232, December 1973.
2. Piersol, A. G. and J. C. Calkins. "SPARROW Missile Captive-Flight Simulation of Dynamic Loads." Naval Missile Center, Point Mugu, California, TP-73-35, 1973.
3. Piersol, A. G. "Vibration and Acoustic Test Criteria for Captive Flight of Externally Carried Aircraft Stores." Digitek Corporation, Marina Del Ray, California, R1D-4-FDL-1/B004, AFFDL-TR-71-158, AD 893-005L, December 1971.
4. Coe, Charles F. "Surface-Pressure Fluctuations Associated With Aerodynamic Noise." NASA Ames Research Center, Moffett Field, California, NASA SP-207, July 1969.

been very important concept. There is another paper that I co-authored with Angelo Spandrio where we performed an acoustic test and we compared our test levels to those in MIL-STD 810C and we wound up actually reproducing the captive flight level for the Phoenix missile.

Mr. Silver: The stresses in the trans-sonic region are pretty high compared to the other periods of time. If your high stresses act on a body it may be that you are only really concerned with testing between the 2 sigma and the 3 sigma level. It is inevitable that you will have to test at those high stress distributions, but do you really have to test all that time below the 2 sigma level?

Miss Burke: You may have to test at all of the different levels and it depends on the purpose of the test. If you are trying to reproduce the different types of failures that you get in captive flight then you need to reproduce the whole vibration distribution because at high level you will not get the numbers of the same types of failures unless you do. You can probably cut out some levels and that depends on the type of test. That is a question we are asking at the Pacific Missile Test Center and we would like to do more work on it.

Mr. Wayman (McDonnell Douglas): What are the factors that you put into your data?

Miss Burke: This would be a overall increase in the vibration level.

Mr. Wayman: When you talk about testing the missile are you talking about testing the complete missile and using this as response data?

Miss Burke: There were different transducers at different points in the missile.

Mr. Wayman: Which one would you use?

Miss Burke: We used all of them. We tried to reproduce the vibration level at each of these positions in the laboratory.

Mr. Wayman: You didn't find any variation in your frequency response regardless of the flight parameter that you monitored. Did you actually investigate angle of attack variations where you got into buffet conditions?

Miss Burke: No, all of the data were steady state. Some of it was very slow acceleration or deceleration.

Mr. Wayman: I think you will find that there is a significant variation in the frequency spectrum as you pull maneuvers as you get into buffet onset and so forth. You would have to or you should consider these environments when you evaluate the missile.

SOME DYNAMIC RESPONSE ENVIRONMENTAL MEASUREMENTS
OF VARIOUS TACTICAL WEAPONS

W. W. Parmenter*
Naval Weapons Center
China Lake, California

This paper reports on pertinent results of several environmental dynamic measurement programs for widely diverse types of tactical weapons. Included are spectra for the SLUFAE weapon mounted on a tracked vehicle, the ASROC missile mounted within launcher cells and magazines of various classes of ships, the FAE-II and GATOR free-fall weapons captive-flown on A-7 and AV-8 aircraft, the Condor weapon captive-flown on an A-6 aircraft, and the MAD-FAE weapon dispenser system suspended beneath a CH-53 helicopter. The character of the dynamic environments during weapon deployment is briefly discussed.

BACKGROUND

An integral and vital part of verifying system reliability is to simulate realistically the significant environments and thus provide better correlation with possible service failures. The methodology of developing environmental criteria for a weapons program is given in MIL-STD-1670A (Reference 1). (The philosophy and guidelines reflected in Reference 1 are general in nature and therefore the use of "AIR LAUNCHED" in that document's title does not necessarily limit its content to that category of weaponry.) Reference 1 addresses, in a logical manner, the development of the environmental design criteria which should then be presented in living traceable documents for a weapons program during its anticipated use during the factory-to-target sequences. In many instances when a new weapon program is being planned, certain environmental areas are questionable and there have been no prior similar operational experiences. Even when such areas have been previously probed there are no known qualitative retrievable data in many cases. These areas must then be given special attention. If these ambiguities are of enough significance to impact a program, formal plans for environmental data acquisition should be submitted early in the program development time scale, so that if design changes are required, the time and cost due to these changes will be diminished. Most of the environmental measurements presented in this paper were taken for the purpose of providing data where none existed or where there were questionable areas.

Many instances can be cited where, in the past, engineers or specification writers involved in a new program have been unaware of the existence of environmental data pertinent to their project or the magnitude thereof. A search for such information should be made in many cases and there are a number of places to begin. To name just a few there are the Sandia Environmental Data Bank (Reference 2), individuals at the Shock and Vibration Information Center, Wright-Patterson Air Force Base, Dayton, OH, and the Naval Weapons Center, China Lake, CA. These data thus located may not apply exactly but may often be tailored to fit or information can be perceived that is applicable to the general nature of the environment for the particular program. In the dynamic environments, problems sometimes do arise as to the applicability of the data, as mentioned in the Introduction of Reference 3. Also, in the light of this discussion, a recent report on specifications and standards has been published (Reference 4). The discussion and conclusions of Reference 4 should be thoroughly reviewed and understood by those concerned with the weapons acquisition process. The methodology of Reference 1 should then be reconsidered, keeping in mind the results of Reference 4.

In the following three data presentations, instrumentation, test acquisition, and methods of analyses are not stressed. These details are fully defined in the respective referenced documents. In general, however, the environmental measurements were made with standard accelerometers whose signals were recorded on

*American Society for Quality Control Certified Reliability Engineer, P.E.

magnetic tape, then digital spectral analyses were performed.

(1) TRACKED VEHICLE CARRIAGE

Shock and vibration measurements were made with an M-548 6-ton tracked cargo carrier configured as shown in Figure 1. Loaded with 30 SLUFAE weapons in the launcher pod assembly, limited road tests were performed in conjunction with the U. S. Army Missile Command at Redstone Arsenal, AL. The effect of the vehicle speed with the tread-laying frequency was very evident in both the time and frequency domains. Typical acceleration power spectral density (PSD) plots for the aft end of the SLUFAE weapon in the launcher pod are shown in Figures 2 and 3. These plots are for an asphalt paved road at 15 and 20 mph, respectively, and contain the highest measured discrete vibration levels; the spectra show the data to be complex periodic. Compared to a paved road, travel over other road conditions such as imbedded rock and wooden ramps provided higher overall RMS-g vibration levels. This is because the background random noise level is increased. The background maximum observed noise level was about $0.001\text{-g}^2/\text{Hz}$ over the 2-kHz data response. Figure 4 results from removing the vibration g-values for the discrete vehicular tread-laying frequencies from the respective acceleration spectra, converting these to peak values, and replotting as a function of the tracked vehicle speed.

Transient responses were measured for a number of vehicle speeds (3, 6, 9, and 12 mph) and varying size bumps (6-, 8-, and 12-inch radius). The maximum observed transient level at the aft end of the weapon was 18.2 g (0-peak) for less than 50 milliseconds.

A complete documentation of the work summarized above is contained in Reference 5.

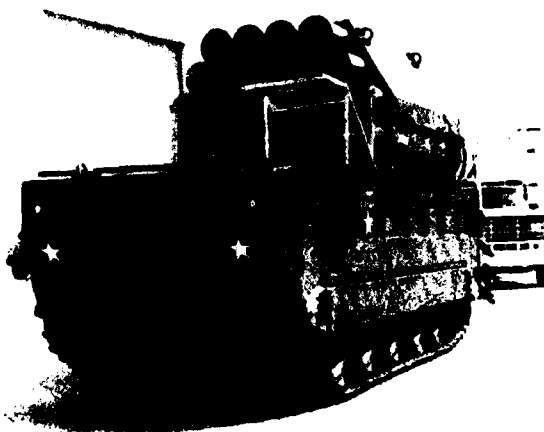


FIGURE 1. Launcher Vehicle M-548 with SLUFAE Round Launcher Mounted in Aft End Cargo Compartment.

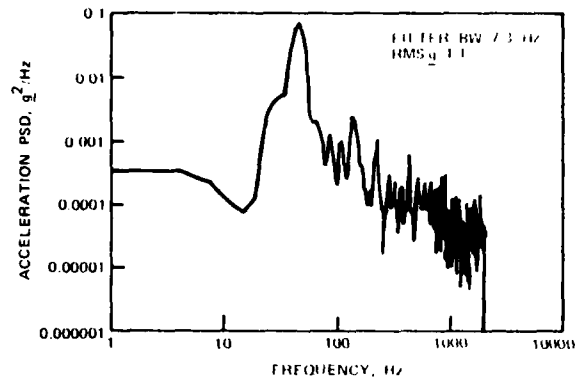


FIGURE 2. PSD Plot for 15 MPH, Vertical Axis, Aft Motor Sensor, SLUFAE Launcher Vehicle Test.

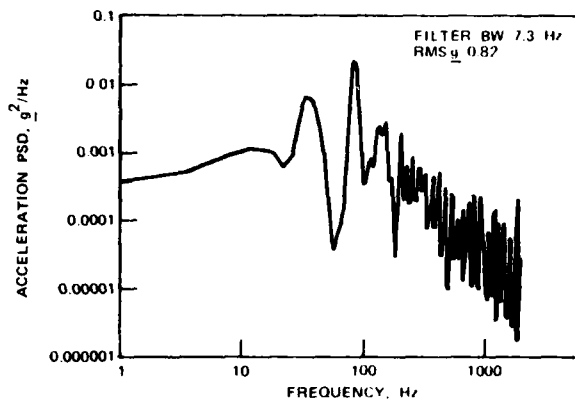


FIGURE 3. PSD Plot for 30 MPH, Vertical Axis, Aft Motor Sensor, SLUFAE Launcher Vehicle Test.

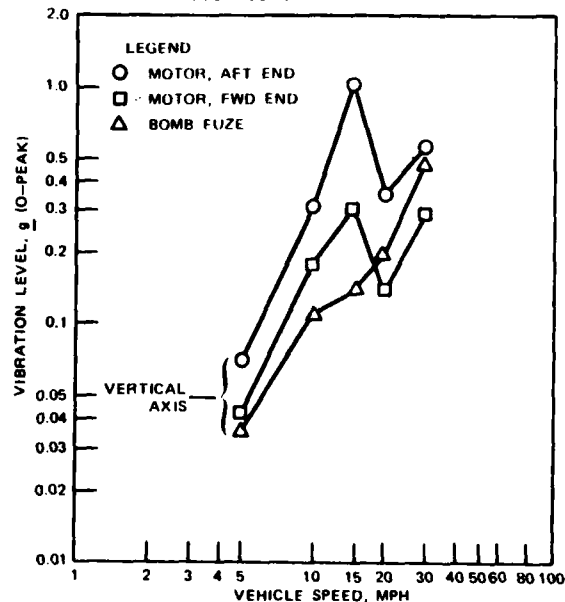


FIGURE 4. Replot of Vibration g Values for Discrete Vehicular Track-Laying Frequencies, Vertical Axis.

(2) SHIPBOARD CARRIAGE

The shipboard vibration test measurement subjects were instrumented ASROC missiles located in the storage magazines and launcher cells of five classes of U. S. Navy ships. The forcing function inputs were measured by accelerometers mounted near the structural support pedestal of the launcher and a chock support in the magazine situation. The ships included in the survey were:

1. USS Elliot (DD-967), Spruance class, five-bladed propellers, twin screw, controllable pitch
2. USS Hepburn (FF-1055), Knox class, five-bladed propeller, single screw, constant pitch
3. USS Hollister (DD-788), Gearing class (FRAM I), five-bladed propellers, twin screw, constant pitch
4. USS Preble (DDG-46), Coontz class, four-bladed propellers, twin screw, constant pitch
5. USS Blandy (DD-943), Sherman class, four-bladed propellers, twin screw, constant pitch.

The data were recorded on straight runs at various speeds, turns at various rudder angles, and crashback maneuvers. The tests were conducted during operations under calm sea conditions. Figure 5 shows a typical ASROC launcher installation. Figure 6 is a PSD plot typical of the newest class ship. Vibration responses were very benign in both the launcher and the magazine. Maneuver effects produced only negligible vibration.

Figures 7 and 8 show the effect on an older class design (Knox) ship. These spectra show the data to be complex periodic. Figure 9 is the result of performing narrow-band sweep analysis on the worst recorded conditions. These were obtained from test measurements on the USS Hollister (Gearing class). Also plotted in Figure 9 is the specified variable frequency curve from MIL-STD-167-1(SHIPS). Comparison is made to show the wide variation in energy between the maximum measured vibration during the five-ship ASROC test program and the shipboard vibration test standard, Reference 6.

It was obvious in all tests that the vibratory forcing functions to the stationary weapon were transmitted through the ship structure from the engines, gearing, and rotating shafts. Also, it was generally apparent that turn maneuvers produced the highest vibration levels to the launcher or magazine area.

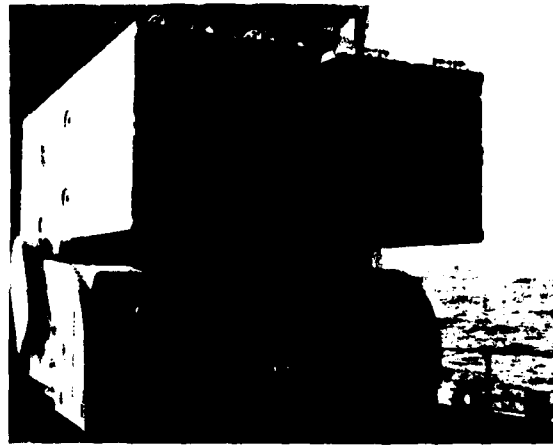
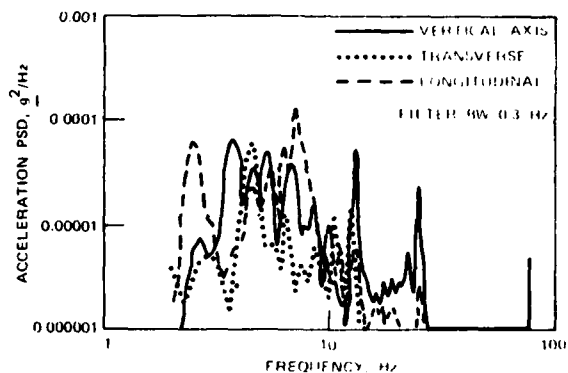
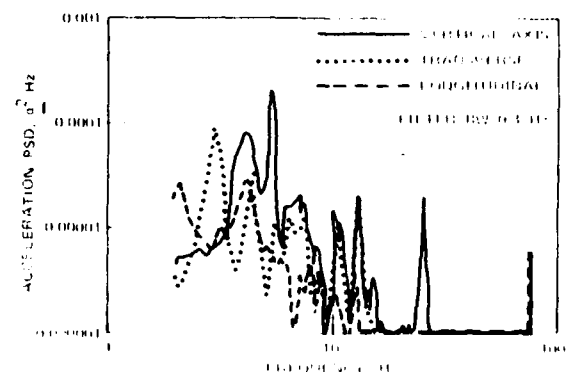


FIGURE 5. Typical Shipboard Installation of the ASROC Launcher.



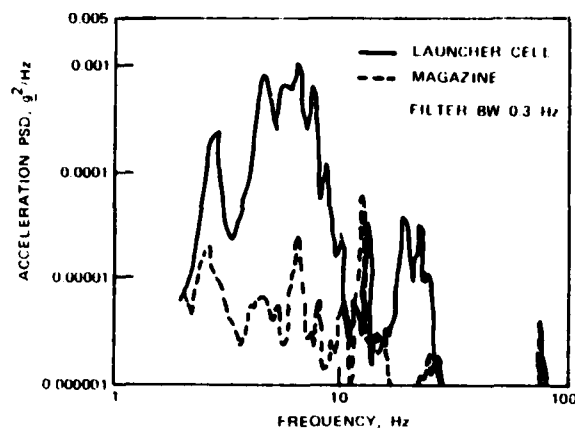
(a) Deck/Pedestal Base Location of the ASROC Launcher.

FIGURE 6. Typical Acceleration Power Spectral Density Plots on the USS Elliot (DD-967): 23 Knots, Starboard Turn.



(b) Magazine Location at Base of Rotary Storage Assembly.

FIGURE 6. Typical Acceleration Power Spectral Density Plots on the USS Elliot (DD-967): 23 Knots, Starboard Turn.



(c) Transverse Accelerometer Located on the Forward End of the ASROC Missile.

FIGURE 6. Typical Acceleration Power Spectral Density Plots on the USS Elliot (DD-967); 23 Knots, Starboard Turn.

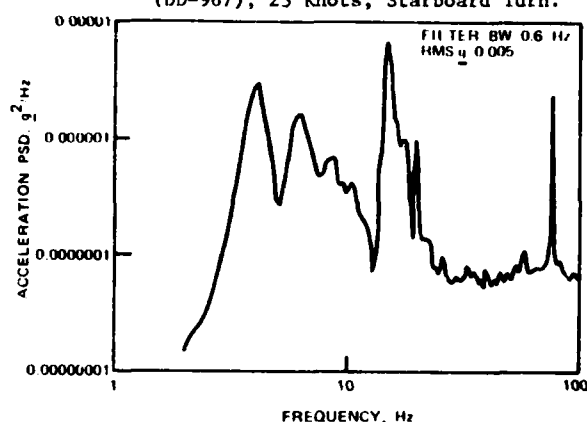


FIGURE 7. Deck/Pedestal Base Location, Vertical Axis, ASROC Launcher, USS Hepburn (FF-1055); 23 Knots, Port Turn.

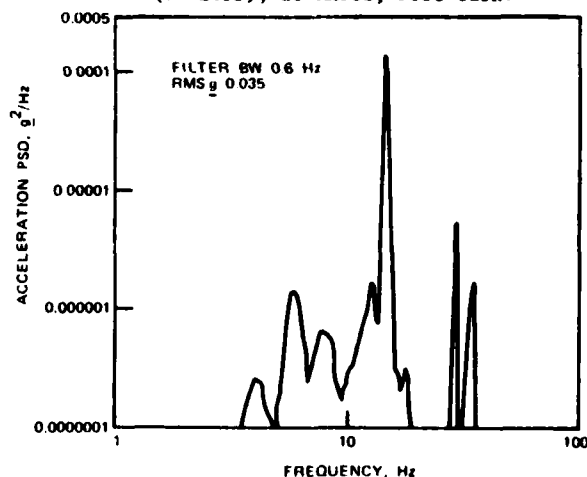


FIGURE 8. Magazine Location, Transverse Accelerometer on the Forward End of the ASROC Missile, USS Hepburn (FF-1055); 23 Knots, Port Turn.

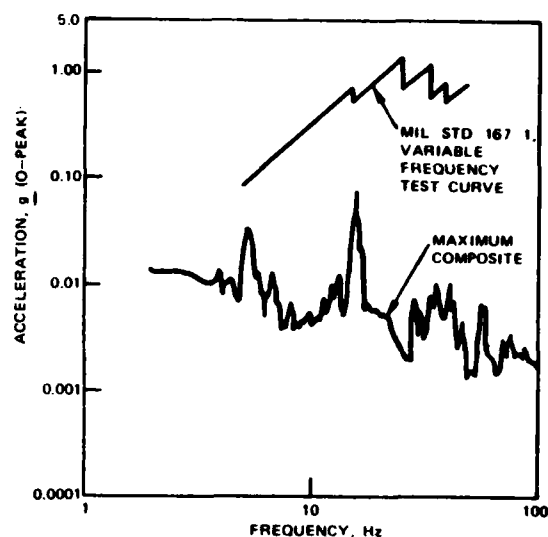


FIGURE 9. Comparison of Maximum Measured ASROC Acceleration Levels with MIL-STD-167-1.

(3) AIRCRAFT CARRIAGE

Captive flight vibration measurements were performed on several aircraft and store configurations. The most recent test programs cover the following aircraft and weapons:

1. A-6 jet aircraft with the Condor missile
2. A-7 jet aircraft with the FAE-II free-fall weapon
3. AV-8 jet aircraft with the GATOR free-fall weapon
4. CH-53 helicopter with the MAD-FAE weapon dispenser system suspended beneath.

Vibration data for the Condor missile were obtained during captive flights on the A-6 aircraft. The spatial distance between the adjacent pylons is apparently great enough so that adjacent store effects are not observed. Typical spectra for different free-stream dynamic pressures (350, 450, 550, and 650 psf) are shown in Figure 10. These are for the vertical axis accelerometer in the forward lug. Generally, they are seen to be more wide-band random with some sinusoids superimposed upon the spectra. Spectra for other missile body stations are presented in Reference 7. During another separate study effort, an interesting series of tests determined the vibration responses of the four actuators for the Condor missile aft control surfaces. Again, these were captive flown on an A-6 aircraft under varying flight conditions and store configurations. What was intuitively apparent was measured and observed: the inboard actuators closest to the undersurface of the aircraft wing had the highest vi-

bration responses. A typical maximum PSD from the summary report of Reference 8 is presented in Figure 11.

The FAE-II free-fall weapon, shown in Figure 12, was captive flown on the A-7 aircraft. The effect of dynamic pressure with measured overall RMS-g for the vertical axis accelerometer at the forward lug during straight and level flight is shown in Figure 13. During rolling maneuvers, the spectra exhibited a 20-Hz resonance (Figure 14). Since this was not a weapon mode found during ground vibration tests, it is most likely a wing-pylon-store mode. The remaining higher frequency of the spectrum is typical of broad-band random noise due to turbulent boundary layer excitation along the surface of the weapon. More test particulars and spectra may be found in Reference 9.

An unusual store response vibration situation was reported in Reference 10. The GATOR weapon, a 500-pound class free-fall device, was mounted at the inboard pylon of the AV-8 aircraft as shown in Figure 15. On the aircraft fuselage, at nearly the same plane as the store and adjacent to the inboard store pylon, is located one of the engine exhaust ducts for the thrust vector control of the aircraft. During high-speed flight, the duct is swept rearward and the weapon response was shown to be the result of turbulent boundary layer flowing over the surface of the weapon. However, during the relatively slow speed hover flight condition, the weapon responds to the flow effects and acoustic field of the exhaust duct when it is pointed down. The result is that the vectoring low-speed flight produces weapon vibration responses of the same magnitude as found during non-vectoring high-speed flight. Acoustic levels and PSD plots are presented extensively in Reference 10.

Vibrations were monitored of a large package suspended beneath a helicopter as depicted in Figure 16. The 4,000-pound MAD-FAE weapon dispenser was hung 20 feet below the CH-53 helicopter. Figures 17 and 18 show the PSD plots during a hover and a 140-knot flight condition, respectively. The vertical axis accelerometer was located near a forward structural suspension point. Obviously, the data are complex periodic and at the 140-knot speed little energy was imparted from the forward air flowing over the dispenser. Other accelerometer data are presented in Reference 11.

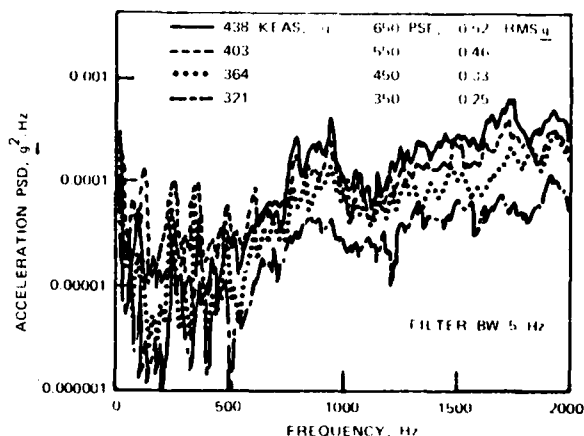


FIGURE 10. Typical Variation of PSD with Dynamic Pressure for the Vertical Axis, Forward Lug, of the Condor Missile; Pylon of A-6 Aircraft, Straight and Level at 5,500 Ft (MSL).

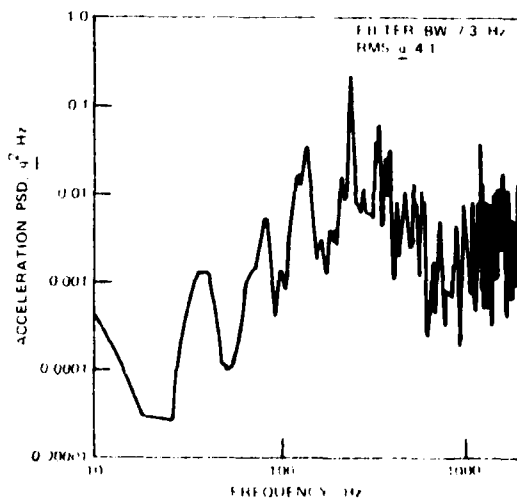
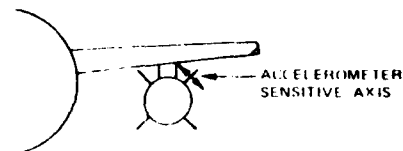


FIGURE 11. Maximum Actuator PSD, Upper Inboard Control Surface of the Condor Missile; Inboard Pylon, Straight and Level A-6 Captive Flight, 527 Knots, 10,000 Ft (MSL).

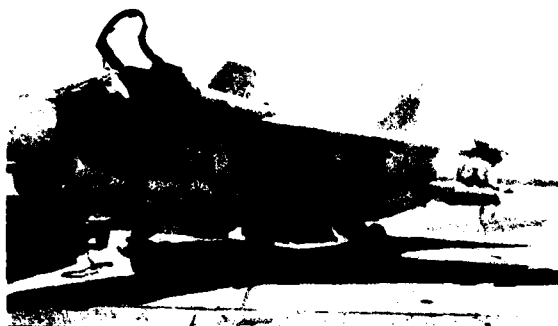


FIGURE 12. Overall View of the 500-Pound FAE-II Weapon Mounted on A-7 Aircraft.

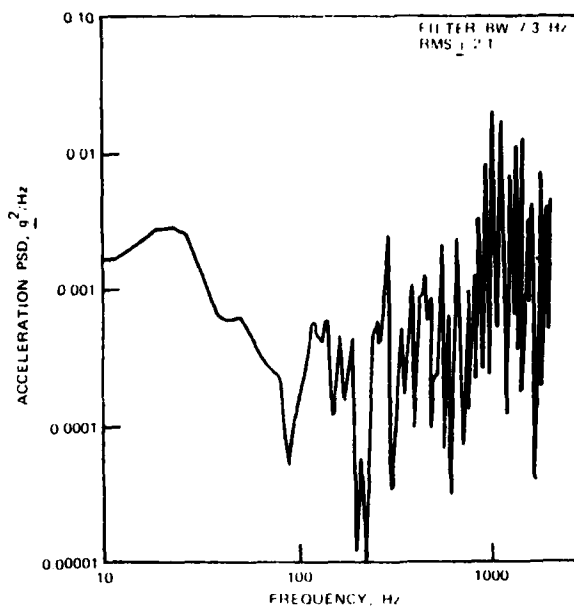


FIGURE 14. Maximum PSD Plot Measured for the Forward Lug, Vertical Axis of the FAE-II Weapon. Rolling 1-g maneuver, 562 Knots, 9,540 Ft (MSL).

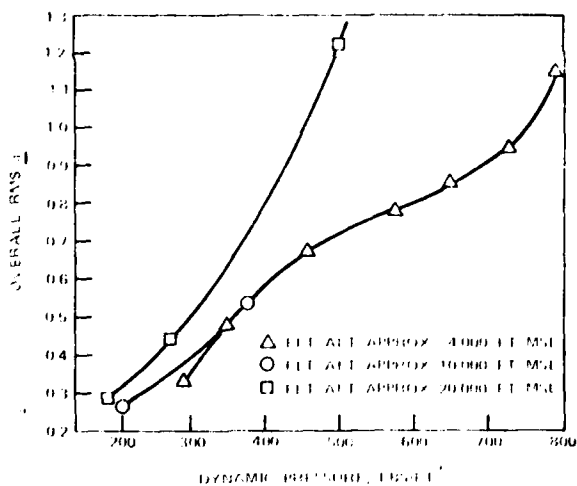


FIGURE 13. Measured Overall RMS-g vs. Free Stream Dynamic Pressure at the Forward Lug of the FAE-II Weapon, Vertical Axis. Straight and Level Flight Conditions.

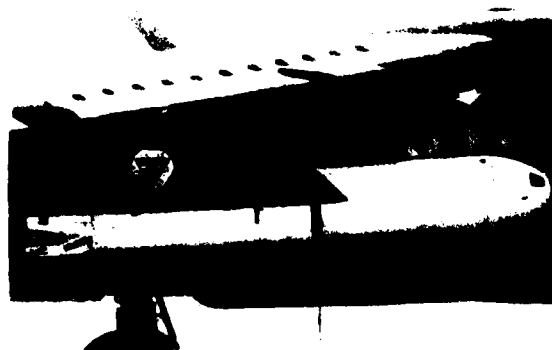


FIGURE 15. GATOR Free-Fall Weapon Mounted at the Inboard Pylon of the AV-8 Aircraft. Note Thrust Vector Nozzle (Arrow).

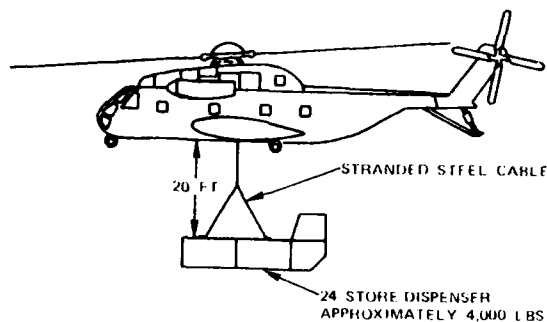


FIGURE 16. MAD-FAE Weapon Dispenser Suspended Below the CH-53 Helicopter.

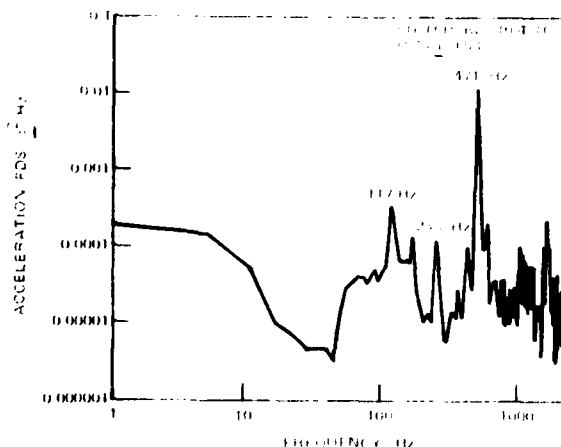


FIGURE 17. Typical PSD Plot at a Forward Suspension Point on the MAD-FAE Dispenser Suspended Below the CH-53 Helicopter. Hover Flight Condition at 100 Ft (AGL).

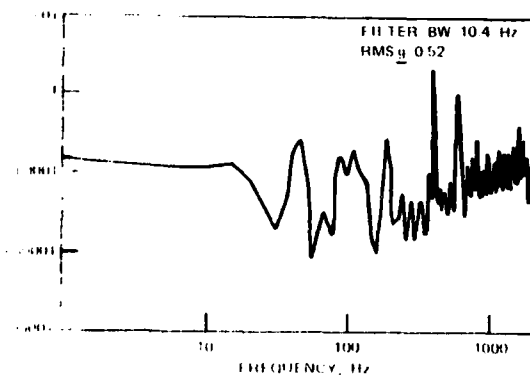


FIGURE 18. Typical PSD Plot at a Forward Suspension Point on the MAD-FAE Dispenser Suspended Below the CH-53 Helicopter. Straight Ahead Flight at 140 Knots.

SUMMARY

Typical results for several environmental measurement programs have been presented. This is the beginning of developing realistic dynamic tests for simulating the use environment for an all-up tactical weapon within the guidelines of MIL-STD-1670A. The next step should be the determination of the optimum inputs and fixturing which will result in the closest reproduction of the weapon response to its service forcing functions. A necessary part of these methods is the careful documentation of all measurements, fixturing, and test and analysis procedures.

The tests reported herein are typical of many such investigations conducted at NWC, China Lake, CA. These test results have been of considerable value in formulating test parameters for use with several weapon programs at this facility. It is the view of this author that such data as that presented herein may well be of practical value to other Government and contractor activities. It is the further opinion that open presentation of the results of efforts such as those reported herein may help to prevent many costly duplications of effort.

ACKNOWLEDGEMENTS

The material presented herein is the result of the effort of several individuals associated with the NWC Environmental Engineering group. These include: Messrs. Joseph Lelis and Ronald Shargots for technical assistance and conducting the ship measurements; Mr. Pasqual Mercado for the SLUFAE/tracked vehicle, GATOR/AV-8, and MAD-FAE/CH-53 measurements; Mr. Kenneth Katsumoto for the GATOR/AV-8 and FAE-II/A-7 measurements; the Digital Development Branch, NWC, and Mrs. Ruth Klever for data processing and analysis assistance.

REFERENCES

1. Environmental Criteria and Guidelines for Air-Launched Weapons. 20 July 1976. (MIL-STD-1670A.)
2. ERDA/DOD Environmental Data Bank Index by C. A. Davidson, J. T. Foley, C. A. Scott; March 1976. SAND74-0255A, Sandia Laboratories.
3. Vibracoustic Environment and Test Criteria for Aircraft Stores During Captive Flight, by Dreher. Supplement, p. 3, 29th Shock and Vibration Symposium. April 1969.
4. Report of the Task Force on Specifications and Standards: Defense Science Board, Office of the Director of Defense and Research and Engineering, Department of Defense, April 1977.
5. Test Report for the Environmental Dynamic Response Measurements tests of the SLU-FAE Round/Launcher Vehicle Carriage, by W. W. Parmenter. Naval Weapons Center, China

Lake, CA, July 1976. (NWC TM 2944.)

6. Mechanical Vibrations of Shipboard Equipment (Type I - Environmental and Type II - Internally Excited. 1 May 1974. (MIL-STD-167-1 (SHIPS).)
7. AGM-53A Guided Missile (Condor), Captive Flight Vibration Measurement and Analysis, Report on Results of. 4 November 1970. (NWC Reg. 4533-55-71, 45332/WWP:ar.)
8. Condor (AGM-53A) Actuator Captive Flight Vibration Environment Measurements, Report on Results of. 20 October 1975. (Reg. 4533-041-76, 4533/WWP:be.)
9. Vibration Measurements Made on a BLU-95 FAE-II Weapon During Captive Flight on an A-7E Aircraft, by K. T. Katsumoto. Naval Weapons Center, China Lake, CA, August 1977. (NWC TM 3266.)
10. GATOR/AV-8A Environmental Captive Flight Vibration Response Tests, by K. T. Katsumoto and W. W. Parmenter. Naval Weapons Center, China Lake, CA, February 1977. (NWC TP 5883.)
11. Results of Captive-Flight Vibration Measurements of the MAD-FAE Weapon System Suspended Under the CH-53 Helicopter. 9 April 1974. (Reg. 4533-118-74, 4533/WWP:ar.)

Discussion

Mr. Luke (Los Alamos Scientific Lab): Was the dynamic response of the ASROC measured when the launcher was in the inclined position or rotated during any kind of maneuver or did you measure the general response of the weapon?

Mr. Parmenter: It was in a stored position all the time.

Mr. Pearson (Air Force Flight Dynamics Lab): It seems to me from looking at your PSD charts that the most severe environment was the tracked vehicle.

Mr. Parmenter: I wouldn't want to answer that yes or no. It depends upon the purpose of the test that you are using to simulate the environment. If you are performing a structural test the sinusoidal vibration of test will have more structural effect on your item. If you are after a subcomponent or a subassembly perhaps one of the more random type environments would be more severe so that can be answered both ways.

TURBULENT-BOUNDARY-LAYER EXCITATION AND
RESPONSE THERETO FOR A HIGH-PERFORMANCE CONICAL VEHICLE

C. M. Ailman
McDonnell Douglas Astro. Corp. Employee for this work.
Currently an independent researcher in Los Angeles, Calif.

Ground and flight test data from a high-performance maneuverable vehicle called ACE suggest several revisions to the empiricisms used to develop dynamic environmental criteria for RV's. Part I of this paper includes 1. a compiled data bank for describing the fluctuating pressures that force the shell of a non-maneuvering RV to vibrate during reentry, and a discussion on the use of local aerodynamic parameter values for the cone when predicting these pressures, and 2. a description of the characteristics of shell-mode vibration peculiar to a conical structure with a multilayered skin. Part II reports flight data from such a structure when maneuvering as a result of flow disturbance at the aft end. The data suggest some angle of attack dependencies not previously detected, and indicate low frequency response of the vehicle as a beam. The beam response is analytically examined as to its probable cause.

INTRODUCTION PART I (NON-MANEUVERING)

This first part, of a two-part paper examines the prediction techniques for dynamic environments of a non-maneuvering conical shell re-entering the earth's atmosphere. The need for such an investigation became obvious when examining the results from a flight vehicle called ACE. ACE was a conical reentry vehicle with a composite shell that employed flaps to produce maneuver. Ground tests and flight data from ACE revealed characteristics that differed from those predicted by conventional cylindrical-vehicle techniques applied to sections of the cone. As a consequence, some engineering effort was performed to verify and explain these differences. It is this effort which is detailed in the following pages. In particular, use of local aerodynamic parameters is discussed as a method to normalize boundary-layer-induced, and base, fluctuating pressure data to permit extrapolation to various geometries. Also, differences between pressure/vibration transfer functions for aluminum cylindrical sections and for laminated cones are explained. Part II of this paper examines two particular data trends from fluctuating pressure and vibration sensors located

on the primary shell of ACE vehicles which were maneuvering part of the time. These two trends deviate markedly from conclusions reached for non-maneuvering reentry vehicles in Part I.

FORCING FUNCTION

This section deals with fluctuating pressures induced by undisturbed aerodynamic flow over the surface of a reentry vehicle, and the equivalence of ground-test acoustic fields (idealized for the purposes of analysis). The intent is to provide pressure magnitude estimates, and to establish the validity of simulating the flight forcing function with a ground-test pressure field which will induce comparable response.

Turbulent-Boundary-Layer-Induced Pressure Fluctuations

Figure 1 is a fairly comprehensive compilation of data for Mach numbers greater than 1 (the historically interesting work at subsonic speeds by the experimental pioneers having been omitted for brevity) describing the fluctuating pressures beneath a turbulent bound-

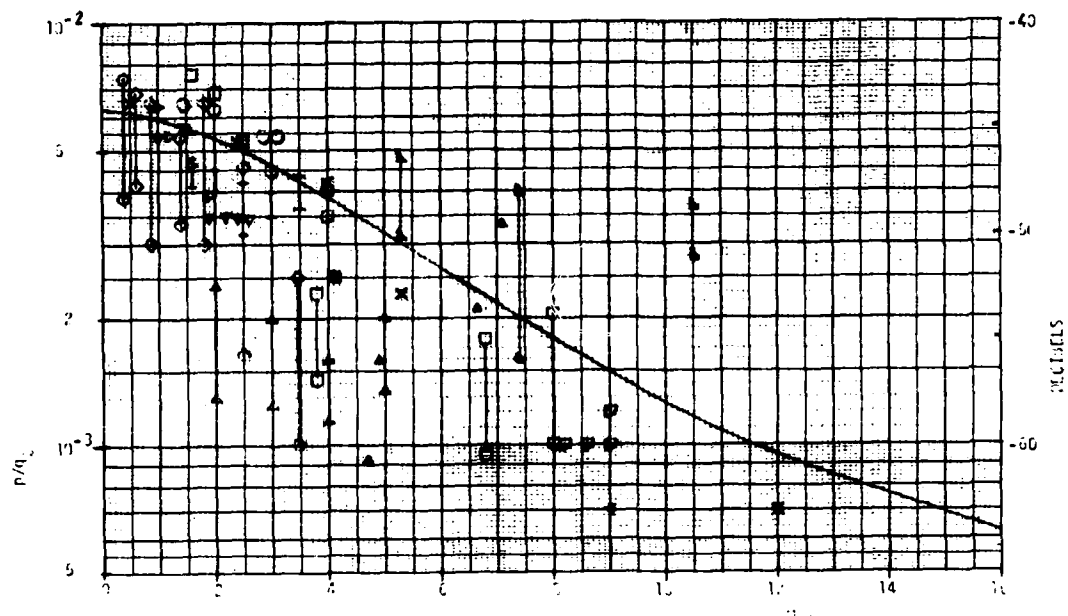


FIGURE 1 SUMMARY OF FLUCTUATING PRESSURE DATA

LEGEND FOR FIGURE 1

- Belcher
- Chaump, et. al. (GE)
- CHYU & Hanly (Freq. Extended)
- Coe & CHYU
- Coe (B70)
- Harvey
- Heller
- Kistler & Laufer
- Maestrello
- Raman
- Speaker & Ailman
- Wallace
- ABC2 Flight Data (65,000 ft.)
- PVTO-3B-02 Flight Data
- Solid Line Curve - Modified Lowson

dary layer. The data suggest that similar dependencies exist for the nonmaneuvering, high-velocity cone as for flat plates and long cylinders if momentum thickness θ , local Mach number M_0 and local dynamic pressure q_0 are utilized as the normalizing parameters. The momentum thickness θ is used in preference to other boundary layer thickness parameters for two reasons; namely, the collapse of normalized data is superior and it has physical interpretation even when dealing with disturbed flows (e.g. separated flow). Figure 1 includes data from high velocity cones by normalizing to the local parameters. By this means, these reentry vehicle data are comparable to the other data. If free stream values had been used, most of the data points would have been off the graph. Use of local parameters is physically plausible. For long cylinders or flat plates (the source of much of the data on Figure 1), the local and free stream Mach numbers are essentially the same. For cones, the characteristics behind the strong, oblique bow shock determine the pressures at the wall (as opposed to the free stream values).

Each datum on Figure 1 has been corrected for frequency limitations. That is, for flight measurements or for those ground tests in which the whole spectrum to cut-off has not been measured, the data are compared on the basis of the limited frequency range. For example, the ABC2 and RVTO-3B-02 data as well as the Chyu

and Hanly measurements have been raised to account for the unmeasured portion of the spectrum to cut-off. Cut-off is here meant to be that frequency beyond which the turbulent-boundary-layer-induced pressure spectrum rapidly decreases. Figure 2 indicates such a cut-off frequency for wall pressure spectra beneath turbulent boundary layers with local Mach numbers greater than 1.0.

The solid line on Figure 1 is the empiricism of Ref. 1 with the coefficients modified to better reflect the data. The analytical expression for the solid line is:

$$\frac{p}{q_\infty} = \frac{0.0063}{1 + 0.04 M_\infty^2}$$

where p is the overall fluctuating pressure in the same units as q_∞ . There are large discrepancies in the Mach range of 2-7, but the modified Lowson curve seems to conservatively represent the majority of the data. Most of the measured spectra agree with the trend of Figure 2. In general then, Figures 1 and 2 depict the wall fluctuating-pressure-data trends exhibited by the well-behaved, slowly-growing, attached, turbulent, supersonic/hypersonic boundary layer.

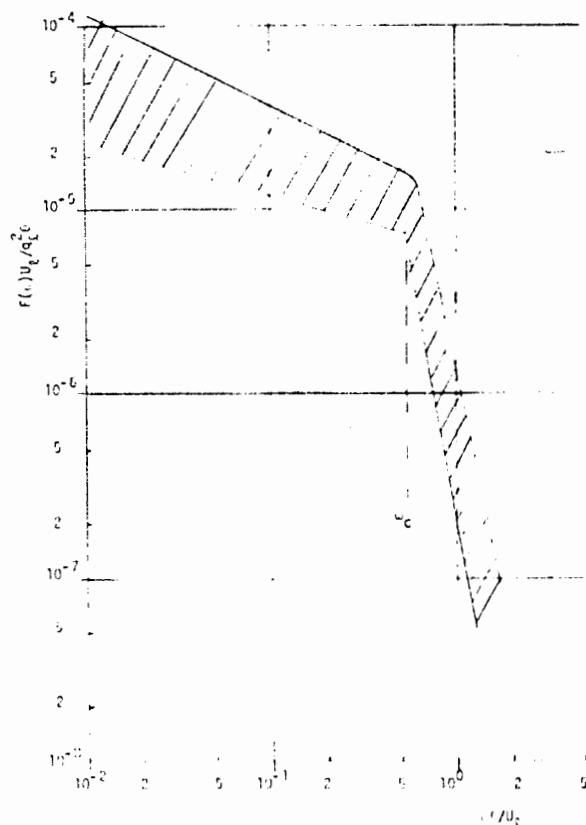


FIGURE 2 NORMALIZED POWER SPECTRUM BENEATH UNDISTURBED, TURBULENT, SUPERSONIC/HYPERSONIC BOUNDARY LAYERS

Fluctuating Pressure Levels Compared to Acoustic Fields

Fluctuating Pressure Levels (FPLs) at the vehicle surfaces due to the flow of turbulent boundary layers were discussed above. However, nothing was said about the spatial and temporal characteristics which influence the transfer of energy from the air flow to the structure. Modal analysis of steady-state response using the concept of "joint acceptance" from Ref. 2, indicates a dependence of the response on the matching of correlated (in-phase) spatial areas of the forcing function with the corresponding spatial extent of the in-phase modal response. This means that when the FPLs of the forcing field are in phase over the response in-phase surface area and oscillating at the same frequency, they will be optimally efficient in driving continued resonance response of that mode; in contrast, an out-of-phase pressure over part of that same surface area will tend to cancel the response (and be proportionately less efficient). Mathematically, the joint acceptance function is a measure of this coupling efficiency between the forcing pressure field and the mode of vibration in question. A qualitative comparison was made to determine the relative efficiency of the pressure field under a high-speed turbulent boundary layer as compared to a ground-test-facility acoustic field (e.g., reverberant field or the field in a progressive wave tube).

The analysis ignored coincidence effects which occur at higher frequencies than were of interest here. The intent was to determine the best acoustical facility to use for simulating the reentry vehicle environment, and thus measure valid responses. The analysis assumed ideal acoustic fields in each of the facilities, and had the restriction noted above. Thus, the most desirable ground test approach was identified, but specific pressure levels required to simulate response from specific FPLs were not analytically defined. Experimental data were used for this latter task.

A reverberant acoustic field was calculated to be the best match to a reentry environment for the measured range of frequencies. This is not surprising since the mathematical form for the narrow-band cross-correlation (Ref. 3) of the boundary layer FPLs (damped cosine) is very similar to a reverberant room description ($\sin kx/kx$) and considerably different from say a progressive wave tube (undamped cosine). Using a compilation of experimental data and the above analysis, the reverberant field was predicted to produce equal responses to that

of the turbulent boundary layer FPLs over a frequency range of 150-2800 Hz within a ± 5 dB accuracy (greater accuracy being achieved if 2 dB was added to the middle two octave band FPLs when estimating equivalent SPLs). The progressive wave tube was calculated to be 10-15 dB less efficient than either of the above for the same frequency range. Hence, measurement of energy transfer functions in a reverberant acoustic field is deemed representative of flight data. Such transfer functions were determined for the reentry vehicle ACE and are discussed in a later section.

Base Pressure Fluctuations

An AIAA paper (Ref. 4) provides a valuable data contribution to the limited information on base pressure fluctuations. In the paper, the data were for a range of free-stream Mach numbers from 0.67 to 2.2. The limited data that were presented collapsed to a single curve reasonably well when free stream values of dynamic pressure (q_∞) and Mach number (M_∞) were used. The expression for this curve, given in the reference, is $OABPL = 20 \log_{10} q_\infty - 20 \log_{10} |M_\infty^2 - 1| + 93$ if q_∞

is in psf., and $OABPL$ = maximum overall fluctuating-pressure-level on the base in dB. Octave band BPLs (in dB) were as follows: the band whose geometrical mean frequency (gmf) was $0.16 U_\infty/D$ (where U_∞ is the free stream velocity and D is the base diameter) had a level of $OABPL - 5.4$. Below this band, the slope was -1.5 dB/octave while above it, the slope was -4 dB/octave. Unfortunately, the whole computation is based on free stream variables, and is derived from 8° half-angle cones with flat bases. When a large angle of attack is in effect, or the geometry is different from that studied, data are not extant to guide the user. The writer, therefore, developed similar equations from the above data using the local values for the normalizing parameters. Since flat surfaces or long cylinders have free stream and local parameters that are essentially the same, these new equations may also be applied to them interchangeably. A maximum overall BPL which depends on the local values of q_l and M_l at the end of a cone is as follows (with a ± 4 dB accuracy): $OABPL = 20 \log_{10} q_l - 80 \log_{10} M_l$

+ 114. The peak octave band level is found in the frequency band whose gmf = $0.16 U_l/D$ (where U_l is the local boundary layer velocity just before the base) with a similar octave-band-spectrum shape as described for the original free stream equation. This local parameter equation should now permit variations in cone geometry (from that on which the data were taken), and may permit an angle of attack

prediction even if there is an asymmetric pressure distribution on the base. Naturally, data should be acquired to substantiate the supposition that the equation holds for local base-pressure fluctuations in the presence of an attack angle.

These new, local-parameter dependences were generated by 1. calculating the local aero-parameters for the geometries and flow conditions given in the reference using an aero-thermo computer program for cones, and 2. plotting the BPL data against these new parameters to determine, and assess the accuracy for, the constants in the above equation.

REENTRY-VEHICLE TRANSFER FUNCTION

This section presents the conical transfer function (CTF) for the ACE primary shell. The CTF is developed by examining the structural response of the shell when exposed to a reverberant acoustic field. The CTF is compared to the Franken Transfer Function (FTF) for aluminum cylinders of large-diameter in Ref. 5. Differences between the two transfer functions are analyzed.

Test Data

The complete ACE vehicle, suspended by bungee, was exposed to a high-level, reverberant, acoustic field. Accelerometers were mounted inside the specimen at various positions of interest as well as on the primary shell itself. The latter locations permit development of a CTF in a fashion first suggested by Ref. 5. Since the ACE structure is conical, the normalizing diameter was taken to be that of the shell at the measurement location. The primary shell locations had various diameters so the ACE data do not all fall at the same normalized frequencies even though the data analysis was performed using standard frequency bands.

Considerable attention to detail was introduced to maintain test validity. For example, 1. extensive calibration ensured good data from all instrumentation, 2. acoustic sealing of the specimen negated response cancellation due to back pressures, 3. air conditioning, for the internal operational electronics, was turned off during the actual test, and 4. a reverberant field was verified over the frequency range of interest. As a result, the CTF for ACE is considered representative of a boundary-layer-induced CTF, and indicates the shell responsiveness versus frequency.

Figure 3 presents the octave band data obtained from two stations during the ACE test, and compares these data

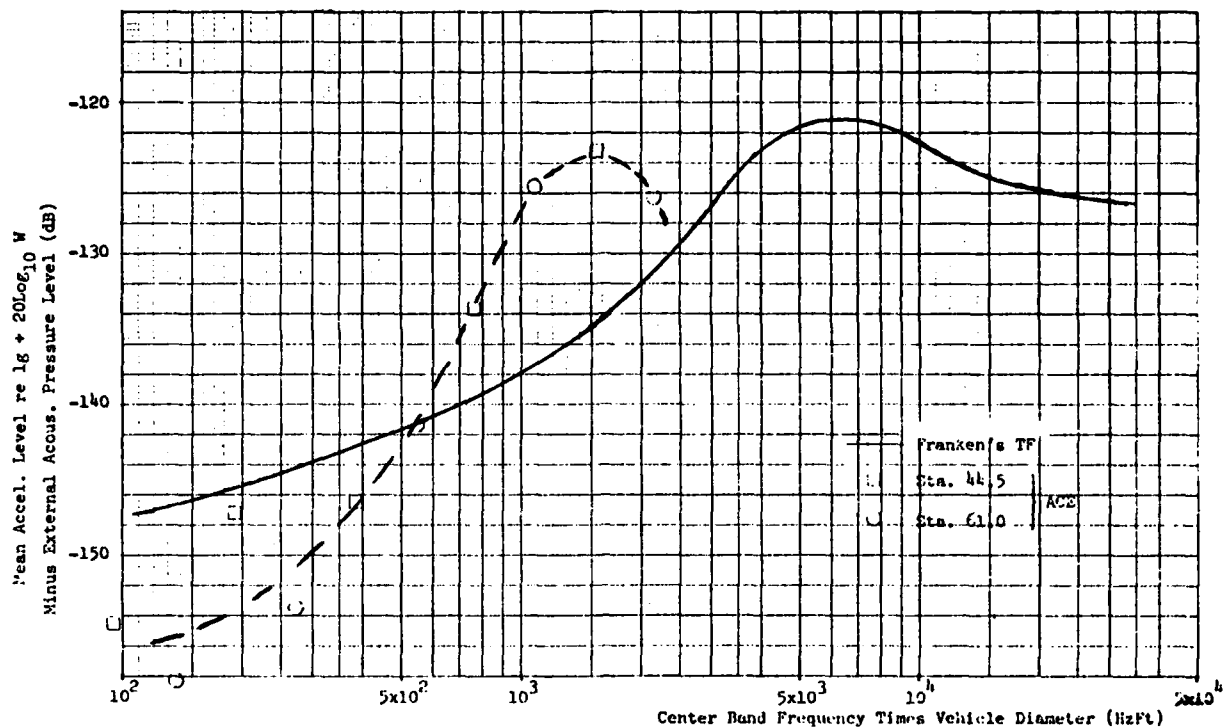


FIGURE 3 COMPARISON OF ACE CTF AND FRANKEN'S TF

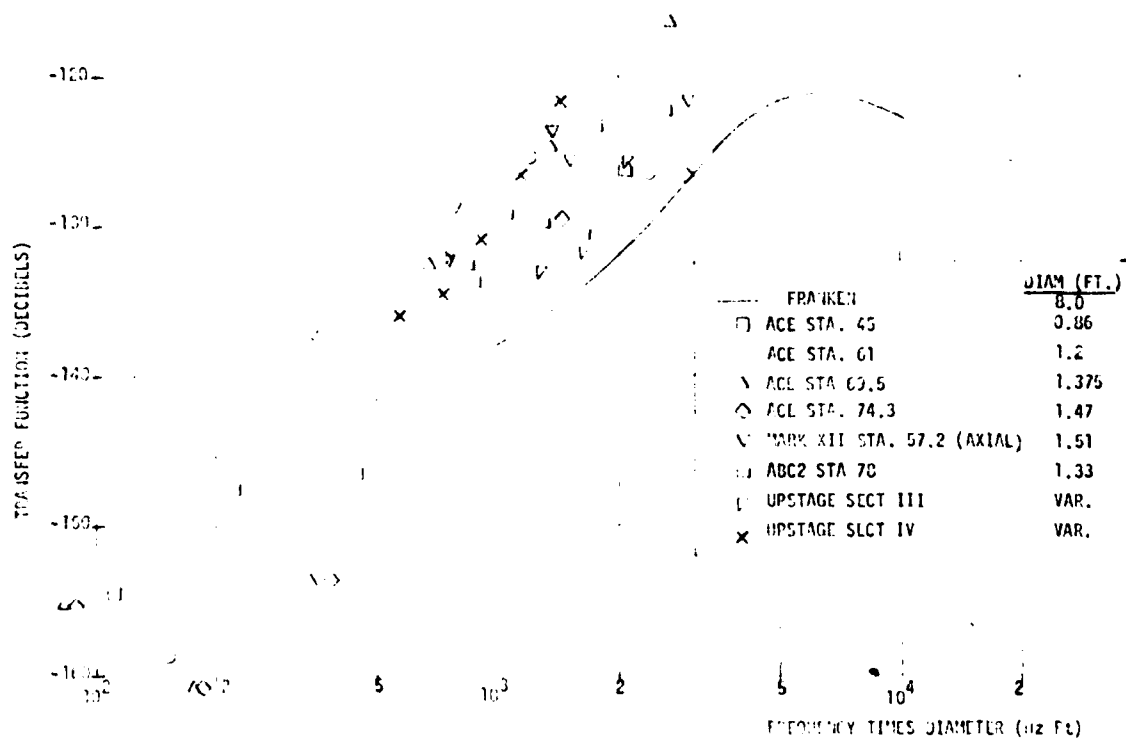


FIGURE 4 REENTRY VEHICLE DATA COMPARED TO FRANKEN TRANSFER FUNCTION

with Franken's TF. The obvious differences prompted comparison of ACE data with other reentry-type vehicles. Again, considerable discrepancy exists between these data and FTF mean curve as shown on Figure 4. The difference between cone and cylinder data is seen to have two distinct characteristics. First, the slope of the data in the low frequencies is much steeper than the FTF. Second, a CTF mean curve would peak at a lower frequency than the FTF. Since Statistical Energy Analysis (SEA) validates (gives a theoretical basis for) the empirically-derived curve of Franken, it seems only logical to examine the cone data from that point of view. This assumes that the CTF is dominated by high modal density response of the shell, and that the peak of the response occurs at the ring frequency (f_r). The next two sections of this paper examine these aspects.

Transfer Function Shape Below f_r

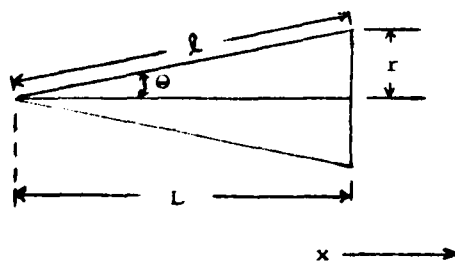
Employing SEA to develop an energy transfer function reveals that the shape of the curve is predominantly controlled by the modal density of the geometry at frequencies below f_r , and the modal density of a small flat plate above f_r . A discontinuity in the modal density curves at f_r indicates the inadequacy of the theory in the region of f_r itself. Examining the frequency region below f_r , Ref. 6 provides one analytical expression for a cylinder's modal density. The ratio of the modal density of a cone to that of a "similar" cylinder was calculated using that expression. The cone was modeled as an infinite series of short cylinders or rings with varying radii (integration). For each ring, f_r is different. The normalized modal density for the cone "ring" is:

$$\eta_{\text{cone}} = \frac{dA_s}{K} \omega^{2/3} \frac{4\pi h}{\sqrt{12} K}^{2/3} a^{2/3}$$

where a = mean diameter of ring = $\frac{r_2 + r_1}{2}$

$$K = \text{a material constant} = 4\pi \sqrt{\frac{Eh^2}{12(1-\nu^2)}}$$

$$\text{and } dA_s = 2\pi x \tan \theta (1 + \tan^2 \theta)^{1/2} dx$$



$$\eta_{\text{cone}} = \frac{2\pi(4\pi h \omega)^{2/3}}{12^{1/3} K^{5/3}} \int_0^L (x \tan \theta)^{5/3} \sec \theta dx$$

$$= \frac{\pi(4\pi h \omega)^{5/2} L^{2/3}}{12^{1/3} K^{5/3} L^{2/3}}$$

the comparable cylindrical η is given by

$$\eta_{\text{cyl}} = \frac{2\pi r' L' (4\pi h \omega r')^{2/3}}{K^{5/3} 12^{1/3}}$$

where r' and L' are the base radius and length respectively. When the shell properties are the same and $L = L'$ and $r = r'$, the ratio of $\eta_{\text{cone}}/\eta_{\text{cyl}}$ is equal to $(L^2 + r^2)^{1/2} / 2L^{5/3}$. Since this ratio is much smaller than 1, the slope of the transfer function must be steeper than that of the cylinder in the region immediately below f_r to allow the CTF to have lower values than the FTF.

Ring Frequency, f_r

The peak of the high-modal-density shell response occurs at the ring frequency. By definition, f_r , the ring frequency, is that frequency whose wavelength just equals the circumference of the "cylinder". It is calculated by dividing the speed of sound in the material by the circumference. Now all of the curves and data shown on Figures 3 and 4 were a result of measurements taken on aluminum shells. The cone data, however, peak at lower frequencies than the cylinder data. Superficially, this would seem to be a contradiction to SEA when applied to cones. However, when the effects of adhesives and heat shield layers are included, such as in the method given in Ref. 7, f_r is lowered. That is, the complex nature of the shell structure results in a reduction, on the average, in the speed of sound in the shell. As a typical example, the ring frequency of ACE, ABC, and Mark XII vehicle's primary shell is calculated to be 70% or less of a pure aluminum shell with equivalent dimensions. Also, the 70% figure does not account for the diversity of sound speeds in a complex heat-shield-material such as is used on most reentry vehicles. If this additional complication were also (somehow) included, it is presumed that the resultant f_r would be even lower. Hence, a reasonable explanation exists for both of the obvious differences between the CTF and FTF curves.

INTRODUCTION PART II (MANEUVERING)

This second part of the paper examines the dynamic data acquired on two ACE flights, and describes indicated trends for such a maneuverable reentry vehicle which differ, in some respects,

from the conclusions reached in Part I for a non-maneuvering vehicle.

An attempt is made to explain the discrepancies between maneuvering and non-maneuvering vehicle results. However, the third and last ACE flight, on which instrumentation had been relocated to specifically address the questions raised by the data from flights 1 and 2, did not provide any usable data for review. Therefore, even though plausible and quantitatively encouraging, the explanations contained in this paper must remain conjecture until more flight data have been gathered.

Each flight vehicle was instrumented with two pairs of dynamic sensors. Each pair consisted of a probe microphone designed to measure the local fluctuating pressure and an accelerometer mounted nearby but internally to measure the primary shell vibration. The output of all four of these sensors were processed on board to provide filtered, mean-squared histories. The pressure data spanned seven octave bands from 89 to 11,300 Hz. The vibration data spanned the frequency range of 50 to 2830 Hz in twelve bands, the lower four of which were 100 Hz wide while the top eight were one-third octave-band widths. Additional information as to sensor descriptions, calibrations, and corrections applied as well as a description of the on-board processing system are contained in the Appendix.

FLUCTUATING PRESSURES MEASURED ON ACE

The first ACE flight vehicle (called FTV-1) had a sequence of severe maneuvers after which the on-board fluctuating pressure sensors failed to provide useful data. Figure 5 shows the predicted versus measured FPLs during the period of rapid maneuvers. The levels at station 43 are over-predicted while those at station 60 have reasonably close agreement between theory and experiment. (Predicted is based on the modified Lowson curve given earlier, an assumed octave band spectrum of ± 2 dB/octave up to f_c , and the values of local aerodynamic parameters determined from flight data and sophisticated computer programs.) Neither of these measurement histories can be discussed with confidence since the rapidity of vehicle maneuvers did not permit quasi-steady-state conditions to exist. The second ACE vehicle (FTV-2) was more successful in acquiring data throughout reentry from the sensor at station 43. The station 60 sensor did not function during the flight. The history from station 43 is shown on Figure 6. The overall levels are overpredicted (as was the case on FTV-1 at this station). The minor, short-term varia-

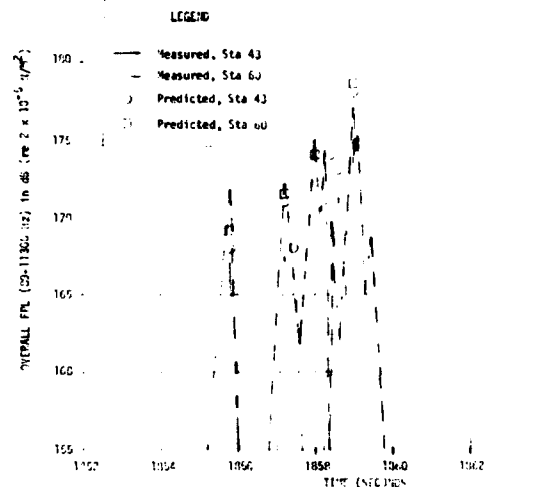


FIGURE 5 COMPARISON OF PREDICTED AND MEASURED OVERALL FPL'S FOR FTV-1

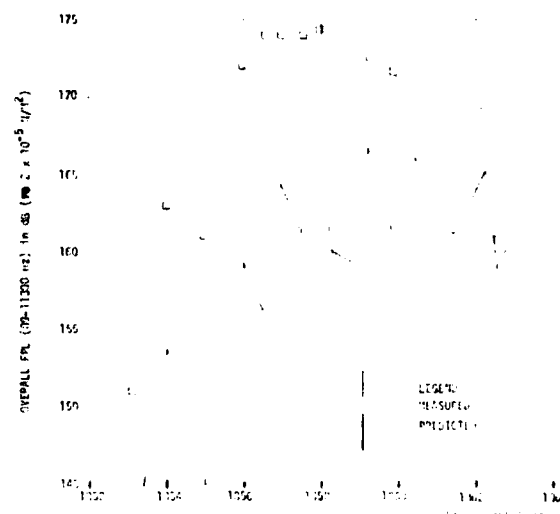


FIGURE 6 COMPARISON OF PREDICTED AND MEASURED FPL'S AT STATION 43 FOR FTV-2

tions in pressure level are not relatable to any parameter such as pitch, roll, local variations in pressure, Reynolds number, etc. It is most interesting to note however, that the average "overprediction" seems to depend on the angle of attack (the sensor being essentially on the windward side of the vehicle). Figure 7 clearly shows this unexpected dependence.

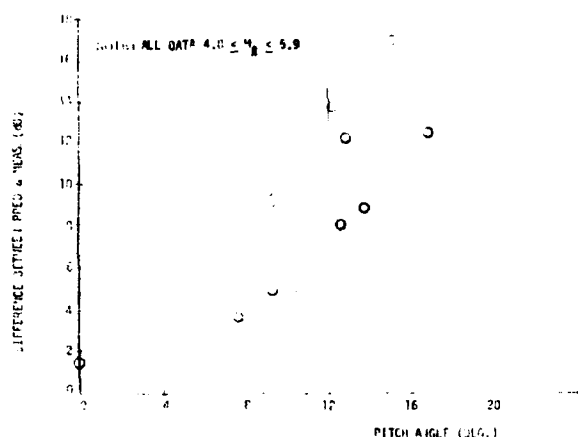


FIGURE 7 OVERALL FPLS (89-11300 HZ) PREDICTED MINUS MEASURED VS. PITCH ANGLE

Attempting to correlate this pitch angle dependence on any parameter already used for normalization or on any other such as Reynolds Number has been unsuccessful in the past (e.g., see Figures 33 and 34 of Ref. 8) as well as for this ACE flight. One possible explanation for the attack-angle dependence is a redistribution of energy in the frequency domain as a result of boundary layer thinning. This assumes that a large pitch angle, in conjunction with the cone angle, causes the boundary layer to flow in a spiral direction rather than longitudinally. Such a condition would tend to move the measurement location closer to the position of transition and hence, cause f_c to be higher. Assuming the total energy level remains constant, the spectrum level at the measured frequencies would drop accordingly. Certainly, further study and data acquisition are required before substantial progress can be made in understanding all the ramifications of these ACE data.

The spectrum of the ACE flight measurements conforms to the expected power spectrum in an "average" sense (the -1dB/octave power spectrum of Part 1 of this paper is equivalent to a +2dB/octave-band slope). However, there are some notable variations. Figure 8 summarizes

data taken during severe maneuvers at two locations on the first flight (upper half of the graph) and data taken from peaks and valleys of the quasi-steady-state history from one location on the second flight (lower half of the graph).

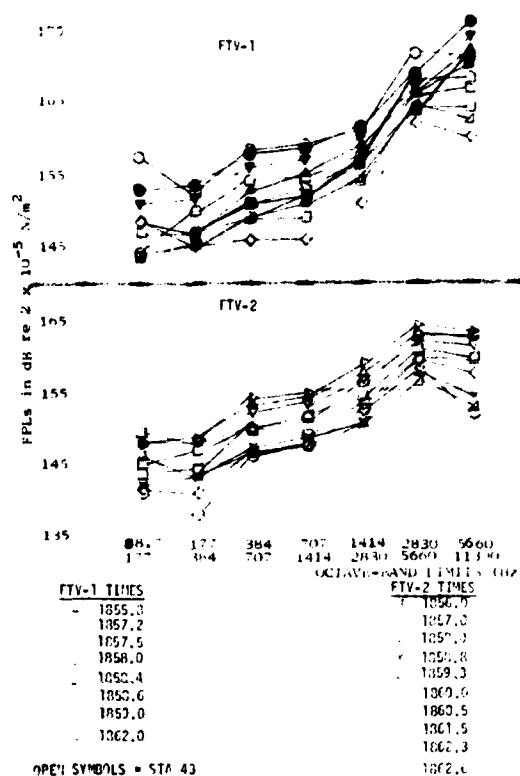


FIGURE 8 OCTAVE BAND SPECTRA FOR FLIGHT FPLS

Measurements taken at the forward station tend to peak in the sixth analysis band ($gmf = 4000$ Hz). The aft station data are still rising sharply into the seventh band. The top two bands are somewhat suspect because they contain corrections for frequency response due to geometry and flow characteristics. Also, they were processed differently than the rest of the dynamic data (see Appendix). Even so, such considerations hardly seem able to explain the departure of the high frequency data from the trends of the lower bands; the latter agreeing substantially with ground test data. If measured spectra differed from the assumed shape the overall levels could be quite different from those predicted. For example, if the spectrum were flat (+3dB/octave band) instead of the assumed -1dB/octave, the predicted levels for ACE would be about

10 dB lower. It is unfortunate that the total boundary layer energy is distributed over such a wide frequency range (0-f_c) as it makes the prediction of levels more difficult for the low end of the spectrum. However, in the case of the ACE data, it's still not clear whether the spectrum shape is different from the assumed or whether flight data corrections are just not well defined.

FLIGHT VIBRATION AND ITS INTERPRETATION

Flight measurements of vibration on the primary shell of the ACE vehicle resulted in good agreement, when compared with predictions, for the region of $f \geq 707$ Hz. However, below 707 Hz, much more response was observed than could be attributed to high-modal-density shell response.

Flight Data

Vibration data were obtained at both sensor locations for both of the successful flights. Since the aerodynamic environment was varying throughout each flight, any time slice had a unique predicted-vibration level. Therefore, only one such time point is examined. However, Figure 9 shows data that are representative of the spectrum distribution for any other time slice for both the measured and predicted spectra at that station. Other time-slices would show measurements which are higher, equal to, or lower than those shown for the 707-2830 Hz range, but, in general, the measured were within ± 3 dB of the predicted in that frequency range. This is somewhat contradictory to the conclusion that the FPLs were overpredicted during maneuvers. However, there is an area of very high FPLs at the aft end of the vehicle during those maneuvers due to separated flow. This high intensity forcing function may be inducing sufficient shell vibration at the high frequencies to offset the measured reduction in local FPLs where the accelerometers are located. The effect of the localized high levels on response forward of the control mechanism was not calculated for ACE due to limitations in schedules and budget, but a comparable analysis was performed on the UpSTAGE vehicle using SEA techniques. There, it was determined that the localized aft "hot spot" effected the vibration levels well forward of the locally-forced structural region.

For all times, the gross discrepancy in the range below 707 Hz was observable as is shown on Figure 9. The predicted vibration response on the figure is based on the ACE ground test in a reverberant acoustical chamber as described earlier. Since the ground test was representative

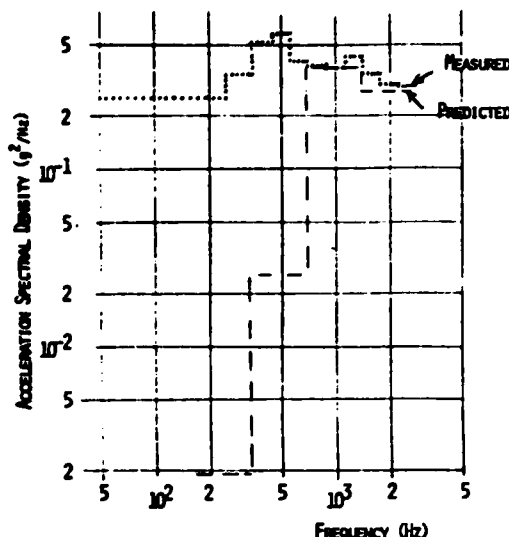


FIGURE 9 COMPARISON OF FTV-2 STA 61 MEASURED AND PREDICTED VIBRATION AT 1858.5 SECONDS

of a ballistic flight condition (symmetric) loading) it seems obvious to suspect the asymmetry of maneuvering loads as the cause of the excess low frequency vibration. This was done analytically, and the results are described in the next section.

Analysis of the Low Frequency Anomaly

The acoustical ground test of ACE indicated that flight-induced FPLs from the normal (attached) boundary layer would be incapable of producing the low frequency response measured in flight. However, the first few beam-bending-mode frequencies are in this same range and local on-board shocks, emanating from the region of the maneuver mechanism are known to have initiated beam bending. To quantitatively assess the beam bending response resulting from maneuver-controlling mechanisms on ACE, a beam model of the vehicle was made. It was a twenty-seven lumped-masses model with interconnecting springs. The bending modes of this flexible model were calculated using the displacement method of analysis. Forced response was then calculated assuming two localized sources of excitation. The first was due to limit cycling of the flap around a mean position which introduces a low frequency, "tail-wags-dog" input. Such a dynamic forcing function, though present on ACE, was found to be inadequate in producing the actual measured levels. Second, the region of separated flow in front of the flaps was used as the forcing function. The beam was caused to vibrate by the localized

high-intensity fluctuating pressures associated with this region (a local hot spot in the aerodynamically-induced FPLs). The surface area over which the pressures acted was estimated to be equal to the flap width times the flow separation distance. This flow separation distance extends from flow separation to the beginning of the flap and is about four times the height of the flaps above the surface. The increase in pressure level is about 24dB at all frequencies (over the attached boundary layer level) if the wind tunnel data of NASA Ames and MDAC researchers can be used here.

When this second forcing function was employed, the comparison between measured and predicted levels for the low frequency bands turned out to be surprisingly good (roughly a factor of 2 or less). Table 1 gives the tabulated data.

TABLE 1

Comparisons Between Predicted and Measured* Low-Frequency Vibration Levels for FTV-2 (In g's)

*Measured at 1857.6 Seconds

STA. 43	MODE 1 (122 Hz)	MODE 2 (272 Hz)	MODE 3 (555 Hz)
Meas.	2.5	2.3	3.3
Pred.	5.1	2.7	5.4
STA. 61			
Meas.	5.5	6.0	7.0
Pred.	2.4	3.1	5.3

The flight data-analysis bands are too wide to permit corroboration of the concept that most of the low-frequency vibration response is concentrated in narrow bands about the beam-bending resonance frequencies. However, the suggested solution for the excess response in the low frequencies has additional merit when it is noted that similar trends exist between predicted and measured levels. That is, at STA. 43, the measured levels dipped for the second mode from the levels of modes 1 and 3, whereas at STA. 61, the levels increased with increasing frequency. The calculated levels show these same trends.

These ACE comparisons gives credence to the conclusion that the region of separated flow, caused by a maneuver-producing mechanism, can induce considerable low-frequency vibratory response not related to the normal aerodynamic-flow-induced dynamics.

The ACE results suggest the need for careful review of expected flight environments for maneuvering reentry vehicles. The analyses should account for 1. unsymmetric loading of the primary shell, 2. base pressure fluctuations (though for ACE they did not significantly exceed boundary-layer-induced pressures even when the vehicle was at an angle of attack), and 3. vibration response should reflect consideration of both high frequency asymmetries due to the aft-end flow disturbances, and the possibility of low frequency response of significant amplitude.

REFERENCES

1. M. V. Lowson, "Prediction of Boundary Layer Pressure Fluctuations", AFFDL-TR-67-167, April 1968.
2. A. Powell, "On the Response of Structures to Random Pressures and Jet Noise in Particular", Chap. 8 of Random Vibration, Ed. S. H. Crandall, Wiley & Sons, New York, 1958.
3. C. M. Ailman and A. S. Hopkins, "Narrow Band Cross-Correlation Analysis of Fluctuating Pressures Beneath a Turbulent Boundary Layer", NASA CR-1066, May 1968.
4. H. H. Heller and A. R. Clemente, "Unsteady Aerodynamic Loads on Slender Cones at Free-Stream Mach Numbers From 0 to 22", AIAA paper No. 73-998, Oct. 15, 1973.
5. P. A. Franken, "Sound Induced Vibrations of Cylindrical Vehicles", J. Acoust. Soc. Am., Vol. 34, No. 4, April 1962, pp. 453-454.
6. V. V. Bolotin, "On the Density of the Distribution of Natural Frequencies of Thin Elastic Shells", Russian Pub. PMM, Vol. 27, No. 2, 1973, pp. 362-364.
7. Lewis H. Abraham, Structural Design of Missiles and Spacecraft, McGraw-Hill, New York, 1962.
8. W. V. Speaker and C. M. Ailman, "Spectra and Space-Time Correlations of the Fluctuating Pressures at a Wall Beneath a Supersonic Turbulent Boundary Layer Perturbed by Steps and Shock Waves", NASA CR-486, May, 1966.
9. H. H. Heller and S. E. Widnall, "Dynamics of an Acoustic Probe for Measuring Pressure Fluctuations on a Hypersonic Reentry Vehicle", J Acoust. Soc. Am., Vol. 44, No. 4, 1968.

APPENDIX

Description of the Pressure Sensor

The fluctuating-pressure sensing system included a probe-type microphone and its associated signal-conditioning package manufactured by the K-West Co. The diaphragm was mounted perpendicular to, and 2.54 cm. from, the shell surface, and was connected to the surface by means of a pin hole. The diaphragm was perforated to reduce the low frequency response (and hence, dependence on abrupt changes in static pressure). Figure 10 presents a typical acoustic response of one of these sensors under static conditions. In addition, Figure 10 also gives an in-flight response as would be predicted using Ref. 9. Note that the latter would vary with time due to geometry and local speed-of-sound changes during reentry. Octave band data were corrected for the high frequency dependence by integrating the in-flight curves over each band for specific time periods, and adding appropriate corrections per band. Typically, only the sixth and seventh octave bands were corrected due to the high frequency roll-off, and though variable with time and location, nominal correction values were one-half and two decibels respectively. The low frequency roll-off never changed and was experimentally determined by comparison with ground test equipment.

Description of the Vibration Sensor

The vibration sensor was an Endevco model 2221E accelerometer combined with a model 2640M39 amplifier. This system had virtually no sensitivity variation over the frequency range of interest in the working environments, so corrections were not required. However, shock events could not be monitored quantitatively due to the high level and high frequency limitations of this system.

Description of the On-Board Data Processor

The output from all four dynamic sensors were processed by a Gulton Mfg. Co. data processor. Each output was fed to a series of bandpass filters. With the exception of the top two bands from the fluctuating pressure measurements, which were processed by analogue techniques, each bandpass filter output was sampled, time multiplexed and then A/D converted. Still in time multiplex, the samples were digitally squared and then demultiplexed and accumulated over 0.1 second intervals. The results were telemetered through a PCM encoder as individual 10 samples/sec. channels both in real time and with a five second delay. Pre-flight calibration of the total FPL on-board system showed ± 0.5 dB accuracy of the value expected by analysis at 500 and 1000 Hz.

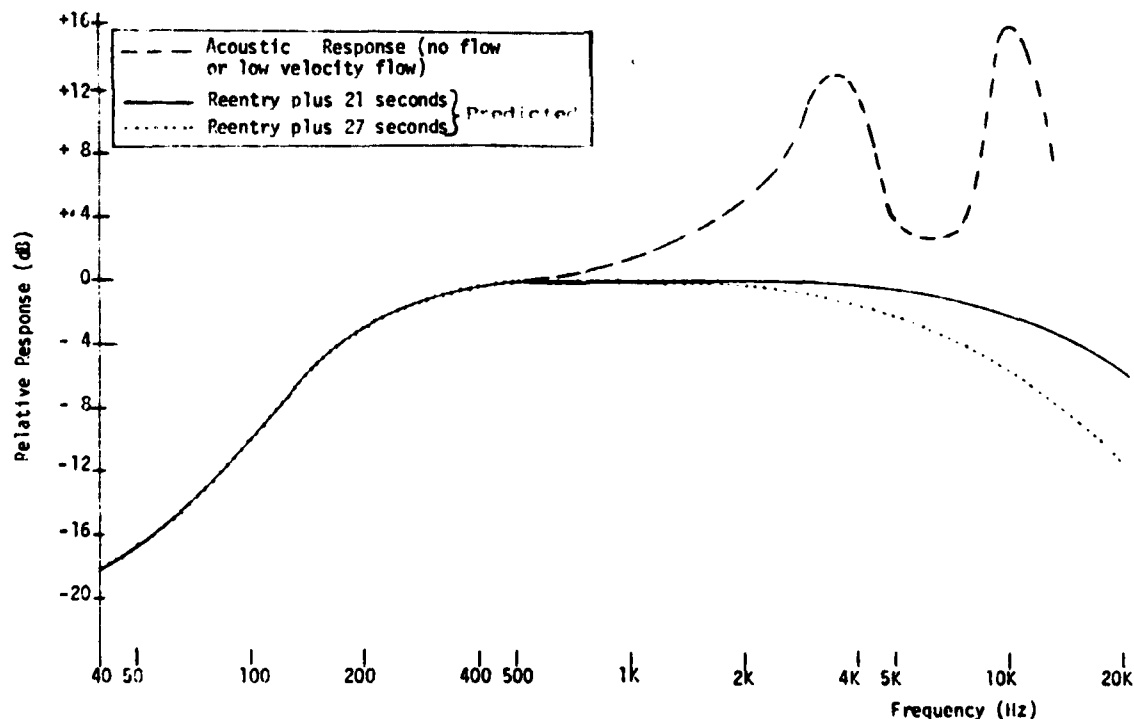


FIGURE 10 TYPICAL SENSITIVITY OF AN ACE PROBE MICROPHONE (S/N 103)

CALCULATION OF ATTACH POINT LOADS DUE
TO POSSIBLE COMBUSTION INSTABILITY IN THE
SPACE SHUTTLE SOLID ROCKET BOOSTERS

F. R. Jensen and D. T. Wang
Hercules Incorporated
Magna, Utah

This paper is based on a structural dynamics study of the Space Shuttle that was conducted at Hercules Incorporated under Contract Number F04611-73-C-0025 with the Air Force Rocket Propulsion Laboratory at Edwards Air Force Base in California. The work took place during the period from June 1975 to June 1976. A final report entitled: "Space Shuttle Response to Acoustic Combustion Instability in the Solid Rocket Boosters", was issued in June 1976. (Refer to AFRPL-TR-76-62.)

The objective of the analysis discussed in this paper was to analyze the Space Shuttle vehicle to determine structural response to possible acoustic combustion instability in the solid rocket boosters. Response of the Space Shuttle vehicle to pressure oscillations in the solid rocket boosters (SRB's) was calculated. The response was expressed in terms of forces and displacements at the attach points between the SRB's and the External Tank (ET), and between the ET and the orbiter.

The NASTRAN computer program was used to analyze various finite element shuttle models. Finite element models of the SRB, ET, and orbiter were supplied by North American Rockwell, Space Division, at Downey, California. A detailed finite element model of the solid rocket motor (SRM) was constructed for use with the cyclic symmetry option in NASTRAN. The models were analyzed separately and results were combined to represent the total structure by using a mechanical impedance-type approach. Acoustic analyses were performed at the Naval Weapons Center (NWC) at China Lake, California. The acoustic natural frequencies and mode shapes were transmitted to Hercules for use in this analysis program.

The analysis approach based on using mechanical impedance methods and the cyclic symmetry option in NASTRAN was demonstrated by calculating shuttle structure response to the first longitudinal acoustic mode in the SRB's. A maximum attach point load of 7.12 kN (1600 lbs) was calculated for a ± 6.89 kPa (± 1.0 psi) pressure oscillation level. Therefore, maximum attach point loads of 71.2 kN to 142 kN (16,000 to 32,000 lbs) can be expected for maximum pressure oscillation levels of ± 68.9 to ± 137.8 kPa (± 10 to ± 20 psi). The attach point loads would be applied at a frequency of 15.25 Hz.

INTRODUCTION

Most solid propellant rocket motors exhibit some degree of combustion instability, which is characterized by chamber pressure oscillations. The hot combustion gasses in the combustion cavity can oscillate in various natural acoustic modes much the same way that the column of air in an organ pipe resonates. Pressure transducers that are designed to measure the alternating component of the chamber pressure are used to measure the unstable pressure oscillations. The oscillations are considered to be unstable because a small perturbation can excite a

particular mode which in turn increases in amplitude in an unstable (e^{2t} envelope) fashion until some limiting amplitude is reached. As burning in the motor continues, the conditions required to sustain oscillation in a particular mode change and the mode typically dies away before the end of motor operations. Motors that exhibit unstable pressure oscillations in more than one acoustic mode during motor operation time are common, however, the lower frequency modes are typically of most concern with aluminum propellants.

In the past, unstable acoustic pressure oscillations in upper stage motors on certain ballistic missiles have produced relatively high amplitude vibration levels on the motor case and attached components. Vibration levels as high as 300 g's have been measured during upper stage motor operation. This past experience with solid rocket motors has been cause for concern with possible acoustic instabilities in the Space Shuttle Solid Rocket Booster (SRB) motors. The objective of the work covered in this paper was to analyze the Space Shuttle vehicle to determine structural response to possible acoustic combustion instability in the solid rocket boosters. The analysis was intended to provide an estimate of the forces to be expected at the attachment points between the Solid Rocket Boosters and the External Tank (ET).

The problem could have been solved directly by constructing a finite element model of the entire shuttle structure and then making computer runs to obtain the forced steady state structural response to the pressure loads in the combustion cavities of the SRB's. (The acoustic mode shape defines the pressure load distribution in space and the load-time variation is sinusoidal.) Such a direct approach was not practical because of the unreasonably large finite element model that would have been required.

The use of modal synthesis techniques would have been a natural way to solve this problem if the viscoelastic propellant grain were not important. The usual modal representation used in modal synthesis could not be accurately applied to the propellant grain because the grain dynamic (complex) modulus changes with frequency.

This paper describes the use of a mechanical impedance approach combined with the cyclic symmetry capability of NASTRAN to obtain a practical solution to the problem.

Work to define the likelihood of any particular acoustic mode being unstable, to define the natural mode shapes, and to estimate limiting amplitudes of unstable modes was carried on at the Naval Weapons Center (NWC) at China Lake, California. For the work reported herein, the first longitudinal mode was assumed to be unstable and the response was calculated for a normalized (6.89 kPa maximum) pressure mode shape. Since the solutions are linear, different pressure oscillation levels can be accounted for by direct multiplication of the 6.89 kPa (1.0 psi) results; e.g., for 68.9 kPa (10 psi), multiply by 10. The acoustic natural mode and frequency were supplied by NWC.

APPROACH

The solid rocket booster structure was represented by a finite element model. Solutions were obtained from the model for unit harmonic forces applied one at a time at each attachment point in each coordinate direction. The unit

force solutions were used to form a mechanical impedance matrix which relates force to displacement at the attachment points. Finite element models of the orbiter and the external tank were analyzed in a similar manner to determine mechanical impedance at the interconnection points. A solution was then obtained for the response of the SRB model to internal acoustic pressure oscillations. By combining the response of the SRB model with the various mechanical impedance matrices the response of the total assembled space shuttle structure was calculated. A similar approach was used previously to calculate the response of components attached to a solid rocket motor. [1]

All computer solutions including matrix manipulations and finite element model responses were obtained by using the NASTRAN computer code. Existing finite element models of the ET, the orbiter, and the forward section of an SRB were furnished for use in this program by North American Rockwell at Downey, California. A detailed finite element model of the solid motor (SRM) portion of an SRB was constructed for this analysis task. The SRM was a general 3-D model that represented the viscoelastic grain, the steel case, the nozzle, and the igniter. The dynamic properties (complex modulus) of the propellant were obtained from a report on properties of Space Shuttle propellant. [2]

A complete 3-D model of an SRM would have contained too many degrees of freedom; computer run times and storage requirements would have been too great to allow practical solutions to be obtained. Therefore, the cyclic symmetry capability of NASTRAN was employed to maintain effective grid refinement with significantly reduced computer run times. The combination of the mechanical impedance approach and the cyclic symmetry option in NASTRAN resulted in a practical way to obtain the response of a rocket motor with unsymmetrical structural attachments. The use of cyclic symmetry combined with a mechanical impedance approach for such problems was first suggested by the McNeal-Schwendler Corp. of Los Angeles, California.

DETAILED ANALYSIS METHOD

The purpose of this section is to provide details on how the analysis was performed. The various finite element models are described, general application of mechanical impedance is discussed, and the equations are provided.

A. FREQUENCY RESPONSE ANALYSES

For a finite element model with viscous damping, the equations of motion are:

$$[M] \{\ddot{U}\} + [B] \{\dot{U}\} + [K] \{U\} = \{F(t)\} \quad (1)$$

where: $[M]$ = the mass matrix
 $[B]$ = the viscous damping matrix
 $[K]$ = the stiffness matrix
 $\{U\}$ = the displacement vector
 $\{F(t)\}$ = the applied load vector

For a harmonic forcing function at a particular frequency, such as $\{F(t)\} = \{F\}e^{i\omega t}$, the equations representing the steady state motion [3] are:

$$(-\omega^2[M] + i\omega[B] + [K])\{U\} = \{F\} \quad (2)$$

A common method of handling the damping is to assume that elements in the damping matrix are proportional to corresponding elements in the stiffness matrix [4]

$$[B] = (g/\omega)[K]$$

Equation (2) then becomes

$$(-\omega^2[M] + (1 + ig)[K])\{U\} = \{F\} \quad (3)$$

The propellant is assumed to be a linear viscoelastic material so that it can be represented at steady state conditions by an elastic material with viscous damping. The viscoelastic properties of the propellant are described by Poisson's ratio and a complex shear modulus, G^* , which is a function of frequency:

$$G^*(f) = G'(f) + iG''(f)$$

where: $G'(f)$ is the shear storage modulus
 $G''(f)/G'(f)$ is the loss tangent

If $[K_p]$ is the stiffness matrix for the propellant elements based on an elastic shear modulus equal to $G'(f)$, then a value of g can be selected so that $(1 + ig)[K_p]$ represents a complex stiffness matrix that corresponds with use of the complex shear modulus $G^*(f)$, ($g = G''(f)/G'(f)$). The advantage of the mechanical impedance approach over the more conventional modal synthesis approach for this situation occurs because the frequency dependent propellant properties can be changed for each analysis frequency in the steady state frequency response analysis, whereas a modal analysis does not permit changing properties for each frequency (eigenvalue).

Equation (3) is solved by the NASTRAN program when analyses are performed using the frequency response rigid format [5]. Let

$$[D] = (-\omega^2[M] + (1 + ig)[K])$$

Then equation (3) can be written

$$[D]\{U\} = \{F\}$$

and the solution to equation (3) can be written

$$\{U\} = [D^{-1}]\{F\} \quad (4)$$

Let

$$[R] = [D^{-1}]$$

Then equation (4) can be written as

$$\{U\} = [R]\{F\} \quad (5)$$

Using the terminology suggested in Reference 6,

$[R]$ is called a receptance matrix.

Where a receptance matrix is desired for only a fraction of the degrees of freedom in the finite element model, the displacement vector can be partitioned

$$\begin{Bmatrix} U_1 \\ U_2 \end{Bmatrix} = \begin{bmatrix} R_{11} & R_{12} \\ R_{21} & R_{22} \end{bmatrix} \begin{Bmatrix} F_1 \\ F_2 \end{Bmatrix} \quad (6)$$

Solving for $\{U_1\}$ with $\{F_2\} = 0$:

$$\{U_1\} = [R_{11}]\{F_1\} \quad (7)$$

If $\{U_1\}$ is the set of displacements on an SRB at the attachment points, then equation (7) relates forces to displacements at the attachment points when no other forces are applied to the SRB.

A more efficient way to obtain a reduced R matrix is to apply unit loads at each of the coordinates in F_1 and solve for U_1 , using the regular NASTRAN R. F.-8 solution. To clarify this approach, equation (7) can be written as follows:

$$\begin{Bmatrix} U_1 \\ U_2 \\ U_3 \\ \vdots \\ U_n \end{Bmatrix} = \begin{bmatrix} r_{11} & r_{12} & r_{13} & \dots & r_{1n} \\ r_{21} & r_{22} & r_{23} & \dots & r_{2n} \\ r_{31} & r_{32} & r_{33} & \dots & r_{3n} \\ \vdots & \vdots & \vdots & \ddots & \vdots \\ r_{n1} & r_{n2} & r_{n3} & \dots & r_{nn} \end{bmatrix} \begin{Bmatrix} f_1 \\ f_2 \\ f_3 \\ \vdots \\ f_n \end{Bmatrix}$$

or:

$$U_1 = r_{11}f_1 + r_{12}f_2 + r_{13}f_3 + \dots + r_{1n}f_n$$

$$U_2 = r_{21}f_1 + r_{22}f_2 + r_{23}f_3 + \dots + r_{2n}f_n$$

$$U_3 = r_{31}f_1 + r_{32}f_2 + r_{33}f_3 + \dots + r_{3n}f_n$$

$$\vdots$$

$$\vdots$$

$$\vdots$$

$$U_n = r_{n1}f_1 + r_{n2}f_2 + r_{n3}f_3 + \dots + r_{nn}f_n$$

In the above equations, when $f_1 = 1.0$ and $f_i = 0, i \neq 1$, the solution for the $\{U_1\}$'s gives the first column in the desired reduced receptance matrix:

$$r_{11} = U_1$$

$$r_{21} = U_2$$

$$\vdots$$

$$r_{n1} = U_n$$

The other columns in the receptance matrix can be determined by solving for other force terms of unit value. For example, a solution with $f_2 = 1.0$ and all other $f_i = 0$ would provide the second column in the receptance matrix.

A DMAP ALTER must be used to save the displacements calculated by NASTRAN:

ALTER 141

OUTPUT2 UDVF, , , , /C,N, -1/C,N, 17/C,N, UDVFTP\$

END ALTER

When the above ALTER is used in the executive control deck, the displacement matrix UDVF is written on tape unit 17 and can be saved for later use. In the same computer run or in another run, UDVF can be partitioned to obtain the R matrix.

In the space shuttle analysis, the receptance matrix at the interconnection coordinates was required for each model. The appropriate receptance matrices were obtained by applying unit forces at each connection coordinate for each finite element model.

B. MECHANICAL IMPEDANCE TECHNIQUES

"Impedance" and "Admittance" are terms generally associated with electrical circuits. The terms "mechanical impedance" and "mechanical admittance" are normally used to indicate that an analogy is being made between an electrical circuit and a mechanical system. The literature on mechanical vibration analysis contains a large amount of information on mechanical impedance-type approaches. For example, the Shock and Vibration Bulletin contains many papers on application of mechanical impedance techniques. [7]

Mechanical impedance is a ratio of force to velocity. Mechanical admittance, commonly called "mobility", is the inverse of mechanical impedance, i.e., a ratio of velocity to force. A basic discussion on mechanical impedance and mobility can be found in Reference 8. The term "receptance" is used to denote the ratio of displacement to force. The concept of receptance is discussed in References 6, 8, and 9. Additional discussion on electromechanical analogies are contained in References 10 and 11.

The term "imittance" has been used to represent impedance or admittance. Mechanical imittance and transmission matrix concepts are discussed in References 12, 13, and 14.

When a sinusoidal force drives a linear system, the steady state response displacements, velocities, and accelerations are sinusoidal at the frequency of the driving force. The relationship between driving force and response can be expressed by algebraic equations involving complex numbers, (such as equation 5). The analysis of such a system is

called a "frequency response analysis." The use of frequency response-type analyses is implied when mechanical impedance is discussed.

The concept of impedance or receptance of the space shuttle structure at a set of points was used to allow the individual shuttle models to be analyzed separately. The results from the individual analyses were combined to obtain solutions that represent the total structure.

Equation (7) represents a linear system. Since the system is linear, the response for two different load sets applied simultaneously can be determined by applying each load set separately and summing the results. Consider one SRB undergoing acoustic pressure oscillations. The SRB would be subjected to two separate loading systems:

- (1) The acoustic natural mode would load the solid motor by means of a certain pressure distribution in the motor combustion cavity.
- (2) The remainder of the space shuttle vehicle would apply loads to the SRB at the SRB attach points as the total vehicle vibrates in response to the pressure oscillations.

The objective of this work is to calculate the second load set.

In the NASTRAN finite element models, a certain set of displacement coordinates represents the SRB attach coordinates. The SRB is attached to the ET at nodes 303, 310, and 311. The node locations and x, y, z coordinate directions are indicated in Figure 1. A plot of the SRM finite element model is shown in Figure 2. The attach point displacement coordinates are:

$$\{U\} = \begin{Bmatrix} U_{303x} \\ U_{303y} \\ U_{303z} \\ U_{310y} \\ U_{310z} \\ U_{311y} \end{Bmatrix} \quad (8)$$

For this linear system, the total response at the attach points, $\{U_T\}$, can be obtained by summing the responses due to the two separate load sets discussed above

$$\{U_T\} = \{U_O\}_{SRB} + \{U_C\} \quad (9)$$

where: $\{U_O\}_{SRB}$ = the response at the attach coordinates due only to the acoustic pressure mode

$\{U_C\}$ = the response at the attach

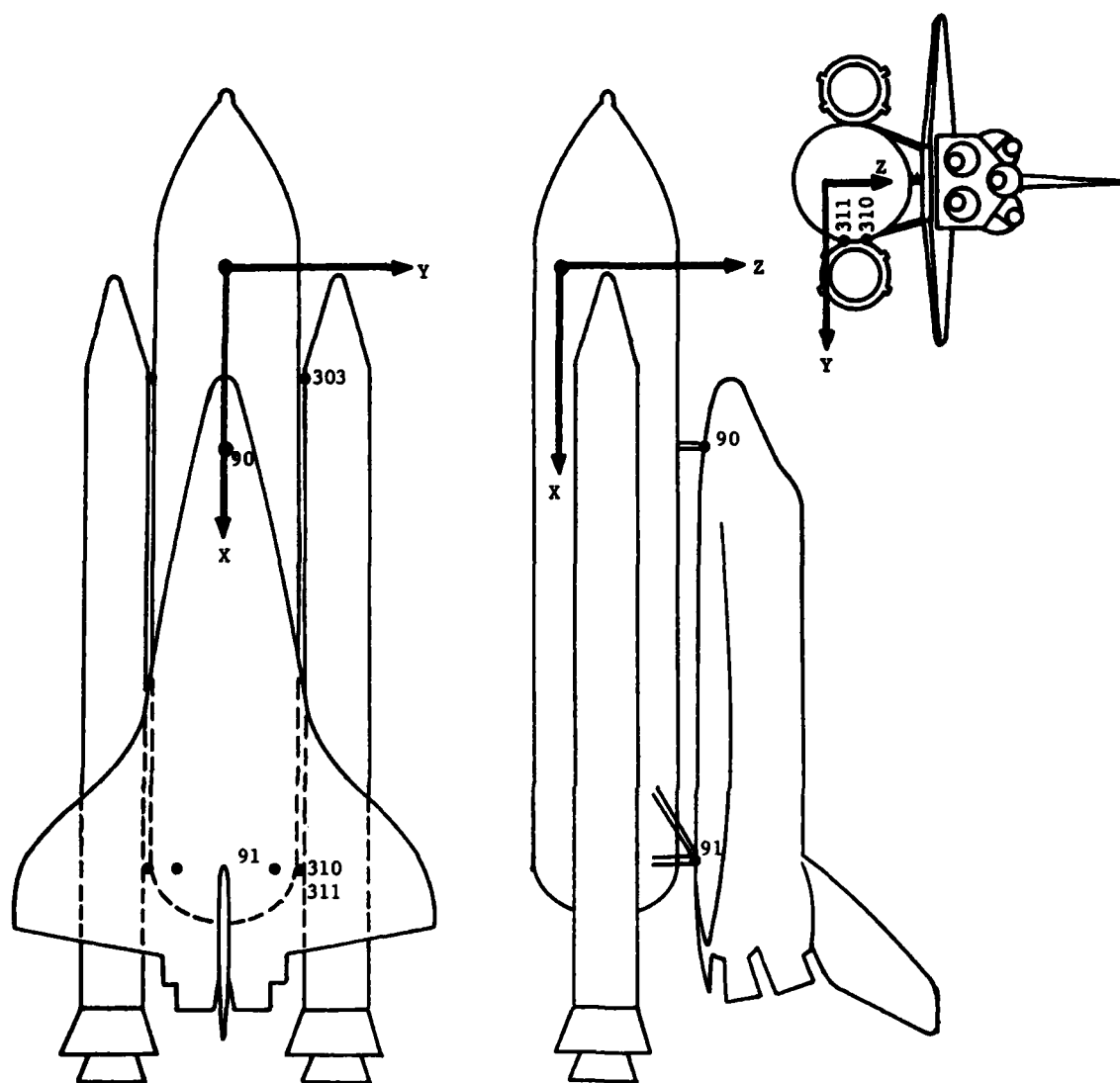


Figure 1. Sketch of the Space Shuttle Vehicle Showing SRB and Orbiter Attach Points and Showing Location of the X, Y, Z Coordinate System

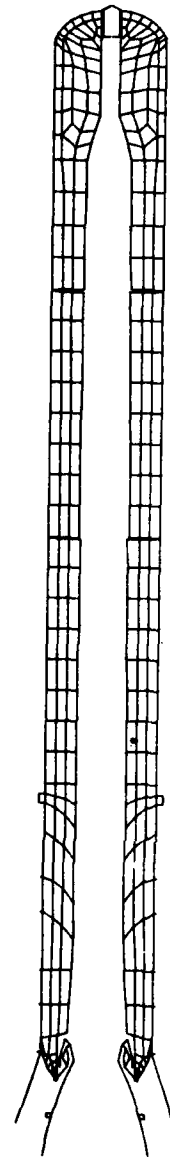


Figure 2. NASTRAN Finite Element Grid Used to Analyze the SRM.
(Full cross section not used in model but shown for clarity).

coordinates due to the attach loads (applied by the remaining shuttle structure, i.e., the total shuttle less one SRB.)

The displacement response $\{U_o\}$ can be calculated directly by using a NASTRAN model of an SRB. To obtain $\{U_o\}$, a cyclic symmetry model of an SRM was analyzed to determine response to the first acoustic natural mode at 15.25 Hz. Details of the $\{U_o\}$ calculations are discussed in the following section.

If the receptance of the SRB at the attach points is denoted $[R_{SRB}]$, then $\{U_c\}$ can be expressed as

$$\{U_c\} = [R_{SRB}] \{F_c\} \quad (10)$$

Where: $\{F_c\}$ = the set of forces applied to the SRB at the SRB attach points

By way of further explanation of $\{F_c\}$, the set of forces $\{F_c\}$ are internal forces that occur at the attach points between the SRB and the ET due to pressure oscillations in the SRM. Cutting the structure at the attach points to show free body diagrams would yield a diagram showing internal forces $\{F_c\}$ applied to the SRB and equal, but opposite, forces, $\{-F_c\}$, applied to the ET.

An equation similar to equation (10) can be written for the remainder of the space shuttle vehicle. When one SRB has been removed, the remaining structure consists of the ET, the orbiter, and the other SRB. If the receptance of the remaining structure at the attach points is denoted $[R_{RSS}]$, then the forces applied result in $\{U_T\}$ displacements

$$\{U_T\} = [R_{RSS}] \{-F_c\} \quad (11)$$

For this analysis, the only forces applied to the remaining shuttle structure are the forces $\{-F_c\}$; therefore, the displacements in equation (11) are the total displacements, $\{U_T\}$, rather than the displacements due to connection forces, $\{U_c\}$, as in equation (10). Equation (11) can be solved for connection forces $\{F_c\}$ and the result substituted into equation (10) to eliminate the unknown forces

$$\{U_c\} = [-R_{SRB}] [R_{RSS}]^{-1} \{U_T\} \quad (12)$$

When equation (12) is substituted into equation (9), then the total displacements are found to be

$$\{U_T\} = ([I] + [R_{SRB}] [R_{RSS}]^{-1})^{-1} \{U_{oSRB}\} \quad (13)$$

The solution to equation (13) represents the desired response of the shuttle to acoustic oscillations. The connection forces can be recovered by using the solution of equation (11)

$$\{F_c\} = [-R_{RSS}]^{-1} \{U_T\} \quad (14)$$

An equation similar to that of equation

(13) was used in the component vibration program. The Component Vibration Final Report [15] contains a simple example showing that equation (13) is applicable. For verification, a conventional frequency response analysis was performed on a simple structure. The structure was then separated into two separate models and the mechanical impedance approach, as characterized by equation (13), was applied. The small differences in the response values obtained by the two methods were attributed to roundoff error.

To obtain the desired solution to equation (13) the matrices $[R_{SRB}]$, $[R_{RSS}]$, and $\{U_{oSRB}\}$ must be available. The calculation of these three matrices is discussed in Reference 16. The calculation of each of the three matrices is somewhat complicated by the fact that each depends on solutions from two different finite element models. Two different models were used to represent the SRB, a cyclic symmetry model of the SRM and a model of the nose section above the SRM. Models of the ET and the orbiter were used to represent the remaining shuttle structure for calculation of $[R_{RSS}]$. Finite element models of the ET and the orbiter represent only one-half of the structure and separate models were supplied for symmetric and asymmetric boundary conditions. The X-Z plane as shown in Figure 1 was taken as the plane of symmetry for the models. When the models with symmetry boundary conditions are analyzed, the results represent a symmetric structure subjected to symmetric loads. Therefore, a solution for a particular acoustic mode using the models with symmetric boundary conditions represents the condition where both solid rocket motors are being subjected to unstable acoustic oscillations that are in-phase. Use of the models with asymmetric boundary conditions represents the condition where both SRM's are oscillating out-of-phase with one another. The difference between the symmetric and asymmetric solutions yields the response for the situation where only one SRM is undergoing unstable acoustic oscillations.

DISCUSSION OF RESULTS

Response of the Space Shuttle Vehicle to the first longitudinal acoustic mode has been calculated. A sketch of the vehicle, indicating nodes at the interconnection points, is shown in Figure 1. As shown in Figure 1, Node 303 represents the forward SRB/ET attach point. Nodes 310 and 311 are the aft SRB/ET attach points. Nodes 90 and 91 represent the connections between the ET and the Orbiter.

The forces from the in-phase analysis are given in Table 1. The largest force for the ± 6.89 kPa (± 1 psi) pressure oscillation level is 7.12 kN (1,610 pounds) at Node 303 in the Y direction. For a pressure oscillation level of ± 68.9 kPa (± 10 psi), the maximum force would increase to 71.2 kN (16,100 pounds). The corresponding forces from the out-of-phase analysis are shown in Table 1. The maximum

force from the "out-of-phase" solution is 4.50 kN (1,012 pounds) at Node 303 in the x direction.

When the in-phase and out-of-phase solutions are added to obtain the results for the situation where only one booster is undergoing unstable pressure oscillations, a maximum interface force of 9.46 kN (2,127 pounds) is obtained at Node 303 in the x direction. However, such addition of the solutions represents a pressure oscillation level of ± 13.79 kPa (± 2 psi). The normalized maximum force for a ± 6.89 kPa (± 1 psi) pressure level would, therefore, be 4.73 kN (1,064 pounds). The "in-phase" condition, therefore, produces the greatest forces.

CONCLUSIONS AND RECOMMENDATIONS

This analysis program resulted in estimates for the attach point forces between the solid rocket motors and the external tank and has, therefore, met the program objectives. Good agreement between hand calculations and computer analysis results show at least that the computer results are of a reasonable order of magnitude.

A method for combining a mechanical impedance approach with the cyclic symmetry capability of NASTRAN has been demonstrated to be advantageous for structures such as rocket motors that have frequency dependent material properties. The method was demonstrated by analysis of the first longitudinal acoustic mode in the SRB's at a zero burn time. Future work could include other modes and other burn times.

REFERENCES:

[1] F. R. Jensen, Analytical Prediction of Motor Component Vibrations Driven by Acoustic Combustion Instability, Final Report AFRPL-TR-76-11, Hercules Incorporated, for the Air Force Rocket Propulsion Laboratory, Edwards, CA, February 1976.

[2] J. H. Stoker and D. R. Mason, Space Shuttle SRM Propellant Dynamic Properties, 26 June 1975, DR No. 3-5, Thiokol/Wasatch Division, for NASA, George C. Marshall Space Flight Center, Alabama.

[3] The NASTRAN Theoretical Manual, (Level 15), R. H. MacNeal, Ed., April 1972, NASA SP-221(01), NASA, Washington, D.C., Page 12.1-3.

[4] The NASTRAN Theoretical Manual, loc. cit., p 9.3-8.

[5] The NASTRAN User's Manual, (Level 15), C. W. McCormick, Ed., June 1972, NASA SP-222(01), NASA, Washington, D.C., p3.9-11.

[6] Bishop, R. E. D., and Johnson, D. C., The Mechanics of Vibration, Cambridge at the University Press, 1960, London, England.

[7] Index to the Shock and Vibration Bulletins, February 1968, The Shock and Vibration Information Center, Naval Research Laboratory, Washington, D.C.

[8] Harris, C. M., and Crede, C. E., Shock and Vibration Handbook, Vol. 1, Chapter 10, McGraw-Hill Book Co., New York, 1961.

[9] Bishop, R. E. D., Gladwell, C. M. L., and Michaelson, S., The Matrix Analysis of Vibration, Section 5.5, Cambridge at the University Press, London, 1965

[10] Crafton, P. A., Shock and Vibration in Linear Systems, Harper and Brothers, New York, 1961.

[11] MacNeal, R. H., Electric Circuit Analogies for Elastic Structures, Vol 2, John Wiley and Sons, New York, 1962.

[12] Rubin, S., Review of Mechanical Immittance and Transmission Concepts, Presented at the 71st Meeting of the Acoustical Society of America, Boston, Mass., June 1966.

[13] Rubin, S., Class Notes Distributed at UCLA Short Course on Structural Dynamics Analysis, Los Angeles, California, 1967.

[14] Rubin, S., On the Use of Eight-Pole Parameters for Analysis of Beam Systems, Soc. of Automotive Engineers, Reprint 925F, October 1964.

[15] Analytical Prediction of Motor Component Vibrations Driven by Acoustic Combustion Instability, op. cit.

[16] F. R. Jensen, Space Shuttle Response to Acoustic Combustion Instability in the Solid Rocket Boosters, Final Report, AFRPL-TR-76-62, Hercules Incorporated, For the Air Force Rocket Propulsion Laboratory, Edwards, CA., June 1976.

Note: A version of NASTRAN that has the cyclic symmetry option in rigid format 8 must be used for the solid rocket motor problem, e.g., The McNeal-Schwendler version of NASTRAN.

TABLE 1

Forces at the Attach Points Due to
Oscillation in the First Acoustic Mode at
15.25 Hz. (± 6.89 kPa pressure oscillation level)

FORCE COMPONENT	SYMMETRIC RESPONSES		ASYMMETRIC RESPONSES	
	FORCE AMPLITUDE (kN)	FORCE PHASE (rad)	FORCE AMPLITUDE (kN)	FORCE PHASE (rad)
F _{303X}	5.81	1.66	4.50	2.48
F _{303Y}	7.16	0.855	1.11	0.890
F _{303Z}	0.125	3.04	0.285	2.04
F _{310Y}	1.74	1.59	2.26	-1.88
F _{310Z}	0.396	-1.12	0.974	-1.34
F _{311Y}	1.58	1.62	2.66	-1.88
F _{90X}	0.004	-0.559	-	-
F _{90Y}	-	-	0.667	1.62
F _{90Z}	0.062	2.58	-	-
F _{91X}	0.676	-1.17	0.818	1.41
F _{91Y}	0.169	1.43	1.05	1.55
F _{91Z}	0.262	-1.82	0.369	1.48

TRACKED VEHICLES

HULL VIBRATORY POWER FLOW AND RESULTING INTERIOR NOISE ON THE M113A ARMORED PERSONNEL CARRIER

Peter E. Rentz
Bolt Beranek and Newman Inc.
Canoga Park, California

The suspension vibration-induced noise levels in the M113A armored personnel carrier were investigated using a statistical energy analysis approach. The acoustic radiation from each hull panel was determined from vibration measurements and summed. This sum was then compared with internal dissipated acoustic power. The agreement confirmed the approach and provided a method for judging the potential for noise control measures, such as damping and shielding. Those measures with high potential were experimentally evaluated. The vibratory energy flow into the hull from the suspension members was determined by measuring the input impedance of the hull along with both the motion of the suspension member (directly) and the force on the member (indirectly). Comparison with structural dissipated power was reasonable. Structural modifications to reduce the power accepting characteristics of the hull were implemented and evaluated with limited success.

INTRODUCTION

The M113A Armored Personnel Carrier (APC) has many attributes which make it attractive for use in the development of advanced concepts for noise reduction in tracked vehicles. In production since 1960, the vehicle has enjoyed immense popularity and has been subject to design refinements. As a result of this process, many design variations have been evaluated and a large store of knowledge exists relative to what is feasible and what is not. But more importantly, the slab-sided, all-aluminum-hulled M113A is very noisy and has resisted piecemeal efforts at noise reduction. Therefore, both the challenge and the opportunity exist for the development of effective noise control technology.

The high noise levels in this vehicle, which was designed for performance, have been recognized as a problem since initial production. Efforts in 1964 [1] identified the track and suspension as the cause of the noise and employed some of the same acoustic radiation and damping relations used in the present study. In spite of this work and similar studies on the M113A and other vehicles, no significant noise re-

ductions were effected on the M113A.

Preceding the work reported herein, a systematic study was conducted to identify and quantify the contributions of the idlers, sprockets, and roadwheels [2]. From this study, the contributions of the three noise sources to the crew area A-weighted noise level were determined, Fig. 1. The A-weighted and octave band noise level speed dependence is presented in Fig. 2. Replotting the speed-dependent octave band values gives spectra for three typical speeds of 15, 20, and 32 mph (24, 32, and 51.5 km/hr*, Fig. 3. The spectral values exceed the specification goal by 10 to 20 dB at 250 Hz, depending on vehicle speed.

The cross section of the vehicle, Fig. 4, illustrates the nature of the vibratory power input and distribution, analysis, and control problem. The roadwheel bearings and idler spindles are bolted directly to the lower side of the hull. The idler attachment is at the intersection of the box beam and back plate which is welded to all hull

*SI units are given in parenthesis following U.S. customary units.

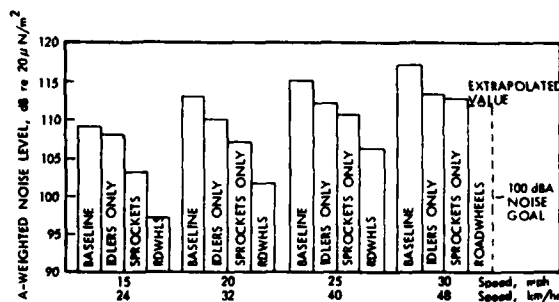


Fig. 1. Track System Source Contributions to M113A Crew Area Noise Levels at Various Speeds [2]

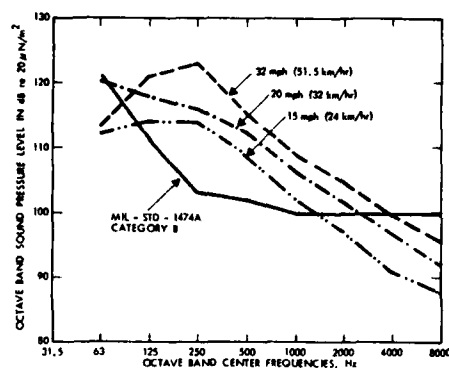


Fig. 3. Baseline Noise Spectra in M113A Crew Area [2]

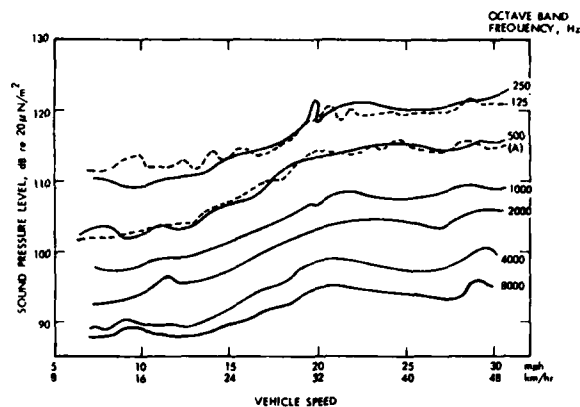


Fig. 2. Speed Dependence of M113A Crew Noise [2]

members shown in Fig. 4. The sprocket is supported by a final drive assembly which is bolted to the hull at the front of the vehicle. In all three cases, efficient mechanical coupling exists between the suspension member and the hull. In addition, all hull plates are well coupled, with flanking paths at the front and rear.

STATISTICAL ENERGY ANALYSIS

In vibro-acoustic systems with more than one or two modes in frequency bands of interest, it is convenient, and usually more accurate, to deal with time and frequency band averaged characteristics. This approach has been developed and extensively applied to room acoustics problems. More recently, the approach

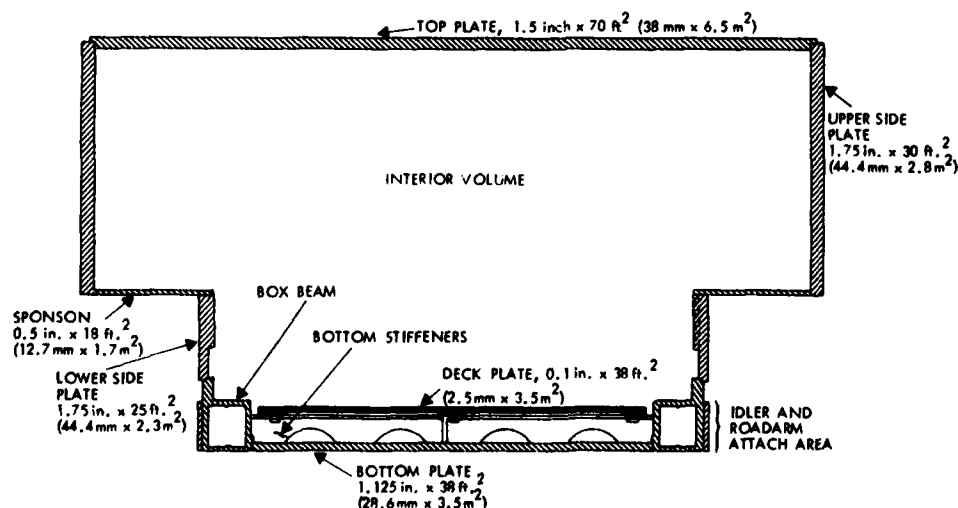


Fig. 4. Cross Section of the M113A Hull Showing Major Plates and Suspension Attachment Area

has been applied to vibrating structures and to the interaction of the vibrating structures and surrounding fluid fields. This discipline has been named Statistical Energy Analysis (SEA) and is summarized in various references [3, 4]. The relations which have been utilized in this study of the vibratory and acoustic power flow within the hull of the M113A APC fall into four categories: panel dissipation, panel radiation, reverberant room acoustics, and power flow into a structure.

The vibratory power dissipated in a structure in a frequency band is given by

$$W_d = 2\pi f n \langle v^2 \rangle m \quad (1)$$

where W_d = power dissipated ft-lb/sec watts,

f = frequency, Hz,

n = internal loss factor averaged over the frequency band centered at frequency f ,

$\langle v^2 \rangle$ = space averaged mean squared velocity, $\text{ft}^2/\text{sec}^2 (\text{m}^2/\text{sec}^2)$,

m = structure mass, $\text{lb sec}^2/\text{ft} (\text{kg})$.

In engineering form

$$\text{PWL} = \text{AL} + 10 \log \frac{\eta W}{f} + 128.4 \quad (2)$$

where PWL = power level, dB re 10^{-12} watt

$\text{AL} = 10 \log \frac{\langle a^2 \rangle}{g^2}$ = acceleration level, dB re $1.0g$,

a = acceleration, $\text{ft/sec}^2 (\text{m/sec}^2)$

$g = 32.2 \text{ ft/sec}^2 (9.81 \text{ m/sec}^2)$,

$w = mg$ = weight, $\text{lbs} (\text{kg m/sec}^2)$.

Subtract 6.5 dB from the right-hand side for SI units.

The power radiated from a reverberant plate can also be estimated from measured plate acceleration levels. The time averaged total power, W_r , radiated from a plate is

$$W_r = R_{\text{rad}} \langle a^2 \rangle / 4\pi^2 f^2 \quad (3)$$

In this equation, R_{rad} is the radiation resistance of the plate and $\langle a^2 \rangle$ is the

space averaged mean square acceleration level in the band centered at frequency f . The radiation resistance is

$$R_{\text{rad}} = \rho c S \sigma \quad (4)$$

Here, ρc is the characteristic acoustic impedance of air, S is the total radiating area, and σ is the radiation efficiency.

The radiation efficiency is a function of the critical frequency of the plates and of a nondimensional parameter $\beta = Ph/S$. P is the sum of the boundary length plus twice the total length of all stiffeners on the surface of area, and h is the thickness of the plate thus enclosed. The critical frequency is the frequency at which the bending wavelength in the plate equals the acoustic wavelength in the air and is (for aluminum plates)

$$f_c = 500/h$$

where h = thickness, inches, or

$$f_c = 12700/h$$

where h = thickness, mm.

Again, the acceleration level, AL , of a plate is related to the mean square acceleration by

$$\text{AL} = 10 \log \langle a^2 \rangle / g^2. \quad (5)$$

By substituting Eqs. (4) and (5) into (3), the radiated sound power level by plates of total area S can be expressed as

$$\text{PWL}_{\text{rad}} = \text{AL} + 10 \log \sigma S - 20 \log f + 140 \quad (6)$$

Add 10 dB to the right-hand side for SI units.

For a reverberant space, with air as the fluid

$$\text{PWL} = \text{SPL} + 10 \log \left(\frac{R}{4} \right) - 10 \quad (7)$$

where SPL = space averaged sound pressure level, dB re $20 \mu\text{N/m}^2$,

$$R = \frac{60V}{1.086c T_{60}} = \text{room constant, ft}^2 (\text{m}^2),$$

V = Volume, $\text{ft}^3 (\text{m}^3)$,

T_{60} = Reverberation time, seconds,

C = Speed of sound, 1128 ft/sec
(344 m/sec).

Add 10 dB to the right-hand side for SI units.

Or, directly in terms of the reverberation time

$$PWL = SPL + 10 \log \frac{V}{T_{60}} - 29. \quad (8)$$

Add 15 dB to the right-hand side for SI units.

The input vibratory power depends on the characterization of the source. Given the velocity at the point of attachment

$$W_{in} = \text{Re}[Z \langle v^2 \rangle] = |Z| \langle v \rangle^2 \sin \xi \quad (9)$$

where Z = Point mechanical impedance,
lb-sec/ft (N sec/m),

v = Point velocity, ft/sec (m/sec),

ξ = Angle between force and velocity, degrees.

In engineering terms, and using the inductance phase angle

$$PWL_{in} = 10 \log |Z| + AL - 20 \log f + 10 \log \sin \phi + 135.5 \quad (10)$$

where ϕ is the angle between force and acceleration, degrees.

Add 19.3 dB to the right-hand side for SI units.

Alternately, given the force at the point of attachment

$$W_{in} = \text{Re} \frac{F}{Z} = \frac{\langle F^2 \rangle \sin \xi}{|Z|} \quad (11)$$

where F = force, lbs (N).

In engineering terms

$$PWL = 20 \log F - 10 \log |Z| + 10 + \log \sin \xi + 121.3. \quad (12)$$

Subtract 1.3 dB from right-hand side for SI units.

Most of the quantities required are directly measurable. One exception is the radiation efficiency of the hull panels which are well coupled. For the major panels, the radiation efficiency was determined analytically from work of Maidanik [5]. In addition, individual panel loss factor values are not conveniently measured. The total vehicle loss factor was measured and used for the individual panel loss factor. With the coupling values between the panels estimated to be greater than the individual panel loss factor values, this approximation was considered valid.

INTERIOR ACOUSTIC AND HULL VIBRATORY DISSIPATED POWER

The power being dissipated in either the interior acoustic volume or the hull structure depends on the respective inherent dissipation and the energy level. The inherent dissipation was evaluated by measuring the rate of decay of the acoustic field in the case of the interior volume and that of the structural vibration field in the case of the hull.

The decay rates were evaluated by exciting the acoustic or structural field in octave bands with a speaker or shaker, disconnecting the excitation, and matching the envelope of the decaying signal with a calibrated decay curve. These decay rates, along with the corresponding loss factor values, are presented in Table I. For a reverberant acoustic field, the average surface absorption is also of interest and is also presented in Table I. The hull structure loss factor values are typical of undamped structures and suggest that the addition of damping would measurably reduce the vibratory levels and resulting interior noise. Values for the average interior surface absorption, α , are also low as would be expected in a hard-walled box. However, the potential for noise reduction with the addition of sound-absorbing material is not great because direct field radiation dominates the reverberant field in most of the crew space.

The energy levels in the interior acoustic volume were calculated from octave band sound pressure level measurements, Fig. 3. The hull vibratory energy was derived from space averaged panel octave band acceleration measurements. For point of physical reference, panel acceleration levels averaged 5 dB re 1.0 g in the 250 Hz octave band and 10 dB re 1.0 g overall. Approximately forty measurements were required to define the motion of the thirteen radiating panels. Therefore, in order to keep the results tractable, the evaluation was limited to

TABLE 1

Reverberation Times and Loss Factor Values Interior Acoustic Volume and Hull Structure

Octave Band Frequency Hz	Hull Structure		Interior Volume		Average Surface Absorption α
	Reverberation Time (60 dB) Seconds	Loss Factor η	Reverberation Time (60 dB) Seconds	Loss Factor η	
125	0.59	0.03	0.7	0.025	0.17
250	0.44	0.02	0.52	0.017	0.10
500	0.41	0.01	0.51	0.008	0.10
1000	0.28	0.008	0.44	0.005	0.12
2000	0.16	0.007	0.34	0.003	0.15
4000	0.13	0.004	0.32	0.002	0.16
8000	0.13	0.002	0.33	0.001	0.16

one speed, 20 mph (32 km/hr).

The dissipated power values were calculated from the loss factor values and energy levels and are presented in Fig. 5. This figure also shows the calculation used the aforementioned space

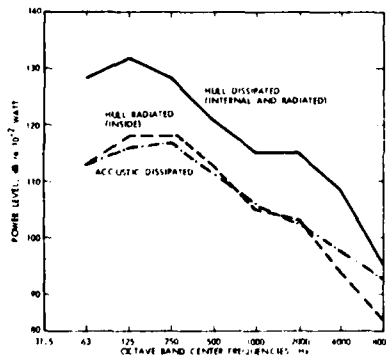


Fig. 5. Comparison of Hull Dissipated, Hull Radiated, and Acoustic Dissipated Power Values, Baseline Vehicle at 20 mph (32 km/hr)

averaged vibration levels and the radiation efficiencies of the individual panels. The radiation efficiencies of the integral hull panels were determined analytically. The radiation efficiencies of various lightweight panels such as the deck were determined experimentally.

Fig. 5 shows that the acoustic power dissipated in the internal volume matches the power radiated from panels. This is important, because it gives confidence in the calculation of the rela-

tive contributions of the individual plates. The figure also shows that the power dissipated in the hull is significantly greater than the acoustic radiated power, as would be expected. However, if the panel radiation is increased by 3 dB to account for radiation from both sides, it becomes apparent that acoustic radiation is accounting for approximately 10 percent of the hull dissipation. This indicates how lightly damped the baseline vehicle is.

For the purposes of noise control, the contributions of the individual panels is even more interesting than the total radiated power. The individual panel contributions to the interior levels are shown in Fig. 6. The top plate, upper side plates, and lower side plates were similar in level and only their average is shown. Many panels with a large combined area contribute to the radiated power. Therefore, the use of barriers for effective noise control would require almost total coverage.

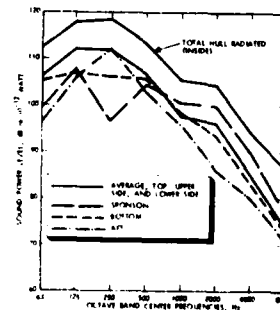


Fig. 6. Contributions of Individual Panels to Hull Radiated Power, Baseline Vehicle at 20 mph (32 km/hr)

The lightest member, the sponson, radiates well at high frequencies but not well in the critical 250 and 500 Hz bands. Nevertheless, the sponson was chosen for damping treatment because of excellent coupling to the rest of the hull and because it forms an energy path to the upper structure. The results of adding a 0.625-inch (16 mm) thick layer of damping tile to the sponson are presented in Fig. 7. Comparison with Fig. 6 shows that not only the sponson, but adjacent plates are reduced in level and radiated power.

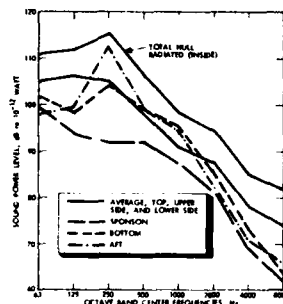


Fig. 7. Contributions of Individual Panels to Hull Radiated Power, Damped Sponson, 20 mph (32 km/hr)

The effectiveness of sponson damping was determined three ways: by direct measurement of interior noise, by calculation of panel radiation, and by the ratio of hull loss factor before and after. The results of these three comparisons are shown in Fig. 8. The results are similar, contributing confidence to the experimental results, especially in the 250 and 500 Hz octave bands. On the other hand, the apparent 6 dB improvement at 125 Hz determined from hull radiation is clearly suspect. The damping material, when tested separately, did not exhibit the loss factor improvement necessary. The apparent improvement is attributed to differences in vehicle track excitation on the tests before and after damping. This obvious error emphasizes the need for evaluating effects in more than one manner.

HULL VIBRATORY INPUT POWER

The contributions of the individual suspension members had been determined by source isolation, Fig. 1. The previous study [2] also evaluated the interior noise to force transfer functions in the horizontal and vertical directions for the idler and sprocket. Sub-

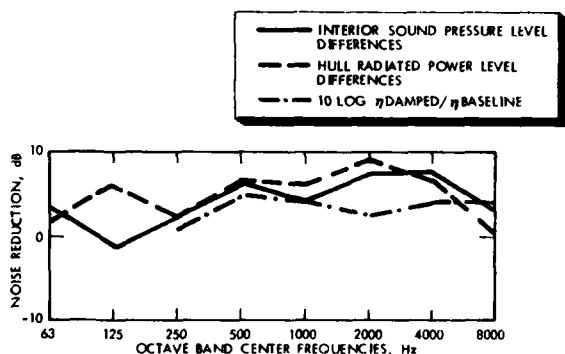


Fig. 8. Interior Noise Reduction Due to Sponson Damping; Measured Directly, from Panel Vibration Levels, and from Hull Loss Factor Values

tracting the magnitude values of a transfer function (expressed in decibels) from the appropriate interior noise level values yields an estimate of the force spectra. These force spectra are utilized along with the impedance measurements, subsequently described, to model the vibratory power input to the hull from the various suspension members.

The instrumentation block diagram for evaluating the impedance characteristics of the hull at the suspension attachments is pictured in Fig. 9. The force applied to the point of interest was held constant and the response acceleration was plotted directly on a graphic level recorder. The ratio of response acceleration to force is called inertance. The testing was performed in a benign environment, and no filtering was required to exclude extraneous noise.

The structural inertance as measured horizontally and vertically at the idler spindle is shown in Fig. 10. The phase angle, indicating the resistive portion of the impedance, is greater in the vertical direction than in the horizontal direction below 400 Hz. This tendency was also evidenced in measurements of impedance made at the hull attachment points. The top attachment of the idler spindle exhibited larger resistive characteristics than either the forward or aft attachment points in the 100 to 250 Hz frequency range.

The relative power accepting characteristics of the idler attachment in horizontal and vertical directions

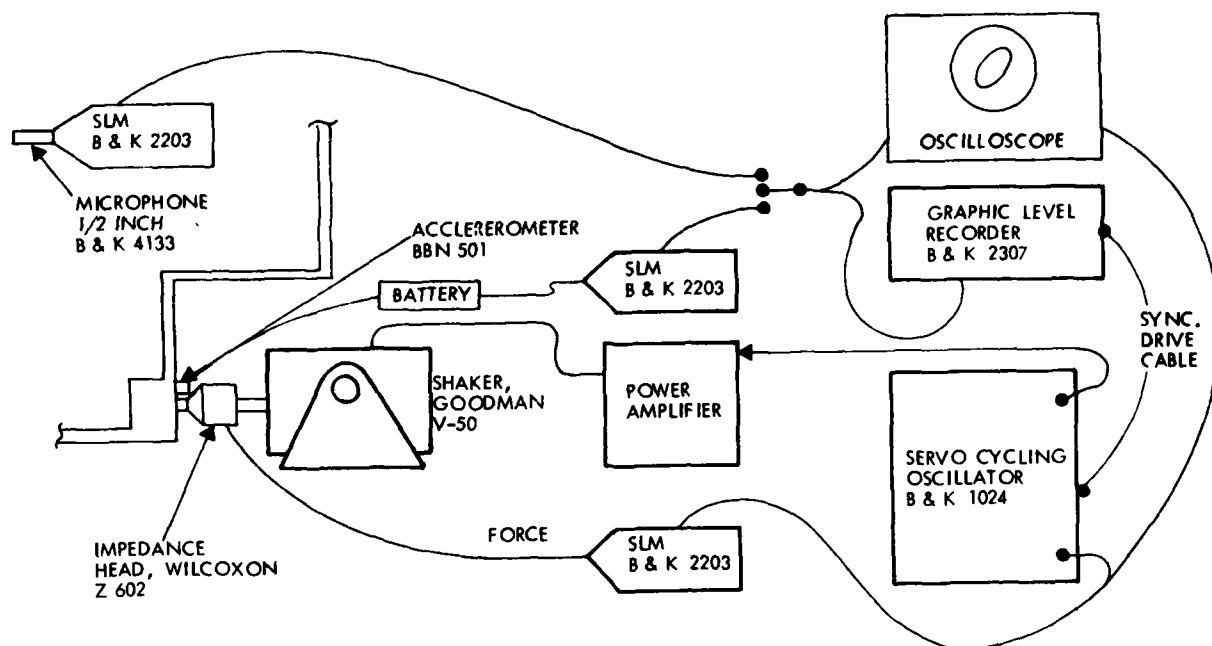


Fig. 9. Impedance and Transfer Function Measurement Instrumentation Block Diagram

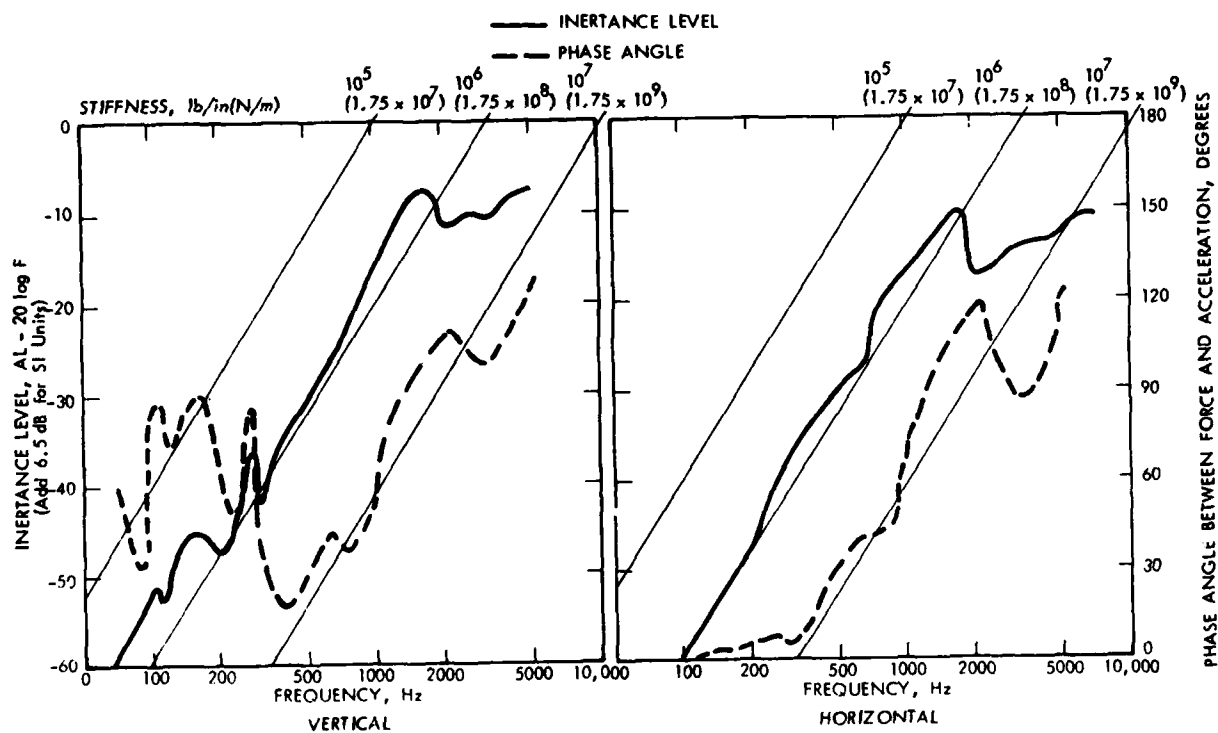


Fig. 10. Acceleration Response of Idler Spindle to Constant Force Input, Vertical and Horizontal Directions

are shown in Fig. 11. This figure shows that the ratio of vertical to horizontal is similar when evaluated from hull impedance measurements, from idler spindle impedance measurements, or from transfer function measurements between the idler rim and interior noise. The determination using hull point impedances is the most dissimilar. This dissimilarity is attributed to using hull point impedance measurements which may not be representative since the idler spindle flange spreads the load over a large area.

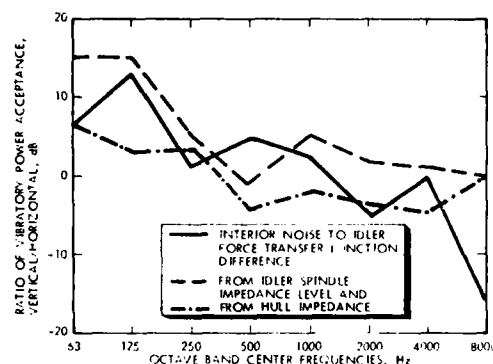


Fig. 11. Comparison of Idler Vertical and Horizontal Vibratory Power Acceptance Characteristics

Next, the input power estimates were compared with the hull dissipated power values. Fig. 12 shows input power estimates determined from three sets of measurements as follows:

Forcing Function	Hull Characteristic
Idler rim force	Spindle impedance
Idler rim force	Hull impedance
Idler arm acceleration	Spindle impedance

Note that none of the forcing functions are applied to the same place that the impedance values are measured. Therefore, the result would be valid only if the idler were a massless spring, which is not true. However, being able to relate the force spectra at the idler or the idler arm acceleration with the hull dynamic characteristics is worth the risk of inaccuracies. The results, Fig. 12, show that all three estimates are reasonable in the 125 and 250 Hz bands. In the high frequency bands, the idler arm tends to be isolated from the hull and forces on the arm are not transmitted to the hull without attenuation. Interestingly, the idler arm accelerometer does not account for the idler

power input in the high frequency bands. This was not the case when using roadarm vibration measurements to estimate input power. Since the vibration of the spindle arm would tend to lead to overestimates of input power, the spindle arm vibration high frequency results are considered suspect.

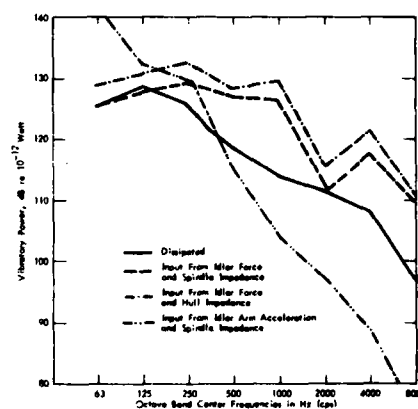


Fig. 12. Comparison of Calculated Input Power and Hull Vibratory Dissipated Power for Idlers

The difference in idler horizontal and vertical power accepting characteristics for a constant force input suggested a modification to the idler spindle, Fig. 13. Flanges were added top and bottom along with bolts into the hull. The bolt locations were in line with the edge of the back plate which is directly behind the lower side plate and idler spindle, Fig. 13. The purpose was to evaluate the potential for reducing the input power by means of minor structural modifications. Measurement of the horizontal and vertical impedance on the spindle, Fig. 13, showed virtually no changes from the baseline configuration. Accelerometer surveys with the excitation at approximately 100 Hz showed a well-defined upper side plate mode. The conclusion reached was that in the low frequency region the impedance of the attachment points are a function of the modes of the overall hull, and that local structural characteristics are not dominant.

CONCLUSIONS AND RECOMMENDATIONS

The thrust of the study was two-fold--first to develop experimental analysis techniques and second to evaluate noise control concepts. With respect to the first, excellent agreement was obtained between panel radiation and interior acoustic dissipation. Similarly, good agreement was obtained on the



Fig. 13. Idler Spindle with Stiffening Tabs and Bolts in Line with Back Plate

relative contribution of horizontal and vertical idler forces. However, the comparison of input and dissipated vibratory power evidenced large discrepancies. It is concluded that panel radiation can be estimated with confidence from acceleration measurements, but the use of point impedances to estimate power flow should be done on a comparative, not absolute, basis.

The recommended methods of extending this work is to examine other vehicles with somewhat different structural and interior noise characteristics and deduce which structural characteristics influence the impedance at the suspension attachments and therefore influence noise transmission.

With respect to noise control concepts, hull damping was proven effective, but minor structural modifications of the hull were not. This result should be extended, making use of the estimates of the relative contributions of the panels to radiated noise.

REFERENCES

1. C. L. Bates and C. R. Sparks, "Development of Measurement Techniques for the Analysis of the Tracked Vehicle Vibration and Noise," Final Technical Report, SWRI Project No. 04-1421, Contract No. DA-23-072-AMC-144(T), Oct. 30, 1964.
2. T. R. Norris, R. B. Hare, A. G. Galaitis, G. R. Garinther, "Development of Advanced Concepts for Noise Reduction in Tracked Vehicles," U.S. Army Human Engineering Lab. Tech. Memorandum 25-77, August 1977.

3. L. L. Beranek, Editor, Noise and Vibration Control, Chap. 11. McGraw Hill, New York, 1971.
4. R. H. Lyon, Statistical Energy Analysis of Dynamical Systems: Theory and Applications. M.I.T. Press, Cambridge and London, 1975.
5. G. Maidanik, "Response of Ribbed Panels to Reverberant Acoustic Fields," J. Acoustic Soc. Am., Vol. 34, No. 6, pp. 809-826, 1962.

DISCUSSION

Voice: We are very interested in the Statistical Energy Analysis approach in fact we have some people who are working on it; we would like to predict the acoustical energy that goes into Air Force electro-optical systems inside aircraft. One of our problems is determining the coupling loss factor between the various sub-components. Could you go a little more into detail about that?

Mr. Hare: We did not develop the coupling loss factor. This hull is so very well coupled that we used a single number for it, based on the overall hull loss factor, and our comparison with the actual measurement showed that that was a good approximation. That is the big problem with that particular analysis method unless you can measure those quantities. I don't have an answer for that.

Voice: I guess we are finding that out, there are not many welded joints in an airplane.

Mr. Hare: This is very convenient.

Voice: I noticed your frequency band. At what frequency do you believe your technique? SEA is really a high frequency high modal density technique.

Mr. Hare: We correlated with actual measurements at low frequencies and we found it was a fairly accurate approximation. You will notice that our low frequency analysis of that inertance graph mislead us, but we still felt that we had to do something there. We know that is not a local disturbance so we could go on and explore the rest of it. Now we know that that is the first mode of the upper side plate that is absorbing all of the energy.

REDUCING TRACKED VEHICLE VIBRATION AND NOISE HARDWARE CONSIDERATIONS

Ronald B. Hare, FMC Corporation

and

Thomas R. Norris, Consultants in Engineering Acoustics

High levels of vibration and noise in light military tracked vehicles result from interaction of the track with sprockets and idlers and is not limited to ground reactions. The use of rubber in the track design and track inertia effects produce less noise than theory predicts. Hardware to further soften track impacts at the idlers and sprockets is now under development. An experimental idler with a predicted 15 dB noise reduction will be tested soon. Reduction of hull vibration and noise has been demonstrated and practical damping concepts are now under development.

INTRODUCTION

Tracked vehicle vibration and noise have been the subjects of a large number of studies in the last 30 years. The most important result of these studies has been the knowledge that high vibration and noise is a result of the interaction of the moving track string with fixed suspension components such as the sprockets and idlers, and is not limited to ground reactions. Many vibration reduction programs have failed because the influence of all vibration sources was not considered. Practical vibration reduction must start with a good definition of the problem so that each vibration source can be dealt with in proportion to its overall importance.

LIMITATIONS - THE TRACKED VEHICLE ENVIRONMENT

Isolator theory has told us that softer impacts result in less transmission of vibration energy. Most lightweight high speed tracked vehicles utilize rubber elements between their tracks and suspension components. Also, some interesting track inertia effects tend to reduce impact forces with increasing vehicle speed. Tracked vehicle vibration is, therefore, already lower than it could have been.

Further increases in softness threaten to increase the chances for damage from unusual forces developed in normal operation of tracked vehicles. Unusual forces are caused by:

- Ingestion of debris (rocks, branches, dirt)
- Suspension bottoming from trench crossing
- Track disengagement

Military tracked vehicles are expected to survive forces of this nature. The challenge is to develop softer hardware that will not impair the "get home" capability of tracked vehicles.

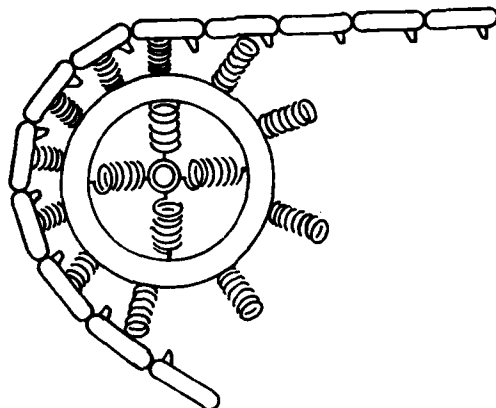
SOME HARDWARE SOLUTIONS

Development testing of quieter tracked vehicle hardware is now in progress. Design concepts of the devices being evaluated are discussed below:

An Experimental Compliant Idler with a Predicted 15dB Noise Reduction

The experimental idler cushions the impacts of track shoes as they enter the idler.

The concept of the device is shown in Figure 1. Note that tangential as well as radial motion is permitted.



NOTE: THE EXPOSED COIL SPRINGS ARE SCHEMATIC REPRESENTATIONS OF COMPLIANT ELEMENTS FOR ILLUSTRATION PURPOSES ONLY.

Fig. 1 - Conceptual sketch of compliant idler

Deflection, compliance, size restrictions, and energy storage requirements dictated the use of rubber in shear for the compliant elements.

Heat buildup is the major hardware problem expected in this design. Compliant elements are now under test to determine dynamic losses and heat transfer rates.

Softer Inner Track Pads

Roadwheel path track pads provide the only compliance between the track and idler in most lightweight tracked vehicles. Their high durometer and position inside of a steel cavity cause track/idler impacts to be rather sharp. Softer pads have been tested statically and several designs have been proposed. However, the pad design must be combined with an idler rim shape for optimum performance which creates compatibility problems if only one component is retrofitted.

Modified Idler Rim and Sprocket Carrier Shapes

Several idler rim shapes have been developed which take advantage of the existing roadwheel path track pad for noise reduction. The best of these has yielded a 5dB idler noise reduction with negligible predicted impact on cost, weight, and durability.

Sprocket vibration generation is similar to idler vibration generation. Forces due to impacts of track shoes on the sprocket carrier can be reduced by optimizing the shape of the impact surface so that a balance between softness and durability is achieved.

Hull Damping Concepts

Vibration has been reduced by damping especially active vehicle panels, such as the horizontal sponson and floor plates. Similar reductions in noise have been achieved by lagging the sponsons in the IFV vehicle.

Constrained layer damping methods are attractive for performance and durability. However, cost and potential fabrication problems have prevented their serious consideration in tracked vehicles when weighed against predicted vibration and noise reduction benefits.

• Softer Roadwheels

Roadwheel noise has been identified as a major source of noise in lightweight tracked vehicles at high speeds. Reduction of roadwheel vibration appears to be more difficult than idler or sprocket vibration reduction because of their vulnerability, space limitations, and their relatively large number. Softer wheels have been built in an attempt to reduce vibration in the roadarms and tests are now in progress.

The only other feasible source of roadwheel noise reduction is hull vibration reduction at the roadarm mounts. Structural requirements at the mount locations have prevented the achievement of major reductions in this area.

SUMMARY

The best potential for reduction of tracked vehicle vibration and noise lies in reduction of the forces imposed by track shoes impacting hull-mounted suspension components. Our recent research programs have shown the reasons for this and have *resulted in concepts that might be applied to quieter tracked vehicle hardware.*

Suspension component durability is critical to the success of a vehicle mission. Noise and vibration performance is necessarily of low priority when durability trade-offs are considered. Cost and weight increases are very undesirable and significantly decrease the chances for incorporation of quieter hardware on production vehicles. On the positive side, reduction of dynamic forces imposed on hull and mount components will result in reduced fatigue problems and could result in lower weight designs as strength requirements are reduced.

We are confident that lightweight tracked vehicles which meet the noise requirement, MIL-STD-1474, Category A requirements, can be produced within the next five (5) years. Our eventual goal is to reduce noise to the levels that permit unlimited safe operation of vehicles without earplug requirements. This will be a significant accomplishment, since no lightweight high speed tracked vehicle has ever consistently achieved this level of noise performance.

THE USE OF AN EARTH BERM TO REDUCE THE ENVIRONMENTAL
NOISE IMPACT OF THE TEST TRACK AT DETROIT ARSENAL

Nelson D. Lewis
Bio-Acoustics Division
US Army Environmental Hygiene Agency
Aberdeen Proving Ground, MD 21010

The opinions or assertions contained herein are the private views of the author and are not to be construed as reflecting the views of the Department of the Army or the Department of Defense.

An environmental noise assessment of the tank test track at Detroit Arsenal revealed sound pressure levels exceeding $L_A = 90$ dB at the fence from tanks passing by. Since residents are located within 10 meters of the fence, an earth berm and barrier is being built. The noise reduction of this earth berm and barrier was predicted using the 1/3 octave band spectrum of the tank. The predicted noise reduction will be verified with measurements after the earth berm and barrier is completed.

INTRODUCTION AND BACKGROUND

In recent years, environmental noise has joined air and water pollution as unnecessary byproducts of our society. The annoyance caused by this pollutant is leading to the filing of complaints against the noise producing activity.

At Detroit Arsenal, a potential complaint area exists. A residential area is located approximately 40 meters from the tank test track. The average maximum A-weighted sound pressure level (L_A) at the fence, approximately 30 meters from the track, is 92 dB during a tank passby. There are approximately 300 passbys per day.

Recognizing the potential problem, the facilities engineer obtained the dirt required from a nearby highway project to construct an earth berm. The Bio-Acoustics Division of the US Army Environmental Hygiene Agency was asked to evaluate the use of an earth berm to reduce the noise impact from the test track. This paper describes the evaluation process used.

FIELD MEASUREMENTS AND ANALYSIS

The noise from the tanks was recorded at three points along the fenceline. The maximum level was $L_A = 92$ dB, with a range from $L_A = 83$ to $L_A = 97$ dB. It was observed that the loudest noise source on the tank was the exhaust, located about 2 meters above the ground.

From the recorded tapes, the 1/3 octave band spectra of the tank passbys were obtained. This average 1/3 octave band spectrum is shown in Figure 1.

BARRIER THEORY

With the insertion of an earth berm or barrier in the path of propagation between the source and receiver, the reduced sound reaches the receiver primarily by diffraction of the sound over the top and around the ends of the earth berm or barrier. Diffraction is loosely defined as the bending of acoustic waves around corners.

The noise reduction of an earth berm or barrier is a function of the difference between the diffracted path length and the direct path length (Figure 2), and the frequency content of the source. The simple model used to predict the noise reduction of a barrier is based on a mathematical approximation to Maekawa's design curve (1,2) (Figure 3). This approximation is

$$NR = 20 \log_{10} \frac{2\pi (\delta f/c)^{1/2}}{\tanh \pi (\delta f/c)^{1/2}}$$

where NR is the noise reduction, δ is the difference between the diffracted and direct path lengths, f is the frequency and c is the speed of propagation of sound. The hyperbolic tangent (\tanh) approaches 1 when $\delta f/c$ is greater than 2.

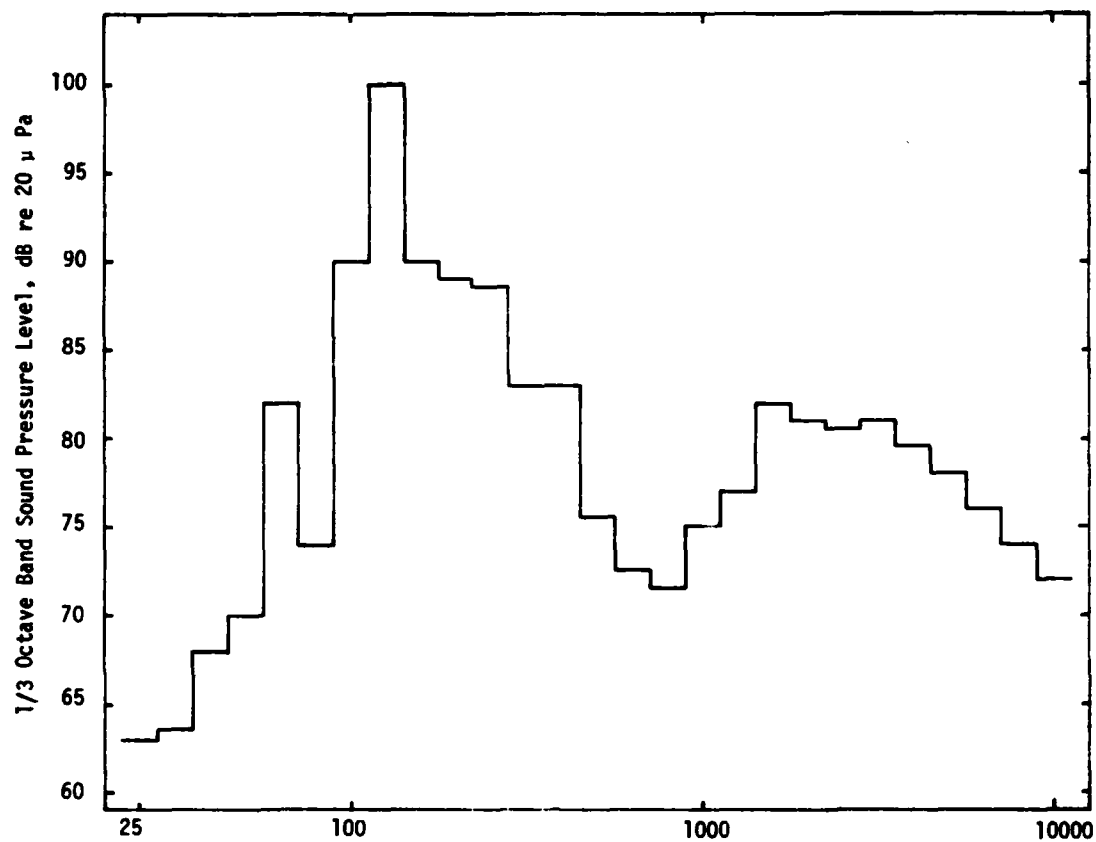


Figure 1, 1/3 Octave Band Spectrum of Tank Passby at 30 Meters

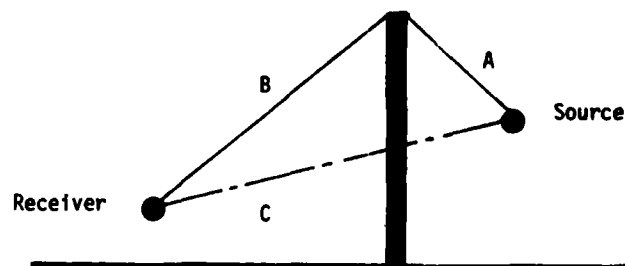


Figure 2, Diffracted Path Length ($A + B$) and Direct Path Length (C)

This simple model has been compared with acoustical scale model measurements (3) (Figure 3) and found to predict from 0 to 5 decibels lower than measured. This model has also been compared with the theoretical prediction models and found to be within plus or minus 2 decibels of these models.

The noise reduction model used has two advantages over the theoretical models. First, it can be easily programmed on a hand-held calculator. More importantly, by looking at the model, it is immediately seen that the noise reduction increases if the path length difference or frequency is increased. These trends cannot be determined by looking at the theoretical models.

EARTH BERM AND BARRIER DESIGN

When designing the earth berm and barrier for the test track, the following parameters were considered: 1. The test track was approximately 2 meters above ground level; 2. The exhaust of the tank, the primary noise source, was approximately 2 meters above the test track; 3. The receiver height was approximately 2 meters; 4. The distance from the centerline of the test track to the fence was approximately 30 meters; and 5. Since for a fixed height barrier, the most noise reduction is obtained by locating the barrier as close to the source or receiver as possible, the barrier was located approximately 10.7 meters from the centerline of the test track. These design parameters are shown in Figure 4. Because of space limitations, a 2 meter high barrier was built on top of the earth berm.

Since the frequency spectrum of the tank differs, that is, contains more low frequency energy, from the typical highway vehicle, the simple highway barrier prediction curve was not used. Instead, the noise reduction was computed for each 1/3 octave band. For the path length difference of the barrier being designed ($\delta = 0.53$ meters), the noise reduction as a function of frequency is shown in Figure 5.

To obtain the noise reduction of the berm, the noise reduction for each 1/3 octave band was subtracted from the 1/3 octave band level, and the resulting levels were added on an energy basis. The predicted 1/3 octave band spectrum is shown in Figure 6.

Thus, it was predicted that the earth berm and barrier will reduce the average maximum linear sound pressure level by 10 decibels from 102 dB to 92 dB. The A-weighted level will be reduced by 14 decibels from $L_A = 92$ dB to $L_A = 78$ dB. If the height of the barrier portion is increased to 4 meters, the linear noise reduction will increase to 13 decibels and the A-weighted to 18 decibels.

EXPECTED FIELD RESULTS

Even though the prediction model used yields lower noise reductions than field and model measurements, it is expected that the actual sound pressure levels will be approximately equal to the predicted levels. The prediction model does not include contributions from refraction, reflection, and ground impedance. The changes in these factors from one location to another can cause a significant difference between the predicted and actual results.

When the earth berm barrier is completed, a second set of field measurements will be made to compare with the predicted levels. If the earth berm barrier reduces the A-weighted sound pressure level by more than 10 decibels, the noise levels from the tank passbys will be less than the local noise criteria at the fenceline.

REFERENCES

1. Z. Maekawa, "Noise Reduction by Screens," Applied Acoustics, Vol. 1, 1968, pp. 157-173.
2. U. J. Kurze, "Noise Reduction by Barriers," Journal of the Acoustical Society of America, Vol 55, No. 3, March 1974, pp. 504-518.
3. N. D. Lewis, "Measurement and Prediction of Sound Attenuation by Highway Barriers using Acoustic Modeling Technique," PhD Dissertation, University of Massachusetts, March 1976.

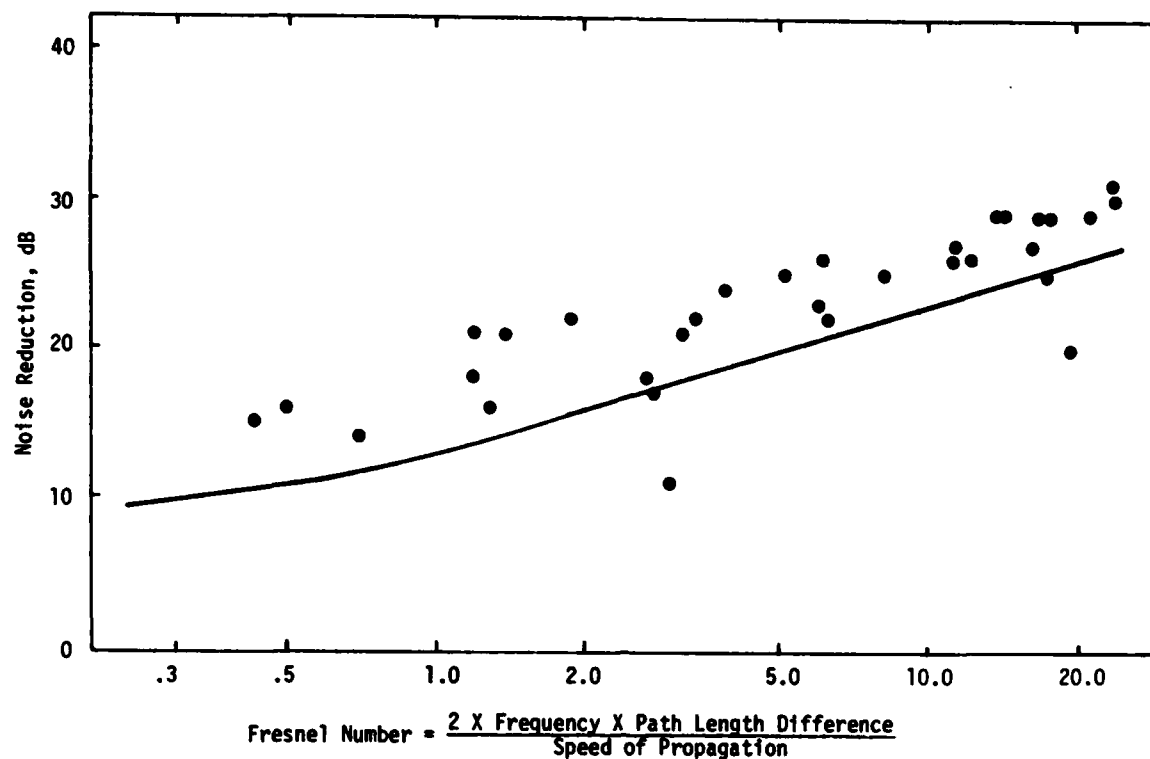


Figure 3, Maekawa's Design Curve for Barriers with Scale Model (●) Results Added.

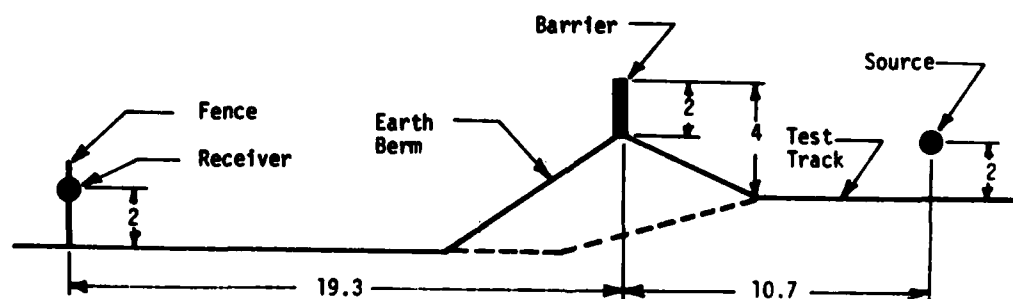


Figure 4, Barrier Design (Dimensions in Meters)

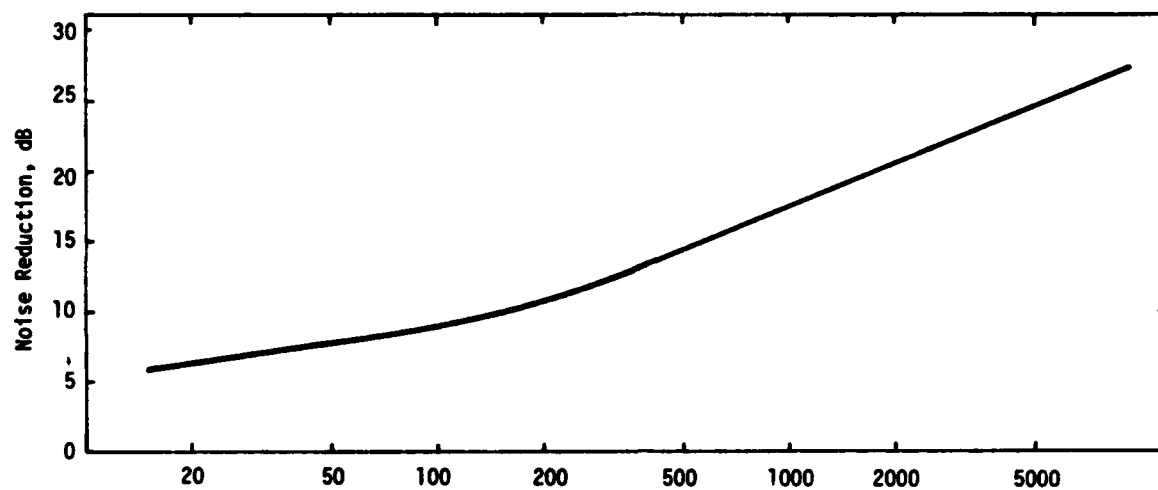


Figure 5, Noise Reduction as a Function of Frequency for the Earth Berm and Barrier

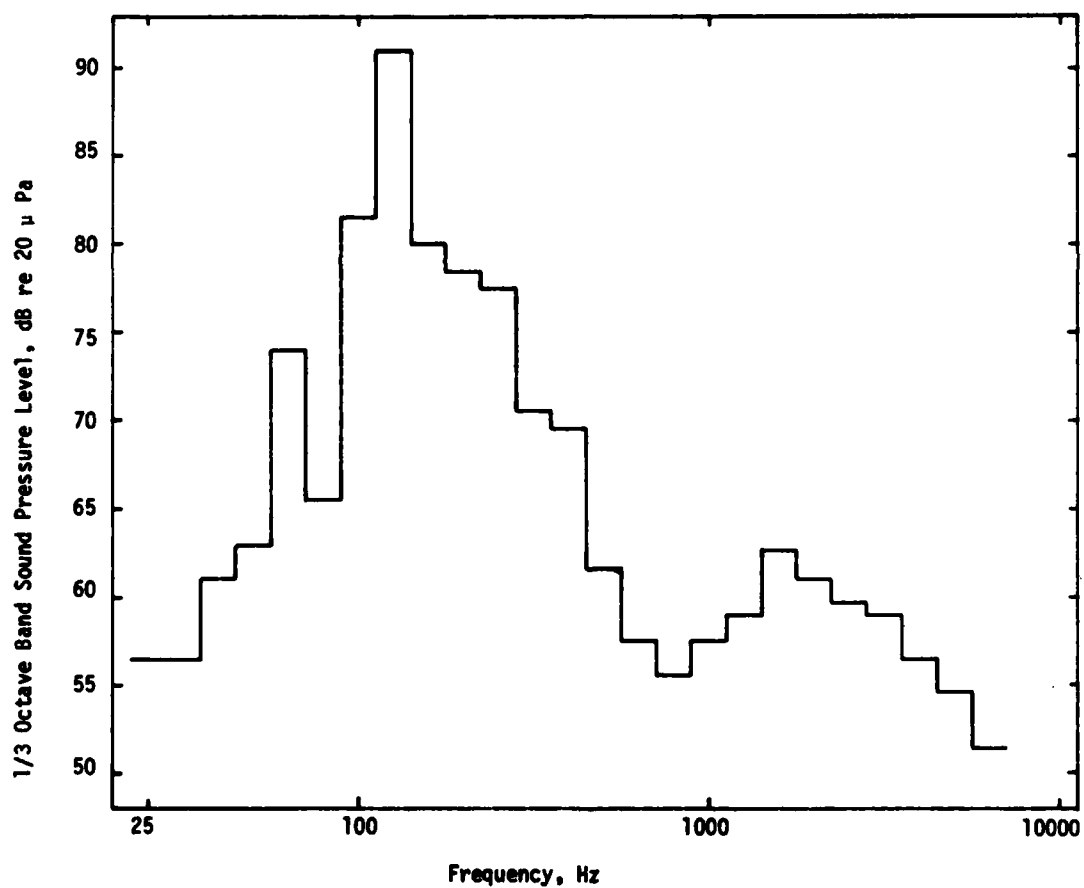


Figure 6, Predicted 1/3 Octave Band Spectrum of a Tank Passby at 30 Meters

DISCUSSION

Mr. Martin (General Electric): What was the barrier material?

Mr. Saks: The berm was dirt and I believe that the barrier was to be any material with an approximate weight of five pounds per square foot. Heavier material would be wasted because of the diffraction over the top of the barrier.

Mr. Rees (US Army Tank Automotive Research and Development Command): The barrier was placed on top of the berm because its base dimension limited its height. There was not enough room on the property to build a wider berm. The noise barrier was constructed because the test truck is heavily used and it is near single family houses. We wanted to avoid the possibility of complaints of excessive noise from the surrounding community.

THE SHOCK AND VIBRATION BULLETIN CLASSIFICATION CHANGE NOTICE (U)

(U) NOTICE #2 (July 1978)

1. Shock and Vibration Bulletin 35, Part 1 of March 1966.

- a. Article Page 1 - "A Simulated 25-30 CPS Deck for Shock Testing", Culver J. Floyd, Raytheon Company - Declassified
- b. Article Page 13 - "Blast Loading of Model Antenna Structures", R. Kirk Gregory, Southwest Research Institute - Declassified
- c. Article Page 23 - "Background and Current Status of Underwater Explosion Shock Specifications and Testing", Gerald M. Mayer, Navy UWSL - Declassified
- d. Article Page 29 - "Magnetic Tape Recording in a Severe Missile Environment-A Case History", J.P. White and J. Montsma, Bell Telephone Laboratories - Declassified
- e. Article Page 101 - "Analysis of Response of Equipment on a Drop Test Shock Machine", R.L. Bort, DTMB - Classified
CONFIDENTIAL by Authority of NAVSHIP INSTR 5510.67,
Exempt from GDS of E.O. 11652, Exempt Category 3,
Automatically declassified 31 December 1996.

2. All of the articles included in Shock and Vibration Bulletin 35, Part 1 of March 1966 have been reviewed for current classification, and only the article on page 101 remains classified (Confidential as indicated in paragraph 1. (e) above).

3. AUTHORITY - NRL ltr 1240-221:HWO:lm of 4 August 77 and NRL ltr 1240-5:HWO:sbn of 1 February 1978

NOTE: Authors and Contributors to previous Shock and Vibration Bulletins are requested to review their submissions and to inform the Shock and Vibration Information Center of any changes in classification and/or declassification.